

Sheffield Hallam University

Computer simulations of tapered particles

ELLISON, Laurence J.

Available from the Sheffield Hallam University Research Archive (SHURA) at:

<http://shura.shu.ac.uk/3821/>

A Sheffield Hallam University thesis

This thesis is protected by copyright which belongs to the author.

The content must not be changed in any way or sold commercially in any format or medium without the formal permission of the author.

When referring to this work, full bibliographic details including the author, title, awarding institution and date of the thesis must be given.

Please visit <http://shura.shu.ac.uk/3821/> and <http://shura.shu.ac.uk/information.html> for further details about copyright and re-use permissions.

Sheffield S1 1WB

101 905 912 5



Sheffield Hallam University
Learning and IT Services
Adsetts Centre City Campus
Sheffield S1 1WB

REFERENCE

ProQuest Number: 10694501

All rights reserved

INFORMATION TO ALL USERS

The quality of this reproduction is dependent upon the quality of the copy submitted.

In the unlikely event that the author did not send a complete manuscript and there are missing pages, these will be noted. Also, if material had to be removed, a note will indicate the deletion.



ProQuest 10694501

Published by ProQuest LLC (2017). Copyright of the Dissertation is held by the Author.

All rights reserved.

This work is protected against unauthorized copying under Title 17, United States Code
Microform Edition © ProQuest LLC.

ProQuest LLC.
789 East Eisenhower Parkway
P.O. Box 1346
Ann Arbor, MI 48106 – 1346

COMPUTER SIMULATIONS OF TAPERED PARTICLES

Laurence J. Ellison

A Thesis submitted as partial fulfillment of the requirements
of Sheffield Hallam University
for the degree of Doctor of Philosophy

September 2008



Abstract

We present here the results of a series of molecular dynamics (MD) simulations of systems of soft repulsive tapered particles. Essentially, the objective of the project was to investigate the effect that changing the degree of taper of these particles has on the collective behaviour of the system. The particle shapes were modelled using the parameterised Gaussian overlap (PHGO) contact function, which had previously been used in Monte Carlo (MC) studies of systems of hard particles with the same range of shapes [*Phys. Rev. E* **68**, 021708 (2003)].

The work carried out falls into three main categories. Firstly we calculated the splay and bend reduced flexoelectric coefficients, e_{11}^* and e_{33}^* , for a number of systems in the nematic phase. This was done using the linear response approach developed by Nemtsov and Osipov [*Kristallografiya* **31** 2, 213-218 (1986)]. The values of e_{11}^* measured for the tapered systems studied were all positive and of the order of +0.1, whilst the e_{33}^* values were of a similar magnitude but negative in all cases. These numbers correspond to values of the order of pCm^{-1} , which is consistent with typical values measured experimentally for the flexoelectric coefficients. The reduced coefficients for systems of uniaxial particles were also calculated and found to be approximately zero, as they should be for particles with this type of symmetry.

The second major theme in the project was the mapping out of the shape-density phase diagram, through both compression and decompression sequences, for tapered particles having a constant length to breadth ratio of 3 but different degrees of tapering, ranging from an extreme tear-drop shape to the uniaxial Gaussian ellipsoid. The results of our MD simulations broadly agreed with those obtained by the MC route [*Phys. Rev. E* **68**, 021708 (2003)]. Isotropic, nematic, smectic and ordered solid phases were clearly identified. In addition a so-called ‘curvy-bilayer’ (CB) phase was observed, which locally possessed similar order to the smectics but did not exhibit any clear long range order.

The structure of the CB phase was investigated further and found to be a type of bicontinuous cubic phase, specifically the $\text{Ia}\bar{3}\text{d}$ or gyroid (G) as it is also known – a phase never before obtained from this type of simulation. Characterisation of the I-G transition was undertaken, which indicated that the gyroid freely self-assembled from precursors present in the isotropic fluid. The Sm-G transition was also characterised and found to take place via the formation, firstly of stalks joining two adjacent smectic bilayers and then subsequently pores which bisect these bilayers and initiate the emergence of the gyroid morphology.

Acknowledgements

I would like to thank my supervisors Dr. Doug Cleaver, Prof. Chris Care and Dr. Fred Barmes for their unstinting support and guidance during this project. I am also very fortunate to have been surrounded by a very friendly and smart bunch of people in the staff and students of the Modelling Lab. Worthy of special mention here is Mr. Terry Hudson who built and maintains the Beowulf cluster, on which I ran my simulations. I would also like to thank the staff in the admin department, for all their assistance, particularly Rosemary Booth, whose support was pivotal in enabling me to complete this thesis.

I want thank Prof. Claudio Zannoni and all the members of his group at the University of Bologna, for helping to make my time in Italy so enjoyable. The same goes for the people I met at the CINECA computing facility, Bologna. They do their country great credit.

I am indebted to Sheffield Hallam University for funding my PhD and also to HPC-Europa for generously funding the trip to Italy.

Finally a massive thanks to all my friends and family, especially my parents, who have been so loyal and supportive to me all my life. A special thanks also to my housemates, and great friends, Kate and Pab who have put up with my grumbling and kept me sane over the last few years!

Dedication

Watch out for minus signs.

Advanced Studies

The following is a chronological list of related work undertaken and meetings attended during the course of study.

- British Liquid Crystal Society Annual Conference (poster presentation), Manchester Metropolitan University 5th-7th April 2004.
- CCP5 Summer School: Methods in Molecular Simulation (poster presentation), Cardiff University 9th-17th July 2004.
- CCP5 Annual Conference: New Perspectives in Modelling and Simulation: Theory and Applications, University of Sheffield 2nd-4th September 2004.
- Northern Atomistic Simulation Group Meeting (oral presentation), Daresbury Laboratory 5th January 2005.
- Visit to CINECA and the Department of Physical and Inorganic Chemistry, Bologna University under the HPC Europa scheme, Bologna, Italy 7th April-21st May 2005.
- Royal Society Discussion Meeting: New Directions in Liquid Crystal Science, Royal Society 5th-6th December 2005.
- CCP5 One-day workshop: parallel DL_POLY, University of Sheffield 7th April 2006.
- British Liquid Crystal Society Annual Conference (poster presentation), University of York 11th-13th April 2006.
- CCP5 Annual Conference: Phase Behaviour from Molecular Simulations (oral presentation), University of Bradford 4th-6th September 2006.
- Meeting on Flexoelectricity in Liquid Crystals, Oxford University 19th September 2006.

Contents

1	Introduction	2
1.1	Overview of liquid crystal phases	2
1.2	Predicting mesophase behaviour	5
1.3	Objective of the project	12
1.4	Outline of the thesis	13
2	A model for tapered particles	16
2.1	Defining the shape	16
2.2	The Gaussian overlap contact function	19
2.3	The pear-pear contact function	28
2.4	The model potential	34
3	Simulation methodology	38
3.1	Overview	38
3.2	Forces, torques and their integration	41
3.3	Runtime Observables	46
3.4	Post processing	50
4	Preliminary simulations	55
4.1	Isotropic compression series	56
4.2	Structural detail	68
4.3	Decompression with anisotropic rescaling	78
4.4	System size effects	88

4.5	Summary and Conclusions	91
5	Measurement of flexoelectric coefficients	93
5.1	The linear response approach	96
5.2	Simulation technique	100
5.3	Results of 0.5 Mstep simulation runs	104
5.4	Results of 10 Mstep simulation runs	110
5.5	Summary and Conclusions	117
6	General phase behaviour	120
6.1	Phase diagram from MC simulations	121
6.2	Phase diagram from compressions	122
6.3	Creation of artificial smectics	138
6.4	Phase diagram from decompressions	146
6.5	Summary and conclusions	151
7	The gyroid phase	155
7.1	Study of a scaled up CB system	156
7.2	The I-G transition	167
7.3	The Sm-G transition	176
7.4	Summary and conclusions	184
8	Summary and Conclusions	187
	Appendices	189
A	Reduced Units	190
B	Potential, forces and torques	192
B.1	Summary of potential for tapered particles	192

B.2 Derivation of forces derivatives	194
B.3 Derivation of torque derivatives	195
C Equations of motion	197
C.1 The Velocity-Verlet integration algorithm	197
D Mathematics	199
E Contact profiles	200
F Flexo data	202
Bibliography	206

CHAPTER 1

Introduction

1.1 Overview of liquid crystal phases

The properties of all materials ultimately derive from the molecules of which they are comprised. However, it is often the case that the most useful properties of a material, rather than deriving solely from the intrinsic characteristics of its constituent molecules, also strongly depend upon the collective organisation of those molecules. An important class of materials which provides an excellent illustration of this are liquid crystals (LCs). LCs are so called because they have properties in common with both the liquid and solid crystalline phases of matter. On the one hand, the molecules that comprise LCs are able to diffuse and change their orientations and so the material is fluid. On the other hand, whilst the molecules have mobilities similar to those found in simple fluids, they have a tendency to collectively adopt configurations which possess long range orientational order and in many cases long range positional order also. LC phases are therefore often referred to as mesophases, from the Greek *meso* meaning ‘intermediate’, the molecules that form them are similarly termed mesogens.

Liquid crystals are an extremely diverse class of materials in terms of their constituents, the structures they form and the physical processes which are responsible

for the formation of the mesophases. What follows is a very basic overview to give a flavour of some of their essential characteristics, for the purposes of putting the objective of this project into context. For a proper introduction to the subject, the reader is directed to the texts [1–3].

In terms of classifying the types of molecules that form liquid crystals, two main categorisations have traditionally been used, which relate to the overall shapes of the molecules. Calamitic LC molecules have an overall shape that is rod-like. A classic example of calamitic mesogens is the n CB family. These consist of an essentially rigid aromatic core of meta biphenyl. At one end of the core, a cyano headgroup is attached and at the other end a flexible alkyl chain, C_nH_{2n+1} . Calamitic LC molecules typically range in size from 20–50Å in length and 3–5Å in width. Discotic LC molecules, on the other hand, have a disk-like form. In general they consist of a flat rigid core made up of several aromatic rings from the perimeter of which radiate flexible alkyl chains. The dimensions of discotic LC molecules typically range from 20–50Å in diameter whilst the thickness of the central disk is 3–5Å.

The simplest mesophase formed by calamitic LCs is the nematic, denoted N, in which the molecules have no long range translational order but do have a preferred orientation. This preferred orientation is defined by a unit nonpolar vector, \hat{n} , called the director. The degree of orientational order is characterised by an orientational order parameter, P_2 , which may be defined as a microscopic average over the molecular orientations with respect to the director

$$P_2 = \left\langle \frac{3}{2} \cos^2 \theta_i - \frac{1}{2} \right\rangle$$

where θ_i is the angle between the major axis of molecule i and \hat{n} . P_2 is zero for the isotropic phase, denoted I, in which the molecular orientations as well as the positions are randomly distributed. For an ideal system in which all the molecules are perfectly aligned $P_2 = 1$. Typical order parameter values for real liquid crystals range from 0.3 to 0.8. Discotic mesogens also form a nematic phase but in these, the orientational correlation is between the minor axes of the molecules,

which are perpendicular to their central disks.

Another important mesophase formed by calamitic mesogens is the smectic phase, denoted Sm, in which the molecules have a mutually preferred orientation and, in addition, stack into layers, thus imbuing the system with one dimensional translational order. If the director is perpendicular to the layers, the phase is termed smectic A (SmA). If it makes an angle other than 90° to the layers, it is known as a tilted smectic phase, denoted SmC. In both SmA and SmC, there is no intralayer ordering of the molecules. However smectic phases do exist in which the mesogens organise themselves into hexagonal or rectangular arrays within the layers, these are termed SmB phases. The variant of this phase in which the director is also tilted with respect to the layer normal is denoted SmI. In the SmB and SmI phases, there are no correlations between the mesogen positions from layer to layer, however the directions of the axes which define the ordered intralayer packing are correlated. This is known as bond orientational order. If smectic LC phases are cooled to sufficiently low temperatures or compressed to high enough density, they crystallise into the solid phase, which by definition possess both intra- and inter-layer long-range order.

So called chiral variants of some of the phases described above are also observed. These form when the mesogens, rather than being uniaxially symmetric, possess a distinct inversion asymmetry – they have a handedness. In the chiral nematic phases, which are by convention denoted by an asterisk like so N^* , the preferred orientation of the molecules rotates as one moves through the sample in a direction perpendicular to the director. In the chiral variants of the tilted smectic phases, the director, whilst maintaining a constant tilt angle with respect to the layers, rotates from layer to layer about the layer normal, thus describing a cone.

Discotic mesogens exhibit a markedly different type of positional order compared to the smectics formed by rod-shaped molecules. Instead of forming layers, they assemble into columns rather like stacks of coins. The positions of the disks along the axis of the layer may be periodic or disordered. Also the minor axes of mesogens may either be parallel to the column axis or tilted at an angle to it. The

columns themselves tend to form into two-dimensional lattice arrangements in which the ordering can be hexagonal, rectangular or oblique.

Besides categorising liquid crystals according to the symmetries of their constituent molecules and those of the structures that they form collectively, liquid crystals are also grouped according to the principle external agents which drive their phase transitions. In this regard, there are two major categories, namely thermotropic and lyotropic. With thermotropic LCs, phase transitions are driven by changes in temperature. Thermotropic LCs are usually composed purely of mesogenic molecules or blends of different mesogens. Mesophases are obtained from these types of materials either by cooling the initially isotropic fluid or else heating an initially crystalline solid. The phase transitions in these systems are brought about principally by the effect that thermal energy has on the conformations and mobility of the flexible parts of the mesogens. Lyotropic LCs on the other hand consist of mesogens in a solvent such as water or oil. Here phase changes are brought about principally by altering the concentration of the solution and, thus, the number of mesogens per unit volume. However in lyotropic LCs temperature will also play a role to a greater or lesser extent.

1.2 Predicting mesophase behaviour

Relating the properties of the constituents of LCs to their collective behaviour and thus gaining a better understanding of how to engineer them in order to better exploit their unique properties is indeed a formidable problem. The theoretical modelling of LCs and indeed of complex fluids in general, is extremely complicated due to the fact that these systems are dense and inhomogeneous, making it very difficult to treat the many body interactions which determine, at the molecular level, how the fluid behaves.

One of the key strategies adopted in theoretical modelling of dense fluids, which

avoids this difficulty, is mean field theory (MFT), also known as self consistent field theory. In this approach, the many interactions of a model fluid molecule with its neighbours are replaced by an average or effective interaction. Several such theories have been developed which makes qualitative predictions for phase transitions in liquid crystals consistent with experiment the most successful of these being Maier-Saupe theory. In general, MFT has been fairly successful in making qualitative predictions for phase transitions in thermotropic LCs that are consistent with experiment. However the approach rarely succeeds in making accurate quantitative predictions. The main reason for this is precisely that they neglect the contributions of short range interactions and also fluctuations in the overall interaction potential from the mean.

A second, more technically challenging approach, that does attempt to take into account short range interactions, is density functional theory (DFT). The most celebrated application of DFT, in relation to liquid crystals, was made by Onsager [4]. In this theory, the liquid crystal molecules are modelled as hard spherocylinders. A spherocylinder (SC) consists of a cylinder of length L and diameter D whose ends are capped by hemispheres also of diameter D . The term ‘hard’ means that each object interacts with its neighbours via an interaction that is repulsive and infinitely steep – in other words a pair of such particles may not overlap. In order to develop the theory, Onsager made the simplifying assumptions that the spherocylinders were extremely thin, i.e. $L \gg D$, and the volume fraction, η , of the system very low, i.e. $\eta = Nv/V = \rho v \ll 1$. Here N is the number of particles in the system, V the system volume, v the particle volume and ρ is the number density. The result of this analysis was an expression for the free energy of the system that could be used to determine its equilibrium phase at a given density. This led to the prediction of an isotropic-nematic transition at a density of the order of $\rho \sim 1/(L^2/D)$.

The crucial point is that Onsager theory predicts that volume exclusion effects alone, mediated by repulsive hard-core interactions, may be sufficient to bring about an LC phase transition. At the fundamental level, the driver of this phase

transition is entropy. In the model system of spherocylinders, the number of particles, N , the system volume, V , and the temperature, T , are constant. As such, the appropriate free energy for the system is the Helmholtz free energy, $F = U - TS$, where U is the internal energy and S the entropy. Since the particles are purely repulsive, their interactions do not contribute any potential energy, and therefore the internal energy is zero. By the same token, their interactions will be unaffected by temperature and so T can be treated as a constant. What remains then is a free energy that is dependent on entropy alone and the phase which is stable, i.e. the one that has the lowest free energy, at a given density, will be the one with the maximum entropy. That this is responsible for an isotropic-nematic transition appears counter-intuitive at first in as much as one would not expect a nematic, with its orientational order, to possess an entropy larger than the apparently more disordered isotropic phase. The reason the nematic is favoured at higher density is that, as the system is compressed and the elongated particles come into closer proximity, the effect of excluded volume will increasingly result in there being, on average, fewer positions available for a given particle to occupy. Consequently there are fewer different ways for the particles to arrange themselves, thus decreasing the positional entropy. If however the particles align with each other, though orientational entropy will be lost, excluded volume is reduced thus freeing up more space and increasing the number of positions the particles may occupy. It so happens that, at the isotropic-nematic transition, the loss in orientational entropy is outweighed by the gain in positional entropy. It should be added that this is not the only evidence for entropy driven phase transitions. In some of the earliest computer simulations performed, Alder and Wainwright [5] observed a liquid-solid transition in hard spheres qualitatively similar to that observed in simple atomic fluids such as argon. Also, experimentally, the tobacco mosaic virus, which has a shape very similar to the spherocylinder, has long been known to undergo a density driven isotropic-nematic transition [6].

Indubitably other agents such as attractive (dispersion) forces, electrostatic interactions, polarisability, intramolecular degrees of freedom and so forth have sig-

nificant roles in influencing the behaviour of real LCs and other complex fluids. However, gross molecular shape is widely held to be one of the most important. Further investigations into the behaviour of dense fluids consisting of anisometric hard particles may therefore provide valuable insight into mesophase behaviour. Theoretical approaches are inherently best suited to treating systems with a high degree of homogeneity and symmetry. It is therefore unsurprising that in the case of complex fluids it is often very difficult, if not practically impossible, to incorporate into them the essential physical details which distinguish these types of system. In particular, the predictions of Onsager theory become increasingly less accurate as the aspect ratio, κ , of the spherocylinders is decreased to the sort of values encountered for real mesogens, say $\kappa = 3 - 5$. Because of these difficulties, computer simulation is increasingly used as a powerful tool for gaining insight into the drivers of phase behaviour in LCs and other forms of soft matter at the microscopic level. A computer simulation could be viewed as a discrete, rather than continuous, mathematical model played out on a machine. Like theory, a computer simulation tries to capture the essential physics of the system of interest and involves numerous simplifications and approximations. However, with the latter there is much more scope in terms of the level of detail that can be included. In particular the many body interactions, that are so difficult to incorporate in analytical models, are an intrinsic feature of the computer simulation.

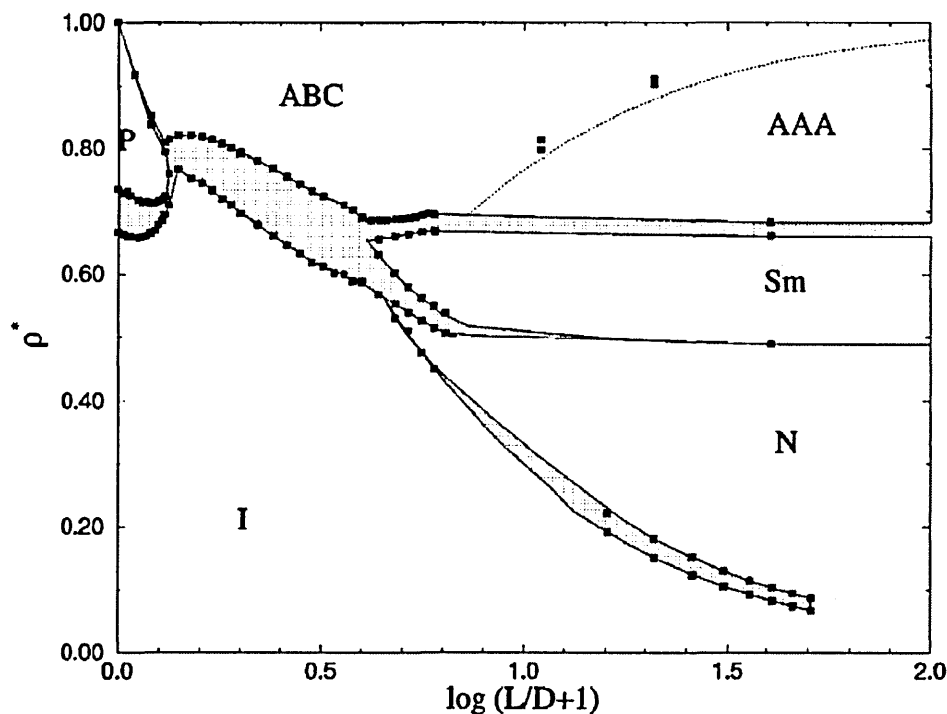
A substantial body of simulation work has been carried out on model systems of hard anisometric (non spherical) particles. For a comprehensive overview, the reader is referred to the reviews by Allen [7] and Cleaver and Care [8]. Here we confine our attention to the hard spherocylinder and the hard ellipsoid of revolution (HER). These are to date probably the most extensively studied single-site anisometric hard particle models.

The first simulations of hard spherocylinders were carried out by Vieillard-Baron in the early 1970s [9]. He used constant volume, constant temperature (NVT) Monte Carlo to simulate a system of 616 hard SCs with an aspect ratio, γ , of 3, the aspect ratio for SCs being defined as $\gamma = (L + D)/D = (L/D) + 1$. The shape

of spherocylinders may alternatively be characterised by their shape anisometry $k = L/D$. The density range explored, as expressed in terms of the volume fraction, was $\eta = 0.30 - 0.54$. Unfortunately in this work, no ordered phases were observed for this aspect ratio and density range; the limitations of computer power at that time made it impractical to run with particles of larger aspect ratios or at higher density.

In the years that followed, more ambitious simulation studies were carried out culminating in those of Bolhuis and Frenkel [10], who comprehensively mapped out the hard spherocylinder phase diagram from the limiting case of hard spheres

Fig. 1.1: The phase diagram for hard spherocylinders as determined by Bolhuis and Frenkel [10]. The shaded areas represent phase coexistence regions. The dashed line is a rough estimate for the phase boundary between the AAA and ABC solid phases.

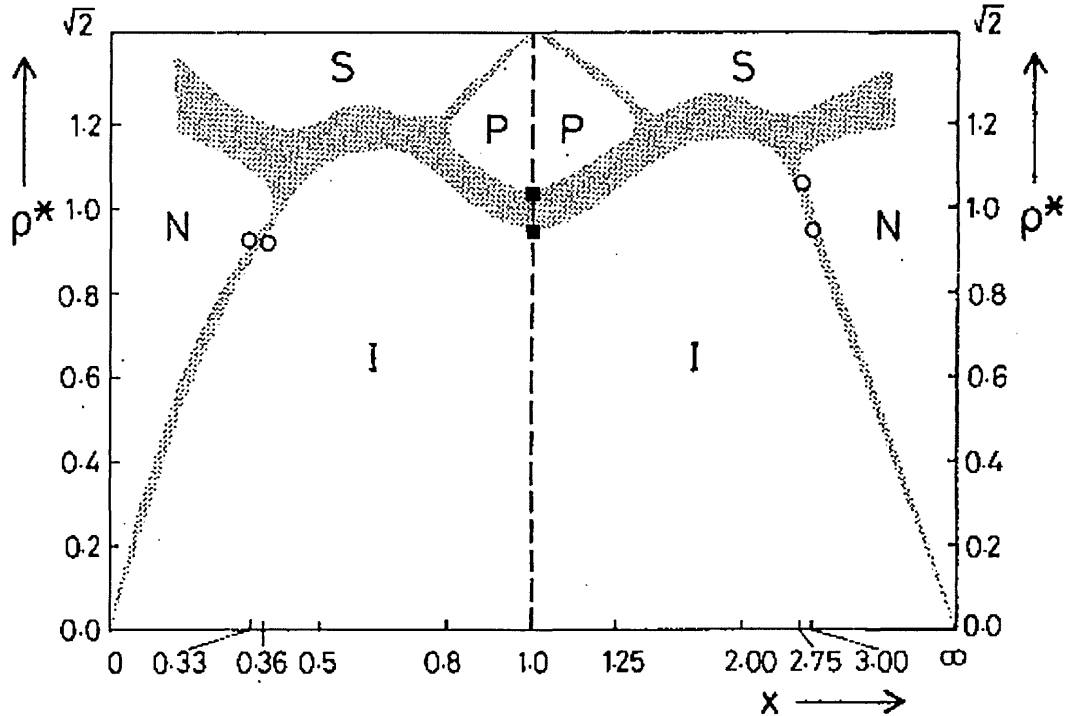


at one extreme ($k = L/D = 0$) to infinitely thin particles at the other ($k = \infty$), the latter corresponds to the model particles featured in Onsager's theory. The phase diagram they obtained is presented in figure 1.1. It should be noted that the density scale they use is normalised by dividing the number density by the

number density for close packing: $\rho^* = \rho/\rho_{cp}$. Systems consisting of particles with a shape anisotropy in the range $0 < k < 0.35$, as they are compressed, freeze into a plastic crystal phase (P) in which the particles have translational order, i.e. their positions define a regular lattice, but their orientations are disordered. For $0.35 < k < 3.1$, an isotropic-solid (I-S) transition is observed; in this k range, the solid consists of layers of SCs stacked one on the other in the ABC hexagonal stacking arrangement. At $k = 3.1$, the smectic phase emerges between the isotropic liquid and the crystal solid. For slightly more elongated particles with $k = 3.7$, the nematic phase also becomes accessible and so for $k > 3.7$ the phase transition sequence is I-N-Sm-S. Also for $k > 7.0$, on freezing, the initial stacking arrangement of the solid becomes AAA.

The first simulations of ellipsoidal particles were again pioneered by Vieillard-Baron [11]. In fact this work was a 2D simulation study of 170 hard ellipses with an aspect ratio, κ , of 6. Nevertheless both solid-nematic and nematic-isotropic phase transitions were observed in this system. Fully three-dimensional simulations of hard HERs were later carried out by Frenkel and Mulder [12] using constant pressure, constant temperature (NPT) Monte Carlo. This work looked at both prolate and oblate ellipsoids with aspect ratios of 3, 2.75, 2, 1.25 and 1/1.25, 1/2, 1/2.75, 3 respectively. The phase diagram obtained is shown in figure 1.2. The phase diagram also included data from previous work: the limiting case for oblate particles, $\kappa = 0$, is the infinitely thin disk, which had been studied previously by Eppenga and Frenkel [13]. The extreme case for prolate HERs meanwhile, with $\kappa = \infty$, corresponds to the needle like particles featured in Onsager's theory of the I-N transition. The other special case, $\kappa = 1$, corresponds to hard spheres whose phase behaviour has been rigorously investigated. To summarise the phase behaviour of HERs, the nematic phase is observed for oblate ellipsoids with $\kappa < 1/2.5$ and for oblate ellipsoids with $\kappa > 2.5$. Oblate and prolate ellipsoids with more moderate aspect ratios in the ranges $1/2.5 < \kappa < 1/1.5$ and $1.5 < \kappa < 2.5$ respectively undergo freezing transitions from the isotropic to the ordered solid (S) phase without an intervening nematic phase. For $1/1.5 < \kappa < 1.5$ the freezing transition is from

Fig. 1.2: The phase diagram for hard ellipsoids of revolution as determined by Frenkel and Mulder [12]. The shaded areas represent the authors best estimates of the phase coexistence regions based on the state points studied. The density has been normalised by dividing it by $8ab^2$ where (a) is the length of the semimajor axes of the ellipsoid studied and (a) is the length of their semiminor axes.



isotropic to plastic solid (PS). No smectic phases are observed, the reason for this is essentially that in the high density fluid, side-to-side arrangements of ellipsoids to collectively form layers is not efficient packing (in contrast to spherocylinders in the same situation), rather fcc packing is favoured. The most striking feature of the phase diagram overall is the near perfect symmetry of the oblate and prolate halves. This symmetry is not fully understood.

1.3 Objective of the project

Clearly then molecular shape is an important factor in determining the mesophases formed by liquid crystals. The essential aim of this project is to contribute to the body of hard particle simulation work by investigating the behaviour of systems of particles with tapered shapes i.e. particles that, unlike the uniaxial spherocylinder and HER, have polar shape anisometry. To this end we have carried out molecular dynamics (MD) simulations of soft repulsive tapered particles, or ‘pears’ for short. The main body of work investigates the effect which systematically altering the degree of taper has on the general phase behaviour of the system. This builds on previous MC studies of purely hard particles having a similar type of shape [14]. The soft repulsive variant of this potential is used here because the hard particle potential is non-differentiable and therefore cannot be used in constant timestep MD, which involves calculating derivatives of the potential in order to obtain the intermolecular forces which drive the dynamics. One may well ask why we bother to carry out this type of simulation at all using MD when a very similar system has been studied using MC? There are two main reasons. Firstly, if the results of the MC simulations are found to be closely reproduced by the analogous MD study, then the latter provides good verification of the former and vice versa. Secondly, MD provides additional dynamical information about the system which cannot be obtained from MC runs.

We have also studied the flexoelectric properties of systems of tapered particles. Flexoelectricity is a property of LCs whereby when a net mechanical distortion is imposed upon a sample of the material, a net polarisation is induced. It is analogous to the more widely known piezoelectric effect observed in certain crystalline materials. According to Meyer, flexoelectric properties may be engendered by certain characteristic shapes of the materials constituent molecules – one of which being a wedge-like or tapered shape. The use of the MD simulation technique was essential in this work since, in the method used to determine of the parameters which characterise flexoelectricity, the calculation of torques is required.

1.4 Outline of the thesis

In chapter 2 we will describe precisely the shapes of the particles to be considered and demonstrate how they are generated. The shapes range from a uniaxial particle, which is very similar to the hard ellipsoid of revolution, to extremely tapered tear-shaped particles. We will then explain the method used to model the particle shape in the simulations. This is known as the parameterised hard Gaussian overlap (PHGO) model as used previously in the simulation work on systems of hard particles [14]. In the final section of this chapter the potential used to mediate the interactions between the particles will be described. This potential is essentially a continuous analogue of the strictly hard particle potential used in the MC studies.

Chapter 3 describes the simulation methodology, beginning with a brief overview of how the MD simulations are organised. The forces and torques which drive the dynamics of the system are then defined as well as the observable properties of the system calculated in the course of the simulation. Since the latter are actually calculated during the simulation, they are referred to as ‘runtime’ observables. The final section describes a battery of distribution functions, which were used to analyse in detail the structure of the phases formed in the simulations once they had reached completion.

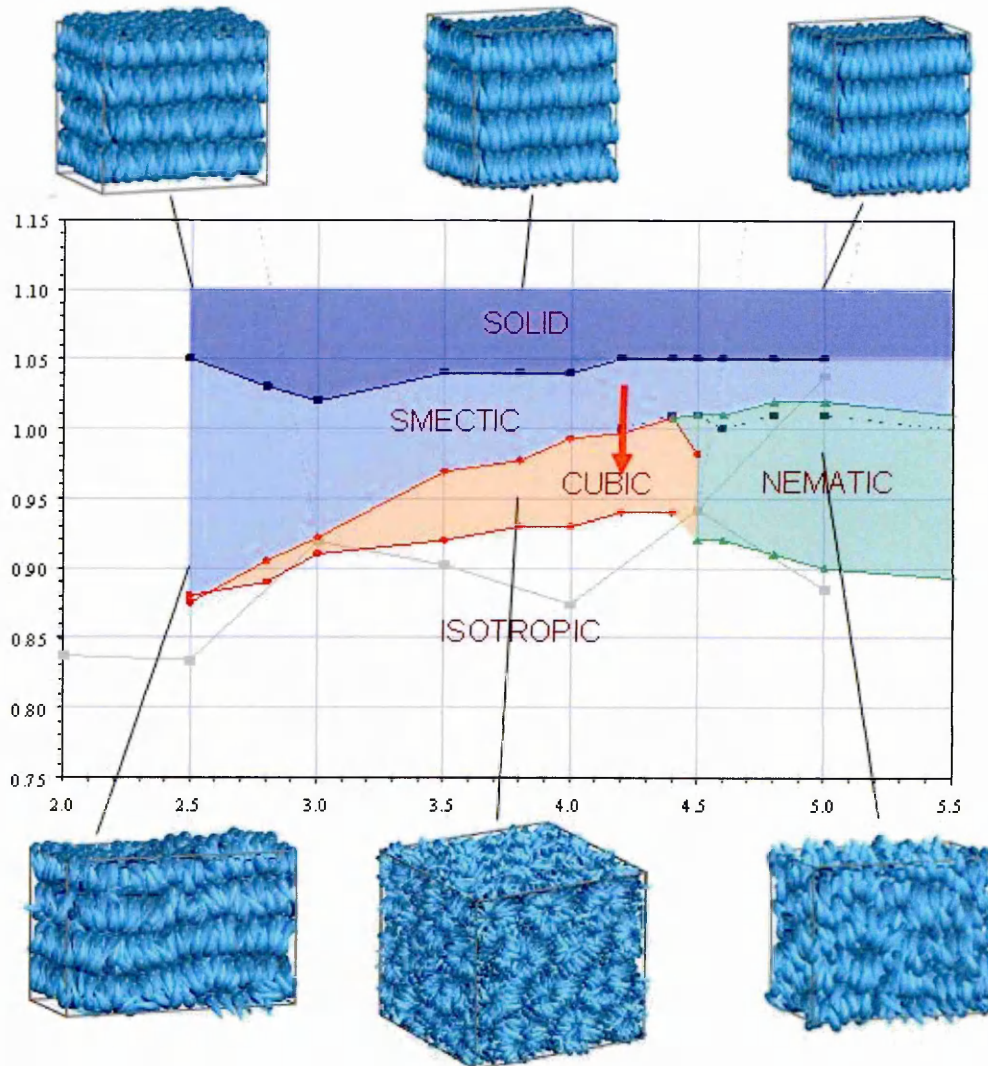
In chapter 4 the results from a series of preliminary simulations are presented. These were designed primarily to test that the code was performing satisfactorily. They also provided an opportunity to develop the analysis techniques later used to elucidate the properties and phase behaviour of the systems generated by the main simulation runs.

Chapter 5 describes how a specialised analysis technique, known as the linear response approach, was used to calculate the flexoelectric coefficients, e_{11} and e_{33} , for our systems of pears. These are respectively the splay and bend flexoelectric coefficients and are the key quantitative measure of the flexoelectric properties of a material. They were calculated for several tapered particle systems at various

densities (and, thus, different values of the nematic order parameter) in order to try to establish if there was any correlations between flexoelectric properties, particle shape and P_2 . The coefficients of systems of Gaussian ellipsoids were also measured. This served as a control test since uniaxial particles, such as ellipsoids, should not possess flexoelectric properties.

In chapter 6 we follow up on the previous MC simulation studies of Barmes et al. [14] by carrying out a systematic survey of the shape-density phase diagram for soft repulsive pears with a length to breadth aspect ratio, κ , of 3. In this, the isotropic, nematic, smectic, crystal and what we refer to as the ‘curvy-bilayer’

Fig. 1.3: The density-shape phase diagram for soft repulsive pears with an aspect ratio of $\kappa = 3$. This was obtained through a series of decompression runs for particles with different degrees of taper.



(CB) regions of the phase diagram are mapped out. This was accomplished by carrying out a series of compressions and decompressions of monodisperse systems of 1250 particles for a range of particle shapes. The phase diagram obtained from the decompression series is presented in figure 1.3.

The structures of the various phases were thoroughly interrogated using the distribution functions defined in the methodology chapter. However, the precise nature of the curvy-bilayer encountered in the $\kappa 3$ survey was not clear. Therefore, a further series of compressions and decompressions was performed on larger systems of 10000 particles, the results of these simulations are presented in the final main chapter. Stored configurations from these simulations were subjected to a cluster analysis technique in order to elucidate the structure. This analysis enabled us to identify the phase as consisting of two identical, interpenetrating periodic networks. Further analysis confirmed that the CB phase was in fact the bicontinuous cubic phase $Ia\bar{3}d$, otherwise known as the gyroid (G). This phase has been observed previously in a small number of simulations which included attractive interactions in the potential but never in a hard particle model. We have recently published a paper [15] summarising this unprecedented result and discussing its significance and wider implications. These matters are also touched on in the final chapter of the thesis in which we draw together the major conclusions from the simulations carried out so far and indicate some promising directions for future work.

CHAPTER 2

A model for tapered particles

2.1 Defining the shape

The particles used in our simulations have two characteristic shape related properties. Firstly, they have an overall aspect ratio, κ , which is simply defined as the ratio of the length of the particle to the width at its mid-section. Secondly they have a degree of taper which is labelled by the parameter k_θ , which will be described shortly. Thus a particle with an aspect ratio of three and a degree of taper of five, say, would be denoted by the short hand $\kappa 3 k_\theta 5.0$ ¹.

The cross-sectional profile of the tapered particle is generated by a pair of cubic Bezier curves [16], each of which is defined by a parametric equation of the form

$$\mathbf{P}(t) = (1-t)^3 \mathbf{a}_0 + 3t(1-t)^2 \mathbf{a}_1 + 3t^2(1-t) \mathbf{a}_2 + t^3 \mathbf{a}_3 \quad (2.1)$$

where \mathbf{a}_{0-3} are the control points which determine the shape of the curve and t lies in the range 0-1. A general example of a cubic Bezier curve is shown in

¹Occasionally ASCII based notation like K3kth5-0 may be encountered, this format having been used for the naming of directories and files associated with simulations of particles of a particular shape

figure 2.1. The curve begins and terminates at the points \mathbf{a}_0 and \mathbf{a}_3 respectively, whilst \mathbf{a}_1 and \mathbf{a}_2 serve as attractors influencing the curve's trajectory between the endpoints.

Fig. 2.1: An example of a Bezier curve.

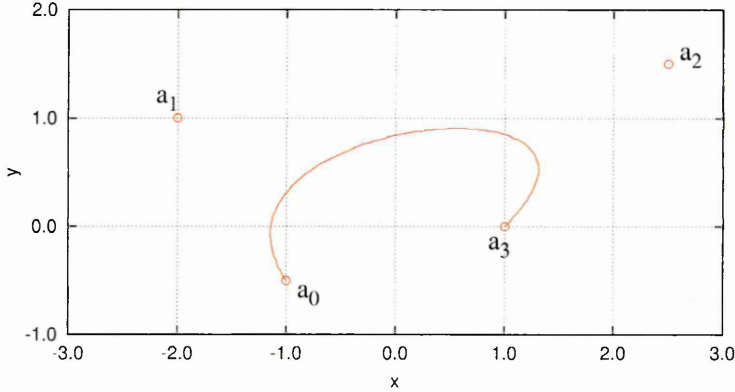
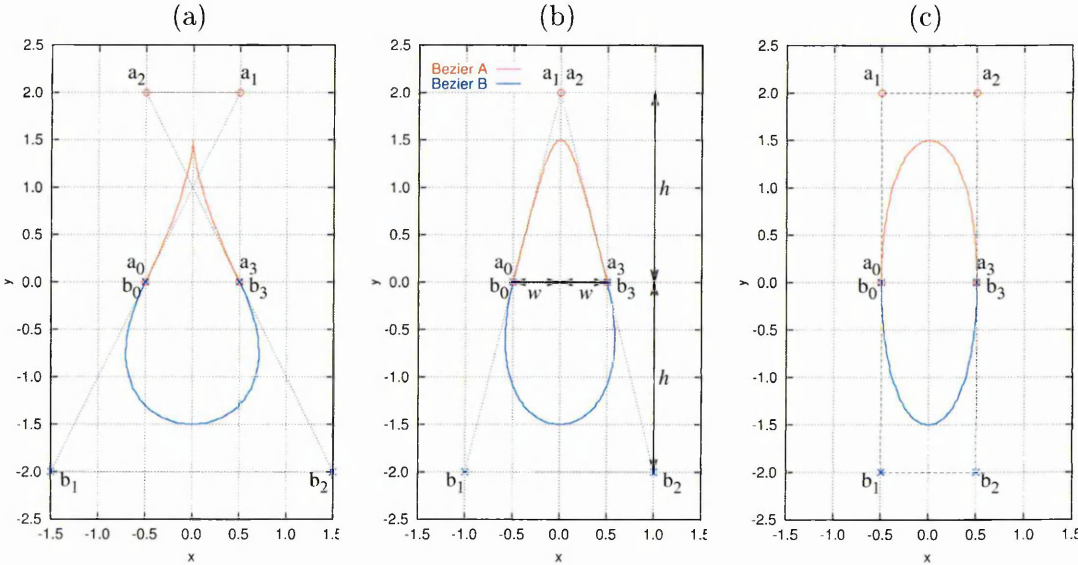


Fig. 2.2: Examples of the cross sectional profiles for particles with an aspect ratio of $\kappa = 3$ and various degrees of tapering, as constructed from a pair of Bezier curves.



The cross-section of a tapered particle is generated using two of these curves with their control points placed in arrangements such as those shown in figure 2.2, wherein the curve defining the profile of the top half of the particle is coloured red and that defining the bottom half is coloured blue. The control points \mathbf{a}_0 , \mathbf{a}_3 and \mathbf{b}_0 , \mathbf{b}_3 of both curves are always placed at $(-w,0)$ and $(w,0)$ respectively (w

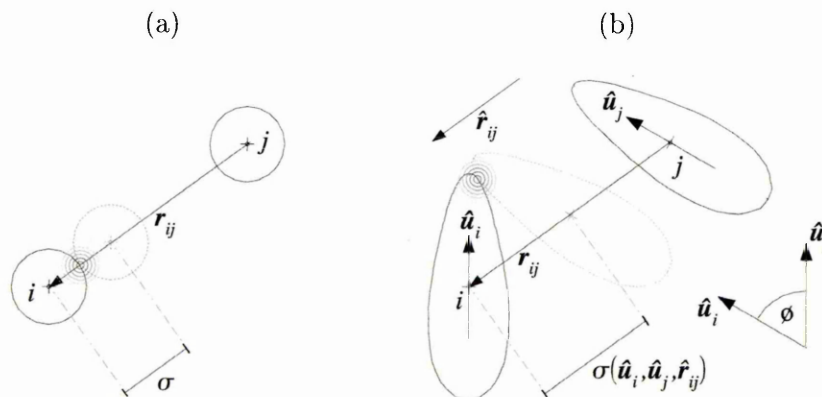
being the half width of the particle at its mid-section) so that the ends of the two curves meet. A second constraint is that the points $\mathbf{b}_1, \mathbf{b}_0, \mathbf{a}_0, \mathbf{a}_1$ must always be positioned so that they are colinear, as must $\mathbf{b}_2, \mathbf{b}_3, \mathbf{a}_3, \mathbf{a}_2$, this is to ensure that there is no discontinuity in the gradient of the profile at the meeting points. Points $\mathbf{b}_1, \mathbf{b}_2$ and $\mathbf{a}_1, \mathbf{a}_2$ have fixed y -coordinates of $-h$ and h respectively. For particles with a particular aspect ratio, the value of h is constant; for $\kappa 3$ particles it is equal to 2.0. The degree of taper is controlled by altering the horizontal positions of $\mathbf{b}_1, \mathbf{b}_2, \mathbf{a}_1, \mathbf{a}_2$ subject to the overall arrangement remaining symmetric about the long axis of the particle. If the control points are positioned such that the line segments a_1b_1 and a_2b_2 intersect at a point lower than the apex of the particle, i.e. below $(0, \kappa/2)$ as illustrated in figure 2.2 (a), then the taper is very pronounced and the particle has a partially concave tear-drop shape. If, on the other hand, the intersection point of these line segments (or the extensions thereof) occurs above the apex, the profile will be less tapered and, in addition, purely convex, as illustrated in 2.2 (b). The situation shown in figure 2.2 (b), where the control points a_1 and a_2 are coincident marks the threshold between concave and convex particle profiles, and corresponds to $k_\theta = \kappa$. So in general, as the intersection point occurs higher up the y -axis, the degree of taper is reduced, which corresponds to increasing k_θ value. In the extreme case, illustrated in 2.2 (c), where $\mathbf{b}_1, \mathbf{a}_1$ and $\mathbf{b}_2, \mathbf{a}_2$ are placed such that the two lines passing through them are vertical, the particle is no longer tapered and is reduced to a symmetric elliptical shape, for this situation, k_θ is equal to infinity².

²The scheme used to generate particle shapes was developed by Zannoni and coworkers and is described in [17], however this description does not include a precise quantitative statement specifying the relationship between θ and k_θ

2.2 The Gaussian overlap contact function

In order to perform simulations of systems of many particles, we require a closed mathematical expression that describes the steric interaction of one particle with another. We refer to this as the contact function, σ . Formally, the contact function defines the distance at which two particles, positioned and oriented arbitrarily with respect to one another, make contact if brought towards each other along the line joining their centres, as shown in figure 2.3. The most trivial form of contact function is of course that of a pair of spheres – it is simply the sum of their radii, since all points on the surface of a sphere lie at a constant distance, namely the radius, from its centre. We might naively expect that, given a precise

Fig. 2.3: Schematic illustrating the contact function for (a) a pair of spheres and (b) a pair of tapered particles. The interparticle vector \mathbf{r}_{ij} is defined as $\mathbf{r}_i - \mathbf{r}_j$, where \mathbf{r}_i and \mathbf{r}_j are the positions of the particles. The unit vectors $\hat{\mathbf{u}}_i$ and $\hat{\mathbf{u}}_j$ define the orientations of uniaxial particles.



geometric definition for the surface of a particular object, we could devise an analytical contact function for a pair of such objects. In fact this is a far from simple problem as illustrated by the fact that it is only recently that an analytical contact function has been devised for two arbitrary *ellipses* in 2D [18]. And so it is that even though the geometric description of the shape of a solid figure, say, an ellipsoid (which we note has a shape very similar to a $k_\theta = \infty$ pear) is itself very simple, there is as yet no analytical expression for the contact function for a pair of ellipsoids, let alone for a pair of tapered particles. For certain classes

of particle, there do exist well defined criteria for *testing* whether particles are overlapping, just touching or not overlapping. For a pair of spherocylinders (SCs) i and j , with diameters d_i and d_j , Vieillard-Baron introduced the following test criteria [9]

$$\Psi_{ij}(\mathbf{r}_{ij}, \hat{\mathbf{u}}_i, \hat{\mathbf{u}}_j) = \begin{cases} < 0 & \text{if } i \text{ and } j \text{ overlap} \\ = 0 & \text{if } i \text{ and } j \text{ are externally tangent} \\ > 0 & \text{if } i \text{ and } j \text{ do not overlap} \end{cases} \quad (2.2)$$

where \mathbf{r}_{ij} is the interparticle vector defining the relative positions of the two ellipsoids, i and j and $\hat{\mathbf{u}}_i$ and $\hat{\mathbf{u}}_j$ are unit vectors defining their orientations. The test function is given by

$$\Psi_{ij}(\mathbf{r}_{ij}, \hat{\mathbf{u}}_i, \hat{\mathbf{u}}_j) = \delta_{ij}^2(\mathbf{r}_{ij}, \hat{\mathbf{u}}_i, \hat{\mathbf{u}}_j) - (d_i + d_j)^2 \quad (2.3)$$

where δ is the closest distance between the line segments along the axes of the cylindrical portions of the spherocylinders. There is also an analogous test criteria, developed by Perram and Wertheim [19], which holds for for non-identical general ellipsoids:

$$f_{ij}(\mathbf{r}_{ij}, \Omega_i, \Omega_j) = \begin{cases} < 1 & \text{if } i \text{ and } j \text{ overlap} \\ = 1 & \text{if } i \text{ and } j \text{ are externally tangent} \\ > 1 & \text{if } i \text{ and } j \text{ do not overlap} \end{cases} \quad (2.4)$$

Here \mathbf{r}_{ij} is the interparticle vector and Ω_i and Ω_j denote sets of coordinates defining the particle orientations. The test function, f_{ij} , meanwhile is given by an expression which is very much more complicated than the analogous one for SCs. Such test algorithms are suitable for use in MC simulations of hard particles, where one simply requires a means of deciding whether a trial move should be accepted or not. However they are unsuitable for constant timestep MD simulations because they do not specify the contact distance in an analytical form. Fortunately an approach exists which has been used to derive an analytical form

of contact function that closely approximates the steric interaction for hard ellipsoids of revolution (HERs). Furthermore, as we will show, this analytical form can be adapted to yield a contact function for tapered particles. This approximation to the contact function for ellipsoids is known as the Gaussian overlap (GO) model, introduced by Berne and Pechukas [20]. We will now describe the model in some detail.

The GO model starts by conceiving an idealised elongated molecule as represented by a three-dimensional ellipsoidal Gaussian distribution.

$$G(\mathbf{r}) = |\underline{\gamma}|^{-1/2} \exp[-\mathbf{r} \cdot \underline{\gamma}^{-1} \cdot \mathbf{r}] \quad (2.5)$$

where \mathbf{r} is a general position vector and $\underline{\gamma}$ denotes the range matrix which serves to modulate the directional variation of the distribution in space. The range matrix is given by

$$\underline{\gamma} = (l^2 - d^2) \hat{\mathbf{u}}\hat{\mathbf{u}} + d^2\mathbf{I} \quad (2.6)$$

where $\hat{\mathbf{u}}$ is a unit vector along the principal molecular axis, $\hat{\mathbf{u}}\hat{\mathbf{u}}$ denotes the outer product and \mathbf{I} is the unit matrix. The parameters l and d quantify the half-length and half-width of the distribution representing the molecule.

The second step is to postulate that the interaction potential, U_{ij} , between a pair of such molecules, i and j , is, in some sense, proportional to the mathematical overlap of their Gaussians

$$U_{ij}(\hat{\mathbf{u}}_i, \hat{\mathbf{u}}_j, \mathbf{r}_{ij}) \sim \int_{-\infty}^{\infty} d\mathbf{r} G_i(\mathbf{r}) G_j(\mathbf{r} - \mathbf{r}_{ij}) . \quad (2.7)$$

The result of this integral is itself a Gaussian function of the intermolecular vector \mathbf{r}_{ij} and the molecular orientations $\hat{\mathbf{u}}_i$ and $\hat{\mathbf{u}}_j$ (on which γ_i and γ_j respectively are dependent).

$$U_{ij}(\hat{\mathbf{u}}_i, \hat{\mathbf{u}}_j, \mathbf{r}_{ij}) \sim \left| \underline{\gamma}_i + \underline{\gamma}_j \right|^{-1/2} \exp \left[-\mathbf{r}_{ij} \cdot \left(\underline{\gamma}_i + \underline{\gamma}_j \right)^{-1} \cdot \mathbf{r}_{ij} \right] . \quad (2.8)$$

For a given particle-particle orientation $(\hat{\mathbf{u}}_i, \hat{\mathbf{u}}_j)$, the principal axes of the distribution are given by the eigenvectors of $(\underline{\gamma}_i + \underline{\gamma}_j)$ and the equipotential surfaces are ellipsoids, which of course share these axes of symmetry. The variation in the potential profile observed along directions in $\hat{\mathbf{r}}_{ij}$ space is modulated by the eigenvalues of $(\underline{\gamma}_i + \underline{\gamma}_j)$ whilst the prefactor $|\underline{\gamma}_i + \underline{\gamma}_j|^{-1/2}$ simply acts as a scaling factor for the magnitude of the potential. Berne and Pechukas emphasised these two controlling factors in the potential by writing Eq.(2.8) in the form

$$U_{ij}(\hat{\mathbf{u}}_i, \hat{\mathbf{u}}_j, \mathbf{r}_{ij}) = \epsilon(\hat{\mathbf{u}}_i, \hat{\mathbf{u}}_j) \exp \left[\frac{-r_{ij}^2}{\sigma^2(\hat{\mathbf{u}}_i, \hat{\mathbf{u}}_j, \hat{\mathbf{r}}_{ij})} \right] \quad (2.9)$$

where ϵ is called the strength parameter, which modulates the strength of the particle-particle interaction, and σ is the range parameter which determines the width of the potential. By equating terms in equations 2.8 and 2.9, it transpires that the task of obtaining ϵ and σ essentially amounts to determining expressions for the determinant and inverse respectively of $\underline{\gamma}_i + \underline{\gamma}_j$. If both particles are identical, i.e. $l_i = l_j = l$ and $d_i = d_j = d$, then the following expressions result. Firstly the strength parameter is given by

$$\epsilon(\hat{\mathbf{u}}_i, \hat{\mathbf{u}}_j) = \epsilon_0 [1 - \chi^2 (\hat{\mathbf{u}}_i \cdot \hat{\mathbf{u}}_j)^2]^{-1/2} \quad (2.10)$$

where ϵ_0 is the basic unit of energy setting the energy scale of interactions. Secondly the range parameter is given by

$$\sigma(\hat{\mathbf{u}}_i, \hat{\mathbf{u}}_j, \hat{\mathbf{r}}_{ij}) = \sigma_0 \left[1 - \frac{\chi}{2} \left\{ \frac{(\hat{\mathbf{u}}_i \cdot \hat{\mathbf{r}}_{ij} + \hat{\mathbf{u}}_j \cdot \hat{\mathbf{r}}_{ij})^2}{[1 + \chi(\hat{\mathbf{u}}_i \cdot \hat{\mathbf{u}}_j)]} + \frac{(\hat{\mathbf{u}}_i \cdot \hat{\mathbf{r}}_{ij} - \hat{\mathbf{u}}_j \cdot \hat{\mathbf{r}}_{ij})^2}{[1 - \chi(\hat{\mathbf{u}}_i \cdot \hat{\mathbf{u}}_j)]} \right\} \right]^{-1/2} \quad (2.11)$$

where $\sigma_0 = \sqrt{2}d$ is the basic unit of length and χ is the shape anisotropy parameter

$$\chi = (l^2 - d^2) / (l^2 + d^2) \quad (2.12)$$

In the special case where one of the molecules, j say, is replaced by a sphere (not necessarily of the same diameter as i) then $\epsilon = \epsilon_0$, $\sigma_0 = (d_i^2 + d_j^2)^{1/2}$ and the range and anisotropy parameters become

$$\sigma(\hat{\mathbf{u}}_i, \hat{\mathbf{r}}_{ij}) = \sigma_0 (1 - \chi (\hat{\mathbf{u}}_i \cdot \hat{\mathbf{r}}_{ij})^2)^{-1/2} \quad (2.13)$$

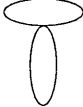
where

$$\chi = (l_i^2 - d_i^2) / (l_i^2 + d_i^2) \quad (2.14)$$

In the case where both molecules are replaced by atoms, the range parameter reduces to $\sigma = \sigma_0 = (d_i^2 + d_j^2)^{1/2}$, which further simplifies to $\sigma = \sqrt{2}d$ if both atoms are the same size i.e. $d_i = d_j = d$.

It is instructive to calculate the value of the range parameter σ_{GO} for selected molecular arrangements and compare the values obtained to the corresponding contact distances, σ_{HE} , for hard ellipsoidal particles. This comparison is made

Tab. 2.1: Comparison between values of the Gaussian overlap contact function and the hard ellipsoid contact distance for various inter-molecular arrangements.

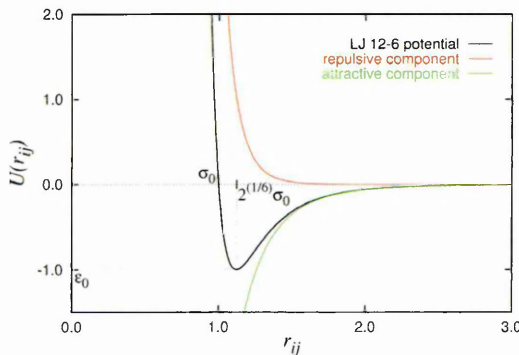
configuration		σ_{HE}	σ_{GO}
side-to-side		$2d$	$\sqrt{2}d$
end-to-end		$2l$	$\sqrt{2}l$
T		$l + d$	$\sqrt{l^2 + d^2}$
X		$2d$	$\sqrt{2}d$

in table 2.1. For the side-to-side, end-to-end and X-configurations, multiplication by a factor of $\sqrt{2}$ maps σ_{GO} exactly onto the equivalent hard particle contact

distance. For the T-configuration the same scaling gives an exact match only when both particles are spheres $l = d$. Nevertheless, it still provides a fairly good approximation for non-unity aspect ratios.

We now return to the main thrust of the GO model, which was the development of model potentials for molecular interactions. While the concept of an elongated molecule being approximated by a Gaussian distribution seems quite acceptable, the Gaussian overlap potential, equation 2.9, is not in itself physically realistic. Real molecular potentials are not simply proportional to the overlap of molecular electron clouds. When atoms come into close contact, very strong repulsive forces of a quantum mechanical nature operate. At somewhat larger separations, the repulsive interaction falls off rapidly and the attractive dispersion forces come into play. These two general characteristics are represented in the Lennard-Jones

Fig. 2.4: The Lennard-Jones 12-6 potential plotted for $\sigma_0 = 1.0$ and $\epsilon_0 = 1.0$.



12-6 potential, equation 2.15 and figure 2.4, which approximates the interaction between a pair of spherically symmetric atoms

$$U_{ij}^{LJ}(r_{ij}) = 4\epsilon_0 \left\{ \left(\frac{\sigma_0}{r_{ij}} \right)^{12} - \left(\frac{\sigma_0}{r_{ij}} \right)^6 \right\}. \quad (2.15)$$

Hence, the parameter σ_0 is the distance at which the interaction between a pair of atoms becomes repulsive; σ_0 could be thought of as analogous to the contact distance for hard spheres. The other parameter, ϵ_0 , defines the depth of the potential at its minimum, which occurs at a value of $r_{ij} = 2^{(1/6)}\sigma_0$. In order then to obtain a physically realistic potential to describe the interactions between a pair

of idealised elongated uniaxial molecules, Berne and Pechukas proposed replacing the constants σ_0 and ϵ_0 in equation 2.15 with the orientation dependent range and strength parameters, $\sigma(\hat{\mathbf{u}}_i, \hat{\mathbf{u}}_j, \hat{\mathbf{r}}_{ij})$ and $\epsilon(\hat{\mathbf{u}}_i, \hat{\mathbf{u}}_j)$, equations 2.11 and 2.10, as follows

$$U_{ij}^{BP}(\hat{\mathbf{u}}_i, \hat{\mathbf{u}}_j, \mathbf{r}_{ij}) = 4\epsilon(\hat{\mathbf{u}}_i, \hat{\mathbf{u}}_j) \left\{ \left(\frac{\sigma(\hat{\mathbf{u}}_i, \hat{\mathbf{u}}_j, \hat{\mathbf{r}}_{ij})}{r_{ij}} \right)^{12} - \left(\frac{\sigma(\hat{\mathbf{u}}_i, \hat{\mathbf{u}}_j, \hat{\mathbf{r}}_{ij})}{r_{ij}} \right)^6 \right\}. \quad (2.16)$$

The result was an anisotropic, stretched version of the Lennard-Jones potential as shown in figure 2.5 (a); the two graphs illustrate the potential for the side-to-side and end-to-end configurations. The crucial point to take on board here is that the Gaussian overlap approach, though it does not automatically yield a potential describing the interactions between atoms and molecules, does provide, in the guise of the range parameter $\sigma(\hat{\mathbf{u}}_i, \hat{\mathbf{u}}_j, \hat{\mathbf{r}}_{ij})$, an extremely useful contact function for describing the hard-core interactions of elongated molecules. We will henceforth refer to Berne and Pechukas' range parameter as the Gaussian overlap contact function, $\sigma^{GO} = \sigma^{GO}(\hat{\mathbf{u}}_i, \hat{\mathbf{u}}_j, \hat{\mathbf{r}}_{ij})$

Some years after its introduction, Gay and Berne [21] made two modifications to the original GO model. In brief, they proposed that the existing contact function be inserted into the Lennard-Jones potential in the following alternative manner

$$U_{ij}^{GB}(\hat{\mathbf{u}}_i, \hat{\mathbf{u}}_j, \mathbf{r}_{ij}) = \epsilon_0 \epsilon^{GB}(\hat{\mathbf{u}}_i, \hat{\mathbf{u}}_j, \hat{\mathbf{r}}_{ij}) \{R^{12} - R^6\} \quad (2.17)$$

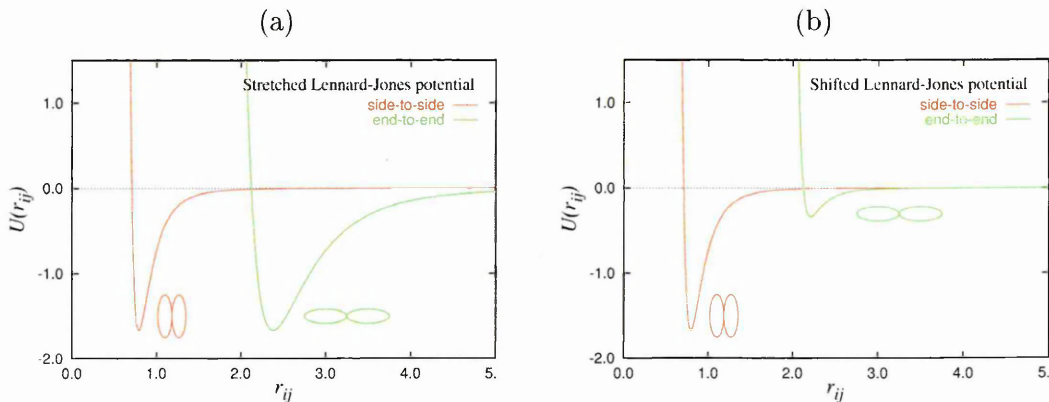
where

$$R = \left(\frac{\sigma_0}{r_{ij} - \sigma^{GO}(\hat{\mathbf{u}}_i, \hat{\mathbf{u}}_j, \hat{\mathbf{r}}_{ij}) + \sigma_0} \right). \quad (2.18)$$

and again $\sigma_0 = \sqrt{2}d$. This generates a shifted rather than a stretched form of the potential. The second modification was to introduce a new and more complex strength parameter, $\epsilon^{GB}(\hat{\mathbf{u}}_i, \hat{\mathbf{u}}_j, \hat{\mathbf{r}}_{ij})$, dependent on the orientation, $\hat{\mathbf{r}}_{ij}$, of the interparticle vector as well as the relative orientations of the particles themselves. These changes were motivated by the discovery that major differences existed between the attractive part of the Gaussian overlap potential and that of an equiv-

alent multi-site representation of a linear molecule (a line of four overlapping Lennard-Jones spheres linked by rigid bonds). Figure 2.5 makes a comparison between the modified and original potentials. The modified Gaussian overlap

Fig. 2.5: Potential profiles for ellipsoidal particles in the side-by-side and end-to-end configurations using (a) the original Gaussian overlap model and (b) the Gay-Berne model. The values used here for the half-width and half-length of the particles are $\sigma_{\perp} = 0.5$ and $\sigma_{\parallel} = 1.5$ respectively.



model, or Gay-Berne potential as it came to be known, has gone on to become the most widely used soft potential for coarse-grained simulations of fluids of elongated molecules. The original GO contact function meanwhile, which furnishes the Gay-Berne potential with its hard-core volume exclusion, continues to be used, on its own, in simulations of anisotropic hard particles. The extensive use of the GO contact function owes much to the fact that it closely reproduces the points of close contact that would be obtained for a pair of HERs whilst having a convenient mathematical form. This means that it can readily be differentiated and that the geometric attributes of the particles and their mutual arrangements appear in the potential in a transparent fashion.

Recalling Eq. 2.8, it is apparent that, in principle, the approach of Berne and Pechukas may be applied to the overlap of two *dissimilar* Gaussians distributions and thus lead to a more general form of contact function. By following this route, Cleaver et al. [22] obtained the following expression for a generalised Gaussian

overlap contact function for non-identical uniaxial ellipsoidal particles

$$\sigma^{GGO}(\hat{\mathbf{u}}_i, \hat{\mathbf{u}}_j, \hat{\mathbf{r}}_{ij}) = \sigma_0 \left[1 - \frac{\chi}{2r_{ij}^2} \left\{ \frac{(\alpha a + \alpha^{-1}b)^2}{1 + \chi c} + \frac{(\alpha a - \alpha^{-1}b)^2}{1 - \chi c} \right\} \right]^{-1/2} \quad (2.19)$$

which contains a new constant appropriate for particles of dissimilar dimensions

$$\sigma_0^{GGO} = (d_i^2 + d_j^2)^{-1/2} \quad (2.20)$$

as well as two new anisotropy parameters

$$\chi = \left[\frac{(l_i^2 - d_i^2)(l_j^2 - d_j^2)}{(l_j^2 + d_i^2)(l_i^2 + d_j^2)} \right]^{1/2} \quad (2.21)$$

$$\alpha^2 = \left[\frac{(l_i^2 - d_i^2)(l_j^2 + d_i^2)}{(l_j^2 - d_j^2)(l_i^2 + d_j^2)} \right]^{1/2} \quad (2.22)$$

Within equation 2.19 we have made, for the sake of compactness, the following substitutions

$$a = (\hat{\mathbf{u}}_i \cdot \mathbf{r}_{ij}) \quad b = (\hat{\mathbf{u}}_j \cdot \mathbf{r}_{ij}) \quad c = (\hat{\mathbf{u}}_i \cdot \hat{\mathbf{u}}_j) .$$

If one of the particles is made oblate then χ and α^2 become imaginary, it is therefore preferable to express the contact function, equation 2.19, as follows

$$\sigma(\hat{\mathbf{u}}_i, \hat{\mathbf{u}}_j, \hat{\mathbf{r}}_{ij}) = \sigma_0 \left[1 - \frac{\chi}{r_{ij}^2} \left\{ \frac{\alpha^2 a^2 + \alpha^{-2} b^2 - 2\chi abc}{1 - \chi^2 c^2} \right\} \right]^{-1/2} \quad (2.23)$$

since the coefficients $\alpha^2\chi$, $\alpha^{-2}\chi$, and χ^2 appearing in this alternative form are always real. It should also be noted that if $l_i = l_j$ and $d_i = d_j$ then α^2 goes to unity and the expressions for σ_0 and χ and, hence, $\sigma(\hat{\mathbf{u}}_i, \hat{\mathbf{u}}_j, \hat{\mathbf{r}}_{ij})$ reduce to the original form for identical particles.

2.3 The pear-pear contact function

We will now describe how the semiaxial lengths d_i , l_i , d_j and l_j , which feature as constants in the above generalised contact function for arbitrary uniaxial ellipsoidal particles, can be parameterised in such a way as to mimic the steric interaction between a pair uniaxial tapered particles of the kind presented at the beginning of this chapter. The first step is to reduce equation 2.23 to the contact function for a single arbitrary ellipsoid, i , and a point particle, j , by setting $d_j = l_j = 0$ and $\hat{\mathbf{u}}_j = \mathbf{0}$, which results in the following particle-point contact function

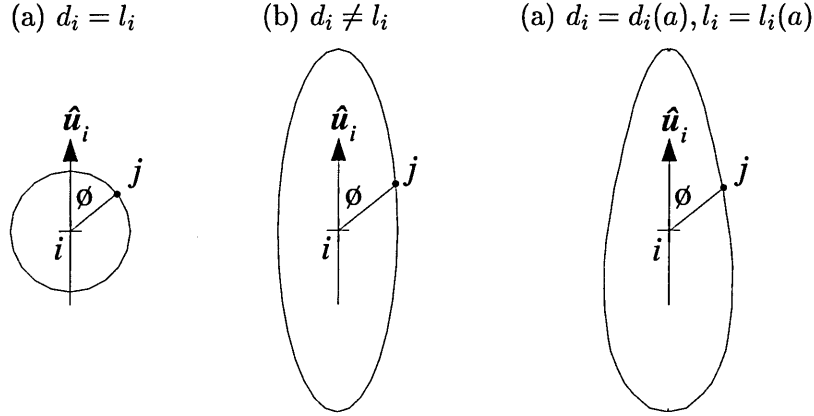
$$\sigma(\hat{\mathbf{u}}_i, \hat{\mathbf{r}}_{ij}) = \frac{d_i l_i}{[l_i^2 + (d_i^2 - l_i^2) \hat{a}^2]^{1/2}} = \frac{d_i l_i}{[l_i^2 + (d_i^2 - l_i^2) \cos^2 \phi]^{1/2}} \quad (2.24)$$

where $\phi = \cos^{-1}(a/r) = \cos^{-1}(\hat{\mathbf{u}}_i \cdot \hat{\mathbf{r}}_{ij})$ is the polar angle between the major axis of ellipsoid, i , and the interparticle vector, $\hat{\mathbf{r}}_{ij}$, as shown in figure 2.6. If we set $d_i = l_i$, then the particle-point contact function will simply describe a spherical surface. If we set $d_i \neq l_i$ then it sweeps out the surface of an ellipsoid. However if d_i and l_i are replaced by functions of a , in other words if they are parameterised so that $d_i \rightarrow d_i(\hat{a})$ and $l_i \rightarrow l_i(\hat{a})$, where $\hat{a} = a/r = \hat{\mathbf{u}}_i \cdot \hat{\mathbf{r}}_{ij}$, then the contact function can be made to sweep out a more complex profiles as a varies, such as the Bezier generated particle cross sections depicted in figure 2.2. A suitable parameterisation scheme is to make $d_i(\hat{a})$ and $l_i(\hat{a})$ polynomials in \hat{a}

$$d_i(\hat{a}) = \sum_n^{N_d} k_d^{(n)} \hat{a}^n \quad l_i(\hat{a}) = \sum_n^{N_l} k_l^{(n)} \hat{a}^n \quad (2.25)$$

where N_d , N_l denote the numbers of terms in $d_i(\hat{a})$ and $l_i(\hat{a})$ respectively whilst the $k_d^{(n)}$ and $k_l^{(n)}$ are the polynomial coefficients. Suitable values for these coefficients, corresponding to the desired Bezier profile, were obtained using a least squares fitting procedure set up on a spreadsheet. In essence, this involved making initial guesses for the coefficients and then, using the spreadsheets solver facility,

Fig. 2.6: Schematic illustrating how the particle-point contact function (Eq.2.24) traces out the profile of different classes of shape.



the coefficients were adjusted recursively until the coordinates generated by 2.24 matched, within an acceptable margin of error, the profiles of interest. The details for this procedure are as follows

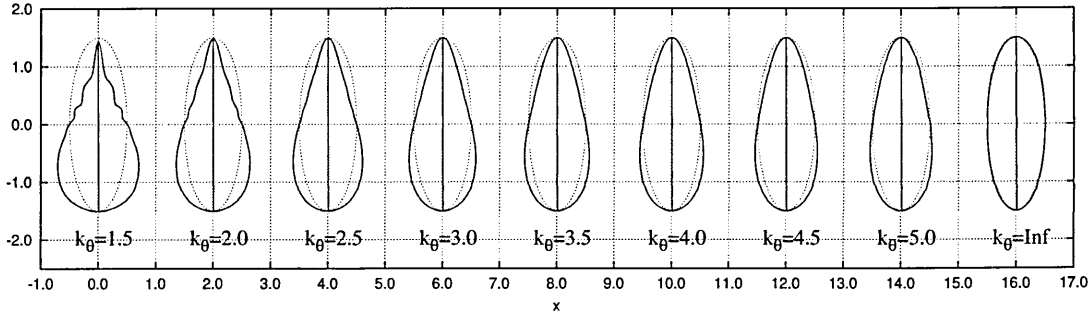
- Define the desired profile of the particle by obtaining a set of 100 points (x_j, y_j) from equation 2.1 (the origin of the coordinate system being the geometric centre of the particle).
- Convert the points to polar coordinates (r_j, ϕ_j) .
- Calculate for each point the scalar product $\hat{a} = \hat{u}_i \cdot \hat{r}_j = \cos(\phi_j)$.

The recursive fitting procedure then proceeds as follows

- For each point, calculate, using equations 2.25 the parametric half width and half length $d_i(\hat{a})$ and $l_i(\hat{a})$.
- Substitute these trial values into the particle-point contact function, equation 2.24.
- For each point calculate the square of the difference between value given by 2.24 and the true particle-point distance, r_j : $\Delta_{ij}^2 = [r_j - \sigma_{ij}]^2$.
- Minimise the sum $\sum_j^{100} \Delta_{ij}^2$ by adjusting the polynomial coefficients.

Figure 2.7 shows the results of this procedure for a range of tapered particle profiles. In nearly all cases the procedure resulted in excellent shape reproduc-

Fig. 2.7: Selected $\kappa = 3$ tapered particle profiles as reproduced by the parameterised $d_i(\hat{a})$ and $l_i(\hat{a})$. Also shown with each particle is an ellipsoid of aspect ratio 3 to give an impression of the degree of taper in each case.



tion, although for the lowest k_θ values one does observe undulations in the fitted profiles.

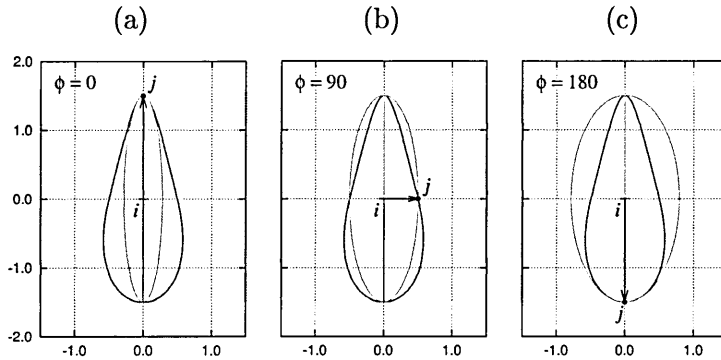
Table 2.2 gives the expansion coefficients for the parameterised $d_i(\hat{a})$ and $l_i(\hat{a})$ for a number of different tapered particle shapes. In general, the expansions for $d_i(\hat{a})$ consist of 11 terms, whilst those for $l_i(\hat{a})$ contain only 2 terms, with $k_l^{(0)}$

Tab. 2.2: Sets of coefficients used in the polynomial expansions of d and l for various pear shapes.

	$\kappa 3 k_\theta 3.0$	$\kappa 4 k_\theta 4.0$	$\kappa 5 k_\theta 5.0$
$k_d^{(0)}$	0.501852454	0.501377232	0.497721868
$k_d^{(1)}$	-0.141145314	-0.129608758	-0.123155821
$k_d^{(2)}$	-0.060542359	-0.074219217	0.024405876
$k_d^{(3)}$	0.225813650	0.484166441	0.723627215
$k_d^{(4)}$	0.832274021	0.923492941	0.389831429
$k_d^{(5)}$	-1.015039575	-1.987232902	-3.018638148
$k_d^{(6)}$	-2.504045172	-2.943008017	-1.951629076
$k_d^{(7)}$	1.375313426	2.808075172	4.413215403
$k_d^{(8)}$	3.196830129	3.815344782	2.998417509
$k_d^{(9)}$	-0.699241457	-1.426641750	-2.241573216
$k_d^{(10)}$	-1.430400139	-1.682476460	-1.416614353
$k_l^{(0)}$	1.498259615	1.995906501	2.493069403
$k_l^{(1)}$	-0.002027616	-0.004518187	-0.008067236

approximately equal to $\kappa/2$ and $k_i^{(1)}$ typically having a value much smaller compared with that of the other coefficients. The consequence of this is that $l_i(\hat{a})$ remains essentially fixed for all \hat{a} , whereas the more numerous and more heavily weighted terms in $d_i(\hat{a})$ play the main role in modulating the parametric ellipsoid shape so as to trace out the required pear profile. These choices for the numbers of coefficients were made on the recommendation of Barmes et al. [14], who found that they consistently gave good polynomial fits to the required Bezier profiles. To summarise: when suitably parameterised half lengths and half widths $d_i(\hat{a})$ and $l_i(\hat{a})$ are inserted into the particle-point contact function, Eq. 2.24, said function accurately reproduces the shapes of tapered uniaxial particles we wish to study. This means that the overall shape of each parametric ellipsoid, i , approximates fairly well to the excluded volume of a hard pear as it would be seen from the perspective of a point particle j . For example, when $\phi = 0^\circ$ and j is at the apex of the particle, as shown in figure 2.8 (a), it ‘sees’ a thin ellipsoid which, in a sense, mimics the three-dimensional shape of that part of the pear which is closest to j . Similarly, when $\phi = 180^\circ$ and j is at the base of the particle, it ‘sees’ a fatter

Fig. 2.8: Plots of the parametric ellipsoids generated by the particle-point contact function for selected polar angles ϕ .



ellipsoid. On this basis, it is reasonable to suppose that, if both sets of semiaxial lengths are parameterised, i.e. $d_i \rightarrow d_i(\hat{a})$, $l_i \rightarrow l_i(\hat{a})$ and $d_j \rightarrow d_j(\hat{b})$, $l_j \rightarrow l_j(\hat{b})$ (where $\hat{b} = b/r = \hat{\mathbf{u}}_j \cdot \hat{\mathbf{r}}_{ij}$) and inserted into the full particle-particle contact function, equation 2.23, then the resulting contact function may serve as a reasonably accurate approximation of a pear-pear contact function. This is known as the parameterised hard Gaussian overlap (PHGO) model.

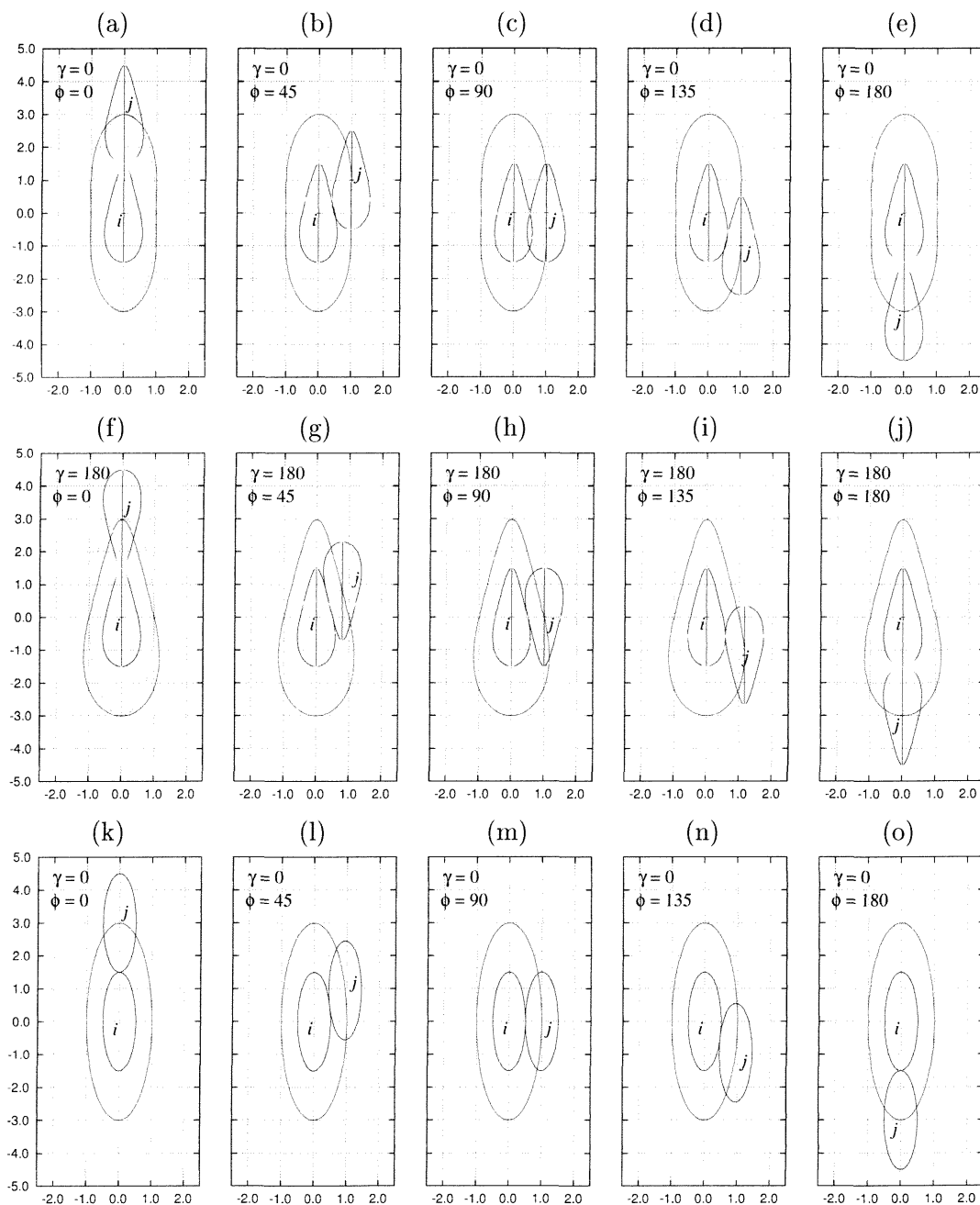
The behaviour of the PHGO model was assessed graphically by plotting, for various mutual orientations of particles i and j , the contact profile generated by the contact function, the contact profile being the locus of contact points traced out as j is translated through 360° about i . In addition, the shapes of the pears and the parametric ellipsoids mimicking their shapes were superimposed onto the plot for selected polar angles, ϕ , in order to gain an impression of how accurately the (PHGO) contact function modelled the steric interaction between two tapered particles. The contact profiles for a pair of parallel and antiparallel $\kappa 3k_\theta 3.0$ pears are presented in figure 2.9 along with that of a pair of parallel $\kappa 3$ Gaussian ellipsoids.

The parallel contact profile has a symmetric torpedo like form reflecting the equivalence of configurations (a) and (e) as well as that of (b) and (d). In general the contact function would appear to represent the steric interaction accurately except for when the particles are side-by-side and the bottom halves of the pears overlap somewhat. This is due to the fact that, for this arrangement in particular, the true contact point lies some distance from the line joining the centres of the two particles. Recall that the parameterisation of the model is based on the particle-point contact function, which best approximates the topography of that region of the pear that is close to this line. In fact, when the particles are exactly side-by-side, the parameterised version of equation 2.23 gives an identical contact distance for both the parallel and antiparallel arrangements.

The anti-parallel contact profile is asymmetric, as it should be, for arrangements (f) and (j) and also (g) and (i) are quite distinct. This time the side-by-side contact distance given by the PHGO contact function is accurate, in fact for antiparallel configurations the contact function would appear to perform well across the entire range of polar angle.

Contact profiles for other pear-pear orientations are shown in appendix E, along with the equivalent profiles for Gaussian ellipsoids. For the $\gamma = 45^\circ$ and $\gamma = 135^\circ$ the contact function again performs quite well in general. For the $\gamma = 90^\circ$ arrangements, the contact distance appears to be somewhat overestimated. However, as

Fig. 2.9: The plots below show contact profiles (red lines) generated as particle j is translated through 360° about a second identical particle, i , in the x - y plane whilst the angle γ subtended by the particles' orientation vectors remains constant. Plots (a-e) show the contact profile for a pair of identical $\kappa 3k\rho 3.0$ pears parallel to each other. Plots (f-j) show the contact profile for a pair of identical $\kappa 3k\rho 3.0$ pears antiparallel to each other. Superimposed on each plot for a selected polar angle ϕ are the shapes of the two pears and the parametric ellipsoids which mimic their tapered shapes. Plots (k-o) show the contact profile for a pair of parallel $\kappa 3$ Gaussian ellipsoids. This contact profile is also included in both (a) and (f) (dashed line) for comparison.



mentioned earlier, the original GO contact function itself departs somewhat from the HER contact distance for the ‘T’ configuration (see table 2.1), which is similar to the $\gamma = 90^\circ$ arrangements.

Though these graphical characterisations of the contact function are not exhaustive (in particular they are only two-dimensional), they strongly suggest that, in general, the parameterised version of the GO contact function provides a satisfactory approximation for the steric interaction of hard tapered particles. Certainly, figure 2.9 confirms that the model is imbued with the correct symmetry properties. Also in the course of analysing the simulation results, particularly the three dimensional renderings of the particles as well as certain distribution functions, there were no indications of excessive overlaps of particles (symptomatic of the underestimation of contact distance) nor of unnatural gaps inbetween them (due to overestimation of contact distance). Given that the PHGO approach is computationally very efficient, requiring little more computational effort than the standard GO shape parameter, these modest imperfections appear justified. Indeed, given current hardware capabilities, the PHGO approach offers the only viable route to producing the volume of results on tapered particles described in this thesis.

2.4 The model potential

To obtain a continuous interparticle pair potential for MD studies, analogous to the hard particle potential used by Barmes et al [14] in their MC simulations, the PHGO contact function, $\sigma^{PHGO}(\hat{\mathbf{u}}_i, \hat{\mathbf{u}}_j, \hat{\mathbf{r}}_{ij})$, was inserted into a potential of the Weeks-Chandler-Anderson (WCA) type, also described as soft repulsive (SR) or hardcore, which resulted in the following potential

$$U_{ij}^{PHGO}(\hat{\mathbf{u}}_i, \hat{\mathbf{u}}_j, \mathbf{r}_{ij}) = \begin{cases} 4\epsilon_0 \{R^{12} - R^6\} + \epsilon_0 & r_{ij} < r_0 \\ 0 & r_{ij} \geq r_0 \end{cases} \quad (2.26)$$

This is simply a truncated, shifted variant of the Lennard-Jones potential. It is shifted in a similar way to the Gay-Berne potential, equation 2.17, that is in equation 2.26, R is given by

$$R = \left(\frac{\sigma_w}{r_{ij} - \sigma(\hat{\mathbf{u}}_i, \hat{\mathbf{u}}_j, \hat{\mathbf{r}}_{ij}) + \sigma_w} \right). \quad (2.27)$$

However note that here we have introduced the new constant σ_w which, for all the simulations reported in this thesis, was arbitrarily set to a value of

$$\sigma_w = \sqrt{(0.5^2 + 0.5^2)} = \frac{1}{\sqrt{2}}. \quad (2.28)$$

This new parameter is required because the prefactor σ_0 appearing in $\sigma^{PHGO}(\hat{\mathbf{u}}_i, \hat{\mathbf{u}}_j, \hat{\mathbf{r}}_{ij})$ is no longer constant since the particle half-widths d_i and d_j are parameterised, i.e.

$$\sigma_0^{PHGO} = \left(d_i(\hat{a})^2 + d_j(\hat{b})^2 \right)^{-1/2} \quad (2.29)$$

The choice of σ_w is in keeping with the nominal half-widths of the tapered particles (or rather the half-widths of their Gaussian distributions, since the contact function ultimately derives from a Gaussian overlap integral). In all cases these half-widths have a value of 0.5. Thus σ_w may be taken as the basic length unit in our simulation studies and corresponds to the separation of a pair of particles when they are placed side-to-side, this is effectively the width of the particle.

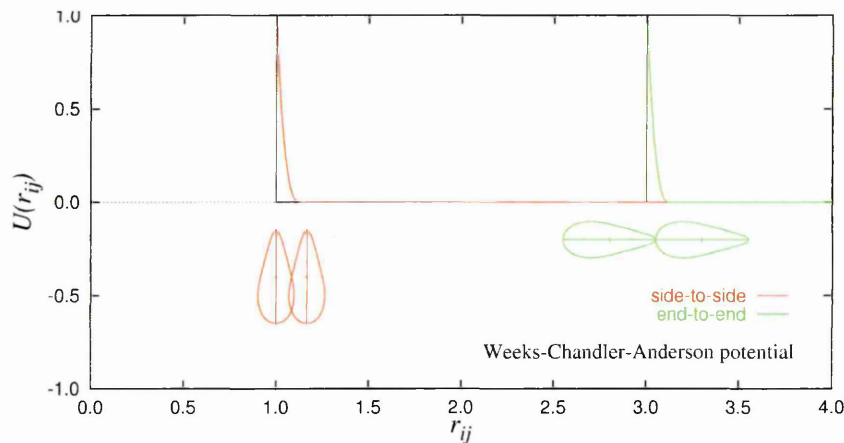
The potential is made purely repulsive by truncating it at the potential minimum by defining the cutoff distance as

$$r_0 = \sigma^{PHGO}(\hat{\mathbf{u}}_i, \hat{\mathbf{u}}_j, \hat{\mathbf{r}}_{ij}) + (2^{1/6} - 1)\sigma_w. \quad (2.30)$$

Finally the potential is shifted vertically by ϵ_0 , with the result that it goes to zero at the cutoff, a property that is essential; this also has the effect of making the gradient equal to zero at the cutoff, a property which, improves the stability of the integration algorithm. The resulting soft repulsive potential is shown in figure 2.10 along with the hard particle potential. Since the former rises so steeply, a

system of particles interacting via this potential should behave very much like ideal hard particles. Also since the soft repulsive potential is purely repulsive and

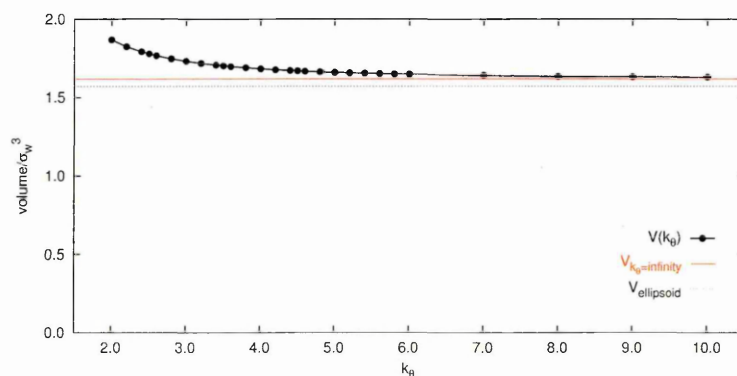
Fig. 2.10: The soft-repulsive potential for the side-to-side and end-to-end arrangements of a pair of $\kappa=3$ pears with $\sigma_0 = 1.0$ and $\epsilon_0 = 1.0$. The black lines indicate the analogous hard particle potential.



given that ϵ_0 is a simple constant, the simulations carried out using it will be essentially athermal.

As a footnote to this section, it is perhaps worth mentioning that the volumes of the solids of revolution corresponding to the fitted profiles, some of which were presented in figure 2.7, were calculated. The results of the volume calculations

Fig. 2.11: Approximate volumes of the solids of revolution corresponding to the fitted profiles for $\kappa = 3$ tapered particle profiles.



are plotted in figure 2.11. It is true that volume is something of a nebulous concept when it comes to the tapered particles as modelled by U_{ij}^{PHGO} , for two reasons. Firstly the potential is not strictly a hard potential – it does not describe

a strictly solid figure – although it is intended to closely reproduce the behaviour of a system of hard particles. Secondly the contact function does not perfectly model the profiles of the particles featured in figure 2.7. Nevertheless it is worth noting that the lower k_θ particles have an appreciably larger nominal volume than their less asymmetric cousins. Whereas the volumes of particles with k_θ greater than about 6.0 are little different from that of the $k_\theta = \infty$ particle. It is also interesting to observe that an ellipsoid of revolution has a distinctly lower volume than the $k_\theta = \infty$ PHGO particle.

CHAPTER 3

Simulation methodology

3.1 Overview

The overarching logic for the simulation and the key computational tasks are summarised in the flow chart, figure 3.1. This sort of organisation is, by and large, generic to all MD simulations. For the studies carried out here, a typical simulation involved a compression or expansion ‘series’ consisting of a succession of ‘runs’ wherein the density was increased or reduced in the early part of each run. The system is then allowed to equilibrate for a certain period prior to the accumulation of time averages of so called ‘runtime’ observables in a second ‘production’ phase of each run. A taxonomy of these observables is set out in section 3.3.

We should state, at this point, that all parameters and observables quoted in this thesis are given in a dimensionless reduced form in that they are expressed in terms of fundamental units of length, energy and mass, σ_w , ϵ_0 and m_0 respectively. The usual convention is to denote reduced quantities by the superscript ‘*’, however since quantities are quoted in reduced form throughout the work reported in this thesis, we choose to omit the superscript henceforth. Appendix A lists the relationships between reduced quantities and their SI counterparts. We

assign the following numerical values to these basic units, $\sigma_w = 1/\sqrt{2}$ i.e. the width of the particle as given by equation 2.28, $\epsilon_0 = 1$ and $m_0 = 1$. In addition we define the moment of inertia of each particle as unity, $I^* = 1$.

Fig. 3.1: Simulation architecture. Here \mathbf{r} , \mathbf{u} , \mathbf{v} , $\dot{\mathbf{u}}$, \mathbf{f} , \mathbf{g} represent the particle positions, orientations, linear velocities, angular velocities, forces and torques respectively. s and r are the timestep and simulation run indices whilst N_{step} and N_{run} are the number of timesteps in a given run and the number of runs in the simulation. The particle indices are i and j and N is the total number of particles in the system.

Read in series parameters: principally system composition.
Define any constants based on series parameters.

```
for( $r=1$ ;  $r \leq N_{run}$ ;  $r++$ )
```

```
  Read in run parameters:  $\rho, T$ , run length, averaging interval etc.  
  Define any constants based on run parameters.  
  Zero runtime observable accumulators.
```

```
  if( $r==1$ )
```

```
    Set up or read in initial configuration.
```

```
  else
```

```
    Get coordinates from end of previous run; compress or expand the system.
```

```
    for( $s=1$ ;  $s \leq N_{step}$ ;  $s++$ )
```

```
      Integration step 1: Calculate  $\mathbf{v}(s+1/2)$ ,  $\dot{\mathbf{u}}(s+1/2)$ 
```

```
      Integration step 2: Calculate  $\mathbf{r}(s+1)$ ,  $\mathbf{u}(s+1)$ 
```

```
      Integration step 3:
```

```
        for( $i=0$ ;  $i \leq (N-1)$ ;  $i++$ )
```

```
          for( $j=0$ ;  $j \leq N$ ;  $j++$ )
```

```
            Calculate  $\mathbf{f}(s+1)$ ,  $\mathbf{g}(s+1)$  along with total potential  $U(s)$ 
```

```
      Integration step 4: Calculate  $\mathbf{v}(s+1)$ ,  $\dot{\mathbf{u}}(s+1)$ 
```

```
      Maintain zero net linear momentum.
```

```
      Calculate runtime observables; accumulate tallies.
```

```
      At intervals log the runtime observables and save configurations.
```

```
      Apply ensemble rescaling as necessary.
```

```
      Attempt anisotropic rescaling if required.
```

```
      At intervals, back up full set of system coordinates to maximum precision.
```

```
Calculate and log averages of runtime observables.
```

```
Save final configurations.
```

All the simulations were carried out within an orthorhombic volume, V , having dimensions L_x, L_y, L_z . This is henceforth referred to as the simulation box or simulation volume. The number density of particles within this volume is simply defined as the number of particles N divided by the volume, $\rho = N/V$. The position of each particle, i , is specified by a position vector \mathbf{r}_i , the origin of the coordinate system being located at the centre of the simulation box. The relative position of another particle, j , with respect to i is defined as $\mathbf{r}_{ij} = \mathbf{r}_i - \mathbf{r}_j$, the corresponding unit vector being specified by $\hat{\mathbf{r}}_{ij} = \mathbf{r}_{ij}/r_{ij}$. In order to perform simulations of bulk fluids, standard periodic boundary conditions (see for example [23]) are applied in all three Cartesian directions.

Changes in density are implemented by rescaling the particle coordinates and the box lengths by the same proportion in each Cartesian direction. On occasions so called anisotropic rescaling is applied, whereby the ratios of the box dimensions are allowed to vary whilst the volume is kept constant. This is intended to prevent pressure anisotropy from developing in systems with anisotropic supramolecular order, in particular the smectic phase. The details of the anisotropic rescaling algorithm will be discussed in the next chapter. The initial configuration for a compression series usually consists of an FCC arrangement of particles, each of which is oriented in the [111] direction. In specifying the initial density, care must be taken that it is sufficiently low that the particles in this starting formation are not overlapping. The particles are then randomly assigned with initial linear velocities from the Maxwell-Boltzmann distribution

$$f_{MB}(T) = \left(\frac{m}{2\pi k_B T} \right)^{3/2} \exp[-mv^2/2k_B T] . \quad (3.1)$$

An analogous distribution could also have been assigned to the angular velocities however, as we will show in chapter 4, energy equipartition between the translational and rotational degrees of freedom occurs very rapidly compared to a typical run length. Therefore, in these simulations at least, assigning an initial rotational velocity distribution is not strictly necessary.

Most of the simulation runs are carried out in the constant NVT or canonical ensemble, although from time to time runs in constant NVE or microcanonical ensemble are performed for the purposes of thermalisation or as acid tests for coding or procedural errors. In the NVT runs, the temperature is maintained by periodically adjusting the linear velocities, \mathbf{v}_i , thus

$$\mathbf{v}'_i = \mathbf{v}_i \sqrt{\frac{T_{set}}{T}} \quad (3.2)$$

where \mathbf{v}'_i is the rescaled velocity, T_{set} is the target temperature and T the instantaneous measured temperature. In addition, the linear momenta of the individual particles are shifted in order to maintain zero net linear momentum for the system as a whole. The shifted momenta are given by

$$\mathbf{p}'_i = \mathbf{p}_i - \frac{1}{N} \sum_i^N m_i \mathbf{v}_i . \quad (3.3)$$

Temperature and momentum rescaling are applied at every time step. The particle positions, orientations linear and rotational velocities are advanced through the four so called integration steps within the time stepping loop featured in figure 3.1. The integrator used here is the velocity-Verlet algorithm [24], which is summarised in the next section along with definitions of the forces which ultimately drive the dynamics of the system.

3.2 Forces, torques and their integration

In our simulations, the net force on a given particle i is assumed to be the vector sum of pairwise forces \mathbf{f}_{ij} . This force may be expressed as an appropriate gradient of the pair potential U_{ij}

$$\mathbf{f}_{ij} = -\nabla_{\mathbf{r}_{ij}} U_{ij} \quad (3.4)$$

The assumption that the interparticle potential contains only pairwise contributions and no higher body terms is entirely justified here. The very nature of the hard particle potential ensures that the interaction between any given pair particles will be in no way affected by the presence of other particles in the vicinity. We observe that U_{ij}^{PHGO} contains three scalar products involving \mathbf{r}_{ij} , namely $a = (\hat{\mathbf{u}}_i \cdot \mathbf{r}_{ij})$, $b = (\hat{\mathbf{u}}_j \cdot \mathbf{r}_{ij})$ and $r = r_{ij} = (\hat{\mathbf{r}}_{ij} \cdot \mathbf{r}_{ij})$. It is therefore convenient to rewrite equation 3.4 as

$$\mathbf{f}_{ij} = - \sum_{\mathbf{s}} \nabla_{\mathbf{r}_{ij}} U_{ij}(\mathbf{s} \cdot \mathbf{r}_{ij}) \quad (3.5)$$

wherein \mathbf{s} represents the set of vectors $\{\hat{\mathbf{u}}_i, \hat{\mathbf{u}}_j, \hat{\mathbf{r}}_{ij}\}$. Manipulation of the right hand side of 3.5 (see appendix B) leads to an expression for \mathbf{f}_{ij} in terms of derivatives with respect to the dot products a , b and r_{ij} .

$$\mathbf{f}_{ij} = - \frac{\partial U_{ij}}{\partial a} \hat{\mathbf{u}}_i - \frac{\partial U_{ij}}{\partial b} \hat{\mathbf{u}}_j - \frac{\partial U_{ij}}{\partial r} \hat{\mathbf{r}}_{ij} \quad (3.6)$$

According to Newton's third law, the force on particle j due to i is the equal and opposite of \mathbf{f}_{ij} , i.e. $\mathbf{f}_{ji} = -\mathbf{f}_{ij}$. The total force on each particle is simply the sum of all the pairwise contributions

$$\mathbf{f}_i = \sum_{j \neq i}^N \mathbf{f}_{ij} \quad (3.7)$$

The full explicit expressions for the derivatives appearing in 3.6 are not given here since they are unwieldy even for a pair of Gaussian overlap particles with constant half-widths and half-lengths, let alone for PHGO particles wherein d_i , l_i and d_j , l_j are parametric in $\hat{a} = (\hat{\mathbf{u}}_i \cdot \hat{\mathbf{r}}_{ij}) = a/r_{ij}$ and $\hat{b} = (\hat{\mathbf{u}}_j \cdot \hat{\mathbf{r}}_{ij}) = b/r_{ij}$ respectively. As far as the coding of these derivatives was concerned, the strategy adopted was essentially repeated application of the chain rule which naturally breaks the calculation down into small steps, which makes checking for errors less daunting. The angular acceleration of a body are related to its moment of inertia and the net torque acting on it by

$$\tau_i = \tilde{I}_i \alpha_i = \tilde{I}_i \dot{\omega}_i = \tilde{I}_i \ddot{\theta}_i \quad (3.8)$$

where \tilde{I}_i is the inertia tensor, α_i is the angular acceleration, ω_i is the angular velocity and θ_i is a vector parallel to ω_i which defines the orientation of the body in space. A linear particle (that is to say one with cylindrical symmetry), whose orientation is defined by a unit vector, $\hat{\mathbf{u}}$, pointing along the long axis, has only two degrees of rotational freedom since it is invariant to rotation about $\hat{\mathbf{u}}$. Further, rotation is at all times perpendicular to $\hat{\mathbf{u}}$ and the inertia tensor reduces to the principal moment of inertia I . The expression for the torque on such an object reduces to

$$\boldsymbol{\tau}_i = \hat{\mathbf{u}}_i \wedge \mathbf{g}_i \equiv \hat{\mathbf{u}}_i \wedge \mathbf{g}_i^\perp \quad (3.9)$$

where \mathbf{g}_i can be thought of as the turning force acting on $\hat{\mathbf{u}}_i$ and is referred to in this context as the ‘gorque’. In the above expression the full gorque can always be replaced by its component perpendicular to $\hat{\mathbf{u}}$, since

$$\hat{\mathbf{u}}_i \wedge \mathbf{g}_i \equiv \hat{\mathbf{u}}_i \wedge \mathbf{g}_i^\perp \quad (3.10)$$

where the perpendicular component is given by

$$\mathbf{g}_{ij}^\perp = \mathbf{g}_i - (\mathbf{g}_i \cdot \hat{\mathbf{u}}_i) \hat{\mathbf{u}}_i \quad (3.11)$$

The gorque, \mathbf{g}_{ij} , on i due to a second linear particle j can be obtained by taking the gradient of the interparticle potential with respect to the unit vector $\hat{\mathbf{u}}_i$ of the former

$$\mathbf{g}_{ij} = -\nabla_{\hat{\mathbf{u}}_i} U_{ij} . \quad (3.12)$$

We note that U_{ij}^{PHGO} contains two scalar products involving $\hat{\mathbf{u}}_i$, namely $\hat{a} = a/r_{ij} = (\hat{\mathbf{u}}_i \cdot \hat{\mathbf{r}}_{ij})$ and $c = (\hat{\mathbf{u}}_i \cdot \hat{\mathbf{u}}_j)$. It is therefore convenient to rewrite equation 3.12 as

$$\mathbf{g}_{ij} = -\sum_s \nabla_{\hat{\mathbf{u}}_i} U_{ij} (\mathbf{s} \cdot \hat{\mathbf{u}}_i) \quad (3.13)$$

where

$$\mathbf{s} = \{ \hat{\mathbf{u}}_j, \hat{\mathbf{r}}_{ij} \} .$$

By manipulation of the rhs of 3.13, in a similar fashion to the treatment of 3.5, we obtain an expression for \mathbf{g}_{ij} in terms of a and c

$$\mathbf{g}_{ij} = -\frac{\partial U_{ij}}{\partial a} \mathbf{r}_{ij} - \frac{\partial U_{ij}}{\partial c} \hat{\mathbf{u}}_j \quad (3.14)$$

and, simply by interchanging $\hat{\mathbf{u}}_i$ and $\hat{\mathbf{u}}_j$, a similar expression for \mathbf{g}_{ji} in terms of b and c

$$\mathbf{g}_{ji} = -\frac{\partial U_{ij}}{\partial b} \mathbf{r}_{ij} - \frac{\partial U_{ij}}{\partial c} \hat{\mathbf{u}}_i \quad (3.15)$$

The total torque on each particle is simply the sum of all the pairwise contributions

$$\mathbf{g}_i = \sum_{j \neq i}^N \mathbf{g}_{ij} \quad (3.16)$$

Singer [25] showed that it is possible to express the dynamics of a linear particle, in terms of the rotation of the axial vector, $\hat{\mathbf{u}}_i$, as a second order differential equation of the form

$$I_i \ddot{\hat{\mathbf{u}}}_i = \mathbf{g}_{ij}^\perp + \lambda \hat{\mathbf{u}}_i \quad (3.17)$$

where λ is a correction factor necessary to maintain the modulus of $\hat{\mathbf{u}}_i$ at unity. Discretised forms of equation 3.17 have proved highly suitable as a means of evolving the rotational dynamics of systems of uniaxial particles in MD simulations. One such integration scheme is the velocity-Verlet algorithm, which we use in our MD simulations, and which we now briefly outline. Within the velocity-Verlet scheme, given the positions, linear velocities and forces on all particles at time step s , the following four steps are applied to obtain $\mathbf{r}_i^{(s+1)}$, $\mathbf{v}_i^{(s+1)}$ and $\mathbf{f}_i^{(s+1)}$

$$\mathbf{v}_i^{(s+1/2)} = \mathbf{v}_i^{(s)} + \frac{\Delta t}{2m_i} \mathbf{f}_i^{(s)} \quad (3.18)$$

$$\mathbf{r}_i^{(s+1)} = \mathbf{r}_i^{(s)} + \Delta t \mathbf{v}_i^{(s+1/2)} \quad (3.19)$$

$$\text{Calculate } \mathbf{f}_i^{(s+1)} \quad (3.20)$$

$$\mathbf{v}_i^{(s+1)} = \mathbf{v}_i^{(s+1/2)} + \frac{\Delta t}{2m_i} \mathbf{f}_i^{(s+1)} \quad (3.21)$$

An analogous set of steps are used to advance the orientations, angular velocities and torques

$$\mathbf{u}_i^{(s+1/2)} = \dot{\mathbf{u}}_i^{(s)} + \frac{\Delta t}{2I_i} \mathbf{g}_{\perp i}^{(s)} + \lambda'' \mathbf{u}_i^{(s)} \quad (3.22)$$

$$\mathbf{u}_i^{(s+1)} = \mathbf{u}_i^{(s)} + \Delta t \dot{\mathbf{u}}_i^{(s+1/2)} \quad (3.23)$$

$$\text{Calculate } \mathbf{g}_i^{(s+1)} \quad (3.24)$$

$$\dot{\mathbf{u}}_i^{(s+1)} = \dot{\mathbf{u}}_i^{(s+1/2)} + \frac{\Delta t}{2I_i} \mathbf{g}_{\perp i}^{(s+1)} + \left(\dot{\mathbf{u}}_i^{(s+1/2)} \cdot \mathbf{u}_i^{(s+1)} \right) \mathbf{u}_i^{(s+1)} \quad (3.25)$$

Note that here, where we denote the first and second time derivatives of the orientation vector as $\dot{\mathbf{u}}$ and $\ddot{\mathbf{u}}$, the hat ($\hat{\cdot}$) above \mathbf{u} has been dropped for clarity. The extra terms in equations C.5 and C.8, as compared to C.1 and C.4, are the correction factors required to maintain the unit modulus of \mathbf{u} . In particular, The factor λ'' in C.5 is a Lagrangian correction factor whose initial value is obtained from equation C.9 and then refined by two identical iterative steps C.10 and C.11

$$\lambda_0 = -\frac{\Delta t}{2} \left\{ \dot{\mathbf{u}}_i^{(s)} \cdot \dot{\mathbf{u}}_i^{(s)} + \frac{\Delta t}{2I_i} \mathbf{g}_{\perp i}^{(s)} \cdot \left(2\dot{\mathbf{u}}_i^{(s)} + \frac{\Delta t}{2I_i} \mathbf{g}_{\perp i}^{(s)} \right) \right\} \quad (3.26)$$

$$\lambda' = \lambda_0 - \frac{(1 + \lambda_0 \Delta t)^2 (\mathbf{u}_i^{(s)} \cdot \mathbf{u}_i^{(s)}) - 1 - \lambda_0 \Delta t}{2\Delta t (1 + \lambda_0 \Delta t)} \quad (3.27)$$

$$\lambda'' = \lambda' - \frac{(1 + \lambda' \Delta t)^2 (\mathbf{u}_i^{(s)} \cdot \mathbf{u}_i^{(s)}) - 1 - \lambda_0 \Delta t}{2\Delta t (1 + \lambda' \Delta t)}. \quad (3.28)$$

If transcribing these equations into computer code, note well that the λ that appears in the final term of the numerator in C.11 retains the original value λ_0 as given by C.9, whilst the λ that appear elsewhere in C.11 have the value λ' obtained from the preceding iteration, C.10. The velocity-Verlet algorithm was selected for use in our simulations because of its stability over long simulation times. In all simulations the time step used was $\Delta t = 0.0015$. This value was chosen for two reasons, firstly this length of time step has been used in many other studies, therefore use of the same value here allows, if needs be, for a more direct com-

parison with those studies. Secondly this length of time step consistently resulted in excellent energy conservation in test runs in the NVE ensemble.

3.3 Runtime Observables

In this section we set down the definitions of the system observables that are computed and accumulated during the course of each run and then time averaged at its end. The total potential energy of the system is simply the sum of all the pairwise interactions

$$U_{tot} = \sum_{i=1}^N \sum_{j>i}^N U_{ij} \equiv \frac{1}{2} \sum_{i=1}^N \sum_{j \neq i}^N U_{ij} . \quad (3.29)$$

The total kinetic energy consists of translational (trans) and rotational (rotor) parts associated with the linear and rotational velocities of the particles. These are calculated separately for the x -, y - and z -components of the velocities

$$KE_{trans\ tot}^{(\alpha)} = \sum_{i=1}^N \frac{1}{2} m_i v_i^{(\alpha)2} \quad (3.30)$$

$$KE_{rotor\ tot}^{(\alpha)} = \sum_{i=1}^N \frac{1}{2} m_i \dot{u}_i^{(\alpha)2} \quad (3.31)$$

$$KE_{trans\ tot} = \sum_{\alpha} KE_{trans\ tot}^{(\alpha)} \quad (3.32)$$

$$KE_{rotor\ tot} = \sum_{\alpha} KE_{rotor\ tot}^{(\alpha)} \quad (3.33)$$

$$KE_{tot} = KE_{trans\ tot} + KE_{rotor\ tot} \quad (3.34)$$

where $\alpha = x, y, z$. The total system energy is the sum of the system potential and kinetic energy

$$E_{tot} = U_{tot} + KE_{tot} . \quad (3.35)$$

The temperature of the system is based on the fundamental energy equipartition relation, which states that the average kinetic energy per degree of freedom is equal to $(1/2)k_B T$. Since each particle has three translational degrees of freedom but only two rotational degrees of freedom, because it is a linear particle, the temperature is given by

$$T = \frac{2}{5Nk_B} K E_{tot} . \quad (3.36)$$

Note that the Boltzmann constant, k_B , simply equals 1.0 when physical properties are expressed in reduced units. The temperatures associated with translational and rotational motion are calculated individually in order to check for energy equipartition

$$T_{trans} = \frac{2}{3Nk_B} K E_{trans} \quad (3.37)$$

$$T_{rotor} = \frac{2}{2Nk_B} K E_{rotor} . \quad (3.38)$$

The ideal pressure, P_{ideal} , is given by the ideal gas equation $PV = Nk_B T$, which assumes that the molecules comprising the gas have negligible volume and exert negligible forces on each other

$$P_{ideal} = \frac{Nk_B T}{V} = \rho T . \quad (3.39)$$

The excess pressure, P_{excess} , which accounts for the finite particle volume and interaction potential, is given by a form of virial equation

$$P_{excess} = \frac{1}{V} W = \frac{1}{V} \frac{1}{d} \sum_{i=1}^N \sum_{j>i}^N \mathbf{r}_{ij} \cdot \mathbf{f}_{ij} \quad (3.40)$$

where d is the dimensionality of the system, which is obviously 3 in this case. Naturally, this quantity is accumulated within the interactions loop. The Cartesian components of the excess pressure are calculated separately in order to provide a

gauge of pressure anisotropy

$$P_{excess}^{(\alpha)} = \frac{1}{V} \frac{1}{d} \sum_{i=1}^N \sum_{j>i}^N r_{ij}^{(\alpha)} f_{ij}^{(\alpha)}. \quad (3.41)$$

The total pressure is simply the sum of the ideal and excess pressures

$$P_{tot} = P_{ideal} + P_{excess}. \quad (3.42)$$

The mobility of particles is characterised by their mean squared displacements

$$\langle (\Delta r(t))^2 \rangle = \frac{1}{N} \sum_{i=1}^N \sum_{\alpha} \left\{ \left(\Delta r_i^{(\alpha)} \right)^2 (t) \right\}. \quad (3.43)$$

where $\Delta r_i^{(\alpha)} = r_i^{(\alpha)}(t) - r_i^{(\alpha)}(0)$. As we shall see, monitoring the mean squared x -, y - and z - components of displacement is useful for determining if diffusion is favoured along a certain axis, whilst the magnitude of the overall mean squared displacement is a good indicator of liquid-solid transitions. The diffusion coefficient is also measured

$$D = \frac{1}{2d} \frac{\langle (\delta r(t))^2 \rangle}{\Delta t} = \frac{1}{6N} \sum_{i=1}^N \sum_{\alpha} \left\{ \left(\delta r_i^{(\alpha)} \right)^2 (t) \right\} \quad (3.44)$$

where $\delta r_i^{(\alpha)} = r_i^{(\alpha)}(t) - r_i^{(\alpha)}(t - \Delta t)$.

The orientational order within the system is characterised by the director, $\hat{\mathbf{n}}$, and the nematic order parameter P_2 . The classic definition of the order parameter is

$$P_2 = \left\langle \frac{3}{2} \cos^2 \theta_i - \frac{1}{2} \right\rangle = \frac{1}{N} \sum_{i=1}^N \left(\frac{3}{2} (\hat{\mathbf{u}}_i \cdot \hat{\mathbf{n}})^2 - \frac{1}{2} \right) \quad (3.45)$$

where θ_i is the angle subtended by the individual particle orientation vectors and the director. To obtain P_2 using this equation, one must have $\hat{\mathbf{n}}$. In principle it is possible to solve this problem by treating $\hat{\mathbf{n}}$ as a variable, and finding the value of it which maximizes P_2 . This would be done by evaluating equation 3.45, at a given timestep, for the particle coordinates $\hat{\mathbf{u}}_i$ and a discrete distribution, on a unit sphere, of trial $\hat{\mathbf{n}}$ values. The maximum P_2 value and hence the director

would then be determined by calculating numerically the gradient with respect to $\hat{\mathbf{n}}$ of the resulting set of P_2 values. This is clearly quite an involved procedure. Fortunately the solution can be arrived at more directly by diagonalising of the Q-matrix,

$$\mathbf{Q} = \frac{3}{2} \sum_i^N \left(\hat{\mathbf{u}}_i \hat{\mathbf{u}}_i - \frac{1}{3} \mathbf{I} \right) \quad (3.46)$$

where \mathbf{I} is the unit second-rank tensor. The Q-matrix contains within it the contributions of all the particles to the collective orientational ordering of the system. According to this procedure, the nematic order parameter is the largest eigenvalue of the Q-matrix and the director is the eigenvector corresponding to this eigenvalue. This is the method we use, it is implemented with the aid of standard mathematical functions from the Numerical Recipes library. A polar order parameter P_1 is also defined. To obtain it we first compute a polar director $\hat{\mathbf{n}}_{P_1}$ thus

$$\begin{aligned} \mathbf{n}_{P_1} &= \frac{1}{N} \sum_i^N \hat{\mathbf{u}}_i \\ \hat{\mathbf{n}}_{P_1} &= \frac{\mathbf{n}_{P_1}}{|\mathbf{n}_{P_1}|} \end{aligned} \quad (3.47)$$

then the polar order parameter itself is calculated using

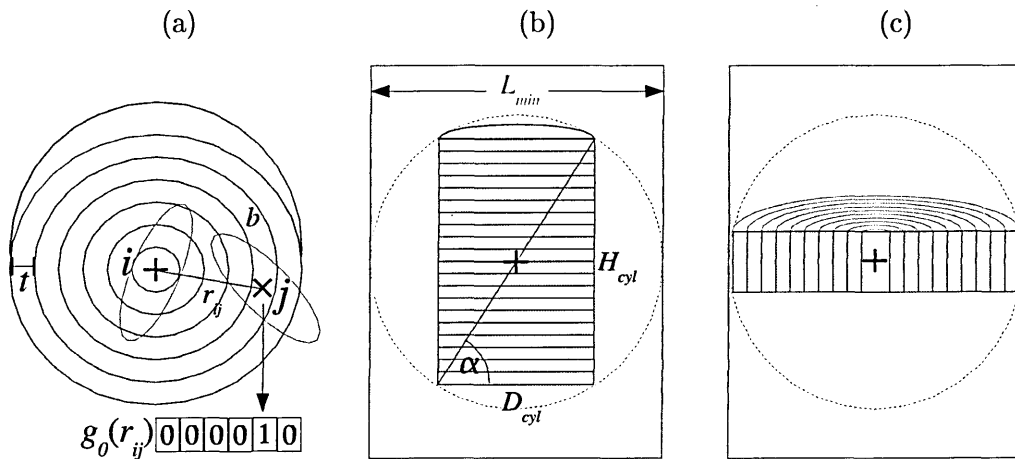
$$P_1 = \frac{1}{N} \sum_i^N \hat{\mathbf{u}}_i \cdot \hat{\mathbf{n}}_{P_1} . \quad (3.48)$$

The runtime observables described above are calculated at each and every timestep in the production phase of each run and accumulated for time averaging at the end of the run. The instantaneous values of observables are saved to file, usually every 100 timesteps, throughout the entire run. Particle positions and orientations are also saved to file, normally just during the production phase, at intervals typically of 10000 timesteps.

3.4 Post processing

As we shall see in the forthcoming results chapters, plotting the averages of certain observables can provide good indications of phase transitions. Also, one can often immediately recognise the type of phase that prevails by inspecting visualisations of the system, as generated using an appropriate computer graphics package. However, for quantitative information relating to phase structure, we often need to compute distribution functions or correlation functions as they are also known. The simplest of these is the radial distribution function $g_0(r_{ij})$. To compute this, a spherical sampling volume centred on a given particle, i , is divided into a series of concentric spherical shells as shown in figure 3.2 (a). We choose to limit the maximum radius of the sampling volume to $R_{sph\ max} = L_{min}/2$, where L_{min} is

Fig. 3.2: Schematics showing cross-sections through the sampling volumes used in the computation of (a) radial, (b) longitudinal and (c) lateral distribution functions.



length of the smallest simulation box dimension¹. The radial distance of each neighbouring particle, j , from i is calculated and is 'binned' according to which shell it lies within. In other words an array element is incremented every time a distance r_{ij} is found which lies within a certain interval and, thus, a histogram of

¹By this we mean the smallest boxlength associated with any of the configurations that contribute to the analysis since this value determines the shell thickness, a parameter that is best kept fixed, for a given class of $g(r)$, throughout the course of its compilation

distances r_{ij} is compiled. The principle of this operation is illustrated in figure 3.2 (a). This is repeated for all particles in the system and for a number of configurations, these having been saved during the simulation run (correlation functions are nearly always calculated after the simulation has finished). The purpose of the exercise, of course, is to reveal distinctive patterns in the way the local population density of particles varies with r_{ij} and, thus, gain insight into the subtleties of the phase structure. The bigger the system and the greater the number of configurations analysed, the better will be the statistics and the finer the structural detail revealed. The totals accumulated in each bin, b , of the distribution function are normalised by dividing by three quantities

$$f_{norm}^{(b)} = \frac{1}{n_{ideal}^{(b)}} \times \frac{1}{N} \times \frac{1}{N_{config}} \quad (3.49)$$

$n_{ideal}^{(b)}$ is the number of particles that would be expected to be found in shell b if the particles were distributed randomly like those of an ideal gas, i.e.

$$n_{ideal}^{(b)} = \frac{N}{V} V_{shell}^{(b)} \quad (3.50)$$

If r_b is the inner radius of the shell b and t the thickness of the shell, then its volume, $V_{shell}^{(b)}$, will be given by

$$\begin{aligned} V_b &= \frac{4\pi}{3} [(r_b + t)^3 - r_b^3] \\ &= \frac{4\pi}{3} [3r_b^2 t + 3r_b t^2 + t^3] \end{aligned} \quad (3.51)$$

The shell thickness is usually defined by specifying the number of bins, so that $t = R_{sph\ max}/N_{bins}$. As for the other two terms in equation 3.49, N is the total number of particles in the system and N_{config} the number of configurations analysed to obtain the distribution function. Thus the normalisation allows for a fair comparison to be made between $g(r)$ s obtained from different system sizes and different numbers of configurations.

The next major type of distribution function is the longitudinal distribution function $g_1(r_{ij}||\hat{n})$, which is designed to capture particle-particle correlations as a func-

tion of the distance parallel to the director. Hence $r_{ij\parallel\hat{n}} = -\mathbf{r}_{ij} \cdot \hat{\mathbf{n}}$. Note that a minus sign is included here due to the fact that we happen to have defined the interparticle vector such that it points from j to i , that is $\mathbf{r}_{ij} = \mathbf{r}_i - \mathbf{r}_j$. This function is used, in particular, to quantify the interlayer distances between the lamellae of smectic phases. The sampling volume for this function is a cylinder divided into a series of disks each of thickness t , as shown in figure 3.2 (b), the axis of the cylinder being parallel to $\hat{\mathbf{n}}$. To ensure that the volume does not overstep the periodic boundaries, its dimensions are constrained by the following inequalities.

$$\begin{aligned} H_{cyl} &< L_{min} \cos \alpha \\ D_{cyl} &< L_{min} \sin \alpha . \end{aligned}$$

where $\alpha = \tan^{-1}(K)$, K being the desired height to diameter ratio of the cylinder. The normalisation factor for $g_1(r_{ij\parallel\hat{n}})$ is similar to that of the radial distribution function, equation 3.49, except that the shell volume for $g_1(r_{ij\parallel\hat{n}})$ is given by

$$V_b = 2\pi(D_{cyl}/2)^2 t$$

In the analysis of the structures formed by tapered particle we also make use of a second variety of longitudinal distribution function, namely $g_1(r_{ij\parallel\hat{u}_i})$. This is similar to $g_1(r_{ij\parallel\hat{n}})$ except that it is a function of the distance parallel to the molecular orientation, $\hat{\mathbf{u}}_i$, as opposed to $\hat{\mathbf{n}}$, hence $r_{ij\parallel\hat{u}_i} = -\mathbf{r}_{ij} \cdot \hat{\mathbf{u}}_i$. Accordingly the axis of the cylindrical sampling volume is parallel to $\hat{\mathbf{u}}_i$.

The final major type of distribution function is the lateral distribution function $g_2(r_{ij\perp\hat{n}})$, which is designed to capture particle-particle correlations as a function of the distance perpendicular to the director, hence $r_{ij\perp\hat{n}} = \sqrt{r_{ij}^2 - r_{ij\parallel\hat{n}}^2}$. The sampling volume for this function is again a cylinder aligned with the director but this time divided into annular shells as shown in figure 3.2 (c), with volumes given by

$$V_b = 2\pi H_{cyl}(2rt + t^2)$$

where once again r is the inner radius of the shell and t its thickness. This function is designed to pick up intralayer correlations in smectic phases i.e. between particles within the same layers. The height of the cylindrical sampling volume is therefore chosen so that it should encompass a single layer. The radius is then automatically set to the largest value it can have without exceeding the periodic boundaries. A second variety of lateral distribution function is defined, namely $g_2(r_{ij\perp\hat{u}_i})$, which is a function of the distance perpendicular to \hat{u}_i as opposed to \hat{n} , hence $r_{ij\perp\hat{u}_i} = \sqrt{r_{ij}^2 - r_{ij\parallel\hat{n}}^2}$. Naturally, in this case, the axis of the sampling volume is perpendicular to \hat{u}_i .

All of the $g(r)$ s described so far give correlations in terms of local particle population densities. However we also find it useful to consider variants of the above functions which reflect the correlations in terms of the relative orientations of particles. For example we define a polar radial distribution function, $g_0(r_{ij})^{(P1)}$, which has a sampling volume identical to $g_0(r_{ij})$. The difference is that with $g_0(r_{ij})^{(P1)}$, the quantity that is accumulated in the histogram is $\Delta P_1 = \cos(\gamma) = (\hat{u}_i \cdot \hat{u}_j)$, γ being the angle subtended by the two orientation vectors. Also the histogram is normalised differently, it is normalised using the corresponding *unnormalised* $g_0(r_{ij})$. Thus a high value of $g_0(r_{ij})^{(P1)}$, for a given distance r_{ij} , would indicate that particles at this separation are strongly correlated in terms of their relative orientation but it does not necessarily mean that such a correlation is commonplace. In a similar vein, a nematic radial distribution function $g_0(r_{ij})^{(P2)}$ is defined in which the quantity that is binned is $\Delta P_2 = (3/2)\cos^2(\gamma) - (1/2)$, Again, the corresponding unnormalised $g_0(r_{ij})$ is used to normalise $g_0(r_{ij})^{(P2)}$. Analogous polar and nematic varieties of the longitudinal and lateral distribution functions are also defined. This menagerie of functions is summarised in table 3.1.

Tab. 3.1: Summary of the distribution functions used to clarify and quantify phase structure. The entries in the ‘shorthand’ column are truncated forms of the full function notation, which are used in the text henceforth as well as for the labelling of graphs of these distribution functions.

function	shorthand	distance	quantity binned
$g_0(r_{ij})$	g_0	$\sqrt{(\mathbf{r}_{ij} \cdot \mathbf{r}_{ij})}$	number density
$g_0(r_{ij})^{(P1)}$	$g_0^{(P1)}$	$\sqrt{(\mathbf{r}_{ij} \cdot \mathbf{r}_{ij})}$	$\cos(\gamma) = (\hat{\mathbf{u}}_i \cdot \hat{\mathbf{u}}_j)$
$g_0(r_{ij})^{(P2)}$	$g_0^{(P2)}$	$\sqrt{(\mathbf{r}_{ij} \cdot \mathbf{r}_{ij})}$	$(3/2) \cos^2(\gamma) - (1/2)$
$g_1(r_{ij} \hat{\mathbf{n}})$	$g_1 n$	$(-\mathbf{r}_{ij} \cdot \hat{\mathbf{n}})$	number density
$g_1(r_{ij} \hat{\mathbf{n}})^{(P1)}$	$g_1^{(P1)} n$	$(-\mathbf{r}_{ij} \cdot \hat{\mathbf{n}})$	$\cos(\theta) = (\hat{\mathbf{n}} \cdot \hat{\mathbf{u}}_j)$
$g_1(r_{ij} \hat{\mathbf{n}})^{(P2)}$	$g_1^{(P2)} n$	$(-\mathbf{r}_{ij} \cdot \hat{\mathbf{n}})$	$(3/2) \cos^2(\theta) - (1/2)$
$g_1(r_{ij} \hat{\mathbf{u}}_i)$	$g_1 u$	$(-\mathbf{r}_{ij} \cdot \hat{\mathbf{u}}_i)$	number density
$g_1(r_{ij} \hat{\mathbf{u}}_i)^{(P1)}$	$g_1^{(P1)} u$	$(-\mathbf{r}_{ij} \cdot \hat{\mathbf{u}}_i)$	$\cos(\gamma) = (\hat{\mathbf{u}}_i \cdot \hat{\mathbf{u}}_j)$
$g_1(r_{ij} \hat{\mathbf{u}}_i)^{(P2)}$	$g_1^{(P2)} u$	$(-\mathbf{r}_{ij} \cdot \hat{\mathbf{u}}_i)$	$(3/2) \cos^2(\gamma) - (1/2)$
$g_2(r_{ij}\perp\hat{\mathbf{n}})$	$g_2 n$	$\sqrt{r_{ij}^2 - (\mathbf{r}_{ij} \cdot \hat{\mathbf{n}})^2}$	number density
$g_2(r_{ij}\perp\hat{\mathbf{n}})^{(P1)}$	$g_2^{(P1)} n$	$\sqrt{r_{ij}^2 - (\mathbf{r}_{ij} \cdot \hat{\mathbf{n}})^2}$	$\cos(\theta) = (\hat{\mathbf{n}} \cdot \hat{\mathbf{u}}_j)$
$g_2(r_{ij}\perp\hat{\mathbf{n}})^{(P2)}$	$g_2^{(P2)} n$	$\sqrt{r_{ij}^2 - (\mathbf{r}_{ij} \cdot \hat{\mathbf{n}})^2}$	$(3/2) \cos^2(\theta) - (1/2)$
$g_2(r_{ij}\perp\hat{\mathbf{u}}_i)$	$g_2 u$	$\sqrt{r_{ij}^2 - (\mathbf{r}_{ij} \cdot \hat{\mathbf{u}}_i)^2}$	number density
$g_2(r_{ij}\perp\hat{\mathbf{u}}_i)^{(P1)}$	$g_2^{(P1)} u$	$\sqrt{r_{ij}^2 - (\mathbf{r}_{ij} \cdot \hat{\mathbf{u}}_i)^2}$	$\cos(\gamma) = (\hat{\mathbf{u}}_i \cdot \hat{\mathbf{u}}_j)$
$g_2(r_{ij}\perp\hat{\mathbf{u}}_i)^{(P2)}$	$g_2^{(P2)} u$	$\sqrt{r_{ij}^2 - (\mathbf{r}_{ij} \cdot \hat{\mathbf{u}}_i)^2}$	$(3/2) \cos^2(\gamma) - (1/2)$

CHAPTER 4

Preliminary simulations

In the first section of this chapter, we present results from simulations of 1000 $\kappa 5k_{\theta} 5.0$ particles, the first simulation proper to be performed using the MD code. The main purpose of this exercise was to check that the code was performing satisfactorily and to allow a comparison to be made with a corresponding MC simulation series performed previously by Barmes et al. [14]. Despite the contrasts between the MC and MD simulation techniques as well as the differences between the representations of the particles i.e. a pure hard particle model versus a soft repulsive potential, we would expect the two studies to produce similar results. The $\kappa 5k_{\theta} 5.0$ was chosen because, in the MC simulations, it underwent an I-N-Sm-solid phase transition sequence. Such phase behaviour, if reproduced in the MD simulations, would, therefore, provide an opportunity to develop effective methodologies for processing the raw simulation data. The I-N-Sm-solid phase transition sequence also provides an excellent testbed for the distribution functions introduced in section 3.4. This is the main focus of the second section of this chapter, where we examine in detail the structures of the various phases formed in the course of the $\kappa 5k_{\theta} 5.0$ simulations. ‘Snapshots’ of the system are also presented to provide visual evidence in support of conclusions drawn from

the distribution functions. The third section discusses a number of supplementary simulations in which so-called anisotropic rescaling is implemented. Anisotropic rescaling is an algorithm which essentially allows the simulation box dimensions to change in order to better incorporate phases with periodic order, in particular the smectic phase. Hence compression sequences which include the application of this rescaling method are referred to as anisotropic compressions as opposed to isotropic compressions in which the ratios of the boxlengths remain fixed. The fourth and final section presents the results of four anisotropic compression series which are identical except for the numbers of particles simulated. The system sizes used here are $N=1250, 2500, 5000$ and 10000 . These simulations were performed to check whether the periodic boundary conditions have a significant influence on the stability and structure of the phases formed.

4.1 Isotropic compression series

The first of our MD simulations for soft repulsive pears to be performed was an isotropic compression of $\kappa 5k_{\theta} 5.0$ particles, as summarised in table 4.1. The initial run, at a number density of $\rho = 0.20$, used, as its starting configuration, the standard arrangement of 1000 particles arranged parallel to each other on an FCC lattice. Having assigned a Maxwellian translational velocity distribution to the

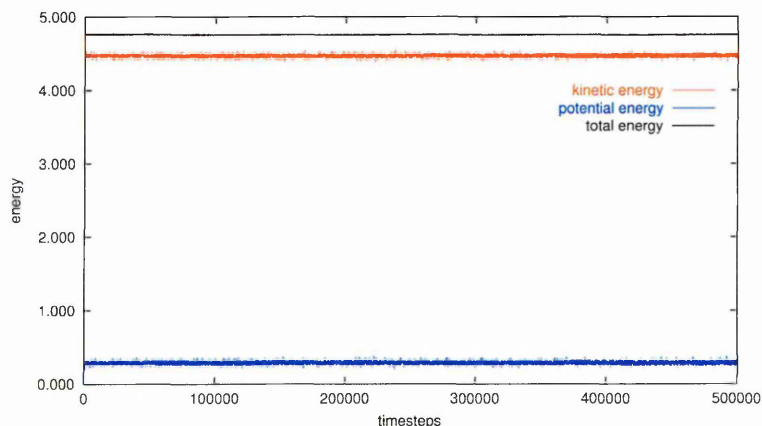
Tab. 4.1: Summary of main run parameters for isotropic compression of 1000 $\kappa 5k_{\theta} 5.0$ soft repulsive pears.

run	ρ	$\Delta\rho$	ensemble	N_{step} (averaging interval)
1	0.20	0.00	<i>NVE</i>	500k (250-500k)
2-43	0.21-0.62	0.01	<i>NVT</i>	500k (250-500k)
44	0.62	0.00	<i>NVE</i>	500k (250-500k)

system, it was then run for 500 ksteps in *NVE* for the purposes of thermalisation. This run also provided an opportunity to monitor the energy conservation of the system. The number density was then increased over a series forty-two *NVT* runs

from $\rho = 0.20$ to 0.62 by applying single density increases of $\Delta\rho = 0.01$ at the start of each run. All runs in the series were 500 ksteps long with a timestep of $\Delta t = 0.0015$; time averages were accumulated and configurations periodically recorded over the interval 250-500ksteps. The series was concluded by a final *NVE* run at $\rho = 0.62$. Running a simulation in the *NVE* ensemble acts an effective, though not infallible, test to check that the MD code is free of mathematical or transcription errors. It also provides reassurance that the simulation has been correctly initialised and appropriate parameters have been assigned. It is self-evident that, over the duration of an *NVE* run, the total energy should remain essentially constant. If any errors have been made in writing the code or setting

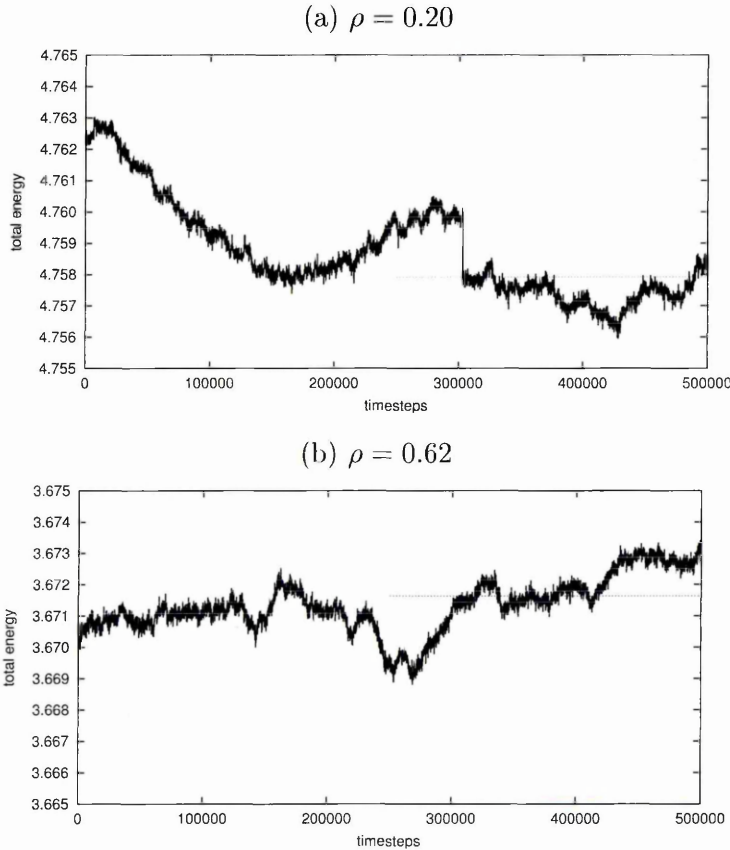
Fig. 4.1: Kinetic, potential and total energy vs. time for a system of 1000 $\kappa 5$ $k_{\theta} 5.0$ running in *NVE* at a density of $\rho = 0.20$.



up the simulation, the total energy of the system will, more often than not, directly increase at a catastrophic rate. Figure 4.1 shows the kinetic, potential and total energy per particle over the course of the initial *NVE* run of the compression series. Note that the potential makes a relatively small contribution to the total energy. This is due to the fact that the soft-repulsive potential is either very steep and repulsive or else zero. Thus, the interparticle potential is finite only when the particles come into close contact and, when they do, the interaction is fleeting since the repulsive force acts to drive the pair away from each other. On the scale used in figure 4.1, there is no perceptible fluctuation or drift in the total

energy. However in figures 4.2 (a) and (b), which show details of the total energy over the course of both the initial and final *NVE* runs of the compression series, a certain amount of fluctuation/drift is observed. We also notice an abrupt drop in the total energy in the $\rho = 0.20$ plot at around 300ksteps. To investigate this

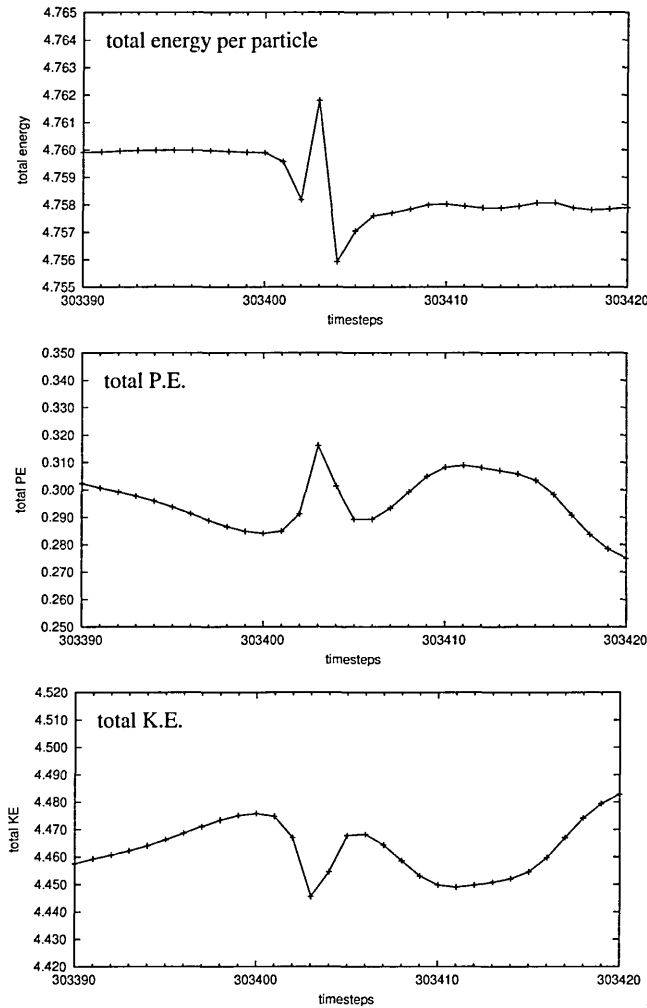
Fig. 4.2: Detail of total energy vs. time for the system of 1000 $\kappa 5k_{\theta} 5.0$ running in *NVE* at a density of $\rho = 0.20$. The horizontal dashed lines indicate the average values determined over the interval 250-500 ksteps.



further, the run was repeated on the same processors as the original simulation in order to reproduce exactly the particle trajectories. The instantaneous values of observables were logged at every timestep over the interval 303000-304000 in order to scrutinise the anomaly at a higher time resolution. The plots in figure 4.3 show the step by step changes in the total, potential and kinetic energies and reveal that the drop in total energy is actually preceded by an equally steep rise in total energy. Moreover, this feature coincides with a peak and a valley in the

potential and kinetic energies respectively. The peak in the potential would seem to suggest that the energy anomaly is due to an excessive overlap of two particles, due perhaps to a high speed collision. This seems reasonable given that the run

Fig. 4.3: Detail of energy anomaly visible in 4.2. Note that the energy scales on the plots of PE and KE are ten times

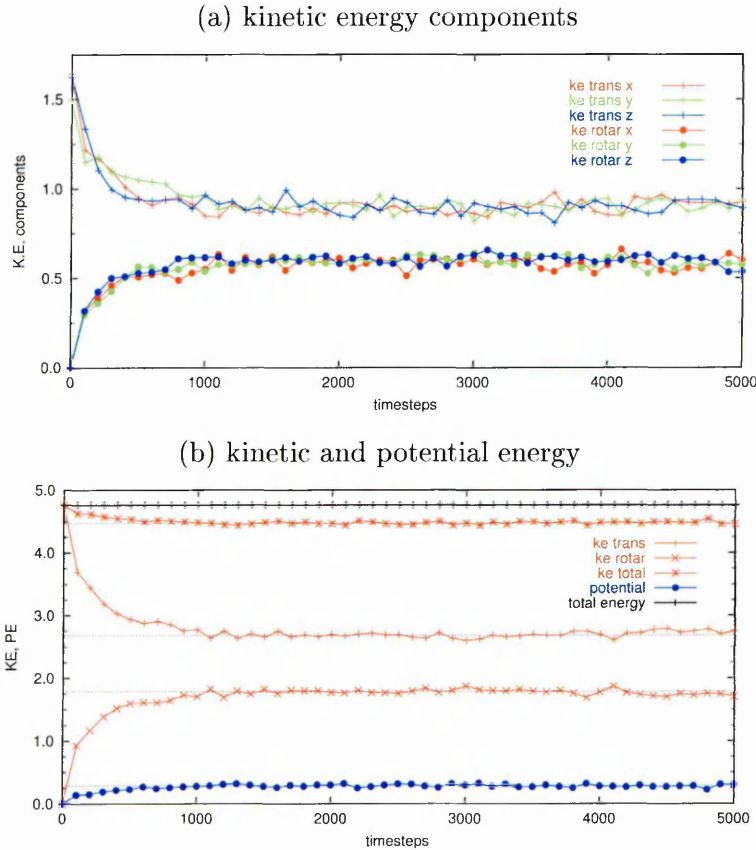


was carried out at low density and under these conditions the particles spend a fair amount of time in ballistic flight¹. Nevertheless, at both densities, the total variation in energy over the course of the run amounts to less than 0.15%. Also there do not appear to be any monotonic long term trends in the energy drift (at least over the time scales studied) which might otherwise indicate a systematic problem

¹This is evidenced by inspection of the configuration files stored during low density runs, they show that at any instant a fair proportion of the particles experience zero total force.

with the simulations. A supplementary validation of the code is to check for the equipartition of kinetic energy between the system's degrees of freedom. Since the particles each have two rotational and three translational degrees of freedom, one would expect the values of the average rotational and translational kinetic energies to be in the ratio 2/3. In the initial NVE run, the average rotational and translational kinetic energies per particle were found to be $\langle KE_{rotor}^{(i)} \rangle = 1.790$ and $\langle KE_{trans}^{(i)} \rangle = 2.681$ (to 3 decimal places), giving a ratio of 0.668, a value which is very close to the theoretical prediction. The evolution of these kinetic energy

Fig. 4.4: Energy equipartition for the system of 1000 $\kappa 5k_{\theta} 5.0$ running in NVE at a density of $\rho = 0.20$. In plot (b), dashed lines indicate the average values of the various energy components.

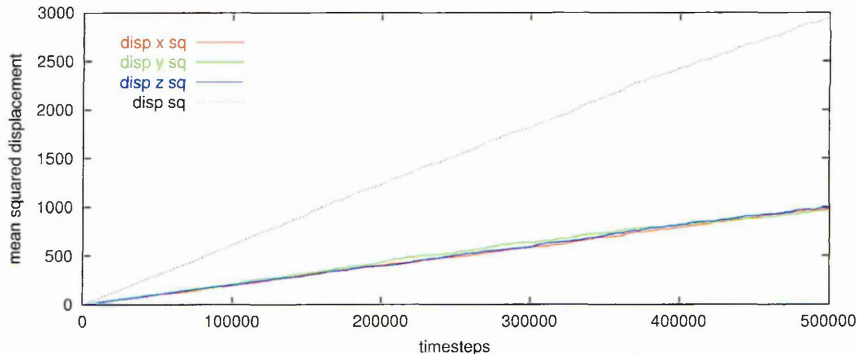


components over the first 5000 steps of the run is shown in figure 4.4. At the very start of the run, the particles possess only the translational kinetic energy initially assigned to them via the Maxwellian velocity distribution. The potential energy at the start of the run is also zero since the particles are initially well

separated from each other on the FCC lattice. However the particles soon begin to collide and the process of transferral of kinetic energy from the translational to the rotational degrees of freedom begins. Also some potential energy is gained at the expense of kinetic energy. The equipartition of energy takes place surprisingly quickly: as figure 4.4 shows, after as little as one thousand time steps the energy components are seen to fluctuate about their equilibrium values. Note that figure 4.4 (a) shows the average kinetic energy components with respect to the lab frame. In the lab frame both the translational *and* rotational kinetic energies have kinetic energy components for each of the three Cartesian directions. These are not to be confused with energy components in the particle based frame, wherein the rotational kinetic energy component along the major axis is zero.

The mobility of particles in the system is quantified by the mean squared displacement per particle as a function of time, this is shown in figure 4.5 for the first run in the low density isotropic phase. By the end of the run, the mean

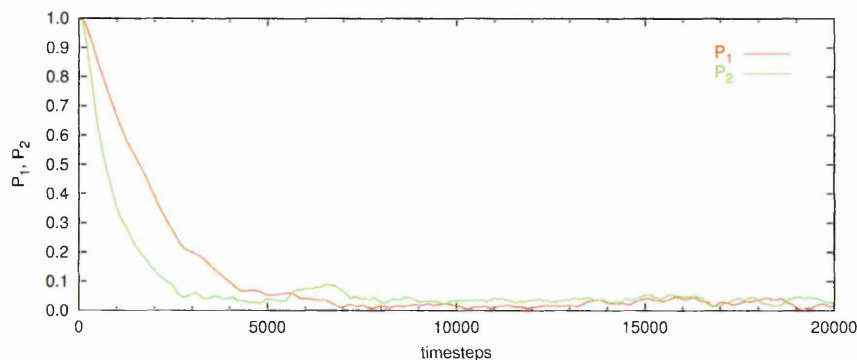
Fig. 4.5: Mean squared displacements as a function of time in the N1000 $\kappa 5k_{\theta} 5.0$ system running in *NVE* at a density of $\rho = 0.20$.



squared displacement is approximately 3000 length units. The rms displacement is therefore approximately 55 units, which corresponds to roughly three times the length of the simulation box (at $\rho = 0.20$, $L_x = L_y = L_z = 17.100$). We note that the three components of the mean squared displacements are equal and increase linearly with time, in other words the particles undergo random walk or Einstein diffusion. Given the low density of the initial configuration and, hence, the considerable latitude for particle translation and reorientation, it unsurprising that

the orientational order in the system also decays very rapidly, as figure 4.6 shows. The features discussed above give us some confidence that the simulation code is performing satisfactorily: energy conservation/equipartition are obeyed and the particles in the system undergo random walk diffusion both of which constitute physically realistic behaviour. A further validation is to compare the results of the

Fig. 4.6: The decay of polar and nematic order in the N1000 $\kappa 5k\theta 5.0$ system at $\rho = 0.20$.



MD compression series with data from the corresponding MC simulations. This constitutes a rather stringent test since although both simulations are based upon the same contact function, the simulation techniques are completely dissimilar and were implemented independently on different platforms.

The most natural observables to compare between the two simulations are the time averages of the order parameters and the pressure at corresponding state points. Figure 4.7 compares the polar and nematic order parameters. The agreement in the P_2 profiles is excellent. We note also in passing, that in the isotropic phase at the lowest density, the finite size error in P_2 is roughly 3%, a value similar to that predicted by Eppenga and Frenkel in their study of infinitely thin disks [13] (see figure A 1 in this reference). There are distinct differences between the MD and MC P_1 data. Specifically, the values for P_1 calculated from the MD simulations are all positive and have magnitude of the order of ~ 0.02 whereas for the MC simulations the magnitudes are smaller, typically 0.001 or less and in addition their sign fluctuates. This discrepancy, however, is thought to be due principally to the different method used to calculate P_1 in the MC studies.

Figure 4.8 meanwhile compares the pressure profiles in which there is excellent agreement up to a density of $\rho = 0.49$ which, as we will discuss shortly, marks the beginning of the smectic phase. At a density of $\rho \approx 0.35$, which coincides with a

Fig. 4.7: The P_1 and P_2 vs. density profiles as obtained from the isotropic compression in NVT of a system of 1000 $\kappa 5k_{\theta} 5.0$ soft repulsive particles compared with the results of an anisotropic NPT compression of an analogous system of hard particles by Monte Carlo simulation.

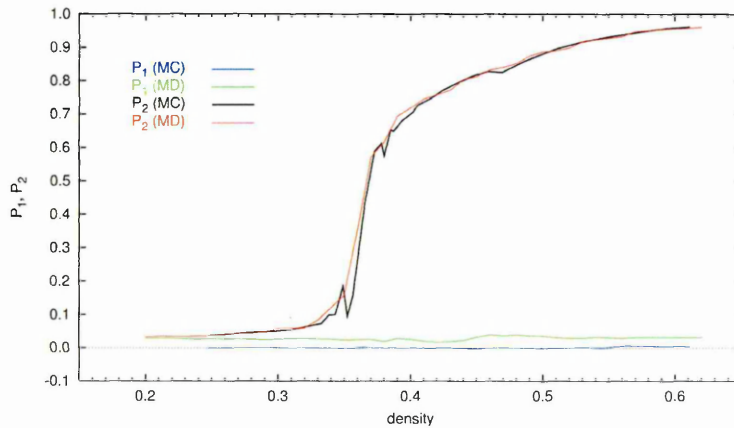
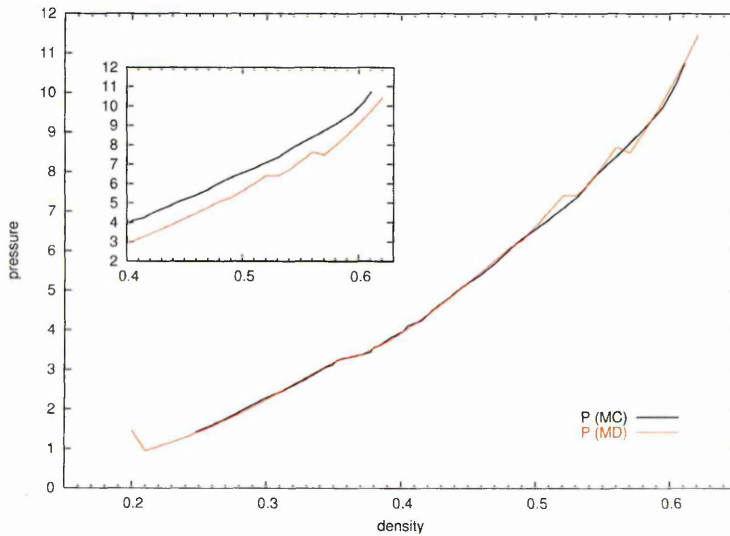


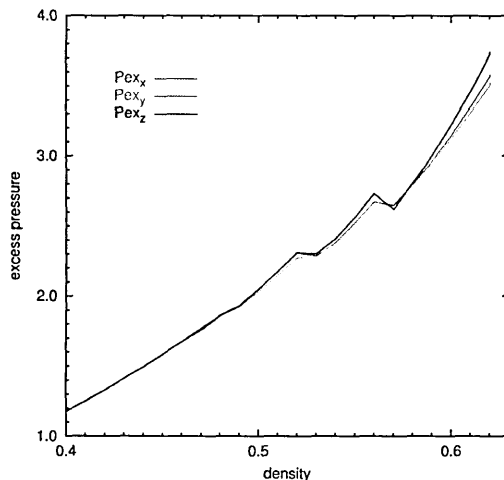
Fig. 4.8: $N1000 \kappa 5k_{\theta} 5.0$ system: Pressure vs. density comparing results of MD simulations to an analogous MC simulation. The insert shows the high density portions of the pressure profiles in more detail with the MD profile vertically offset by -1.0 to allow the data to be inspected more clearly.



marked rise in P_2 , the pressure levels off until the density reaches $\rho \approx 0.38$. This type of discontinuity is the classic signature of a first order phase transition, of which the I-N transition is an example. A second order phase transition, on the

other hand, would be marked only by an inflection in the pressure profile. The MD pressure profile also exhibits two distinct discontinuities around $\rho = 0.52 - 0.53$ and $\rho = 0.56 - 0.57$, which are not observed in the the MC profile. An additional feature observed in the MD pressure data is the increasing disparity between the z-component of the excess pressure and the x- and y-components at high density. This is readily seen in figure 4.9. Such pressure anisotropy almost certainly derives from the fact that the simulation box used in this compression remains cubic at all times. It is often the case that high density ordered phases such as the smectic have difficulty ‘fitting’ into a volume of fixed aspect ratio if the dimensions of

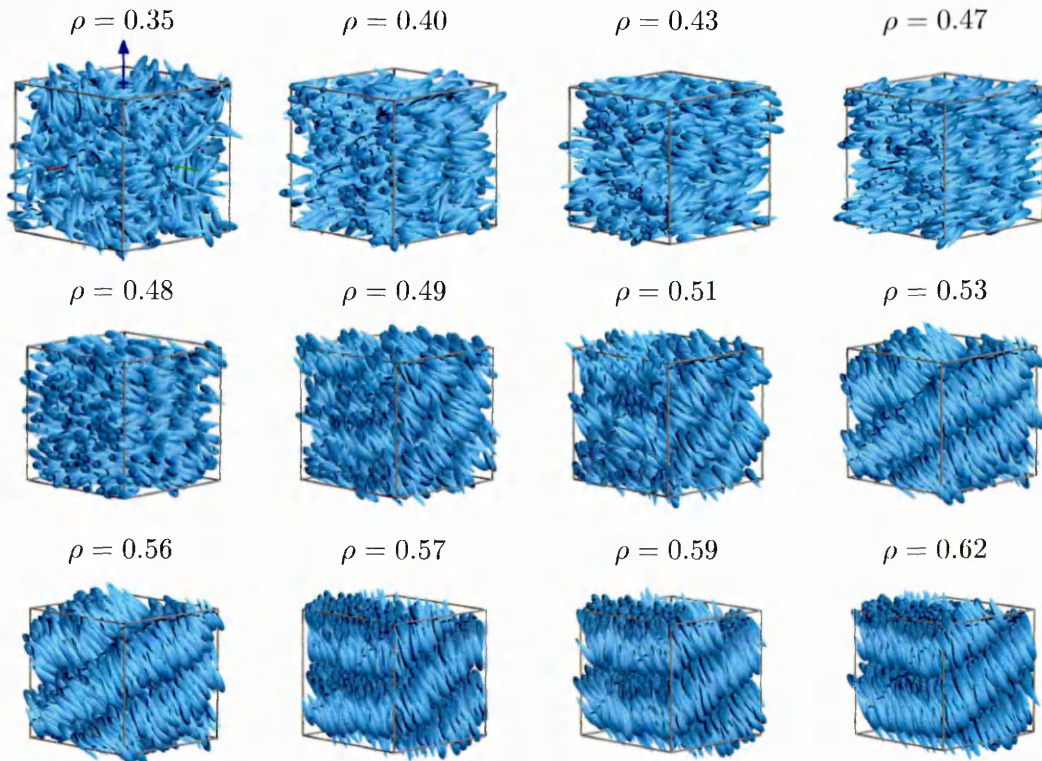
Fig. 4.9: Excess pressure components vs. density for the MD *NVT* compression.



that volume do not happen to be commensurate with the periodicity of the phase (in this case the repeat distance between smectic layers). Evidence that this is indeed what has occurred in our simulation is provided by inspection of selected snapshots of the simulation box as shown in figure 4.10, which we will now discuss. In the density range $\rho \approx 0.37 - 0.48$, the system is in the nematic phase as evidenced by high P_2 value and flat longitudinal distribution function profiles (see section 4.2). Throughout the nematic phase, the director is aligned with the x-axis or [100] direction, as indicated by the director components (not shown) and, at the higher density end of the nematic phase, by inspection of the snapshots (figure 4.10). At $\rho = 0.49$, the system begins to take on a distinctly layered character,

marking its transformation into a smectic bilayer phase. At the same time the director begins to reorient itself until, by the time the density has reached $\rho = 0.53$, it is aligned approximately in the $[1\bar{1}\bar{2}]$ direction. This collective rearrangement of the system would appear to allow for an alternative commensurability of bilayers within the simulation box and coincides with the discontinuity in the pressure profile at $\rho = 0.52 - 0.53$. By the end of the $\rho = 0.57$ run, we find that a second rearrangement of the bilayers has taken place and the director now points in the $[10\bar{2}]$ direction. Again this process is accompanied by a discontinuity in the pressure and, indeed, a noticeable decrease in its value (see figures 4.8 and 4.9). Looking carefully at figure 4.9, both reorientations appear to be preceded by a small but steady drift of the z-component of the excess pressure away from the other two components. This strongly suggests that the rearrangements are driven by the need to better accommodate the layered phase within the cubic box and, thus, alleviate pressure anisotropy. In the final stages of the compression, the

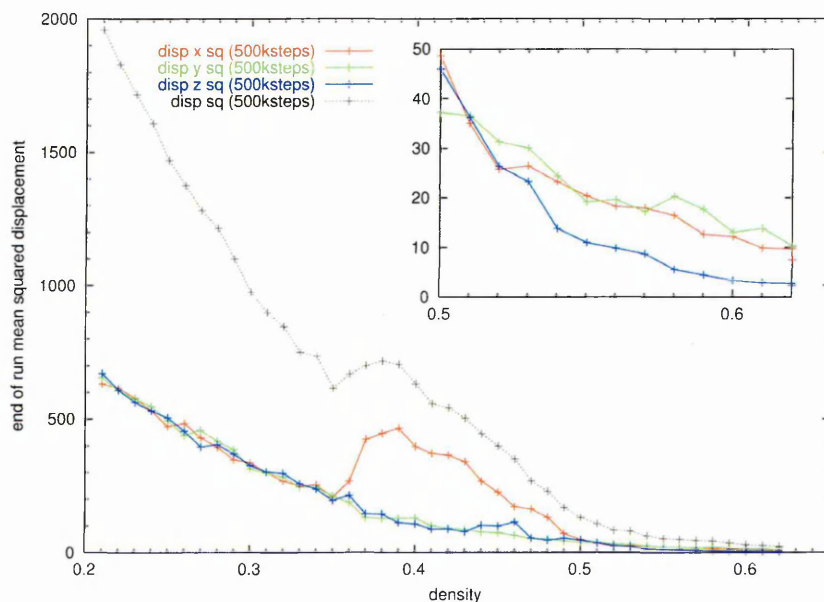
Fig. 4.10: N1000 $\kappa 5k\theta 5.0$ system: Snapshots of the simulation box at the end of selected runs. The x,y,z axes are coloured red, green and blue respectively.



increase in pressure anisotropy goes unchecked. This could be due the fact that there is no rearrangement of the layers within the given volume that could lead to the alleviation of the pressure anisotropy or that even if such an arrangement did exist, the particle mobility is too low at these high densities for the system to rearrange itself. We will return to the issue of how the simulation box dimensions influence the formation of ordered phases and vice versa in section 4.3.

To conclude this section, we examine how particle mobility is affected by increasing density. This is best illustrated by plotting the rms displacements at the end of each run as shown in figure 4.11. We might naively expect the mobility of the particles within the system to decrease monotonically with density as the free volume accessible to each diminishes. However an interesting phenomenon

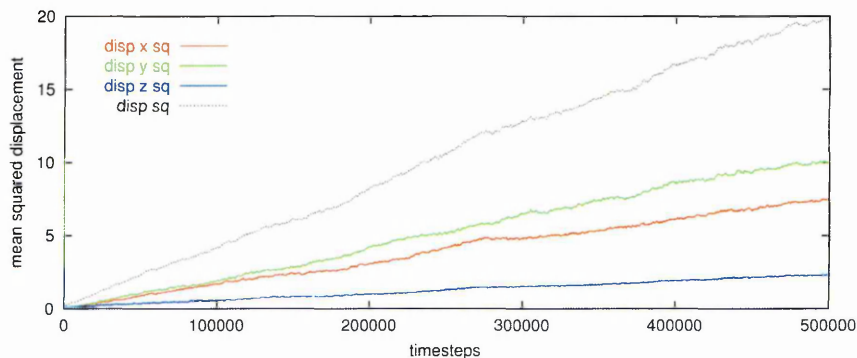
Fig. 4.11: N1000 $\kappa 5k\theta 5.0$ system: Mean squared displacements at the end of each run vs. the density at which the run was performed (all runs in this compression series were of 500ksteps duration).



is observed at the isotropic-nematic transition density. As the phase transition begins, the mean squared displacements of the particles in the y - and z - directions continues to decrease with increasing density. However along the x -direction, which approximately coincides with the director axis, diffusion is enhanced. This has been observed before in simulations, notably by Allen in a system of hard

ellipsoids of both the prolate and oblate varieties [26]. As a consequence, from $\rho = 0.35$ to 0.38 the overall mean squared displacement actually increases, an effect that is concomitant with the increase in the nematic order parameter in that interval. This simultaneous increase in orientational order and gain in mobility nicely illustrates the entropy handover between rotational and translational degrees of freedom. The increase in orientational order, representing a loss of orientational entropy, is compensated for by an increase in translational entropy via the enhanced mobility facilitated by the former. If the system were to remain in the disordered isotropic phase, the overall entropy would be lower since the system's ability to explore its translational degrees of freedom would be increasingly curtailed by the decrease in mobility brought about by the increasing density. By the end of the compression series, at $\rho = 0.62$ as shown in figure 4.12, the mean squared displacement has decreased by some two orders of magnitude compared with that at the start of the series at $\rho = 0.20$. However the system remains fluid and the mean squared displacement still varies linearly with time. We note also that the mean squared displacement in the y -direction is roughly

Fig. 4.12: N1000 $\kappa 5k_{\theta} 5.0$ system, $\rho = 0.62$ *NVE*: Mean squared displacement vs. time.



four times greater than that in the z -direction. The fact that the director (which is perpendicular to the smectic layers) has a large z -component but roughly zero y -component, suggests that intralayer diffusion of particles within a given leaflet of a bilayer is considerably easier than interlayer diffusion of particles between adjacent layers. This type of behaviour has been observed in several previous

simulations. For example Aoki and Yonezawa [27] observed, in a smectic phase formed by soft-repulsive spherocylinders, that the rate of diffusion of the particles in the two directions parallel to the layers was approximately four times that in the perpendicular direction.

4.2 Structural detail

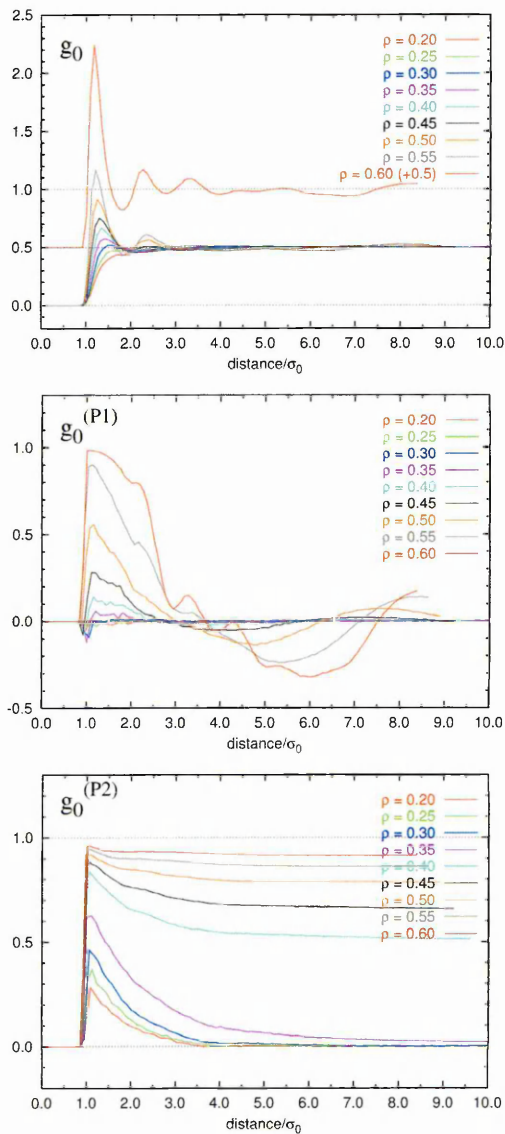
The previous section provided an assessment of the nature and location of the key changes undergone by the $\kappa 5k\rho 5.0$ system during its compression. This section presents a more thorough characterisation of the structures of the phases formed via a detailed examination of their distribution functions, as defined in section 3.4, in conjunction with further visualisations of the simulation configurations.

We begin by considering the radial distribution functions shown in figure 4.13. These were compiled by dividing the spherical volume around each particle i into 100 spherical shells. The number of configurations sampled at each density was 51, these having been recorded in the production phase of each run i.e. in the interval 250-500 ksteps. In the plots shown in figure 4.13, and indeed in all subsequent plots of $g(r)$ s, the interparticle distances are normalised by dividing by the particle diameter σ_w (the basic length unit in our simulations, as defined in equation 2.28), thus making it easier to interpret the distributions in terms of particle dimensions.

At all densities during the compression, the $g_0(r)$ are zero for $r \approx < \sigma_w$, as they must be, for this is the minimum distance that particles can approach without significant overlap. Obviously, for elongated particles such as our $\kappa 5$ pearls to reach this minimum separation, they must be more or less parallel or antiparallel and side-by-side. As the density increases beyond $\rho = 0.35$, a peak starts to develop at $r \approx 1.25\sigma_w$ just beyond the minimum separation value. This coincides with the emergence of the nematic phase. The fact that the $g_0^{(P1)}(r)$ profile is, for the most part, positive up to $r \approx 3.0\sigma_w$ indicates that, particles closest to each other have

a preference to lie parallel, particularly in the ordered phases at higher densities. The negative hollow in the distribution at larger distances, on the other hand, reflects the tendency of groupings of mutually parallel particles to interdigitate with similar groupings aligned in the opposite direction. This is particularly true

Fig. 4.13: N1000 $\kappa 5k\theta 5.0$ system: The effect of increasing density on the radial distribution functions (g_0).

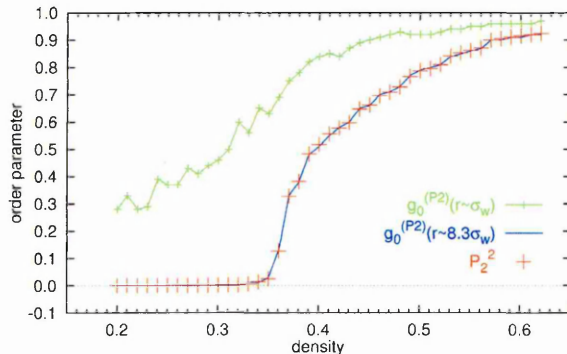


in the smectic phase which, as figure 4.16 (f) clearly indicates, consists of bilayers each of which is comprised of a pair of antiparallel ‘leaflets’.

The family of plots of the radial nematic order distribution $g_0^{(P2)}(r)$ illustrates the

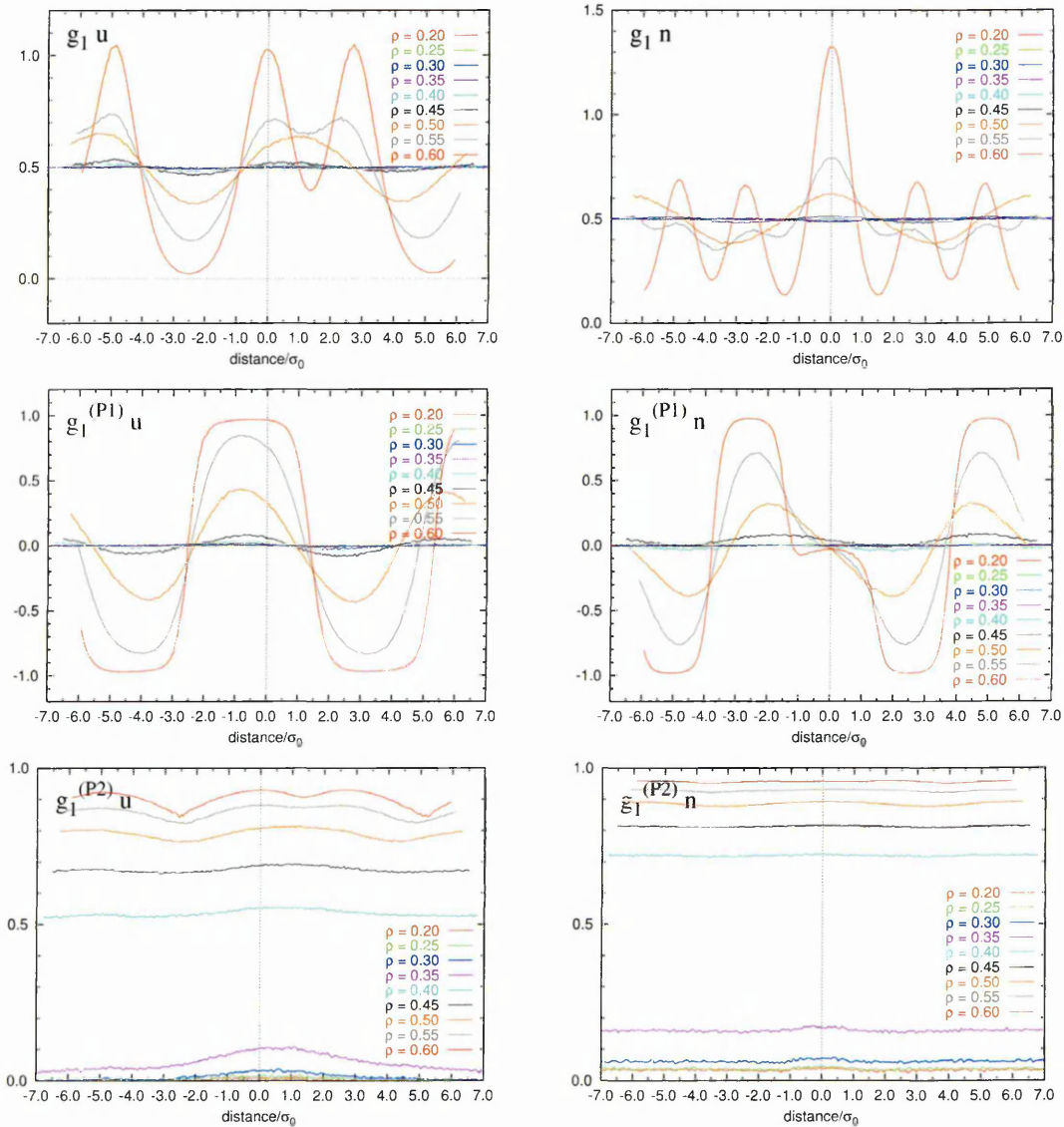
difference between short-range orientational correlations and long-range orientational order. At all densities, short-range orientational correlations are present. In the isotropic region ($\rho = 0.20 - 0.35$) the order naturally falls to approximately zero at long distances. In the nematic and smectic phases on the other hand, orientational order persists at long distances and, as the density increases, the difference between the peak value of P_2 associated with strong nearest-neighbour correlations and the long range order is reduced. This is illustrated in figure 4.14 wherein the peak values of the nematic radial distribution function, as measured at $r \approx \sigma_w$, are compared with the values at $r \approx 8.3\sigma_w$. Also plotted are the

Fig. 4.14: N1000 $\kappa 5k\rho 5.0$ system: Comparing the order parameter value calculated in standard way at runtime with the ‘local’ and ‘distant’ values given by $g_0^{(P2)}(r \approx \sigma_w)$ and $g_0^{(P2)}(r \approx 8.3\sigma_w)$.



squared values of time-averaged P_2 as calculated in the standard way at runtime. The latter are in excellent agreement with $g_0^{(P2)}(r \approx 8.3\sigma_w)$, this is in agreement with the prediction made by statistical theory that $P_2 = \sqrt{g_0^{(P2)}(r \rightarrow \infty)}$. Next we turn to the longitudinal distribution functions, g_1 , presented in figure 4.15. These provide quantitative information regarding the spacing of the smectic layers and, by observing how they change as the system is compressed, indicate the density at which the phase emerges from the nematic. According to these data, the onset of the smectic occurs at approximately $\rho = 0.50$, since at this point both the g_1u and g_1n profiles become distinctly sinusoidal having been essentially flat at lower densities. This is slightly lower than $\rho = 0.52 - 0.53$, the density at which the second discontinuity in the pressure is observed (see figure 4.8).

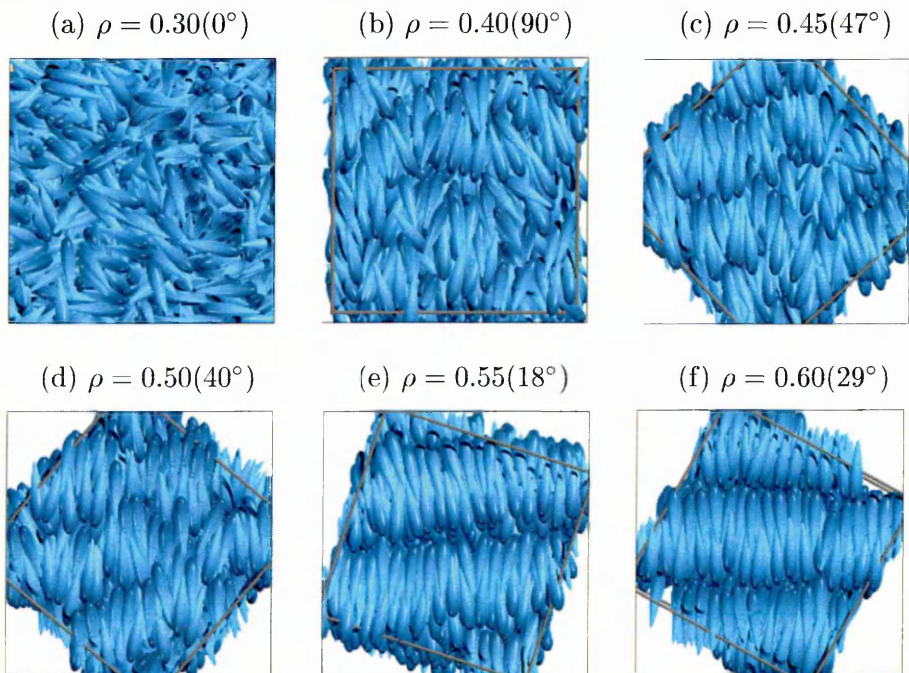
Fig. 4.15: N1000 $\kappa 5$ $k\theta 5$ system: The effect of increasing density on the longitudinal distribution functions. Two variants of the functions are shown. On the left are versions based on the particle orientation vector whereby the longitudinal distances are defined as $r_{\parallel} = (-\mathbf{r}_{ij} \cdot \hat{\mathbf{u}}_j)$. Positive r_{\parallel} corresponds to objects in front of particle i whilst negative r_{\parallel} corresponds to objects behind particle i . On the right are the director-based versions, here the longitudinal distances is defined as $r_{\parallel} = (-\mathbf{r}_{ij} \cdot \hat{\mathbf{n}})$. They were compiled by dividing the cylindrical volume around each particle i into 200 thin disks, 100 for positive r_{\parallel} and 100 for negative r_{\parallel} and sampled from 51 production run configurations.



The structure of the smectic at $\rho = 0.50$ is somewhat ambiguous, in particular the maximum of the first peak in $g_1 u$ is offset from zero by $r \approx \sigma_w$ and coincides with a switch in $g_1^{(P1)} u$ from positive to negative. In a well ordered smectic, as shown schematically in figure 4.17 (c), one expects $g_1 u$ to peak at zero and to

correspond to positive $g_1^{(P1)}u$, in keeping with well ordered layers of particles lying more or less parallel to each other. However as figure 4.16 (d) shows, the smectic at $\rho = 0.50$, though it has a decidedly layered structure, is not very orderly. The layers appear disjointed and perhaps somewhat slanted as sketched in figure 4.17 (b). This characteristic perhaps goes some way towards explaining why the peak in g_1n is offset from zero although the full picture may be more complicated. It is

Fig. 4.16: N1000 $\kappa 5k_{\theta}5.0$ system: Close up snapshots taken at various densities. In all cases the view is down the positive y-direction; the angles in brackets are camera rotation angles about the y-axis.

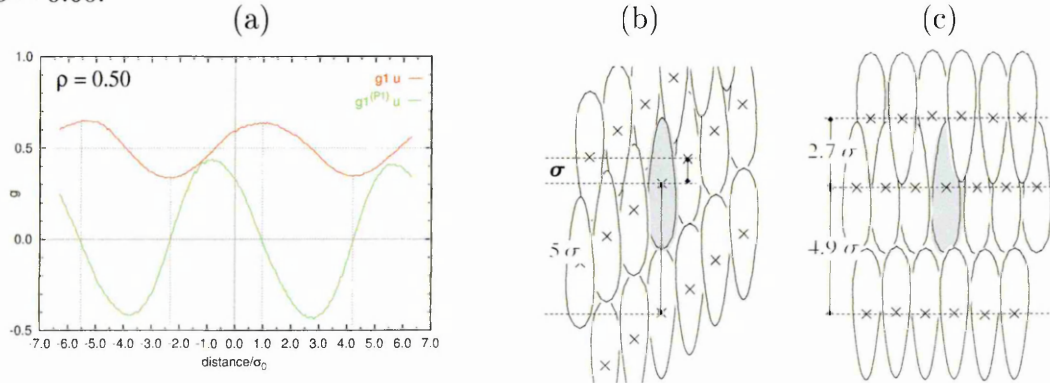


possible that at $\rho = 0.50$, the density around which the system is in the process of transforming from the nematic to the smectic phase, the system adopts some sort of intermediate domain structure, although extensive supplementary analysis would be necessary in order to ascertain if this was indeed the case. It may also be the case that this weakly ordered smectic is a metastable phase which arises as a result of the incompatibility of the emergent true smectic with the periodic boundary conditions. Yet another possibility is that the simulation runs are simply not long enough to allow the smectic to form properly. Nevertheless, at high density the smectic ordering becomes more regimented and, as a result,

the longitudinal distribution functions become easier to interpret.

This is particularly true for $g_1 u$ and $g_1^{(P1)} u$ (the upper and middle left plots in figure 4.15). The $\rho = 0.50$ profiles indicate that looking down the orientation vector of any given particle, i , one sees a layer of antiparallel particles (the opposing leaflet of the bilayer in which i resides) at a distance of $\approx 2.7\sigma_0$. Looking behind particle i , one sees another layer of antiparallel particles (the closer leaflet of the adjacent bilayer in contact with i) at a distance of $\approx 4.9\sigma_0$. Both versions of g_1

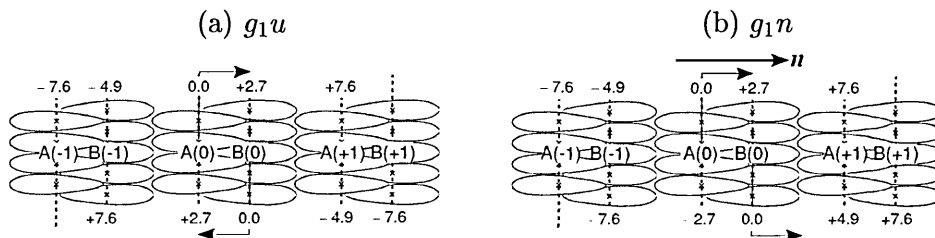
Fig. 4.17: N1000 $\kappa 5k\theta 5.0$ system: (a) Local distribution functions for smectic phase at $\rho = 0.50$. (b) Sketch of smectic phase at $\rho = 0.50$. (c) Sketch of smectic phase at $\rho = 0.60$.



are shown in figure 4.15 to illustrate the different interpretations of the smectic structure that they provide. Recall, from section 3.4, that for $g_1 u$, r_{\parallel} is defined as $(-\mathbf{r}_{ij} \cdot \hat{\mathbf{u}}_j)$ so that the function picks up correlations as seen from the perspective of the orientations of individual particles i . Accordingly, the contributions to the corresponding polar distribution function $g_1^{(P1)} u$ are given by $\cos(\theta) = (-\hat{\mathbf{u}}_j \cdot \hat{\mathbf{u}}_i)$. On the other hand for $g_1 n$, r_{\parallel} is defined as $(-\mathbf{r}_{ij} \cdot \hat{\mathbf{n}})$, This distribution function therefore picks up correlations with respect to the orientation of the director and the contributions to the corresponding polar distribution function $g_1^{(P1)} n$ are given by $\cos(\theta) = (-\hat{\mathbf{u}}_j \cdot \hat{\mathbf{n}})$. Figure 4.18 and tables 4.2 and 4.3 are designed to show how the structure of the smectic phase relates to the g_1 and $g_1^{(P1)}$ data. In the figure, we arbitrarily label leaflets with particles facing left to right as ‘A’ and those facing in the opposite direction as ‘B’. A(0) and B(0) denote reference layers from which r_{\parallel} is measured whilst A(-1),B(-1) and A(+1),B(+1) denote the leaflets be-

longing to the bilayers left and right respectively of the reference bilayer. The tables then summarise the correlations seen with respect to A(0) and B(0), the symbols \oplus and \ominus denoting whether the correlation makes a positive or negative contribution to $g_1^{(P1)}u$. ‘Strength’ is simply the number of distinct correlations

Fig. 4.18: Schematics of smectic phase showing how the various correlations between the leaflets of aligned particles contribute to the two versions of longitudinal distribution functions, namely the particle orientation vector based g_1u and the director based g_1n (see text for further explanation).



Tab. 4.2: Summary of the pair correlations with respect to the two opposing leaflets in a smectic bilayer for the particle orientation vector based distribution function g_1u (see text for further explanation).

r_{\parallel}	-7.6	-4.9	-2.7	0.0	2.7	4.9	7.6
wrt A(0)	A(-1) \oplus	B(-1) \ominus	-	A(0) \oplus	B(0) \ominus	-	A(+1) \oplus
wrt B(0)	B(+1) \oplus	A(+1) \ominus	-	B(0) \oplus	A(0) \ominus	-	B(-1) \oplus
strength	2	2	-	2	2	-	2
polarity	\oplus	\ominus	-	\oplus	\ominus	-	\oplus

Tab. 4.3: Summary of the pair correlations with respect to the two opposing leaflets in a smectic bilayer for the director based distribution function g_1n (see text for further explanation).

r_{\parallel}	-7.6	-4.9	-2.7	0.0	2.7	4.9	7.6
wrt A(0)	A(-1) \oplus	B(-1) \ominus	-	A(0) \oplus	B(0) \ominus	-	A(+1) \oplus
wrt B(0)	B(-1) \ominus	-	A(0) \oplus	B(0) \ominus	-	A(+1) \oplus	B(+1) \ominus
strength	2	1	1	2	1	1	2
polarity	0	\ominus	\oplus	0	\ominus	\oplus	0

that contribute at a given distance, whilst ‘polarity’ indicates the net polar order associated with the resultant correlation. Note that the contributions to $g_1^{(P1)}n$ cancel each other out when r_{\parallel} is a multiple of the basic repeat distance. In general the director based distribution functions are, therefore, more difficult to interpret;

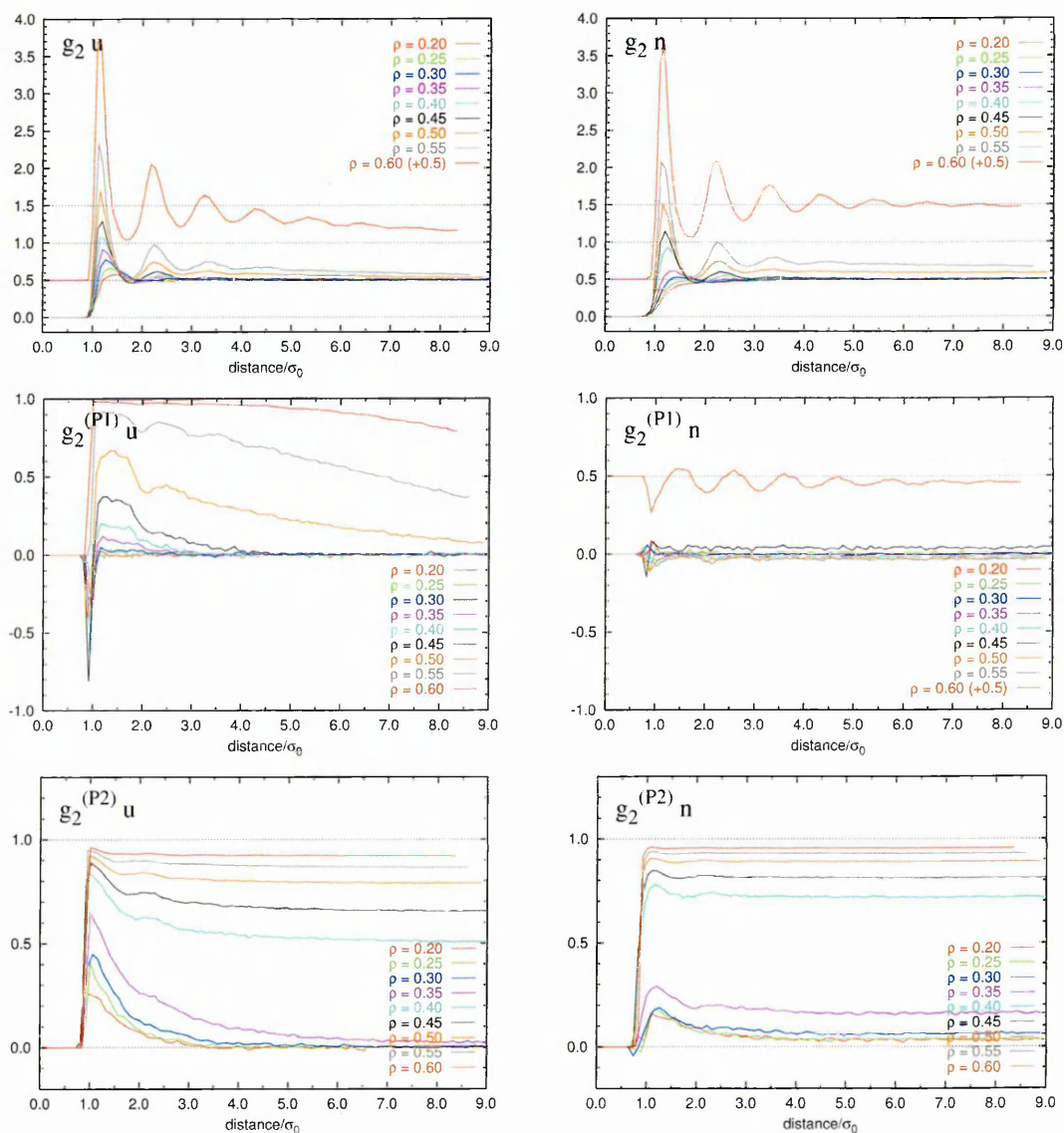
$g_1 n$ does, however, give a more accurate quantitative measure of the intra- and inter-bilayer distances since r_{\parallel} is the distance measured parallel to the director and, thus, perpendicular to the layers. The nematic distribution functions $g_1^{(P2)} u$ and $g_1^{(P2)} n$ are relatively featureless.

The third class of distribution function g_2 , shown in figure 4.19, provides information about intralayer ordering. These data were compiled by dividing the cylindrical volume around each particle i into 100 cylindrical shells. The height of each shell was set at σ_w , the intention being to restrict the correlations picked out to those between pairs of particles in the *same* leaflet of a given bilayer. Once again, 51 production run configurations were sampled. At $\rho = 0.60$, both $g_2 u$ and $g_2 n$ exhibit a sequence of five peaks of diminishing height at perpendicular distances of approximately 1.15, 2.20, 3.28, 4.30 and 5.40 σ_0 . This is somewhat reminiscent of the distribution function for close packed spheres. A snapshot of of the simulation box looking down at the smectic layers is shown in figure 4.20. Due to the orientation of the layers in the box, we see several alternating dark and light bands of particles comprising the opposing leaflets of the bilayers (recall that the rounded end of our tapered particles are coloured dark blue and the pointed ends light blue). The intralayer packing of the particles is roughly hexagonal, however at this density particles are still fairly mobile, particularly in directions parallel to the layers, consequently the arrangement is fairly disordered.

It would be interesting to run this system on to higher densities to obtain a highly regimented smectic phase in order to elucidate the fine detail of the intralayer ordering. One would suspect that the leaflets of the bilayers pack hexagonally in an ABAB sequence so that the pointed ends of particles in opposing leaflets of a bilayer can interdigitate. Similarly the rounded ends of particles on the surface of a bilayer can sit in the interstices formed by the rounded ends of particles on the surface of an adjacent bilayer. Intuitively this would seem to be the most efficient space filling arrangement.

A slight difference between $g_2 u$ and $g_2 n$ worth commenting on is that at the highest density shown, the particle based distribution function decays towards a value

Fig. 4.19: N1000 $\kappa 5k_{\theta}5.0$ system: The effect of increasing density on the lateral distribution functions.



of 0.5 at large distances whilst the director based version approaches a value of 1.0. The reason for this is that the particles in the bilayers are not perfectly aligned with the director, therefore the cylindrical sampling volumes centred on each particle will in general be slightly tilted out of the plane of the leaflet in which particle i resides. Therefore, at large r_{\perp} , the in-layer correlations begin to be lost as the sampling volume encroaches on the adjacent leaflets as shown in figure 4.21. A similar effect is observed in the profile of $g_2^{(P1)u}$. As for $g_2^{(P1)n}$, the $\cos(\theta)$ contributions from leaflets parallel and antiparallel to the director more

Fig. 4.20: N1000 $\kappa 5k_{\theta} 5.0$ system: Snapshot looking down at smectic layers at $\rho = 0.60$.

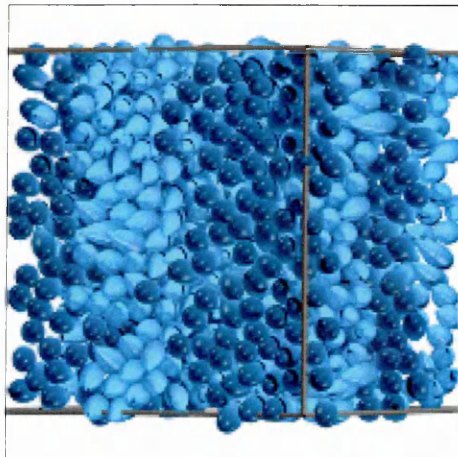
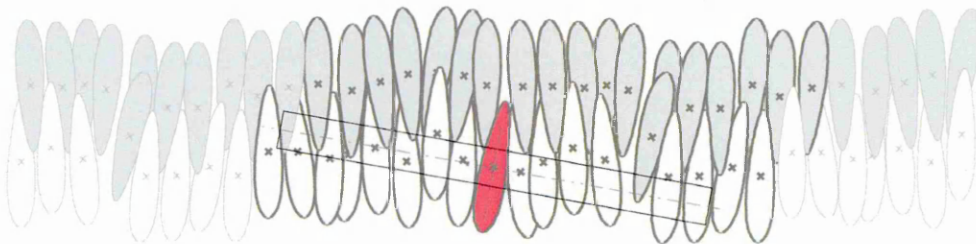


Fig. 4.21: N1000 $\kappa 5k_{\theta} 5.0$ system: Schematic of a smectic bilayer at $\rho = 0.60$ based on the central bilayer across the simulation box shown in figure 4.16 (f). The particles drawn with bolder darker lines are those of the central repeat unit of the bilayer, the lighter particles are the adjacent repeat units. The sampling volume has a diameter of $\approx 11.7 \sigma_w$ whilst its thickness is $1.0 \sigma_w$.



or less cancel out. The longitudinal distribution function $g_2^{(P2)} u$ is very similar to its radial counterpart $g_0^{(P2)}$: at all densities there are short-range orientational correlations but as the density increases, and the system becomes more highly ordered, these correlations persist at large distances. The limiting values for $g_2^{(P2)} n$ are higher than those of $g_2^{(P2)} u$ because, on average, the orientation vectors $\hat{\mathbf{u}}_j$ are more closely aligned to $\hat{\mathbf{n}}$ than they are to $\hat{\mathbf{u}}_i$.

4.3 Decompression with anisotropic rescaling

In section 4.1 we noted that, on two occasions during the compression, the smectic bilayers rearranged themselves, apparently in response to the build up of pressure anisotropy in the system. At high density the pressure anisotropy became more severe as the box dimensions were reduced and the simulation volume increasingly became incompatible with the periodicity of the bilayers. There is, therefore, a danger that the simulation box may unduly influence the structure of the ordered phases which form within it and/or the density ranges over which they exist. To try to prevent this, a procedure was devised which allows the aspect ratio of the simulation box to change so as to better accomodate ordered phases. The scheme, which we refer to as anisotropic rescaling, is now outlined.

- At a given timestep, calculate the potential energy of the system as it stands, this value we will call $U^{(old)} = \sum_i^{N-1} \sum_{j>i}^N U_{ij}$.
- Define a random scaling factor $\alpha = 1 + (\text{ran}(0, 1) \times \Delta L_{max})$ where $\text{ran}(0, 1)$ denotes a random number between 0 and 1 and ΔL_{max} is a predefined parameter specifying the maximum allowable change in the box dimensions.
- Choose at random which of the box dimensions L_x, L_y, L_z to rescale, then choose randomly whether to multiply or divide that dimension by the rescaling factor.
- Rescale the other two dimensions in order to conserve the volume of the simulation box. For example if an increase in L_y was randomly chosen i.e. $L_y^{(new)} = L_y^{(old)} \times \alpha$ then the other two dimensions should be decreased thus $L_x^{(new)} = L_x^{(old)} \div \alpha^{\frac{1}{2}}$ and $L_z^{(new)} = L_z^{(old)} \div \alpha^{\frac{1}{2}}$.

- Create a trial new configuration by similarly rescaling the corresponding components of the coordinates $\mathbf{r}^{(i)}$ in the box:

$$r_x^{(i)(new)} = r_x^{(i)(old)} \div \alpha^{\frac{1}{2}}$$

$$r_y^{(i)(new)} = r_y^{(i)(old)} \times \alpha$$

$$r_z^{(i)(new)} = r_z^{(i)(old)} \div \alpha^{\frac{1}{2}}$$

Calculate the potential energy $U^{(new)}$ for this configuration.

- Accept or reject the new configuration on the basis of the difference in energy, $\Delta U = U^{(new)} - U^{(old)}$, between the old and new configurations:
 if $\Delta U \leq 0$ Accept new configuration
 if $\Delta U > 0$ Accept new configuration if $\exp[-\Delta U/k_B T] > \text{ran}(0, 1)$
- If the rescaled configuration is rejected then the old one is retained.

The assumption is that pressure anisotropy is a manifestation of excessive overlap of particles along a certain direction. For example if smectic layers lying perpendicular to the z-direction, say, are constrained by the simulation box to take on a repeat spacing smaller than that which they would naturally adopt, overlaps in the z-direction will tend to be greater than they would in the unconstrained system. An increase in the simulation box size in the z-direction would then serve to decrease the overall overlap and, in so doing, reduce the potential. As a consequence, trial increases in L_z (or equally reductions in either L_x or L_y) should be favoured, via the ΔU based acceptance criterion, until such time as the pressure anisotropy is lifted.

The anisotropic rescaling scheme described above was first put to the test in a decompression series of the $\kappa 5k_05$ system. This simulation used the final configuration from the compression series as its starting point. The decompression sequence is summarised in table 4.4. It essentially amounts to a reversal of the compression series but with rescaling applied from $\rho = 0.62$ to $\rho = 0.52$ – the density range over which the smectic phase is present. Figure 4.22 shows data

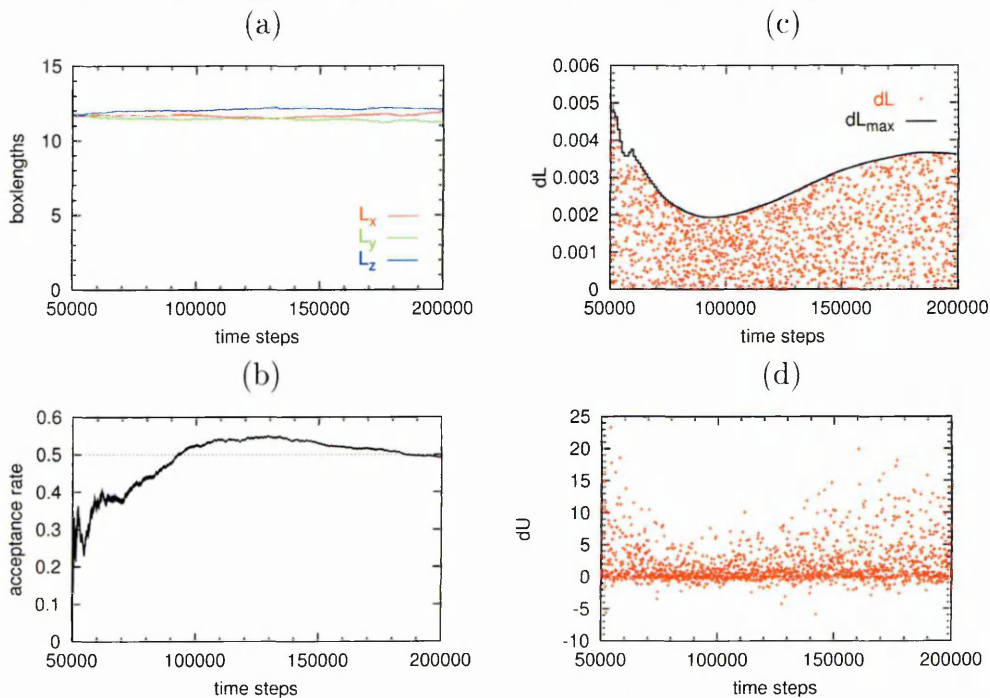
relating to the simulation box rescaling for the $\rho = 0.62$ run. In all runs, rescaling was applied between steps 50000 and 200000, during which time dimension changes were attempted every 100 timesteps. Figure 4.22 (a) reveals that over the

Tab. 4.4: Summary of main run parameters for decompression of 1000 $\kappa 5k\theta 5.0$ soft repulsive pearls. Rescaling moves were attempted every 100 time steps over the interval 50025-200025 in runs 2-12, the moderator was 0.25 and the sample size 10.

run	ρ	$\Delta\rho$	ensemble	N_{step} (averaging interval)	rescaling
1	0.62	0.00	<i>NVE</i>	500k (250-500k)	OFF
2-12	0.62-0.52	0.01	<i>NVT</i>	500k (250-500k)	ON
13-43	0.51-0.21	0.01	<i>NVT</i>	500k (250-500k)	OFF
44	0.20	0.00	<i>NVE</i>	500k (250-500k)	OFF

course of the run, L_x and L_z increased somewhat at the expense of L_y . Figure 4.22 (b) shows the acceptance rate for box rescaling moves. The required rate is 0.5, to achieve this ΔL_{max} was dynamically altered via a simple feedback mechanism

Fig. 4.22: N1000 $\kappa 5k\theta 5.0$ decompression: Box rescaling data for run 2 at $\rho = 0.62$. (a) boxlengths, (b) overall acceptance rate for box rescale moves (c) fractional change in box dimension, (d) energy change associated with trial box rescaling move.



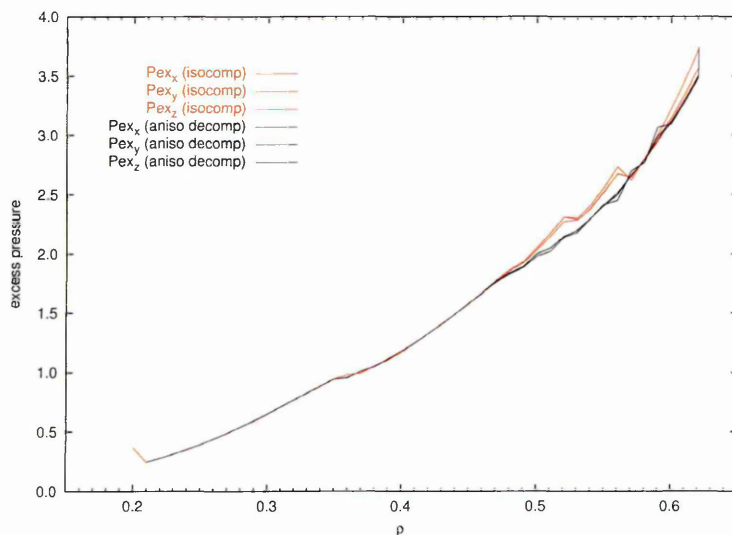
which consisted of the following. For every 10 attempted rescaling moves, a block average of the acceptance rate, R_{block} for those 10 moves was compared to 0.5 to give a difference $\delta = R_{block} - 0.5$. ΔL_{max} was then adjusted as follows:

$$\Delta L_{max}^{(new)} = \Delta L_{max}^{(old)} \times \left(1 - \frac{M \times \delta}{\Delta L_{max}^{(old)}} \right) \quad (4.1)$$

The adjustment factor in brackets takes into account the difference between the required and actual acceptance rate as well as the magnitude of $\Delta L_{max}^{(old)}$. In addition it includes a damping term M , which after some trial and error was set to 0.25, the purpose of which was to temper the magnitude of the change to ΔL_{max} and thus steer the acceptance rate more smoothly towards its required value (without it the acceptance rate tended to oscillate about 0.5 and took longer to converge towards the target value). Figure 4.22 (c) shows how ΔL_{max} is modified by this feedback mechanism from an initial guess of 0.0050 to around 0.0035 in order to get the required acceptance rate. Note that the maximum energy changes ΔU associated with trial box rescalings roughly correspond to the profile of ΔL_{max} .

As figure 4.23 shows, the application of anisotropic rescaling and, thus, the

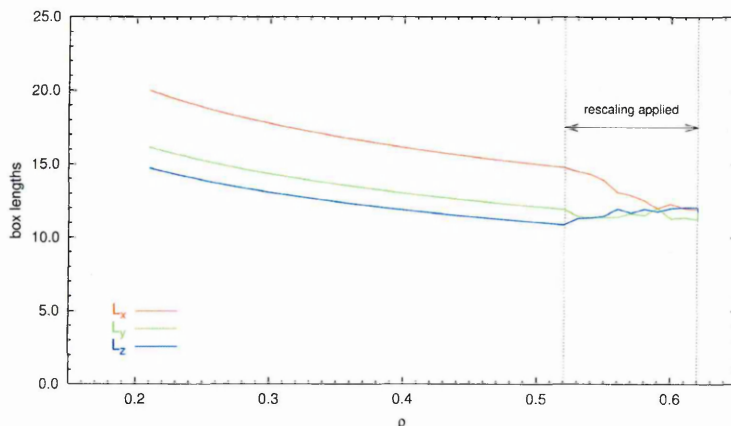
Fig. 4.23: N1000 $\kappa 5k_{\theta} 5.0$: Comparing the excess pressure components during compression and decompression.



change in the aspect ratio of the simulation box, immediately leads to a reduction in the anisotropy of the average excess pressure components. There is also

a considerable drop in the overall pressure as compared to the corresponding run in the compression series. In the early stages of the decompression, the average boxlengths are nearly equal, but, as figure 4.24 reveals, at $\rho = 0.59$ they start to differ from each other. It is not clear whether this is a purely random effect

Fig. 4.24: N1000 $\kappa 5$ $k_{\rho} 5$ decompression: Average box lengths.

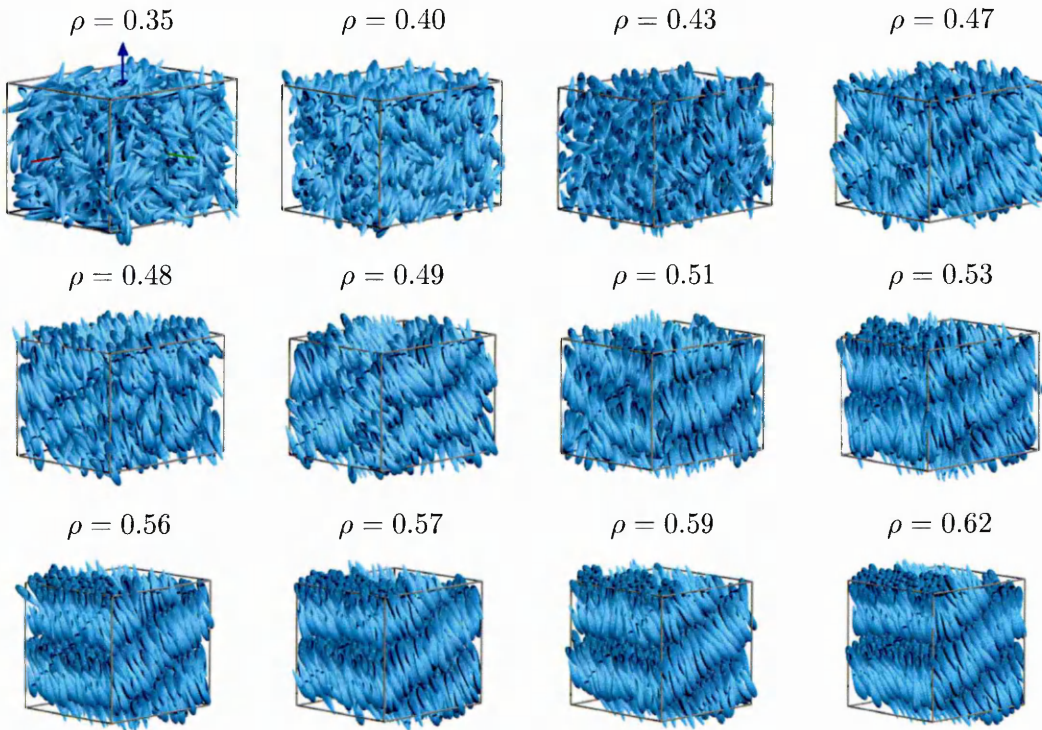


or is related in some way to structural changes in the smectic phase. At several points in the decompression, namely $\rho = 0.59$, 0.57 , 0.56 and 0.51 - 0.50 , the excess pressure components exhibit some disparity, albeit temporarily. Also the overall pressure profile exhibits a number of kinks over the smectic region although the large discontinuities that were observed in the compression are not repeated. Thermodynamically, fluctuations in pressure in response to volume changes are connected by changes in the compressibility of the system. The kinks in the pressure profile at high density may therefore relate to changes in the compressibility of the system that arise as a result of the changing orientation of the smectic layers within the simulation box as it struggles to accommodate itself to the box shape.

Figure 4.25 presents snapshots from the decompression series, these show that the smectic bilayers remain oriented along the $[10\bar{2}]$ planes down to a density of around $\rho = 0.51$. Subsequently at $\rho = 0.49$, the bilayers rearrange themselves in the $[1\bar{1}\bar{2}]$ orientation. Recall that this same reorientation occurred during the compression, but at the higher density of 0.56 . Shortly afterwards, between $\rho = 0.48$ - 0.47 , the

smectic layers break up and the system returns to the nematic phase. Thereafter, the pressure profile for the decompression series is almost identical to that of the compression. Throughout the entire decompression, the order parameter profile (not shown) closely reproduces that of the decompression. There are also few differences between the corresponding sets of distribution functions, as figure

Fig. 4.25: N1000 $\kappa 5k\theta 5.0$ system: Snapshots of the simulation box at the end of selected runs from the decompression series. Anisotropic rescaling was applied in the density range $\rho = 0.62-0.52$. The x,y,z axes are coloured red, green and blue respectively.

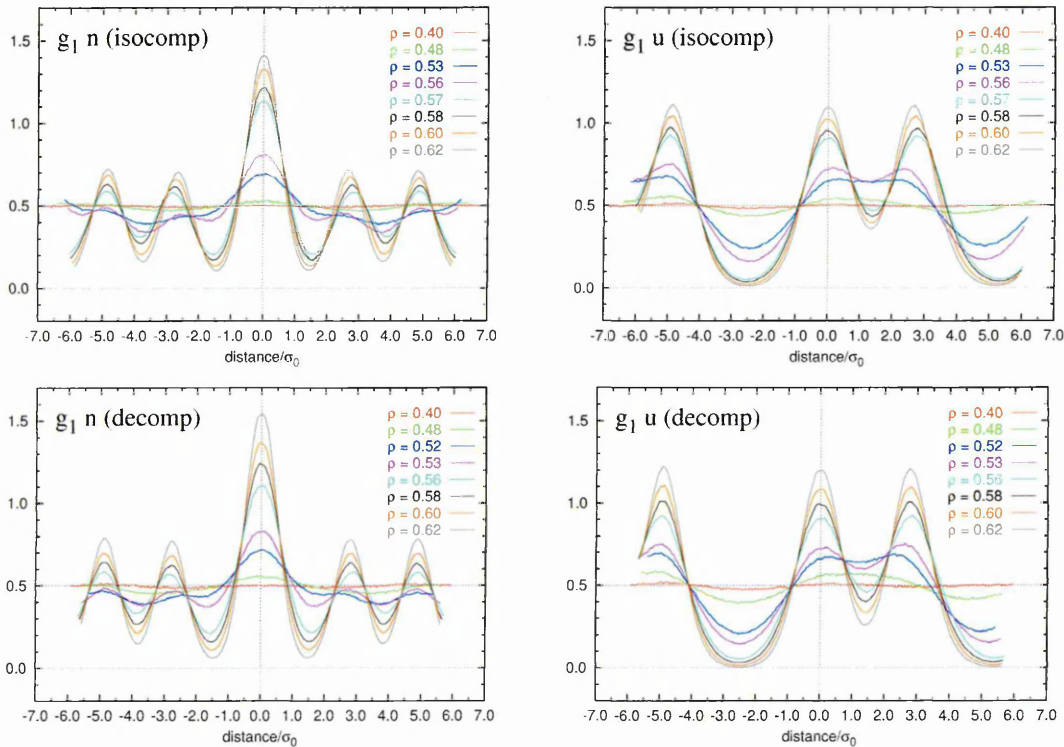


4.26 illustrates. The only dissimilarity is that in the high density phase of the isotropic compression, the intralayer separation of opposing leaflets in the same bilayer shrinks somewhat, whereas at the corresponding density in the anisotropic decompression this distance is essentially constant.

Further testing of the rescaling scheme was carried out by performing two supplementary compressions for the $\kappa 5k\theta 5.0$ system. In the first, rescaling was activated from $\rho = 0.37$ onwards, the density around which the isotropic-nematic transition

takes place. The initial configuration for this simulation was taken from the end of the $\rho = 0.36$ run from the isotropic compression discussed in section 4.1. Snapshots from the anisotropic compression, as presented in figure 4.27, show that on this occasion the bilayers arrange themselves in the $[\bar{2}11]$ planes. Figure 4.28 (a)

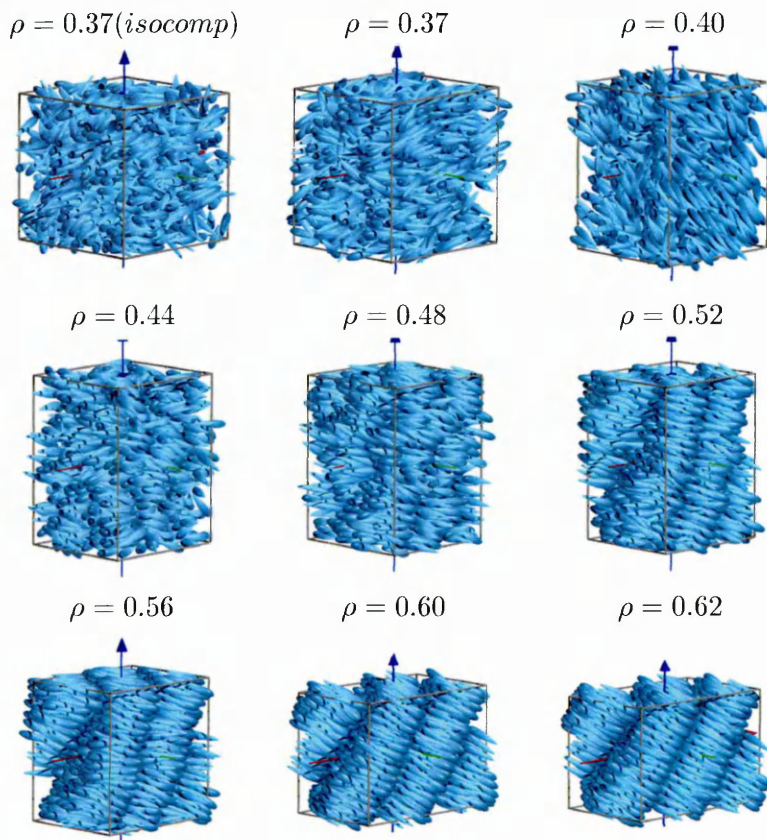
Fig. 4.26: N1000 $\kappa 5k_{\theta} 5.0$ system decomp: Comparing loc g_1 . for the isotropic compression series and the decompression series with anisotropic rescaling.



meanwhile shows the average boxlengths as a function of density. Initially L_z grows at the expense of L_x and L_y . Given that the pressure tensor is isotropic in the nematic phase [28], one would conclude that what we observing is a random walk in L_x, L_y, L_z – there is no driving force present to induce the simulation volume to expand or contract in any particular direction. As the system enters the smectic phase, however, the trend is reversed – L_x begins to increase whilst L_z shrinks – presumably in order to allow the smectic phase to accomodate the nascent smectic phase.

In the second anisotropic compression, rescaling was applied from $\rho = 0.51$ onwards, the density around which the N-Sm transition occurs. Again the initial configuration was taken from the original isotropic compression. Figure 4.28 (b) shows that here the boxlengths rapidly deviate from each other in a virtually

Fig. 4.27: N1000 $\kappa 5k\theta 5.0$ system: Rescaling applied from I-N transition onwards ($\rho = 0.37 - 0.62$)



monotonic fashion with L_x and L_z growing at the expense of L_y . During the $\rho = 0.57$ run, the latter fell below $2r_{cut}$ causing the simulation to be automatically aborted. There is no sense in continuing the simulation beyond this point since the system would subsequently be subject to spurious periodic boundary effects i.e. the particles would begin to interact with their own periodic ‘images’. Snapshots from the simulation, as presented in figure 4.29, show that on this occasion the smectic phase forms along the $[202]$ planes. The observed rescaling of the box in conjunction with this alignment of the bilayers, suggests that the former

is driven by the longitudinal expansion of the bilayers. As the system is compressed, the average lateral distance between particles in the layers must decrease so that they have less space in which to tilt with respect to one another and also

Fig. 4.28: N1000 $\kappa 5k_{\theta} 5.0$ system: Box rescaling data for anisotropic compression sequences $\rho = 0.62$. (a) Series relaunched with rescaling on at $\rho = 0.36$. (b) Series relaunched with rescaling on at $\rho = 0.51$. The latter was automatically aborted before it was due to finish as a result of L_y falling below $2r_{cut}$.

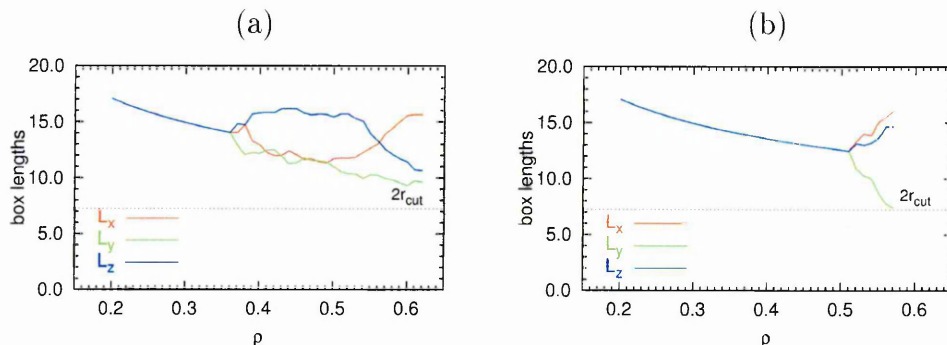
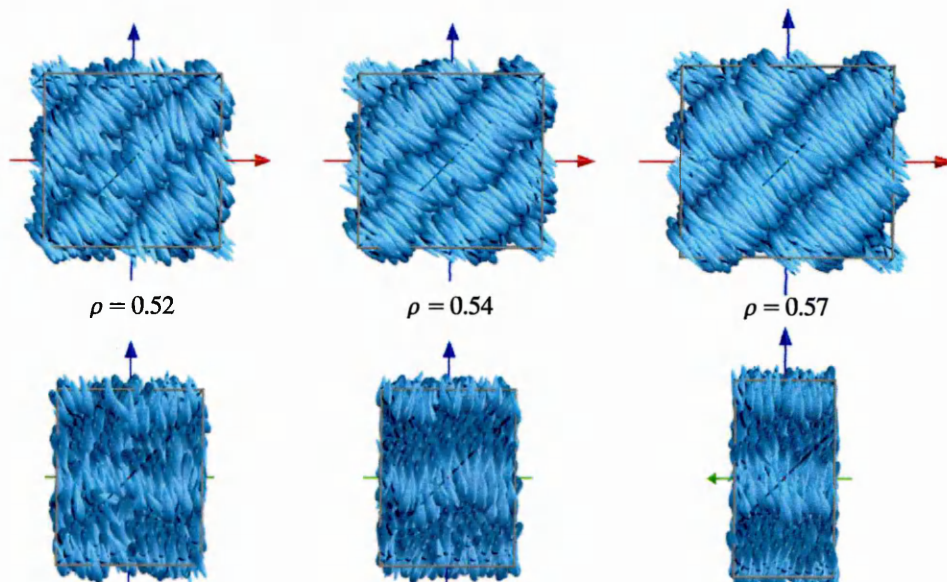


Fig. 4.29: Snapshots of the simulation box at the end of selected runs during compression of the N1000 $\kappa 5k_{\theta} 5.0$ system with rescaling activated from $\rho = 0.51$ onwards. The x,y,z axes are coloured red, green and blue respectively.



to interdigitate. The result is that the bilayers tend to ‘swell’ in the direction perpendicular to the layers. Barmes et al. [14] made similar observations in their MC studies of this system. If the system was being compressed isotropically, the result would be elevated pressure in this direction, however when rescaling of the

box dimensions is implemented the system is able to expand in order to relieve the pressure anisotropy. In this particular simulation then, the expansion of the bilayers drives the increase of L_x and L_z , via the rescaling scheme, whilst the L_y must shrink in order to preserve constant volume. Reduction of the L_y is expedited by the relative ease of lateral movement of particles within the layers.

In conclusion, the rescaling scheme is successful in so much as it would appear to allow the smectic phase to take on its natural periodicities and, thus, relieve pressure anisotropy. However, in some instances it does seem prone to instability which can result in rather extreme simulation box aspect ratios. As we have seen, this may ultimately lead to the cessation of a simulation. Another concern is that excessive fluctuations of the box dimensions may actually disrupt the formation of periodic structures. The most obvious way to avoid these undesirable side effects would be to apply rescaling more judiciously, i.e. to adjust the box dimensions for only as long as is necessary to relieve pressure anisotropy. Since it is usually impractical for a human to monitor simulations as they actually unfold, the decision as to whether to rescale or not would need to be based on some sort of algorithm. A natural basis for this would be to block average the excess pressure components and use the difference between them as a criterion for toggling rescaling on or off. However great care would need to be exercised in the design of such an automated procedure not least because inappropriate application of rescaling may in itself lead to pressure anisotropy.

4.4 System size effects

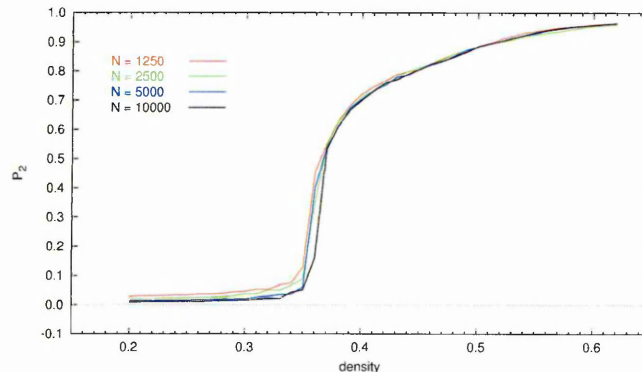
As a final road test of the simulation code and procedures, identical compressions were carried out on systems containing, 1250, 2500, 5000 and 10000 particles. The parameters for these compressions are summarised in table 4.5. Figure 4.30

Tab. 4.5: Summary of main run parameters for compression of systems of $N = 1250, 2500, 5000, 10000$ soft repulsive pears. Rescaling moves were attempted every 100 time steps over the interval 50025-200025 in runs 33-43, the moderator was 0.25 and the sample size 10.

run	ρ	$\Delta\rho$	ensemble	N_{step} (averaging interval)	rescaling
1	0.20	0.00	<i>NVE</i>	500k (250-500k)	OFF
2-32	0.21-0.51	0.01	<i>NVT</i>	500k (250-500k)	OFF
33-43	0.52-0.62	0.01	<i>NVT</i>	500k (250-500k)	ON
44	0.62	0.00	<i>NVE</i>	500k (250-500k)	OFF

shows the order parameter data obtained for the four systems to be in close agreement. Quantitatively the profiles differ slightly in two respects. Firstly P_2 in the isotropic phase is a little higher for the smaller system sizes, owing to the fact that the relative contribution from close range correlations is greater for systems of smaller size, as discussed in section 4.2. Secondly the isotropic-nematic transi-

Fig. 4.30: System size effects: Order parameter profiles. P_2 vs. density

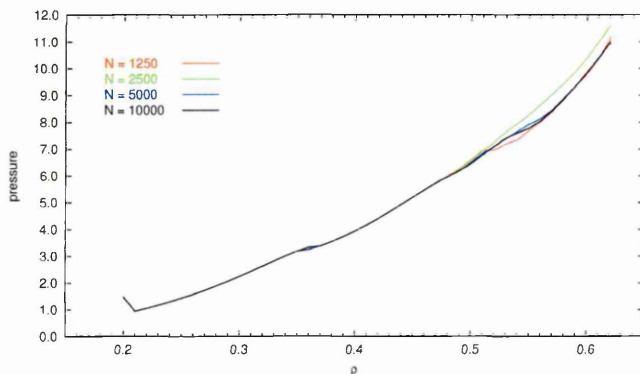


tion takes place at a slightly higher density for the N10000 system.

The pressure data presented in figure 4.31 indicate that the onset of smectic ordering, corresponding to the second inflection in the pressure profiles, occurs at

around $\rho = 0.47$ for all the system sizes. However at higher densities there are noticeable differences, the third inflection appears at $\rho = 0.51 - 0.52$, $\rho = 0.55 - 0.56$ and $\rho = 0.53 - 0.55$ for the N1250, N5000 and N10000 systems respectively,

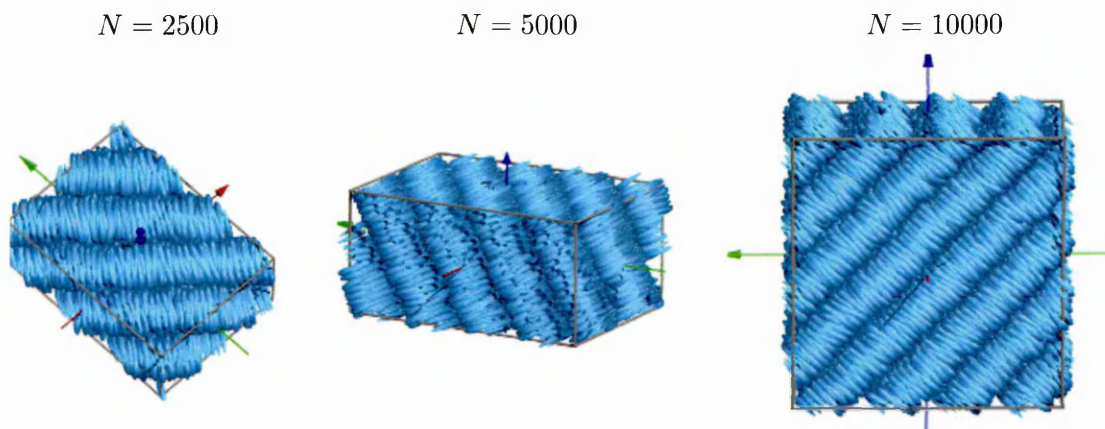
Fig. 4.31: System size effects: total pressure profiles. P vs. density



although at densities higher than $\rho = 0.57$ the profiles of these three systems converge once more. The most noticeable difference is that the N2500 profile exhibits only a very slight inflection, at around $\rho = 0.53$, and remains at a higher pressure than the other three for the remainder of the compression.

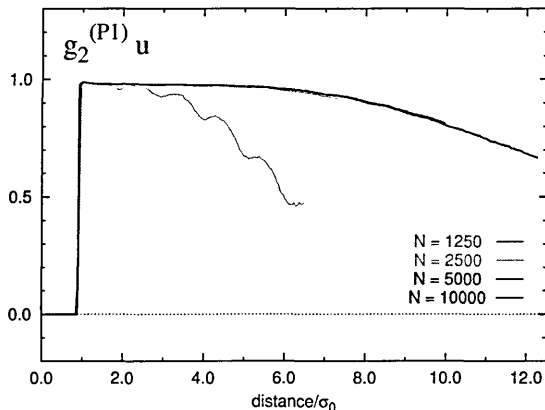
The origin of this disparity is apparent when we inspect snapshots of the final configurations from the four simulations as shown in figure 4.32. The N1250 system (not shown to save on space) formed a well-ordered smectic bilayers oriented in the $[300]$ direction, the N5000 and N10000 systems too exhibit orderly bilayers

Fig. 4.32: System size effects: Final configurations.



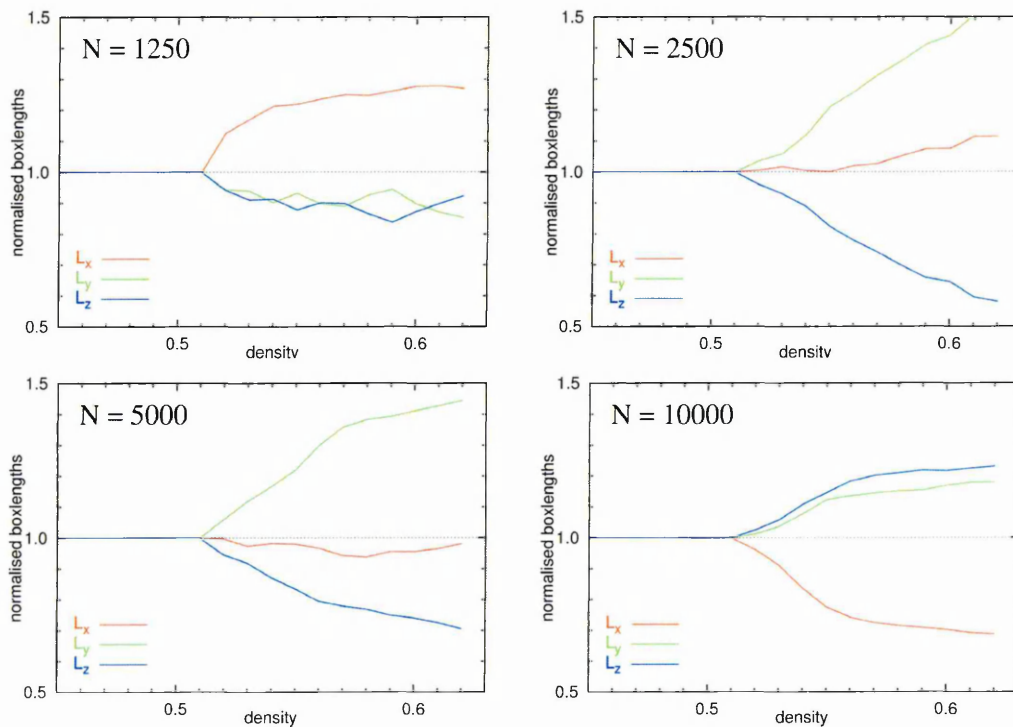
but in the $[2\bar{4}1]$ and $[0\bar{4}\bar{4}]$ planes of their simulation boxes respectively. The N2500 system meanwhile has formed bilayers in the $[2\bar{3}1]$ planes which appear decidedly distorted, in particular the particles have an noticeable tilt with respect to the bilayer normal. This is confirmed by the $g_2^{(P1)u}$ profile for the N2500 system, as shown in figure 4.33, which decays much more rapidly with distance than for

Fig. 4.33: N1000 κ 5 $k\rho$ 5 system: The effect of system size on the lateral distribution function ($g_2^{(P1)u}$) as measured at a density of $\rho = 0.62$.



the other three systems. In fact most of the distribution functions for the N2500 system exhibit significant differences when compared to the corresponding functions for the other three systems, the latter being almost identical to each other. It would appear that the N2500 system failed to find an arrangement within the simulation box that comfortably incorporates the interlayer repeat distance for this species of particle. This is further evidenced by the evolution of the boxlengths (figure 4.34) which continued to diverge right up to the end of the sequence. This contrasts with the other systems whose boxlengths, whilst changing considerably in the course of the compression, appear to have settled down in the latter stages. Finally we note that the N10000 system has formed bilayers in an orientation similar to that which was observed in the similar compression of the N1000 system, the latter having been aborted when its L_y dimension fell below $2r_{cut}$. In the N10000 system the bilayers are in the $[0\bar{4}\bar{4}]$ planes so that their swelling causes the L_y and L_z increase at the expense of L_x , whereas in the N1000 system wherein the layers formed in the $[20\bar{2}]$ planes, L_x and L_z increase at the expense of L_y .

Fig. 4.34: System size effects: System size effects: boxlengths.



4.5 Summary and Conclusions

The MD code and procedures used for the compression and expansion of systems of soft-repulsive tapered particles appear to be sound. When run in NVE , total energy is conserved within an acceptable margin, with variations over the course of 500kstep runs carried out at low and high densities not exceeding 0.15% of the average value. Also kinetic energy is distributed between the systems degrees of freedom in the correct ratio, this equipartition being achieved rather swiftly, within 1000 timesteps of the beginning of the simulation. The mean squared displacement is assuredly linear at all densities; at the I-N transition we observe an enhancement of the mobility along the director axis whereas in the smectic phase, in plane diffusion perpendicular the director and confined to particular

leaflets of the bilayers would appear to be favoured. The results of the MD NVT compression studied here agree well with those obtained from an MC NPT compression of an identical system of hard particles, both in terms of the positions of the phase transitions and the characteristics of the phases formed.

The anisotropic rescaling scheme introduced in section 4.3 is effective at relieving pressure anisotropy, however in some situations, both during compression and expansion, the boxlengths can diverge to an extent which disrupts the simulation. A pragmatic solution to this problem would be simply to apply rescaling moves at a reduced frequency and perhaps over a more restricted density range. Results presented in the final section indicate that system size in of itself does not appear to have a significant effect on the structural characteristics of the phases formed and has only a minor impact on the density at which phase transitions take place. Nor are the structural characteristics of ordered phases affected by the particular orientation at which they form in the simulation box except on the occasions when they fail to achieve commensurability with it.

CHAPTER 5

Measurement of flexoelectric coefficients

In general, when external stresses are applied to a sample of liquid crystal, they result in a deformation of the director field, $\hat{\mathbf{n}}(\mathbf{r})$. If the material has flexoelectric properties, the distortions will result in a reorientation of its constituent particles such that a net polarisation, \mathbf{P} , is induced. This is analogous to the piezoelectric effect in crystalline materials, the main difference being that in the latter case, the charges are ions which are anchored to the crystal lattice, whereas in a liquid crystal the charges sit on particles, which, of course, form a fluid state. Conversely, if an external electric field, \mathbf{E} , is applied to a flexoelectric material, the constituent particles will experience torques, by virtue of their charge distributions, causing their reorientation and, thus, a deformation of the director field. This is often referred to as the inverse flexoelectric effect. The latter effect clearly has ramifications for the switching properties of liquid crystals in devices. Therefore there is considerable interest in understanding and harnessing this property.

Two mechanisms have been proposed to explain how the effect occurs. In the theory of Prost and Marcerou [29], the liquid crystal molecules are uniaxial in shape but possess an electric quadrupole, that is to say they possess a pair of equal and opposite dipoles and thus have zero net dipole. When a splay deformation, for example, is applied to a system of molecules of this type, the change that this effects in their packing arrangement results in changes of the relative positions of the charges on different molecules, so producing a net polarisation.

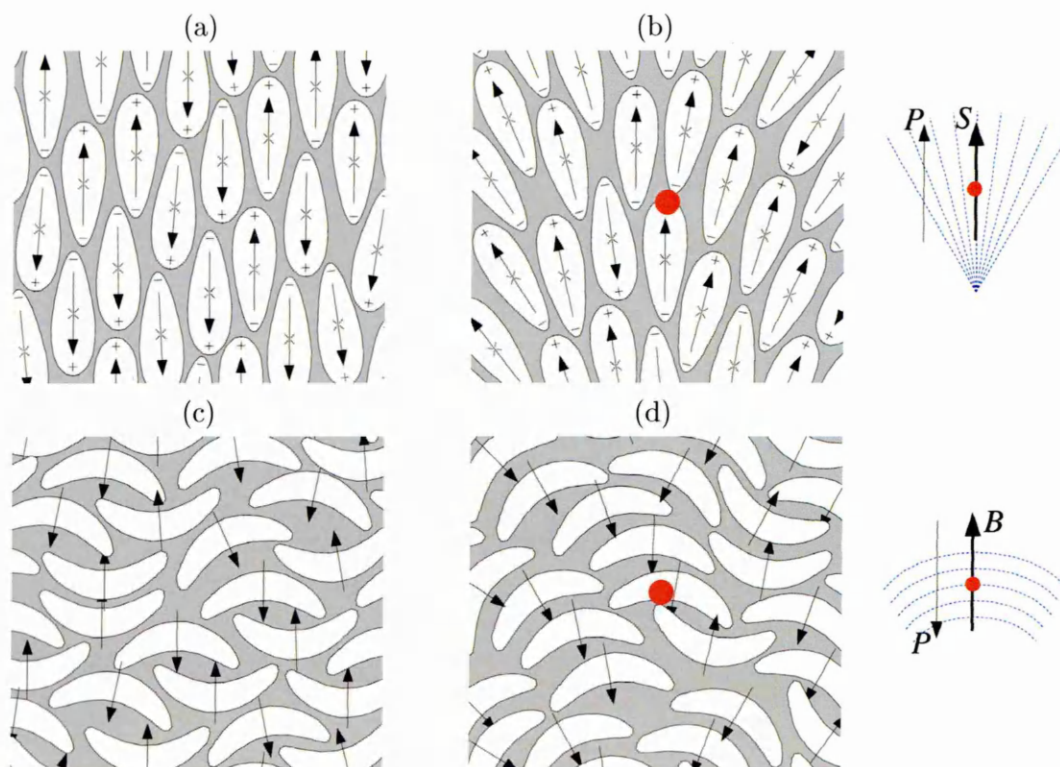
In a second theory developed by Meyer [30], the liquid crystal molecules are assumed to possess electric dipoles, \mathbf{p} and, in addition, polar shape anisotropy. Specifically, the types of particles considered are tapered and crescent-like as featured in figure 5.1. In the quiescent state (5.1 (a) and (c)), the particles in the system will tend to arrange themselves in a nematic like fashion with, on average, as many dipoles pointing up as point down. However, when the system is deformed, the particles are forced to pack in ways which result in an excess of dipoles pointing up and, thus, a net polarisation. For the tapered particles, such polarisation will be induced by a splay deformation (5.1 (b)) whilst for the banana like particles it will be induced by a bend deformation (5.1 (b)). Meyer derived the following equation relating the net polarisation to the splay and bend deformations.

$$\mathbf{P} = e_{11}\hat{\mathbf{n}}(\nabla \cdot \hat{\mathbf{n}}) + e_{33}\hat{\mathbf{n}} \wedge (\nabla \wedge \hat{\mathbf{n}}) \quad (5.1)$$

where $\hat{\mathbf{n}}(\nabla \cdot \hat{\mathbf{n}})$ and $\hat{\mathbf{n}} \wedge (\nabla \wedge \hat{\mathbf{n}})$ are the splay and bend vectors \mathbf{S} and \mathbf{B} respectively, which characterise the distortions of the director field at any given point. The prefactors e_{11} and e_{33} are the splay and bend flexoelectric coefficients, which characterise the flexoelectric properties of a particular material. For a liquid crystal consisting of purely tapered particles, with dipoles pointing towards their rounded ends, one would expect to observe positive e_{11} and zero e_{33} , since, for this shape of particle, bend deformation would not be expected to bring about the kind of rearrangements resulting in a net polarisation. Similarly for the banana-shaped particles, with their dipoles oriented as shown, e_{33} would be expected to be finite and negative and e_{11} zero. These coefficients have been determined experimentally

and so, in a very real sense, reflect how the microscopic packing arrangements of liquid crystal molecules, which cannot themselves be directly observed, affect the bulk material properties. If these same coefficients could be measured from simulations, specifically simulations in which the degree of shape asymmetry, be it taper or bend, can be varied systematically, then the results may provide insight into how molecular attributes affect the bulk flexoelectric properties. As it happens, a method does exist which allows one to obtain e_{11} and e_{33} from simulation data. This is known as the linear response approach, which we will outline in the following section.

Fig. 5.1: Schematics illustrating the effect of splay and bend deformations on systems of tapered and banana-shaped molecules respectively. The panels on the far right show the relationship between the the director fields (dashed blue lines) and the splay and bend vectors \mathbf{S} and \mathbf{B} at the points in the fields marked by the red spots.



5.1 The linear response approach

In the absence of an applied field there is no net splay or bend deformation of the director field and therefore, on average, no net polarisation of the material. However, random thermal fluctuations can produce short-lived, localised perturbations of the director field producing a transient contribution to the polarisation. The coupling of thermally induced director deformations to the polarisation is a manifestation of the flexoelectric effect and as such provides a means of calculating the flexoelectric coefficients, as we will now show.

Small director deformations may be described by incremental rotations $\partial\underline{\theta}$ of the director about an axis $\underline{\theta}$. Formally, the incremental rotation and the change in the director are related by [31]

$$\partial\underline{\theta} = \hat{\mathbf{n}} \wedge \partial\hat{\mathbf{n}} \quad (5.2)$$

$$\partial\hat{\mathbf{n}} = -\hat{\mathbf{n}} \wedge \partial\underline{\theta} \quad (5.3)$$

Or alternatively in component form

$$\partial\theta_\alpha = \epsilon_{\alpha\beta\gamma} \hat{n}_\beta \partial\hat{n}_\gamma \quad (5.4)$$

$$\partial\hat{n}_\alpha = \epsilon_{\alpha\beta\gamma} \hat{n}_\gamma \partial\theta_\beta \quad (5.5)$$

where ϵ is the third rank Levi-Civita tensor as defined in Appendix D. The components are generated using the summation convention, whereby any subscript that appears twice in any term should be summed over all possible values. Here, the range of values is 1,2,3 corresponding to the three Cartesian directions x, y, z . So, for example, the x -component of $\partial\underline{\theta}$ would be given by:

$$\partial\theta_x = \partial\theta_1 = \epsilon_{1\beta\gamma} \hat{n}_\beta \partial\hat{n}_\gamma \equiv \sum_{\beta=1}^3 \sum_{\gamma=1}^3 \epsilon_{1\beta\gamma} \hat{n}_\beta \partial\hat{n}_\gamma \quad (5.6)$$

where β and γ serve as the so called dummy variables. The variation of the director at any given point in space is described by the gradient tensor, $\nabla\underline{\theta}$, of the

rotation axis. This quantity is referred to as the orientational deformation tensor, with components denoted $\gamma_{\alpha\beta}$.

$$(\nabla\theta)_{\alpha\beta} = \gamma_{\alpha\beta} = \partial_{\alpha}\theta_{\beta} \equiv \frac{\partial\theta_{\beta}}{\partial r_{\alpha}} \quad (5.7)$$

The conjugate property to the orientational deformation tensor is the orientational stress tensor $\tilde{\Pi}$. Microscopically, this quantity is obtained by summing the vector products of interparticle vectors and torques

$$\tilde{\Pi} = -\frac{1}{2} \sum_{i \neq j}^N \mathbf{r}^{ij} \wedge \tau^{ij} \quad \Pi_{\alpha\beta} = -\frac{1}{2} \sum_{i \neq j}^N r_{\beta}^{ij} \tau_{\alpha}^{ij} \quad (5.8)$$

where i and j are the particle indices and N is the total number of particles in the system.

The linear response theory of Kubo [32] is a general theory which relates the changes in a dynamic property of a system to small mechanical disturbances taking place within the system. Nemtsov and Osipov [33] turned to this theory in order to derive a relationship between the polarisation (the dynamic property) and the director deformations (the mechanical disturbances) in a model anisotropic medium. In this work, the model system was assumed to consist of a set of particles with translational and rotational degrees of freedom, each possessing a unit dipole moment $\hat{\mathbf{p}}_i$. The total polarisation of the system is given by the sum of these dipoles, $\sum_{i=1}^N \hat{\mathbf{p}}_i$. The mechanical disturbance, meanwhile, was modelled as a cyclical deformation. Using this approach, the following linear response relation was obtained

$$P_{\alpha} = E_{\alpha\beta\gamma} \gamma_{\beta\gamma} . \quad (5.9)$$

Nemtsov and Osipov refer to $E_{\alpha\beta\gamma}$ as the flexoelectric tensor, although elsewhere [34–36] it is called the response function. In what follows we will use the latter nomenclature. In the long wavelength limit, i.e. when the frequency of the cyclical

deformation tends to zero, $E_{\alpha\beta\gamma}$ reduces to the correlation function

$$\tilde{E} = -\frac{\beta}{V}\langle \mathbf{P} \wedge \tilde{\Pi} \rangle \quad E_{\alpha\beta\gamma} = -\frac{\beta}{V}\langle P_\alpha \Pi_{\beta\gamma} \rangle \quad (5.10)$$

where β is the Boltzmann factor $1/k_B T$ and V is the volume of the system. The response function relates the bulk polarisation of the material to the microscopic interactions occurring between its constituent particles. Nemtsov and Osipov then went on to show that the linear response relation 5.9 may be cast in a form which is similar to Meyer's formula by use of the following results. Firstly the response function may be expressed as

$$E_{\alpha\beta\gamma} = E_1 \epsilon_{\alpha\beta\gamma} + E_2 \epsilon_{\mu\alpha\beta} \hat{n}_\gamma \hat{n}_\mu + E_3 \epsilon_{\mu\gamma\beta} \hat{n}_\alpha \hat{n}_\mu + E_4 \epsilon_{\gamma\alpha\mu} \hat{n}_\beta \hat{n}_\mu \quad (5.11)$$

where E_1, E_2, E_3 and E_4 are simple constants. Secondly, using 5.4 and 5.5, the deformation tensor $\gamma_{\beta\gamma}$ can be written as

$$\gamma_{\beta\gamma} = \partial_\beta \theta_\gamma = \frac{\partial \theta_\gamma}{\partial r_\beta} = \epsilon_{\gamma\mu\nu} \hat{n}_\mu \frac{\partial \hat{n}_\nu}{\partial r_\beta}. \quad (5.12)$$

Substituting these two expressions into 5.9 gives us

$$\begin{aligned} P_\alpha = E_{\alpha\beta\gamma} \gamma_{\beta\gamma} = & E_1 (\epsilon_{\alpha\beta\gamma} \epsilon_{\gamma\mu\nu}) \hat{n}_\mu \frac{\partial \hat{n}_\nu}{\partial r_\beta} \\ & + E_2 (\epsilon_{\mu\alpha\beta} \epsilon_{\gamma\mu\nu}) \hat{n}_\mu \hat{n}_\gamma \hat{n}_\mu \frac{\partial \hat{n}_\nu}{\partial r_\beta} \\ & + E_3 (\epsilon_{\mu\gamma\beta} \epsilon_{\gamma\mu\nu}) \hat{n}_\mu \hat{n}_\alpha \hat{n}_\mu \frac{\partial \hat{n}_\nu}{\partial r_\beta} \\ & + E_4 (\epsilon_{\gamma\alpha\mu} \epsilon_{\gamma\mu\nu}) \hat{n}_\mu \hat{n}_\beta \hat{n}_\mu \frac{\partial \hat{n}_\nu}{\partial r_\beta} \end{aligned}$$

each term on the rhs may be simplified using identities relating the Levi-Civita tensor and the Kronecker delta function δ_{ij} (see Appendix D). When applied to

the first term on the rhs this approach yields

$$\begin{aligned}
E_1(\epsilon_{\alpha\beta\gamma}\epsilon_{\gamma\mu\nu})n_\mu \frac{\partial \hat{n}_\nu}{\partial r_\beta} &= E_1(\delta_{\alpha\mu}\delta_{\beta\nu} - \delta_{\alpha\nu}\delta_{\beta\mu})\hat{n}_\mu \frac{\partial \hat{n}_\nu}{\partial r_\beta} \\
&= E_1(\delta_{\alpha\alpha}\delta_{\beta\beta} - \delta_{\alpha\beta}\delta_{\beta\alpha})\hat{n}_\alpha \frac{\partial \hat{n}_\beta}{\partial r_\beta} E_1(\delta_{\alpha\beta}\delta_{\beta\alpha} - \delta_{\alpha\alpha}\delta_{\beta\beta})\hat{n}_\beta \frac{\partial \hat{n}_\alpha}{\partial r_\beta} \\
&= E_1(1 - 0)\hat{n}_\alpha \frac{\partial \hat{n}_\beta}{\partial r_\beta} E_1(0 - 1)\hat{n}_\beta \frac{\partial \hat{n}_\alpha}{\partial r_\beta} \\
&= E_1 \left(\hat{n}_\beta \frac{\partial \hat{n}_\alpha}{\partial r_\beta} - \hat{n}_\alpha \frac{\partial \hat{n}_\beta}{\partial r_\beta} \right)
\end{aligned}$$

and similarly for the other three terms

$$\begin{aligned}
E_2(\epsilon_{\mu\alpha\beta}\epsilon_{\gamma\mu\nu})\hat{n}_\mu \hat{n}_\gamma \hat{n}_\mu \frac{\partial \hat{n}_\nu}{\partial r_\beta} &= E_2 \hat{n}_\beta \frac{\partial \hat{n}_\alpha}{\partial r_\beta} \\
E_3(\epsilon_{\mu\gamma\beta}\epsilon_{\gamma\mu\nu})\hat{n}_\mu \hat{n}_\alpha \hat{n}_\mu \frac{\partial \hat{n}_\nu}{\partial r_\beta} &= E_3 \hat{n}_\alpha \frac{\partial \hat{n}_\beta}{\partial r_\beta} \\
E_4(\epsilon_{\gamma\alpha\mu}\epsilon_{\gamma\mu\nu})\hat{n}_\mu \hat{n}_\beta \hat{n}_\mu \frac{\partial \hat{n}_\nu}{\partial r_\beta} &= 0
\end{aligned}$$

Substituting these results into 5.1 we obtain

$$P_\alpha = E_{\alpha\beta\gamma}\gamma_{\beta\gamma} = E_1 \left(n_\beta \frac{\partial \hat{n}_\alpha}{\partial r_\beta} - \hat{n}_\alpha \frac{\partial \hat{n}_\beta}{\partial r_\beta} \right) + E_2 \hat{n}_\beta \frac{\partial \hat{n}_\alpha}{\partial r_\beta} + E_3 \hat{n}_\alpha \frac{\partial \hat{n}_\beta}{\partial r_\beta}$$

Finally, by equating terms, we obtain the following expression

$$\begin{aligned}
P_\alpha = E_{\alpha\beta\gamma}\gamma_{\beta\gamma} &= (E_3 - E_1)\hat{n}_\alpha \frac{\partial \hat{n}_\beta}{\partial r_\beta} + (E_1 + E_2)\hat{n}_\beta \frac{\partial \hat{n}_\alpha}{\partial r_\beta} \\
&= (E_3 - E_1)\hat{\mathbf{n}}(\nabla \cdot \hat{\mathbf{n}}) + (E_1 + E_2)\hat{\mathbf{n}} \wedge (\nabla \wedge \hat{\mathbf{n}}) \quad (5.13)
\end{aligned}$$

Comparing this to Meyer's equation

$$\mathbf{P} = e_{11}\hat{\mathbf{n}}(\nabla \cdot \hat{\mathbf{n}}) + e_{33}\hat{\mathbf{n}} \wedge (\nabla \wedge \hat{\mathbf{n}}) \quad (5.14)$$

we immediately see that 5.13 is equivalent to the latter when we set $e_{11} = (E_3 - E_1)$ and $e_{33} = (E_1 + E_2)$. We can obtain the constants E_1 , E_2 and E_3 explicitly in terms of the response function, $E_{\alpha\beta\gamma}$, by manipulation of 5.11. The resulting

expressions for the flexo coefficients are

$$e_{11} = -\frac{1}{2}E_{\alpha\beta\gamma}\epsilon_{\mu\beta\gamma}\hat{n}_\alpha\hat{n}_\mu \quad (5.15)$$

$$e_{33} = +\frac{1}{2}E_{\alpha\beta\gamma}\epsilon_{\alpha\beta\mu}\hat{n}_\gamma\hat{n}_\mu \quad (5.16)$$

Thus, the linear response approach provides a link between the microscopic details of a system, namely particle positions, orientations and torques, from which the response function $E_{\alpha\beta\gamma}$ and the flexoelectric coefficients can be obtained.

5.2 Simulation technique

We now specify the precise details of how the linear response approach described in the previous section was applied to our simulation data in order to compute e_{11} and e_{33} . The procedure is based on the methods described in references [34–37]. In what follows the superscript (s) is used to indicate explicitly the instantaneous value of an observable, s being the time step at which the calculation is made. The analysis begins by calculating the intermolecular torques, as defined in section 3.2, within the interactions double loop

$$\tau_{ij}^{(s)} = \hat{\mathbf{u}}_i^{(s)} \wedge \mathbf{g}_{ij}^\perp = \hat{\mathbf{u}}_i^{(s)} \wedge (-\nabla_{\hat{\mathbf{u}}_i} U_{ij})^{(s)} = \hat{\mathbf{u}}_i^{(s)} \wedge \left(-\frac{\partial U_{ij}}{\partial a} \mathbf{r}_{ij} - \frac{\partial U_{ij}}{\partial c} \hat{\mathbf{u}}_j \right)^{(s)} \quad (5.17)$$

$$\tau_{ji}^{(s)} = \hat{\mathbf{u}}_j^{(s)} \wedge \mathbf{g}_{ji}^\perp = \hat{\mathbf{u}}_j^{(s)} \wedge (-\nabla_{\hat{\mathbf{u}}_j} U_{ij})^{(s)} = \hat{\mathbf{u}}_j^{(s)} \wedge \left(-\frac{\partial U_{ij}}{\partial b} \mathbf{r}_{ij} - \frac{\partial U_{ij}}{\partial c} \hat{\mathbf{u}}_i \right)^{(s)} \quad (5.18)$$

where $a = \hat{\mathbf{u}}_i \cdot \mathbf{r}_{ij}$, $b = \hat{\mathbf{u}}_j \cdot \mathbf{r}_{ij}$ and $c = \hat{\mathbf{u}}_i \cdot \hat{\mathbf{u}}_j$. As the torques and intermolecular vectors are computed, the stress tensor components for the system as a whole are accumulated

$$\Pi_{\alpha\beta}^{(s)} = -\frac{1}{2} \sum_{i \neq j}^N r_\beta^{ij(s)} \tau_\alpha^{ij(s)} = \sum_i^N \left\{ \sum_{j>i}^N r_\beta^{ij(s)} \tau_\alpha^{ij(s)} + \sum_{j>i}^N r_\beta^{ji(s)} \tau_\alpha^{ji(s)} \right\} \quad (5.19)$$

We arbitrarily assign a reduced dipole moment to each particle with a magnitude of unity and a direction which is the same as the particles orientation vector, i.e. $\mathbf{p}_i \equiv \hat{\mathbf{u}}_i$. The polarisation is then obtained simply by summing the orientation vectors of all the particles in the system

$$P_\alpha^{(s)} = \sum_i^N \hat{\mathbf{u}}_\alpha^{i(s)} \quad (5.20)$$

The components of the stress tensor and the polarisation, along with the director components, are written to file at regular intervals. These stored data are subsequently processed to obtain the response function and, thence, the flexo coefficients. Given the finite system size and limited simulation time, the response function $E_{\alpha\beta\gamma}$ must be approximated by a time average

$$E_{\alpha\beta\gamma} = -\frac{\beta}{V} \langle P_\alpha \Pi_{\beta\gamma} \rangle \approx -\frac{1}{N_{data}} \frac{\beta}{V} \sum_n^{N_{data}} \left(P_\alpha^{(n)} \Pi_{\beta\gamma}^{(n)} \right) \quad (5.21)$$

where N_{data} is the number of lines of data saved to file. Finally e_{11} and e_{33} can be calculated using the expressions derived using the linear response approach described in the previous section i.e.

$$\begin{aligned} e_{11} &= -\frac{1}{2} E_{\alpha\beta\gamma} \epsilon_{\mu\beta\gamma} \hat{n}_\gamma \hat{n}_\mu \\ e_{33} &= +\frac{1}{2} E_{\alpha\beta\gamma} \epsilon_{\alpha\beta\mu} \hat{n}_\alpha \hat{n}_\mu \end{aligned}$$

In fact three modes of processing were implemented to arrive at the response function:

1. $E_{\alpha\beta\gamma}$ was calculated from $P_\alpha^{(s)}$ and $\Pi_{\alpha\beta}^{(s)}$ expressed in the usual lab-based coordinate frame.
2. $E_{\alpha\beta\gamma}$ was calculated from $P_\alpha^{(s)}$ and $\Pi_{\alpha\beta}^{(s)}$ after the latter were rotated into a director-based coordinate frame; this is essentially the method followed in [34–36].

3. $E_{\alpha\beta\gamma}$ was calculated from the covariants of the director-based polarisation and stress tensor. The covariants are defined as $(P_\alpha^{(s)} - \overline{P_\alpha})$, $(\Pi_{\alpha\beta}^{(s)} - \overline{\Pi_{\alpha\beta}})$ where the overline indicates the time average. This follows the procedure used in [36].

Regarding the second mode of processing, it is not clear from the literature whether rotating the polarisation and stress tensor into the director frame is actually a *necessary* feature of the linear response approach as applied to this type of system. References [34–36] merely allude to the change of coordinate system as being *convenient*. It is certainly true that switching to the director frame simplifies the expressions for e_{11} and e_{33} , for if we rotate \mathbf{P} and $\mathbf{\Pi}$ into the director frame so that $\hat{\mathbf{n}} = \hat{\mathbf{z}}$ we have $\hat{n}_x = 0$, $\hat{n}_y = 0$ and $\hat{n}_z = 1$. Then, in summing over the indices $\alpha, \beta, \gamma, \mu$ to obtain e_{11} , we find that the summation contributes only when $\alpha = \mu = z$ and $\hat{n}_\alpha \hat{n}_\mu = \hat{n}_z \hat{n}_z = 1$. Furthermore the Levi-Civita tensor elements are non-zero for just two permutations of $z\beta\gamma$ namely $\epsilon_{zxy} = 1$ and $\epsilon_{zyx} = -1$ thus

$$\begin{aligned} e_{11} &= -\frac{1}{2} E_{\alpha\beta\gamma} \epsilon_{\mu\beta\gamma} \hat{n}_\gamma \hat{n}_\mu \rightarrow -\frac{1}{2} E_{z\beta\gamma} \epsilon_{z\beta\gamma} = -\frac{1}{2} (E_{zxy} - E_{zyx}) \\ &= \frac{\beta}{2V} (\langle P_z \Pi_{xy} \rangle - \langle P_z \Pi_{yx} \rangle) \quad (5.22) \end{aligned}$$

In a similar fashion, the bend flexo coefficient reduces to

$$\begin{aligned} e_{33} &= \frac{1}{2} E_{\alpha\beta\gamma} \epsilon_{\alpha\beta\mu} \hat{n}_\alpha \hat{n}_\mu \rightarrow \frac{1}{2} E_{\alpha\beta z} \epsilon_{\alpha\beta z} = \frac{1}{2} (E_{xyz} - E_{yxz}) \\ &= \frac{\beta}{2V} (\langle P_y \Pi_{xz} \rangle - \langle P_x \Pi_{yz} \rangle) \quad (5.23) \end{aligned}$$

The simulation technique described above was applied to a number of monodisperse N10000 $\kappa 3$ systems, namely $\kappa 3$ $k_\theta = \{5.0, 6.0, 7.0, \infty\}$. The expectation was that the value of e_{11} calculated would be greater for particles with more pronounced taper, i.e. those with lower k_θ value. For the $k_\theta \infty$ particles, we would anticipate e_{11} being approximately zero, since these particles are uniaxial. The

$\kappa 5k_{\theta} 5.0$ system was also studied to see if an increase in aspect ratio would have any noticeable impact on the flexoelectric properties. Each of the above systems was also studied for a range of densities to try to uncover trends in e_{11} as a function of order parameter, since the value of P_2 in these systems increases with density. In all cases, the observed value of e_{33} would be expected to be negligible since tapered particles do not intrinsically possess the required shape necessary to engender bend flexoelectric behaviour.

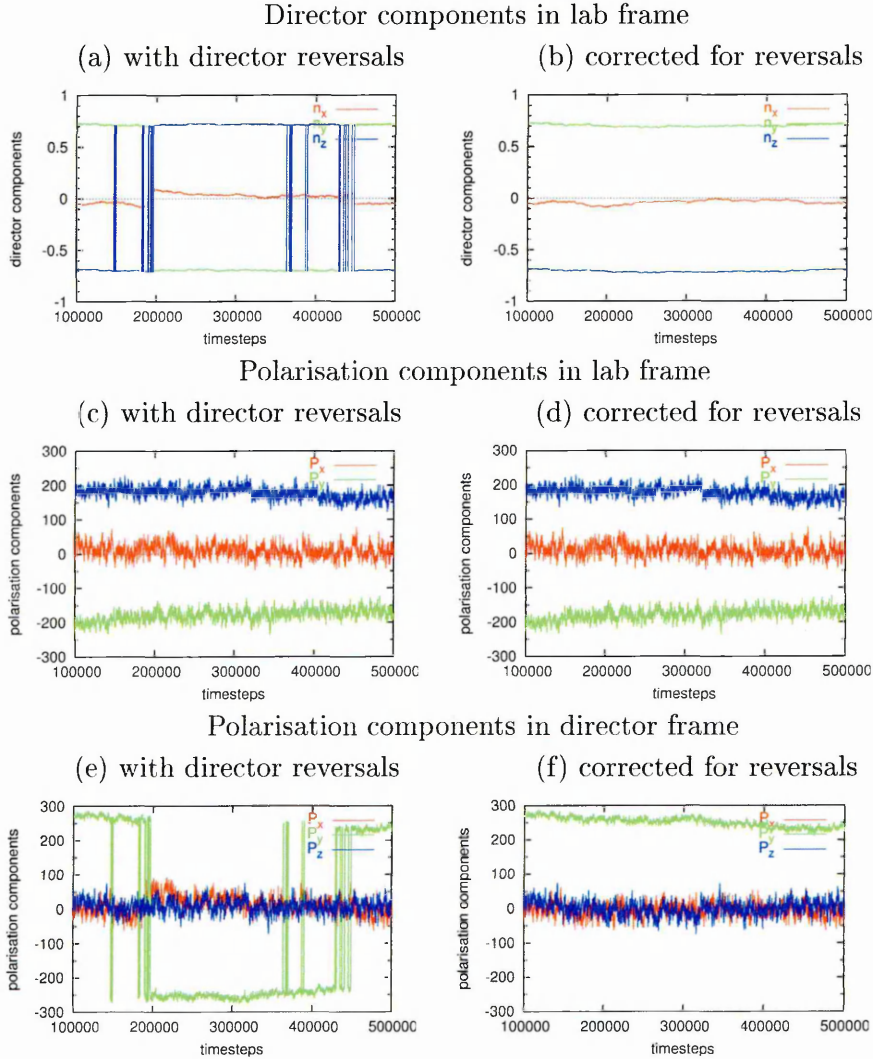
The systems were prepared by first performing isotropic compression runs in *NVT* of smaller systems of 1250 particles. The simulation method used here was similar to that followed for the preliminary simulations, described in section 4.1. The $\kappa 3$ systems were first compressed from FCC starting configurations at $\rho = 0.15$ to a density of 0.75, at which the system is an isotropic fluid. Compression was then gradually continued from $\rho = 0.75 - 1.15$ in a sequence of 1000kstep runs taking the system into the nematic phase. For the $\kappa 5k_{\theta} 5.0$ system, the initial fast compression was from $\rho = 0.15 - 0.30$ it was then compressed gradually to $\rho = 1.00$ in a sequence of 500kstep runs. End configurations from various points in these compressions were then tessellated to generate the N10000 systems as required for the flexoelectric studies. This was achieved simply by replicating the N1250 systems 8 times and joining the configurations together. This enlargement was performed in order to ensure that statistics of sufficient quality were obtained in order to make accurate calculations of the flexoelectric coefficients. These systems were then run on in *NVE* for 500ksteps (or 0.5Msteps). The first 100 ksteps were reserved for equilibration, in particular to allow the periodicity engendered by the scaling up procedure to fade away. For the remainder of the run, data and configurations were regularly saved. In particular, the instantaneous values of the director, polarisation and stress tensor were recorded every 10 time steps thus providing 40,000 data points for the subsequent analysis.

5.3 Results of 0.5 Mstep simulation runs

Before discussing the results obtained for the 0.5 Mstep runs, a practical issue that arose during the data processing should be mentioned. The director \hat{n} defines the axis of symmetry of a nematic phase, a symmetry that is invariant under a rotation of 180° . Therefore, as far as nematic order is concerned, it is irrelevant which way along the the symmetry axis the director points. Consequently, it is not uncommon for the director, as calculated via the diagonalisation of the Q-matrix, (see section 3.3), to flip polarity from time to time in the course of a simulation: This has an important practical implication in relation to the calculation of the flexo coefficients using covariants, as we will now illustrate. Figure 5.2(a) shows data from the simulation of the $\kappa 5k_\theta 5.0$ system at a density of $\rho = 0.47$; the average order parameter value at this density being $\bar{P}_2 = 0.834$ (to 3 d.p.). The lab-frame director components presented in panel (a) clearly exhibit spontaneous sign reversals. Meanwhile the polarisation in the lab-frame, as shown in figure 5.2(c), naturally remains steady, since it is the sum of the orientation vectors of the individual particles, which cannot of course change direction in an instant. However, the rotated components, of the director-frame polarisation shown in figure 5.2(e)) *are* subject to the same reversals in sign as the director. Director flips are therefore compensated for by monitoring the sign of the largest director component as each line of the (lab-based) simulation data is read by the processing programme. A change in sign of this component occurring between consecutive logging intervals could only be caused by a reversal in director polarity. If such a flip is registered, a counter sign-change is automatically imposed until such time as the director reverses once more and in doing so reverts back to its original polarity. Figure 5.2(b) shows the director components after having been compensated for in this manner. The result is the set of stable director-frame polarisation components shown in figure 5.2(f).

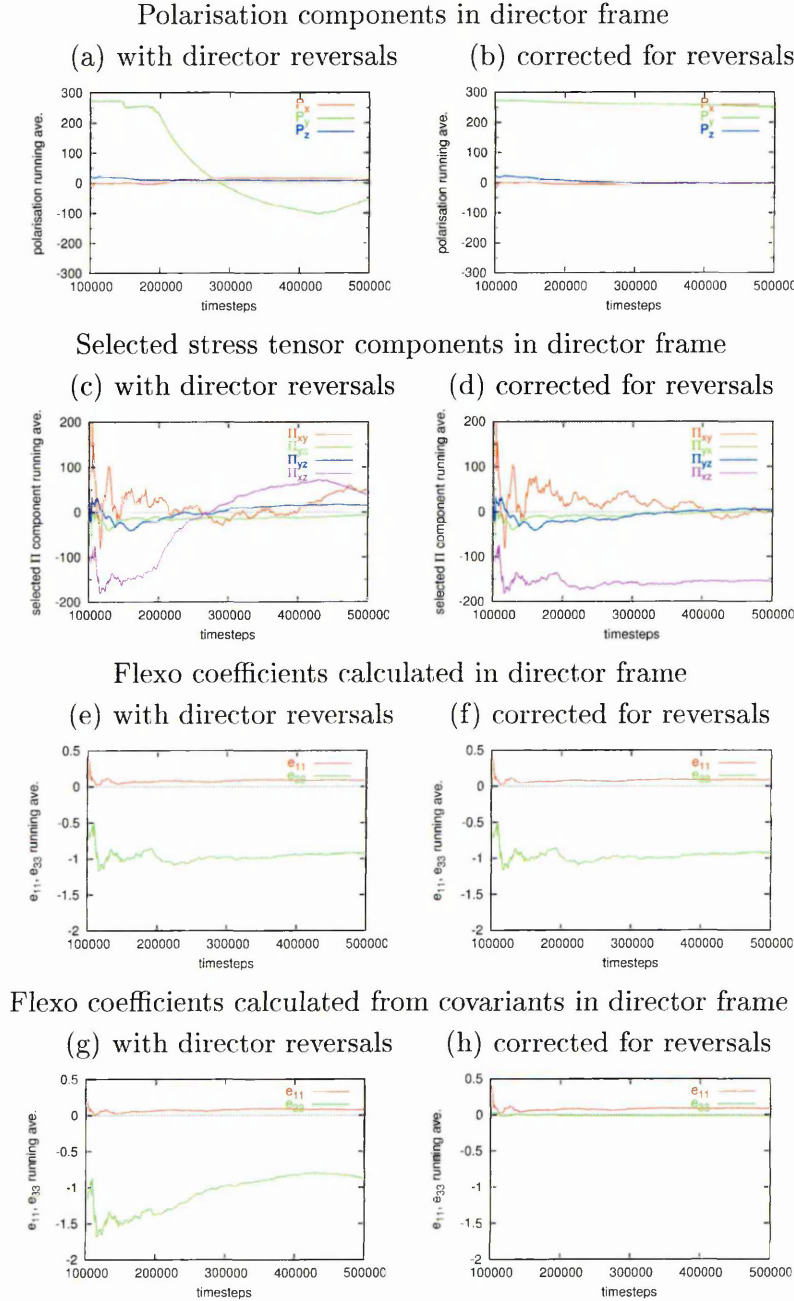
Figure 5.3 (a) to (f) show that, although director flips affect the polarisation and stress tensor components and hence their respective time averages, the flexo co-

Fig. 5.2: Time series data of the director and polarisation over the course of a 0.5Mstep run for $\kappa 5 k\theta 5$ system at $\rho = 0.47$ ($\bar{P}_2 = 0.834$). Plot (a) shows the spontaneous reversals that occur in the polarity of the director and (e) how this is passed on to the polarisation components when they are rotated into the director frame. Plot (b) shows the director after compensation has been made for the reversals and (f) the resulting stable polarisation.



efficients calculated from their *instantaneous* values either with or without compensation are identical. This is because e_{11} and e_{33} are scalars and, therefore, intrinsically immune to any change of reference frame – it makes no difference whether the calculation is made in the \hat{n} or $-\hat{n}$ frame. However, when the flexo coefficients are calculated from the covariants $(P_\alpha^{(s)} - \bar{P}_\alpha)$ and $(\Pi_{\alpha\beta}^{(s)} - \bar{\Pi}_{\alpha\beta})$, failure to compensate for director reversals can have a profound effect on the values calculated for them, the reason being that the time averages of the polarisation

Fig. 5.3: Running averages of polarisation, stress tensor components and flexo coefficients calculated over the course of a 0.5Mstep run for $\kappa 5 k_{\rho} 5$ system at $\rho = 0.47$ ($\bar{P}_2 = 0.834$). The plots on the right are derived from data in which director reversals have been compensated for whereas for those on the left no corrections were applied.



and stress tensor are involved. For the particular case illustrated in figure 5.3, there is a marked disparity between the values obtained for e_{33} with and without compensation for director reversals. The corresponding values of e_{11} on the other hand are only marginally different. This is due mainly to the fact that, in this par-

ticular case, P_y happens to have a large magnitude in the director frame whereas P_z remains close to zero throughout the simulation. Recall from equations 5.22 and 5.23 that in the director frame e_{33} depends on P_x and P_y whereas e_{11} depends only on P_z . It goes without saying that in all subsequent results presented in this chapter, director sign changes have been compensated for.

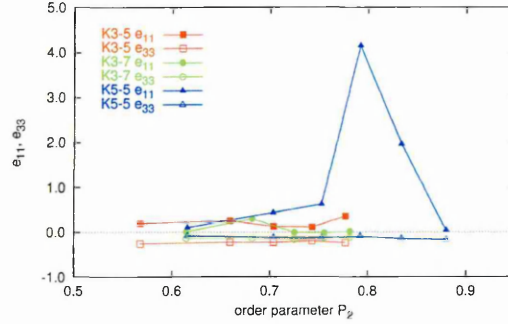
We return now to our chief concern – the attempt to uncover physically meaningful trends in the values of e_{11} and e_{33} . Figure 5.4 shows the coefficients calculated for the $\kappa 3k_\theta 5.0$, $\kappa 3k_\theta 7.0$ and $\kappa 5k_\theta 5.0$ systems as a function of order parameter. The corresponding numerical data appear in table F.2, of appendix F. The main observations are that the e_{11} values are nearly all positive whilst the e_{33} values are nearly all negative. We also find that both coefficients generally have similar magnitudes of the order of 0.1. Notable exceptions are the two large e_{11} values calculated in the lab-frame for the $\kappa 5k_\theta 5.0$ system and the corresponding e_{33} values calculated in the director-frame. Taking covariants would appear to eliminate these extreme values but, overall, the spread of data points is still too large to infer any physically meaningful trends from the results. Moreover the magnitudes of the e_{33} values are by and large still comparable to those of the e_{11} s. This runs contrary to our assumption that tapered particles should not possess bend flexoelectric properties due to their axial symmetry.

Figure 5.5 shows the flexoelectric coefficients calculated for the rod-like $\kappa 3k_\theta \infty$ systems. Since $\kappa 3k_\theta \infty$ particles lack a steric dipole we would expect both e_{11} and e_{33} calculated for these systems to be approximately zero. However comparing the results from these simulations with those obtained from the tapered particles, we find that the coefficients calculated for rodlike particles are in general roughly of a similar magnitude to those obtained for the tapered particles, if not larger. This manifestly unphysical trend strongly suggests that either there is a fundamental oversight inherent in the linear response approach as applied to this type of system, or else the statistics obtained from the simulations are not good enough to produce sufficiently accurate results.

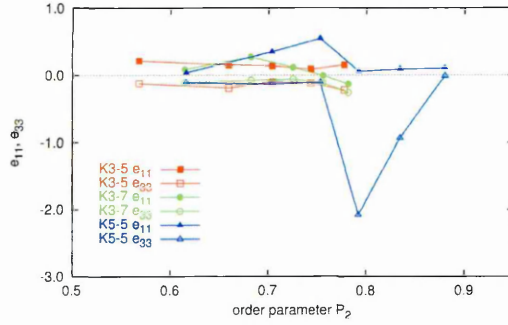
In order to better assess whether the latter was the case, the time series data from

Fig. 5.4: Flexoelectric coefficients calculated from 0.5 million step runs for various systems of tapered particles.

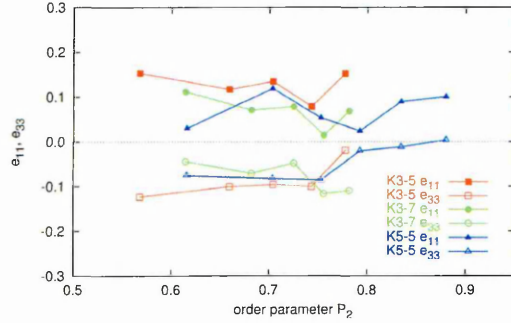
(a) as determined in the lab based frame



(b) as determined in the director frame

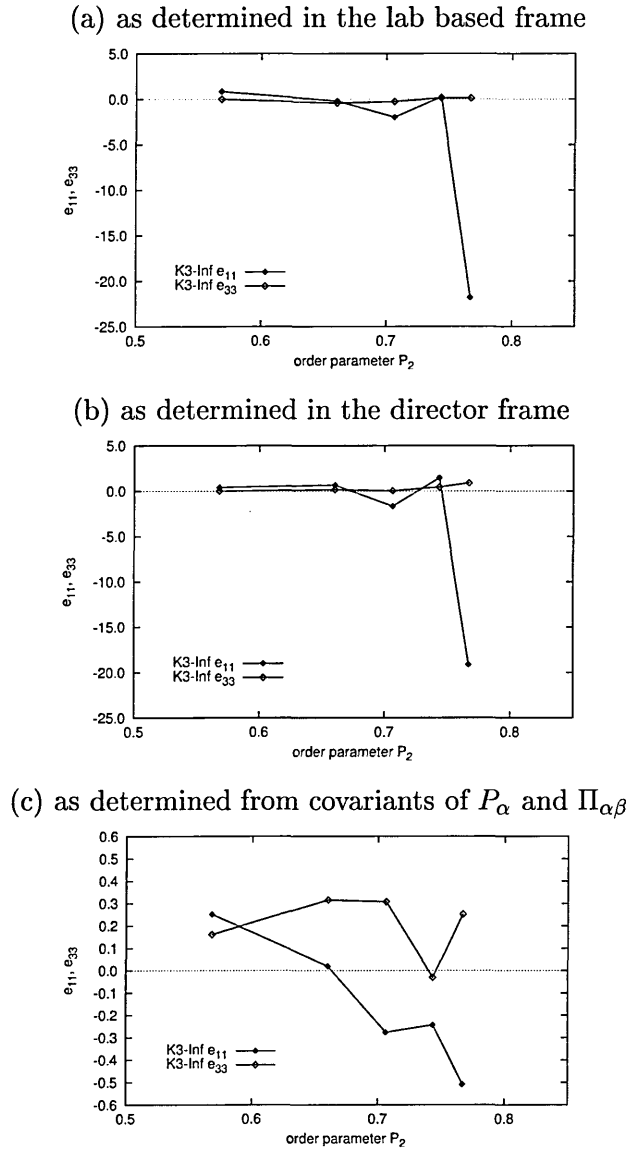


(c) as determined from covariants of P_α and $\Pi_{\alpha\beta}$



the $\kappa 3k_\theta \infty$ system at $\rho = 0.945$ (corresponding to $\bar{P}_2 = 0.767$), were examined in more detail. Out of all the 0.5Mstep simulations, this one gave the highest e_{33} value as calculated from covariants. Figure 5.6 shows the polarisation components and selected stress tensor components, as calculated from this simulation in the director frame, over intervals of 100, 1000, 10000 and 100000 timesteps. First of all we note that the character of the fluctuations in the polarisation and the stress tensor differ markedly from each other. The polarisation exhibits fluctuations of a relatively low frequency and small amplitude whereas the stress tensor shows

Fig. 5.5: Flexoelectric coefficients calculated from 0.5 million step runs for the $\kappa 3 k_{\theta}\infty$ system.



higher frequency fluctuations of a much larger amplitude. Another crucial difference is that the polarisation components remain fairly steady over the course of the run and, in this particular case P_z also remains far from zero. The stress tensor components on the other hand cross the horizontal axis many times in the course of a run, although, as figure 5.7 (b) shows, the running averages of the stress tensor components Π_{xy} and Π_{yx} actually retain negative and positive signs respectively for most of the run. Recall that when e_{11} is calculated within the director frame it depends only on P_z , Π_{xy} and Π_{yx} .

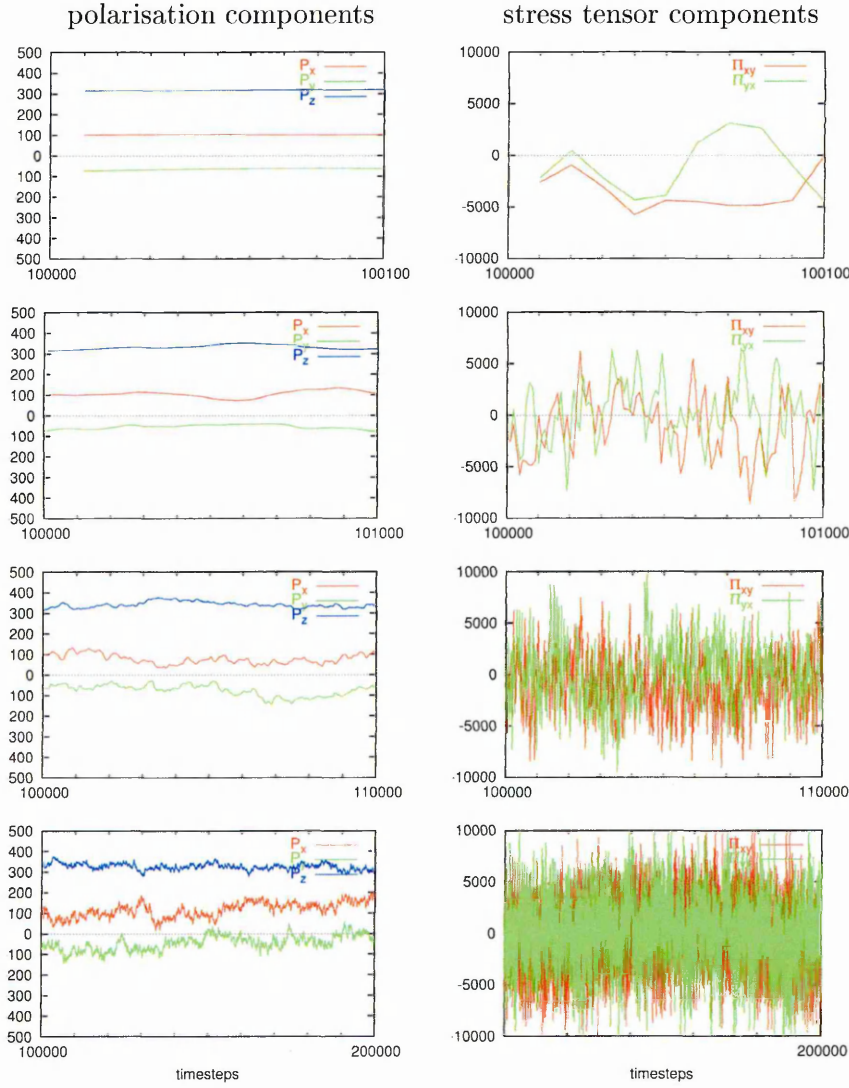
$$e_{11} = -\frac{1}{2}(E_{zxy} - E_{zyx}) = \frac{\beta}{2V}(\langle P_z \Pi_{xy} \rangle - \langle P_z \Pi_{yx} \rangle)$$

This being so and given that P_z remains fairly steady, it follows that the running average of the splay flexo coefficient should be closely related to the difference $\Pi_{xy} - \Pi_{yx}$. This is evidenced by the noticeable correlation between the running average of $\Pi_{xy} - \Pi_{yx}$ and that of e_{11} seen in figure 5.7. It is also worth commenting that, since P_z remains large and positive throughout the course of this particular run, it is not so surprising to find that the value of e_{11} calculated from the covariants $(P_z - \overline{P_z})$, $(\Pi_{xy} - \overline{\Pi_{xy}})$ and $(\Pi_{yx} - \overline{\Pi_{yx}})$ is considerably smaller than that determined from correlations of the unaltered instantaneous values. This does not necessarily mean that taking covariants will improve the accuracy of the calculation. Such an approach would only succeed in instances when the key observables are subject to a *steady state* bias. However, the time series data hint that the polarisation and/or the stress tensor components may be suffering fluctuations/drift of a somewhat random nature over time scales comparable to or greater than the 0.5Mstep simulation duration. This might account for the lack of meaningful trends observed in figures 5.4 (c) and 5.5 (c). With this in mind, a series of longer simulations was carried out in the hope that the improved statistics would result in better convergence of the flexo coefficients. The starting points for these runs were the end configurations from the 0.5Mstep runs.

5.4 Results of 10 Mstep simulation runs

Before discussing the results of the 10 Mstep runs it is worth highlighting another practical point, this time relating to the size of the data sets generated by these longer simulations. In the initial 0.5 Mstep runs, flexoelectric data were saved every 10 timesteps with double float precision resulting in datafile sizes of approximately 50Mb per run. This is a rather large file size but it is still relatively easy to move or copy the file to a different location. Also inspection or plotting of the

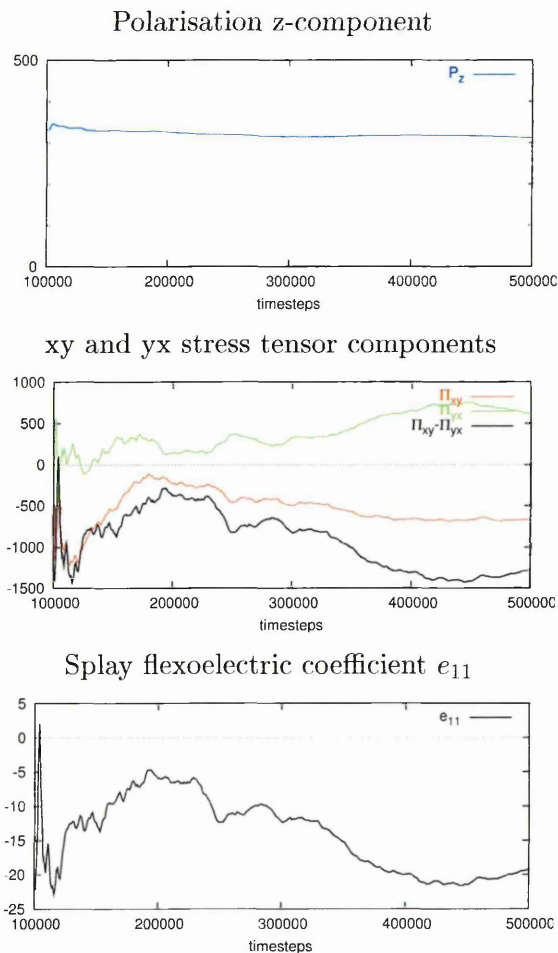
Fig. 5.6: Director frame time series data for $\kappa 3 k_{\theta \infty}$ system at $\rho = 0.945$ ($\bar{P}_2 = 0.767$) plotted over intervals of 100, 1000, 10000 and 100000 timesteps.



data using standard Linux applications did not present any difficulties. However files of a similar format generated by 10Mstep runs were around a gigabyte in size and these turned out to be cumbersome to move around. Moreover it was impractical to routinely inspect or plot the data. The files were therefore reformatted into a more manageable format as follows.

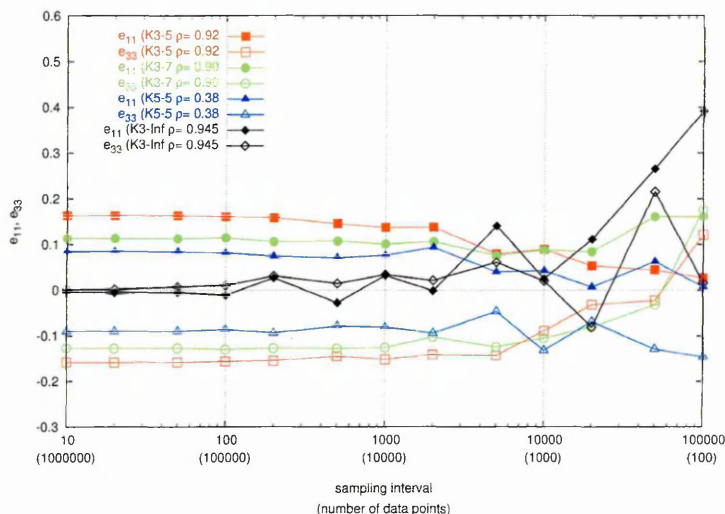
Firstly the twenty seven response function components recorded during the simulation were removed from the files since these can always be calculated later from P_α and $\Pi_{\alpha\beta}$ if required. Also the $E_{\alpha\beta\gamma}$ recorded at run time were calculated in the

Fig. 5.7: Running averages accumulated during the 0.5Mstep simulation of the $\kappa_3 k_{\theta\infty}$ system at $\rho = 0.945$ ($\bar{P}_2 = 0.767$).



lab based frame but we are more interested in the values of observables calculated in the director frame. Secondly the precision of the numbers was reduced to six decimal places, this has a negligible effect on the final averages calculated since the decimal part of the instantaneous values of the observables is insignificant relative to the fluctuations in these observables. Thirdly the data was sampled at one tenth of the frequency at which the original data was saved i.e. in the reformatted files data appears at intervals of 100 time steps as compared to 10 timesteps in the original file. To check that this would not significantly affect the results of calculations made from the data, the e_{11} and e_{33} were calculated for a range of sampling intervals as shown in figure 5.8. Clearly an increase in the sampling interval from 10 to 100 (which in this case reduces the number of data

Fig. 5.8: Effect of sampling interval on the calculated flexoelectric coefficients for a range of systems run over 10 Msteps.



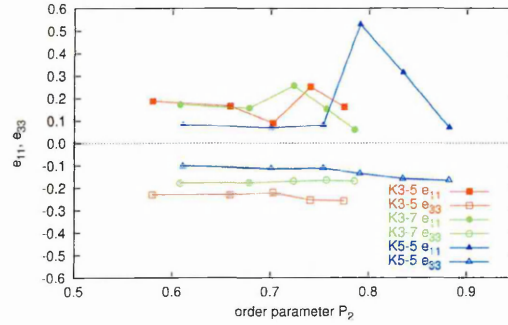
points from 10^6 to 10^5) does not have much impact on the calculated averages.

It should be added that reformatting all the data from the 10Mstep runs and ensuring that they were not, through some oversight or error, distorted in the process, was not a trivial task and contributed significantly to the work load involved in this part of the research. It illustrates that, whilst ensuring that all important information is saved during simulation time, one should also be mindful of the effort and possible technical difficulties associated with subsequently processing that information.

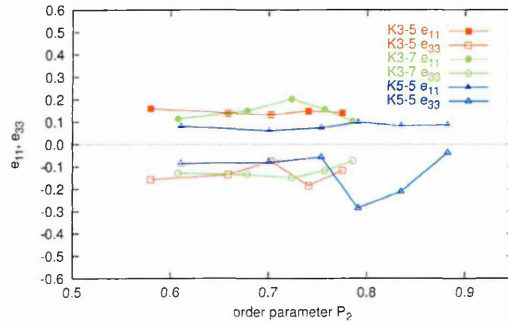
The coefficients, as determined from the 10 million step runs, for the tapered particle systems are shown in figure 5.9. Whether calculated in the lab-frame, the director-frame or by covariants (which are also based in the director-frame), there are no conspicuously wayward values as were seen for some of the calculations based on the 0.5 Mstep runs. We note also that there is little difference between the director-frame and covariant based datasets shown in figures 5.9 (b) and (c) respectively. Furthermore, the e_{11} s and e_{33} s determined from the covariants obtained from the 10 Mstep runs are of a similar order of magnitude to the corresponding ones determined from the 0.5 Mstep runs. The spreads in the datasets from the two sets of simulations are also comparable so, despite the

Fig. 5.9: Flexoelectric coefficients as calculated from 10 million step runs for various systems of tapered particles.

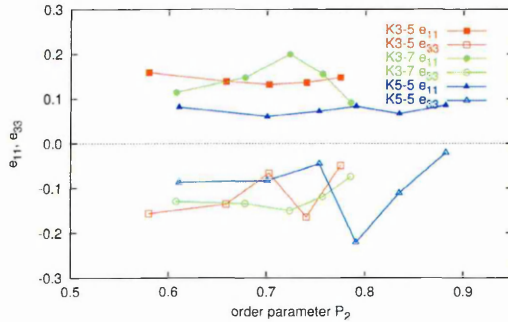
(a) as determined in the lab based frame



(b) as determined in the director frame



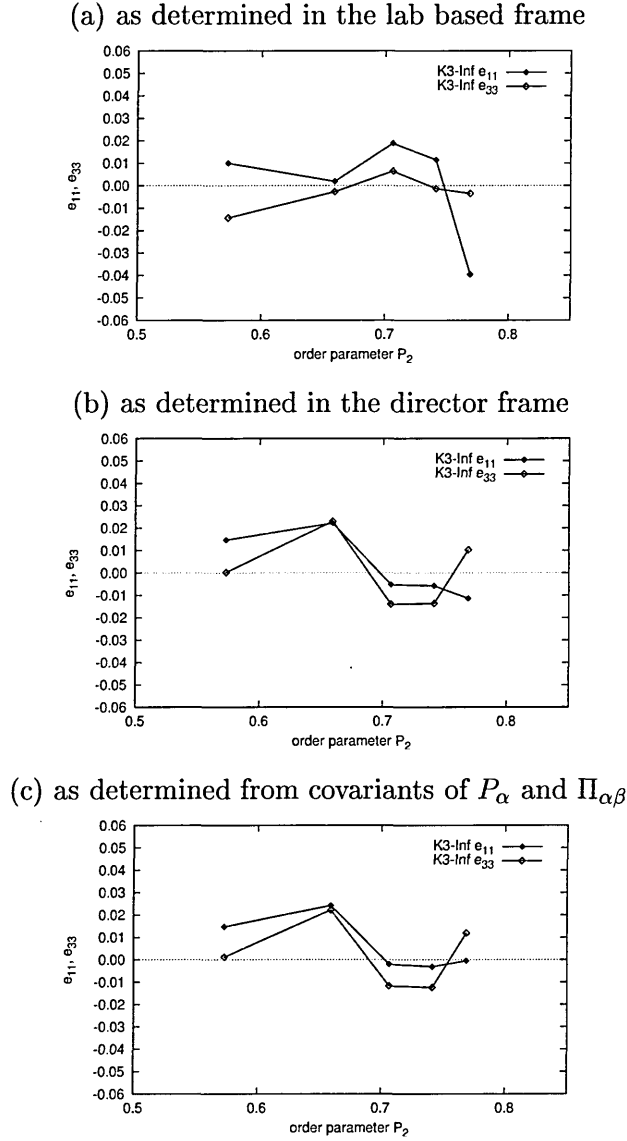
(c) as determined from covariants of P_α and $\Pi_{\alpha\beta}$



longer simulation times, clear physical trends in the values are still not apparent. The coefficients calculated from the $\kappa 3k_\theta \infty 10$ Mstep simulations, by all methods of calculation, are all smaller than the 0.5 Mstep values by at least an order of magnitude. This gives some hope that longer simulation times may result in more accurate calculation of the flexo coefficients.

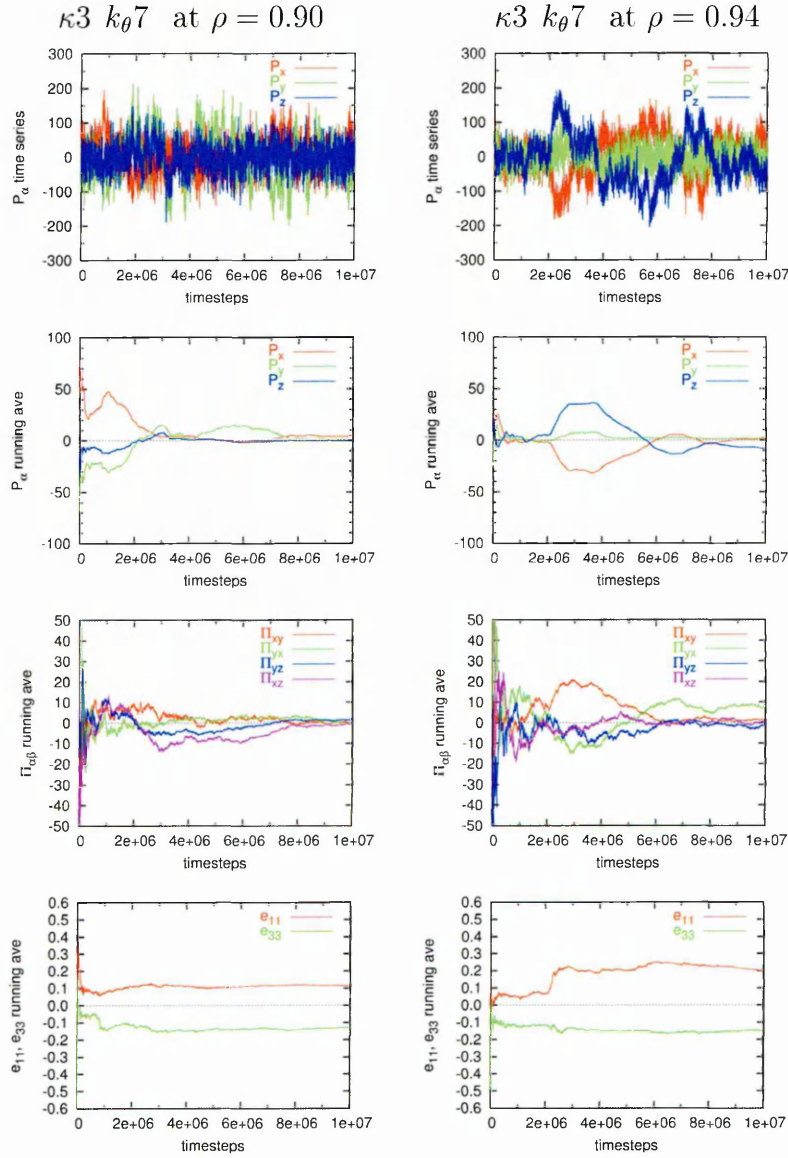
Looking at the running averages from some of the simulations, as calculated from the director-based polarisation and stress tensor (without the average subtracted

Fig. 5.10: Flexoelectric coefficients as calculated from 10 million step runs for the $\kappa 3k_\theta\infty$ systems.



i.e. these data are *not* computed from the covariants of P_α and $\Pi_{\alpha\beta}$), there is a suggestion that the coefficients are converging towards steady values. For example, the e_{11} and e_{33} running averages for the $\kappa 3k_\theta 7.0$ system at $\rho = 0.90$, shown on the bottom left panel of figure 5.11 are stable throughout most of the run and nearly flat for the last 400 ksteps or so. The final averages are approximately +0.1 and -0.1 respectively. In contrast, for the same type of system at a slightly higher density of $\rho = 0.94$, the running average of e_{11} undergoes a relatively large and rapid increase at 200 ksteps as shown in the bottom right panel of figure 5.11.

Fig. 5.11: 10 Mstep time series and running averages of polarisation along with and running averages of selected stress tensor components and the running averages of flexo coefficients as calculated in the director-frame.



This shift seems to be correlated with large changes in the polarisation. It appears to have a major influence on the final value of e_{11} , which is approximately double the value obtained for the lower density system.

5.5 Summary and Conclusions

The flexoelectric coefficients have been calculated for systems of particles with a variety of degrees of taper and across a range of densities, and thus a range of average order parameter values. The values of e_{11} and e_{33} as determined from director-based polarisation and stress tensor components collected in the course of simulations of 10 million steps duration are consistently of the order of $\sim +10^{-1}$ and $\sim -10^{-1}$ respectively. To assess whether these values correspond favourably with the values typically measured experimentally for molecular liquid crystals, we define a basic unit, \mathbf{p}_0 , for the dipole moment having a value of $1\text{Debye} = 3.336 \times 10^{-30}\text{Cm}$ and assume that its diameter σ_w is 5\AA , these values are of the appropriate order of magnitude. The relationship between the flexoelectric coefficients as measured in real units and its reduced equivalent is

$$e_{ii} = \frac{\mathbf{p}_0}{\sigma_w^2} e_{ii}^* \quad (5.24)$$

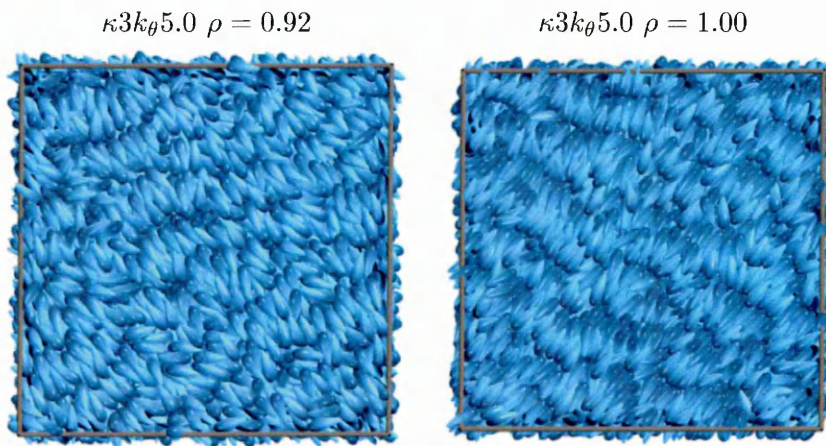
Substituting the values of \mathbf{p}_0 and σ_w into this equation along with the order of magnitude of our calculated reduced flexoelectric coefficients, we obtain $e_{ii} \approx 6.7 \times 10^{-12}\text{Cm}^{-1}$. This is indeed similar to the type of magnitude measured for the flexo coefficients of real liquid crystals. This gives us some confidence that the method and its implementation in our simulations is basically sound. Also, control studies, as it were, were carried out on systems of rod-like particles. Symmetry dictates that both coefficients for these systems should be zero within experimental error margins. In the longest simulation runs performed, the calculated values do indeed appear to be tending to zero. However, despite the length of the runs and the relatively large systems of 10000 particles used, no clear meaningful trends in the coefficients, either as a function of shape or of order parameter have emerged from the data. Comparison of the running averages of the key quantities calculated in the simulations (see figure 5.11) suggest that long period fluctuations in the polarisation may be biasing the results. An obvious extension to the work reported here would be therefore be to run for even longer times to see if

sufficiently long simulations have the effect of smoothing out the effects of these fluctuations. Another approach would be to Fourier transform the polarisation and stress tensor components and subtract the low frequency components before calculating the flexo coefficients, although that does raise the question as to how much of the frequency spectrum should be filtered out.

The observed fluctuations may have something to do with the nature of the simulated nematic phase itself. In fact as figures 5.12 show, the nematics formed by the moderately tapered particles studied here, have something of a smectic character about them. The particles have a tendency to interdigitate and form what might be regarded as loose domain-like associations. Perhaps it is the formation and breaking up of these domains that causes the fluctuations in the properties relating to the flexo coefficients. In fact it is probably true to say that the properties of these nematic phases should have been studied more thoroughly before attempting to derive values for the flexo coefficients from them.

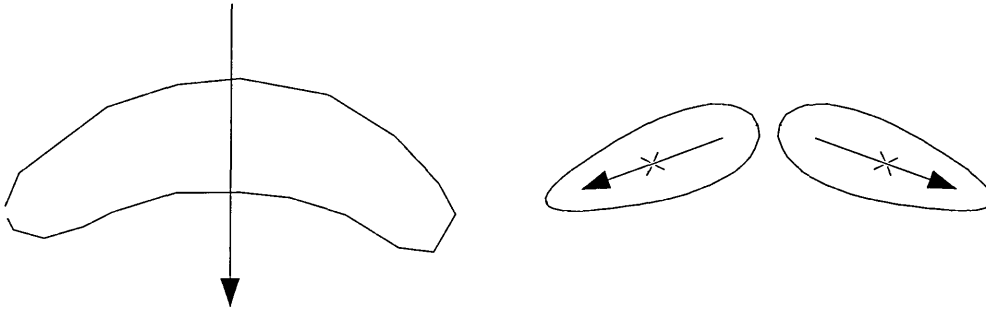
Finally, the consistently finite and negative value calculated for e_{33} needs to

Fig. 5.12: Snapshots of the $\kappa 3k_{\theta} 5.0$ half way through the 10Mstep runs.



be explained. Tapered particles of the type used in our simulations should not be intrinsically capable of imbuing the system with a bend flexoelectric character. However detailed interrogation of appropriate distribution functions suggests that pairs of particles have a preferred azimuthal angle as shown schematically in figure 5.13. The Collectively two particles in this arrangement resemble the

Fig. 5.13: Schematic showing an arrangement of a pair of tapered particles that resembles a single banana-shaped particle.



banana-shaped particles depicted in 5.1 (c) and (d). It is known that pairs of liquid crystal molecules tethered to each other, so-called bimesogens, can exhibit bend flexoelectricity and that the extent to which they do depends partly on the average angle subtended by the long axes of their two halves, see for example [38]. It is possible that the pairs of particles in our simulations behave, albeit transiently, like bent bimesogens and this may explain the finite values calculated for e_{33} .

CHAPTER 6

General phase behaviour

This chapter draws together the results of a set of simulations carried out on systems of 1250 κ 3 particles with varying degrees of tapering. These studies revisit the phase diagram mapping carried out by Barmes et al. [14], which we review in the first section. The second section describes the phase transitions that were observed in our own MD simulations when the systems were compressed from initial low density configurations. For the most part, the methods used to interrogate the results follow along the lines of those described in chapter 4 describing the preliminary simulations. Broadly the phase diagram from compression was found to consist of three distinct regions in qualitative agreement with the work of Barmes et al. At low k_θ values, there is a direct transition from the isotropic to the smectic phase which eventually freezes at high density. At high k_θ values, the systems undergo first an isotropic-nematic transition which subsequently transforms into a smectic and freezes at high density. Although, for k_θ values of 6.0 or so and above, the N-Sm transition virtually coincides with the freezing point. In the central portion of the phase diagram, we again encounter what Barmes termed the ‘domain-ordered’ (DO) phase although here we rechristen it the ‘curvy-bilayer’ (CB) phase. In order to confirm that the curvy-bilayer is a genuine phase and not

merely a metastable state i.e. a frustrated smectic phase, we generated so-called ‘artificial’ smectic configurations which were subsequently expanded to obtain the phase diagram from decompression. The artificial smectics were derived from a repeat compression of one of the systems that entered the CB phase but with an orienting field applied along the z-axis, which encourages the particles to align in that direction and, at high density, assemble into smectic bilayers. This procedure is described in more detail in section 3. The fourth section draws together the results of the decompression simulations. The chapter concludes with a general appraisal of the phase diagrams obtained and suggestions for further work that could be carried out both to refine them and to lead to a better understanding of the fundamental drivers of the phase behaviour of tapered particles.

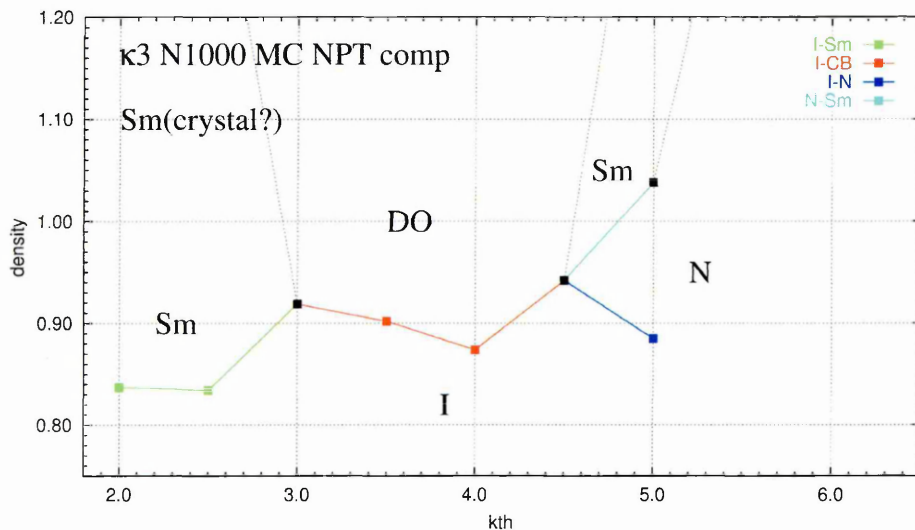
6.1 Phase diagram from MC simulations

Barnes et al. had previously carried out MC simulations of hard $\kappa 3k_\theta 3.0$, $\kappa 4k_\theta 4.0$ and $\kappa 5k_\theta 5.0$ particles [14]. These made use of the same PHGO contact function as was used in our MD simulations of soft-repulsive particles. Subsequently a series of similar simulations were performed for hard $\kappa 3$ particles across a range of k_θ values (unpublished), the results of which were used to map out a $k_\theta - \rho$ phase diagram. The simulation methodology for these studies is now summarised.

Systems of 1000 particles were compressed in a series of *NPT* runs from initial low density configurations in which the distributions of particle orientations were isotropic. The equilibration and production phases of the runs consisted of 0.5-1.0 million MC ‘sweeps’ (a sweep consisting of one attempted MC move for every particle in the system). The types of moves attempted were standard translations and rotations as well as a orientation inversions, which constituted 20% of the attempted moves. A form of anisotropic rescaling was employed which involved volume changes was attempted, on average, once every two sweeps by allowing each box dimension to change independently. The resulting phase diagram is

presented in figure 6.1 For particles with k_θ values of between 2.0 and 3.0, a transition from the isotropic to an interdigitated smectic A phase was observed upon compression. For intermediate values, $k_\theta = 3.0 - 4.5$, a transition into a so-called domain-ordered (DO) phase was observed so called because it was characterised by localised smectic like order but lacked long range order. This

Fig. 6.1: Phase diagram obtained from Monte Carlo *NPT* compressions of systems of 1000 $\kappa 3$ hard particles [14]. The diagonal dashed black lines are estimated phase boundaries.



was apparent from snapshots of the simulation box and was also confirmed by low order parameter values as well as the decay of the peaks in molecule-centred correlation functions. There was some uncertainty as to whether this DO structure was a genuine phase or a metastable state. Resolution of this issue was one of the motivations for carrying out further investigations of the $\kappa 3$ phase diagram by way of the MD simulations. At the high end of the k_θ scale, the system first underwent an I-N transition followed by an N-SmA transition.

6.2 Phase diagram from compressions

The initial configurations for the compressions consisted of 1250 particles arranged, as usual, on an FCC lattice at a density of $\rho = 0.20$. These were rapidly

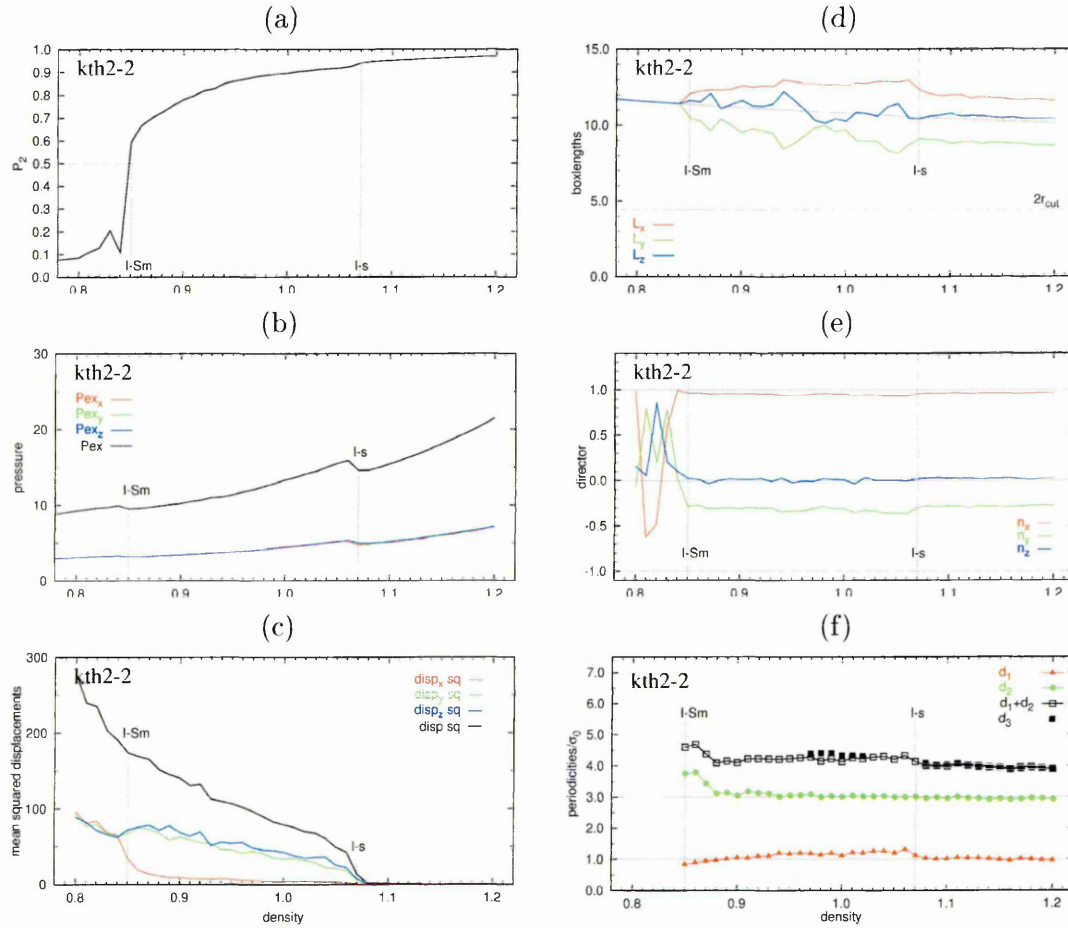
compressed to $\rho = 0.80$ by increasing the density in increments of $\Delta\rho = 0.001$ every 100 timesteps. The systems were then compressed to $\rho = 1.10$ via a sequence of 1000 kstep runs in each of which the density was increased by 0.01. This change of density was applied gradually by small increases of $\Delta\rho = 0.00001$ every 100 timesteps over the interval 100-200ksteps.¹ From 500-1000ksteps, averages were accumulated and configurations stored periodically. Additional runs were later carried out to compress the systems further to $\rho = 1.20$ in order to ensure that the liquid-solid transitions were properly captured. Anisotropic rescaling was applied to all of the systems, the density at which rescaling was switched on was generally chosen to coincide approximately with the onset of smectic or CB phases, based on the experience of previous simulations. Compressions were carried out for the following set of shape parameter values: $k_\theta = 2.0, 2.2, 2.4, 2.5, 2.6, 2.8, 3.0, 3.2, 3.4, 3.5, 3.6, 3.8, 4.0, 4.2, 4.4, 4.5, 4.6, 4.8, 5.0, 5.2, 5.4, 5.6, 6.0, 10.0, 50.0, \infty$. Recall that with increasing k_θ value, the degree of tapering of the particles decreases; in the limiting case of $k_\theta = \infty$ the particle is essentially uniaxial. A similar compression series for a system of $\kappa 3$ soft-repulsive Gaussian ellipsoid particles (K3 rods for short) was also performed for the purposes of comparison with the $\kappa 3k_\theta\infty$ ‘pears’ simulation.

On compression, the k_θ 2.0 and 2.2 systems were found to enter the smectic phase directly at densities of $\rho = 0.82$ and 0.85 respectively. Figure 6.2 shows the evolution of various properties of the k_θ 2.2 system as a function of density. The location of the isotropic-smectic transition point can be related to a number of features in these data. Primarily, the nematic order parameter rises steeply, of course, and there is an inflection in the pressure profile. Also the rate of decrease in the overall mean squared displacement lessens somewhat and its components diverge – diffusion becomes enhanced in the x - and z -directions but diminished in the y -direction, the latter being the Cartesian direction to which the director

¹This contrasts with the preliminary simulations, in which the same density change of 0.01 was imposed in a single step immediately at the start of each run. The use here of a more gentle compression procedure was motivated by the concern that the imposition, at a stroke, of the full density increase might conceivably perturb the system and thus affect the observed phase behaviour.

is most closely aligned. This indicates that intralayer diffusion is more favourable than interlayer diffusion, as was also found to be the case for the $\kappa 5$ system discussed in the preliminary results chapter. On entering the smectic phase, the

Fig. 6.2: N1250 $\kappa 3$ $k_\theta 2.2$ compression data. The dashed vertical lines indicate the densities ascribed to the isotropic-smectic (I-Sm) and liquid-solid (I-s) transitions.

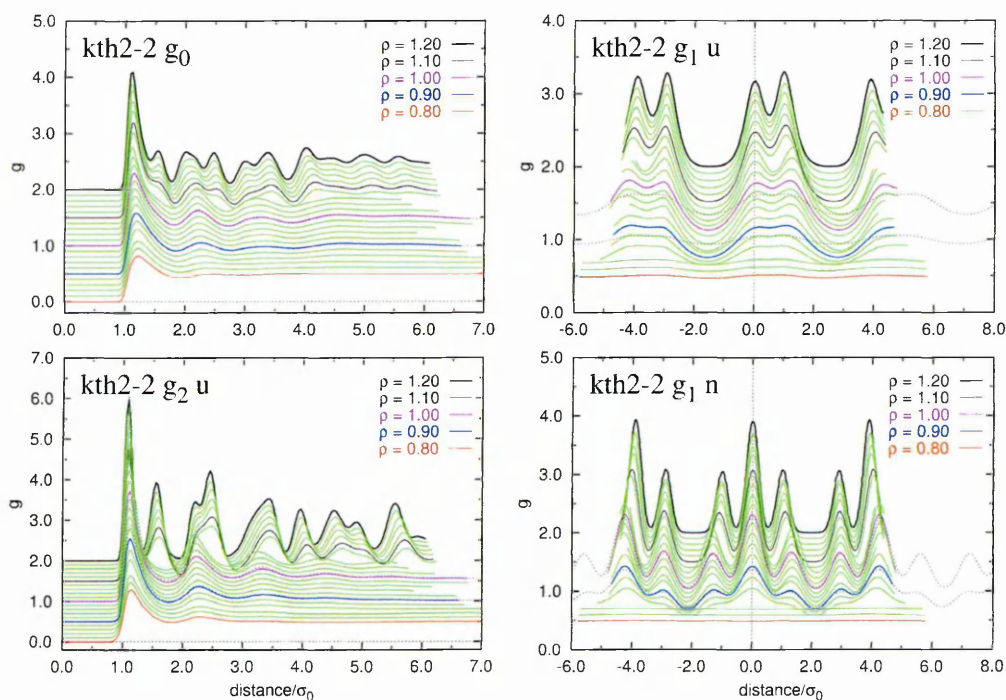


director components settle down to essentially fixed values, which suggests that the disposition of the smectic bilayers within the simulation box at this point is commensurate with the periodicity of the phase. That the phase is comfortably accommodated by the simulation box is confirmed by the parity that exists between the excess pressure components throughout the compression.

At high density, the systems solidify, with the liquid-solid transitions occurring at $\rho = 1.08$ and 1.07 for the $k_\theta 2.0$ and 2.2 systems respectively. The freezing point is indicated by a small step in the P_2 value, a marked drop in pressure and a falling off of the mean squared displacement. A slight reorientation of the director

is also observed. An additional effect of solidification is that fluctuations in the boxlengths become very much reduced and, as a consequence, the aspect ratio of the simulation box remains essentially fixed following the liquid-solid transition. Figure 6.3 presents distribution function profiles for the k_θ 2.2 system, across the full density range of the compression. Note that in these figures each profile has been displaced vertically by 0.1 with respect to the preceding profile so that

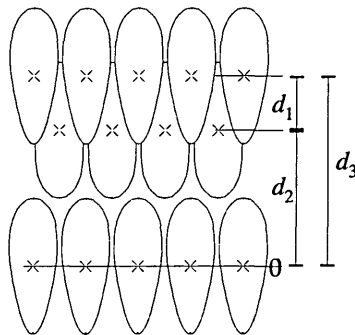
Fig. 6.3: Evolution of selected distribution functions for the N1250 κ 3 k_θ 2.2 compression series. The sampling volumes were divided into 200 shells; the distributions were accumulated from 100 configurations stored over the interval of 500-1000ksteps every 5ksteps. These same parameters were used for the computation of all the $g(r)$ s presented in this section.



changes in their appearance with increasing density are more easily discerned. The radial distribution function, g_0 , does not change much at the I-Sm transition. However the lateral distribution function g_2u begins to show second and third peaks at this density. Moreover regular peaks emerge in the longitudinal distribution functions g_1u and g_1n from $\rho = 0.86$ onwards, a clear signature of the onset of smectic ordering. At first, the central peak, corresponding to the in-plane correlations, and next nearest peak, corresponding to correlations between

particles in opposing leaflets of the same bilayer, are not clearly distinguishable. This is particularly so in the case of the g_{1u} profiles where the two peaks merge into a hump centred at approximately $r_{\parallel} = 0.8\sigma_w$. However at higher density, beyond $\rho = 0.90$ or so, the hump clearly begins to split into a double peak. The positions of the maxima corresponding to these peaks were determined simply by inspection of the distribution function datasets, in order to quantify, in a rudimentary fashion, the changes in the intra- and interlayer separations as a function of

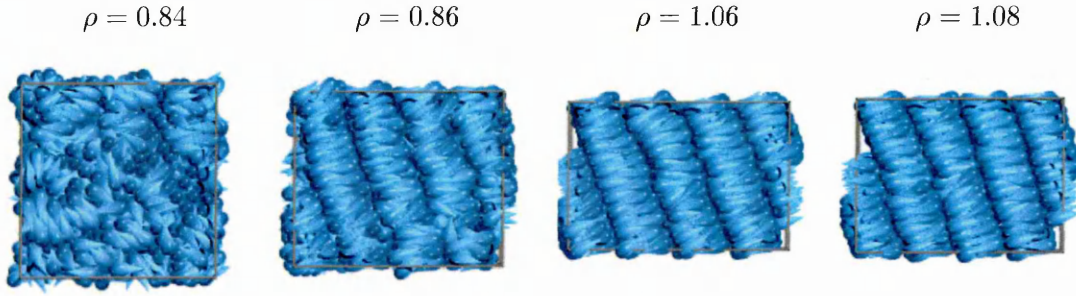
Fig. 6.4: Schematic representation of part of the smectic bilayer phase with the intra- and interlayer distances as discussed in the text labelled.



density. The distance between the central peak (at $r = 0$) and next nearest peak (at roughly $r = +1.2\sigma_w$) corresponds to the modal separation between particles in antiparallel leaflets of the same bilayer as shown in figure 6.4, i.e. the intralayer distance, which we will label d_1 . The distance between the central peak and the second nearest peak (at roughly $r = -3.0\sigma_w$) corresponds to the modal separation between particles in antiparallel leaflets of adjacent bilayers, we refer to this distance as d_2 . Finally, the distance between the central peak and its equivalent in the next double peak, in either the positive or negative direction, corresponds to the modal separation between particles in equivalent, i.e. parallel, leaflets in adjacent bilayers. This, the interlayer distance *per se*, we refer to as d_3 . The resulting plot of these bilayer periodicities, for the k_{θ} 2.2 system, is plotted as a function of density in figure 6.2 (f), alongside the usual runtime averages. It should be mentioned that, given that we are dealing with a fairly small system size and that the aspect ratio of the simulation box can change considerably over the course of a

compression series, the volume from which particle-particle correlations are sampled, for certain runs, is not large enough to encompass the interlayer correlations corresponding to d_3 . Therefore, this data set is not complete over the full density range. Ideally, d_3 should be equivalent to $d_1 + d_2$. However, due to the approximate manner in which the modal separations have been determined here, as well as the uncertainties in the individual longitudinal separations, r_{\parallel} , measured for each pair of particles², the two quantities will in practice differ somewhat. As

Fig. 6.5: N1250 $\kappa 3$ compression K3kth2-2 snapshots.



the system is compressed, in the liquid smectic region, the intralayer separation increases slightly as the particles are squeezed closer together laterally within the bilayers. Note that the increase in d_1 is reflected, in figure 6.2 (e), by an increase in L_x , the box length most closely aligned to the director. At the freezing transition, between $\rho = 1.06$ and 1.08, d_1 decreases abruptly. Also, as figure 6.3 shows, there is a general sharpening of positional order, along with the appearance of additional peaks in g_0 and g_2n . Thus at the liquid-solid transition, the entropy associated with particle disorder and translational motion is sacrificed for the sake of packing efficiency. The distance d_2 between particles sitting base-to-base in adjacent bilayers remains virtually unchanged throughout the compression at a value of approximately $3\sigma_w$, the particle length. Figure 6.5 shows visualisations of the system before and after the I-Sm transition ($\rho = 0.84$ and 0.86) as well as before and after the liquid-solid transition ($\rho = 1.06$ and 1.08). These provide visual confirmation of what the distribution functions tell us, i.e. that upon compression

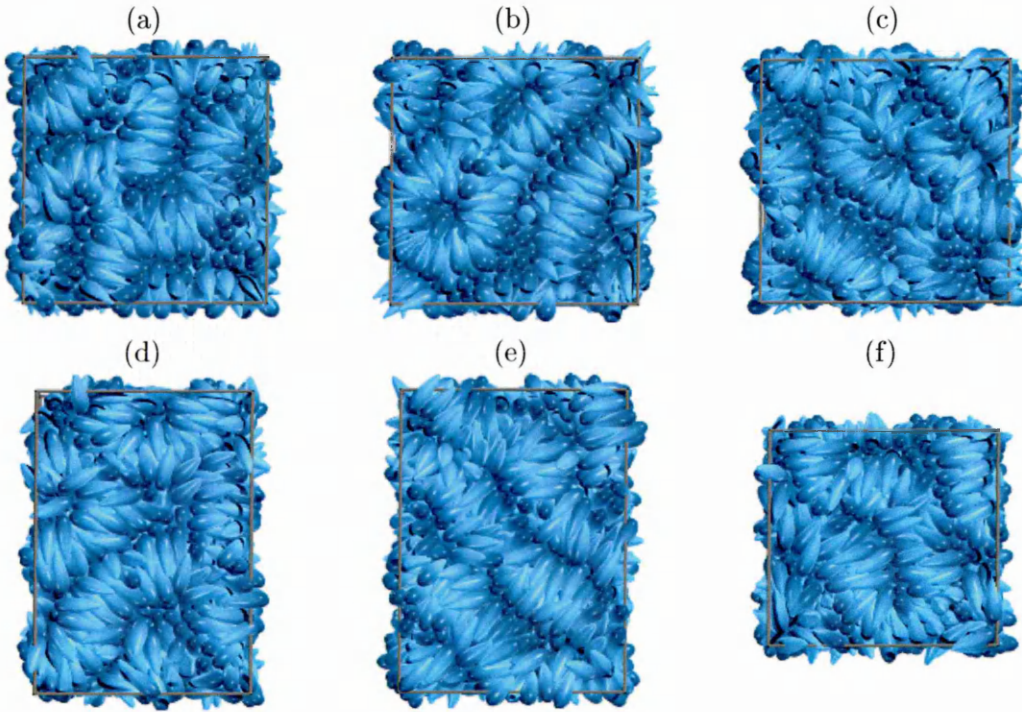
²The tilt of particle orientations with respect to the normal to the bilayer in which they sit (see section 3.4) will affect the value of the distance $r_{ij\parallel\hat{u}_i} = (-\mathbf{r}_{ij} \cdot \hat{\mathbf{u}}_i)$

the low k_θ systems form well-ordered, highly interdigitated smectic phases.

For systems defined by k_θ values from 2.4 to 4.5 inclusive, we observe a compression driven transition from the isotropic to the so-called curvy-bilayer (CB) phase.

This phase consists of bilayers which, locally at least, appear structurally similar to those of the low k_θ bilayer smectic systems. However the layers are contorted

Fig. 6.6: N1250 κ 3 compression. Representative snapshots of the curvy-bilayer (CB) phase. Images (a), (b) and (c) are visualisations of the $\kappa 3k_\theta 2.5$ system looking down the x -, y - and z - directions respectively. Images (d), (e) and (f) are visualisations of the $\kappa 3k_\theta 4.5$ system looking down the x -, y - and z - directions respectively. Both sets of visualisations are derived from the end configurations of each system's $\rho = 1.00$ run.



into curved structures, of which examples are shown in figure 6.6. The upper three panels show views of the $\kappa 3k_\theta 2.5$ system looking in the x -, y - and z - directions respectively, whilst the lower three feature similar views of the $\kappa 3k_\theta 4.5$ system. In some of the images, such as figures 6.6 (a) and (e), the bilayers appear to undulate in a zig-zag fashion from one end of the simulation box to the other. In others they loop back on themselves, sometimes forming almost circular features such as those in figures 6.6 (b) and (d). Whatever the morphology of this arrangement

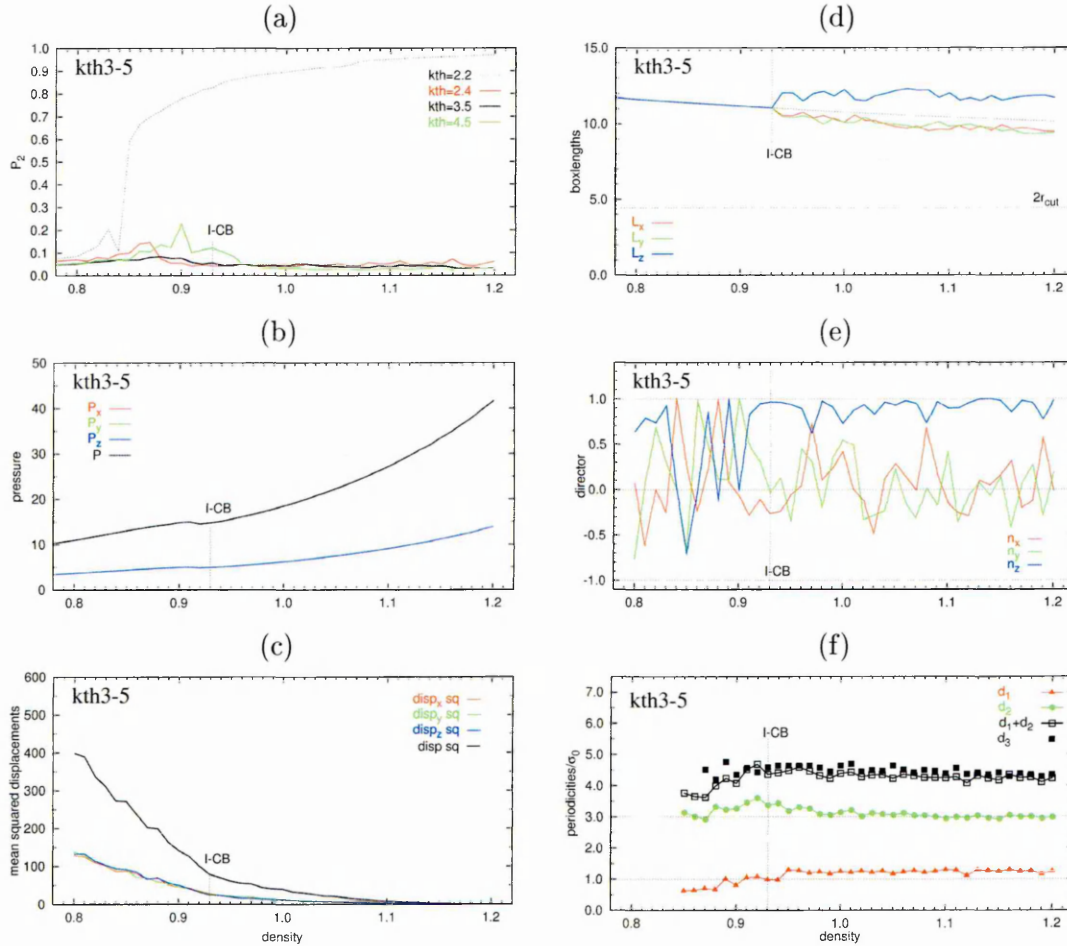
phase, the constituent bilayers, in general, appear to be continuous rather than disconnected fragments.

Figures 6.7 (a)-(f) present basic simulation data for the $k_\theta = 3.5$ system, which turns out to lie approximately at the centre of CB region of the $\kappa 3$ phase diagram. This system, like most of those that enter the CB phase, has an essentially flat P_2 vs. ρ profile, although $k_\theta=2.4$ and 4.5 , which mark the low and high k_θ boundaries the CB region, do exhibit small, short-lived elevations of nematic order. The P_2 profiles for these three systems, as well as that of $k_\theta=2.2$, are shown in figure 6.7 (a) for comparison. The onset of the CB phase is more difficult to pinpoint than the classic I-N or I-Sm order-disorder phase transformations. However two fairly distinct features in the data would seem to be associated with the I-CB transition. Firstly, there is a gentle inflection in the pressure profile, as shown in figure 6.7 (b). Secondly, coinciding with the end of the pressure inflection, there is a decrease in the rate of decline of the overall mean squared displacement (figure 6.7 (c)). The latter suggests that the curved bilayers, disorganised as they may appear to be, must provide a somewhat more effective mechanism for particle mobility than a completely disordered isotropic phase would otherwise do. Presumably the particles migrate chiefly within the bilayers in a similar manner to which they move within smectic bilayers. We note also that the mean squared displacement does not exhibit a distinct fall-off at high density, in other words there is no definite liquid-solid transition, the diffusion simply tails off. For all the CB systems, throughout the compression, both the diffusion and the pressure remain isotropic. With higher k_θ values, the inflections in the pressure and diffusion profiles indicating the I-CB transition, move to higher density. The datasets for the boxlengths and director components, figures 6.7 (d) and (e), do not exhibit any significant features or trends. We merely note that the simulation box dimensions remain fairly stable throughout the compression. Also, the fluctuations in the director components lessen as the system enters the CB phase but this is largely irrelevant since this phase has no long-range orientational order.

The distribution functions for the curvy bilayer phase, shown in figure 6.8 for the

$k_\theta = 3.5$ system, are relatively featureless, which is only to be expected given the apparent lack of long-range order present in the CB phase. There are, however, some subtle features to indicate the onset of the CB phase, notably the emergence of very shallow double peaks in $g_1 u$ as well as more distinct peaks and troughs in

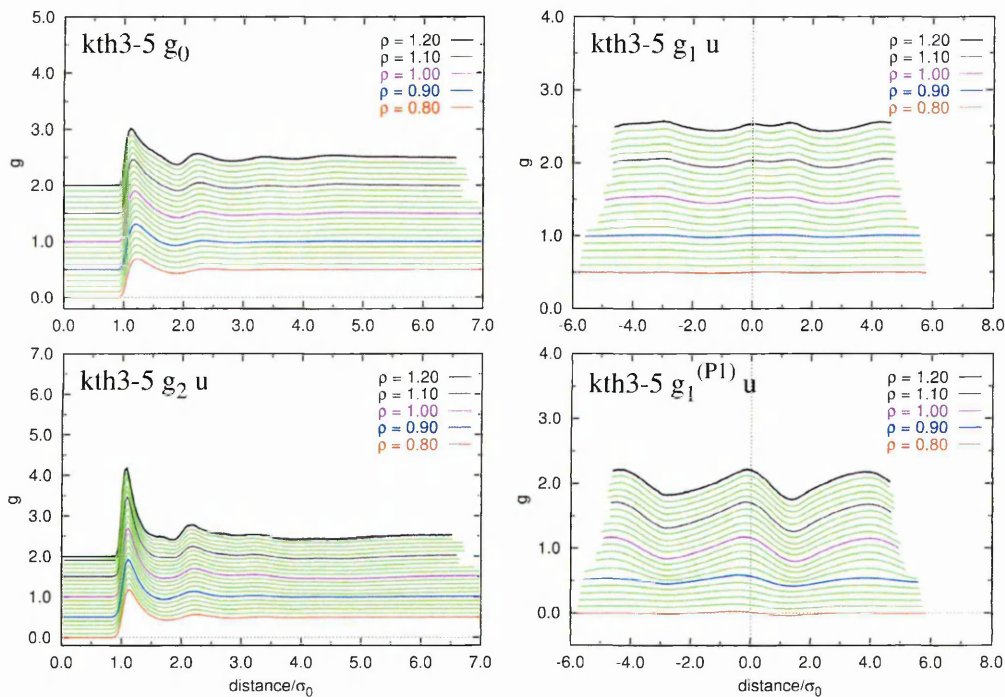
Fig. 6.7: N1250 $\kappa 3$ $k_\theta 3.5$ compression data. The dashed vertical lines indicates the density ascribed to the isotropic-curved bilayer (I-CB) transition for this particular system. Graph (a), for the order parameter, also includes the P_2 profiles for a number of other systems for the sake of comparison.



$g_1^{(P1)} u$. The positions of the maxima in the former were determined, as they had been previously for the $k_\theta = 2.2$ system, and are presented in figure 6.7 (f). The intralayer distance, d_1 , is of a similar value to that of the $k_\theta = 2.2$ smectic system but, in contrast to the latter, remains essentially constant throughout the compression. The separation, d_2 , between particles in antiparallel leaflets of adjacent bilayers meanwhile appears to decrease gradually with density and, along with it,

the overall interlayer distance. It should be emphasised though that we should not read too much into the longitudinal distribution functions presented here for the CB phase. This is because for *all* the systems surveyed in this chapter, for the sake of both practicality and consistency, the height and width of the cylindrical sampling volume for the g_1 are both automatically set at $(L_{min}/2)*\cos(45^\circ)$, where L_{min} is the smallest simulation box dimension over all the contributing configurations for as given density. A cross-section through the cylinder is, thus, a square whose length of side which, for a system size of 1250, is typically of the order

Fig. 6.8: N1250 $\kappa 3$ $k_\theta 3.5$ compression; selected distribution functions.

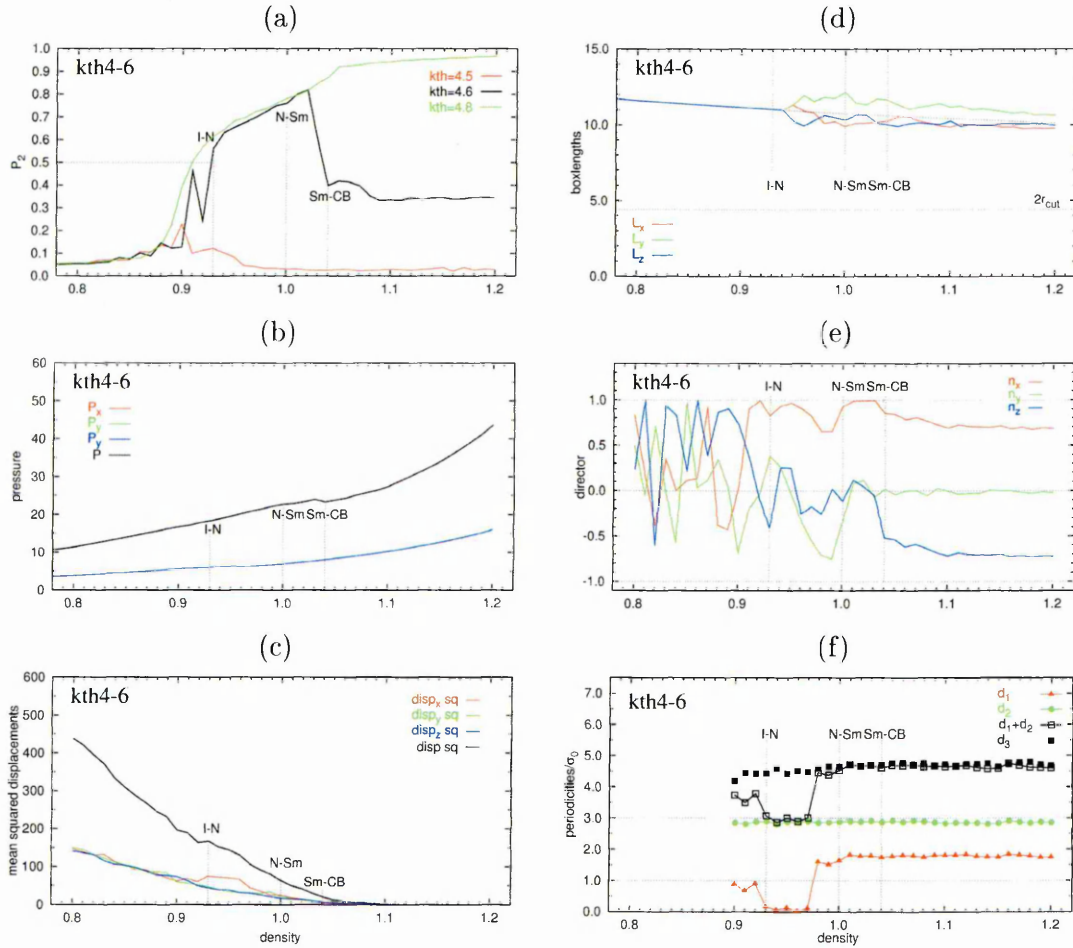


of $10\sigma_w$. This is a suitable sampling volume when it comes to characterising the smectic phases, which, of course, consist of essentially flat bilayers. However for the CB phase, a sampling volume of these dimensions will, to some degree, take in the curvature of the bilayers. In other words, the computation of the longitudinal distribution function, as it stands, averages out some of the fine structural detail of the CB phase. For a more accurate characterisation of the structure we could, perhaps, recompute the g_1 using narrower sampling volumes that take in less of the curvature of the bilayers. On balance though, one is drawn to the conclusion

that a proper investigation of the phase in question calls for the development of more advanced analytical tools, in particular algorithms to characterise and take account of bilayer curvature.

When we reach $k_\theta=4.6$, we find long-range orientational order returning once more, at a density of approximately 0.93. However, this time the disorder-order transi-

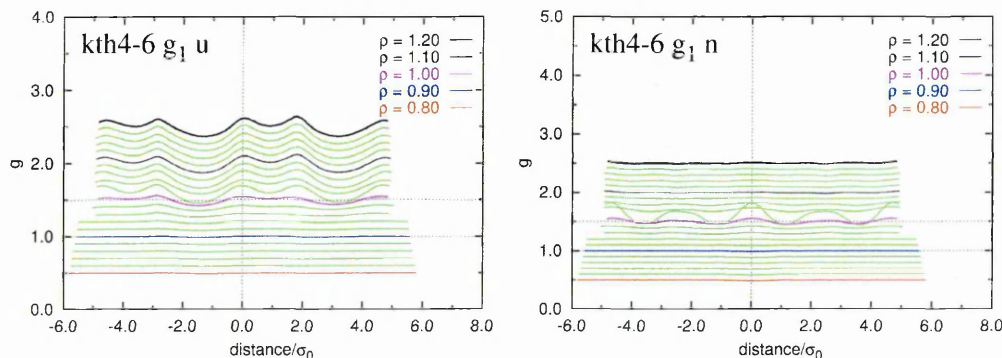
Fig. 6.9: N1250 κ_3 $k_\theta=4.6$ compression data. The dashed vertical lines indicate the densities ascribed to the various transitions undergone by this system.



tion is from the isotropic into the nematic phase rather than from the isotropic into the smectic as it was for the highly tapered k_θ 2.0 and 2.2 systems. That the ordered phase is nematic, rather than smectic, is indicated by the diffusion data, shown in figure 6.9 (c), which, coinciding with the rise of P_2 (figure 6.9 (a)), exhibits a characteristic increase in the overall mean squared displacement. Also the mean squared displacement components diverge at this point with diffusion in

the x -direction enhanced from approximately $\rho = 0.93$ to 0.98 (the director points roughly in the x -direction at the transition). For as long as the nematic phase persists, there are no peaks in the g_1 profiles, as featured in figure 6.10. Conse-

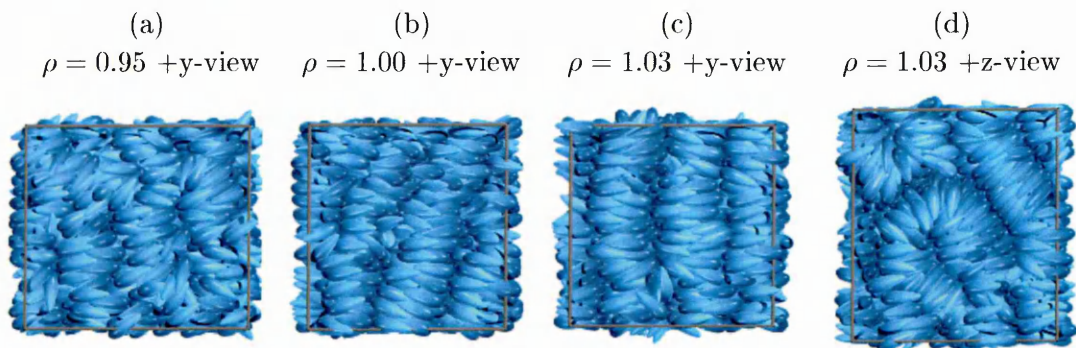
Fig. 6.10: N1250 $\kappa 3$ $k_{\theta} 4.6$ compression; selected distribution functions.



quently the intralayer separations, d_1 , plotted in figure 6.9 (f), hover around zero for much of the nematic phase because peaks in g_1 that correspond to this correlation simply cannot be identified. At a density of around 1.00, however, peaks do begin to emerge in the longitudinal distribution functions, indicating a transformation into the smectic phase. In fact when one looks at visualisations of the system at densities lower than this, for example at $\rho = 0.95$ as shown in figure 6.11 (a), precursors of smectic bilayers appear to be visible, although apparently the nascent bilayer structure is too disordered and fragmented to be picked up by the correlation functions until the density reaches 0.97.

The smectic phase turns out to be short-lived, for at $\rho = 1.03$ the peaks in $g_1 n$

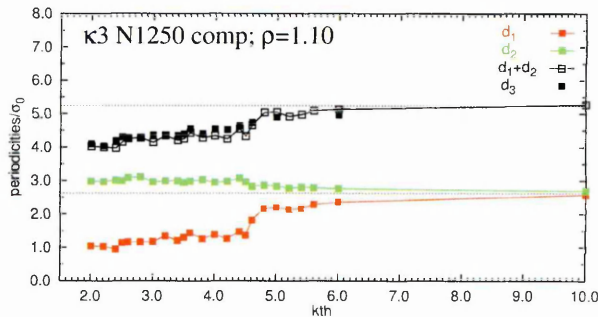
Fig. 6.11: N1250 $\kappa 3$ compression K3kth4-6 snapshots showing the system in the process of transforming from the smectic to the CB phase.



disappear and, at the same time, the order parameter drops rapidly to a value of approximately 0.4. Looking once again at visualisations of the system, we recognise the cause for this rather unusual intermediate P_2 value. In figure 6.11 (c), wherein we view the simulation box looking along the positive y -direction, the system appears to be in the smectic phase, but if we instead look along the positive z -direction it looks much more like a CB phase. As the system is further compressed, it maintains an order parameter of $P_2 \approx 0.35$ and seems to retain some level of vestigial smectic character. This may simply be a result of the low mobility over this density range impeding the transformation into a pure CB phase. Alternatively, this arrangement may be representative of phase coexistence. The observed finite order parameter is probably also partly an artefact of the small system size.

Moving on to the $k_\theta=4.8$ system, we find that long-range orientational order now persists throughout the compression, as clearly shown by the P_2 profile for this system (figure 6.13 (a)). The system initially enters the nematic phase, this time

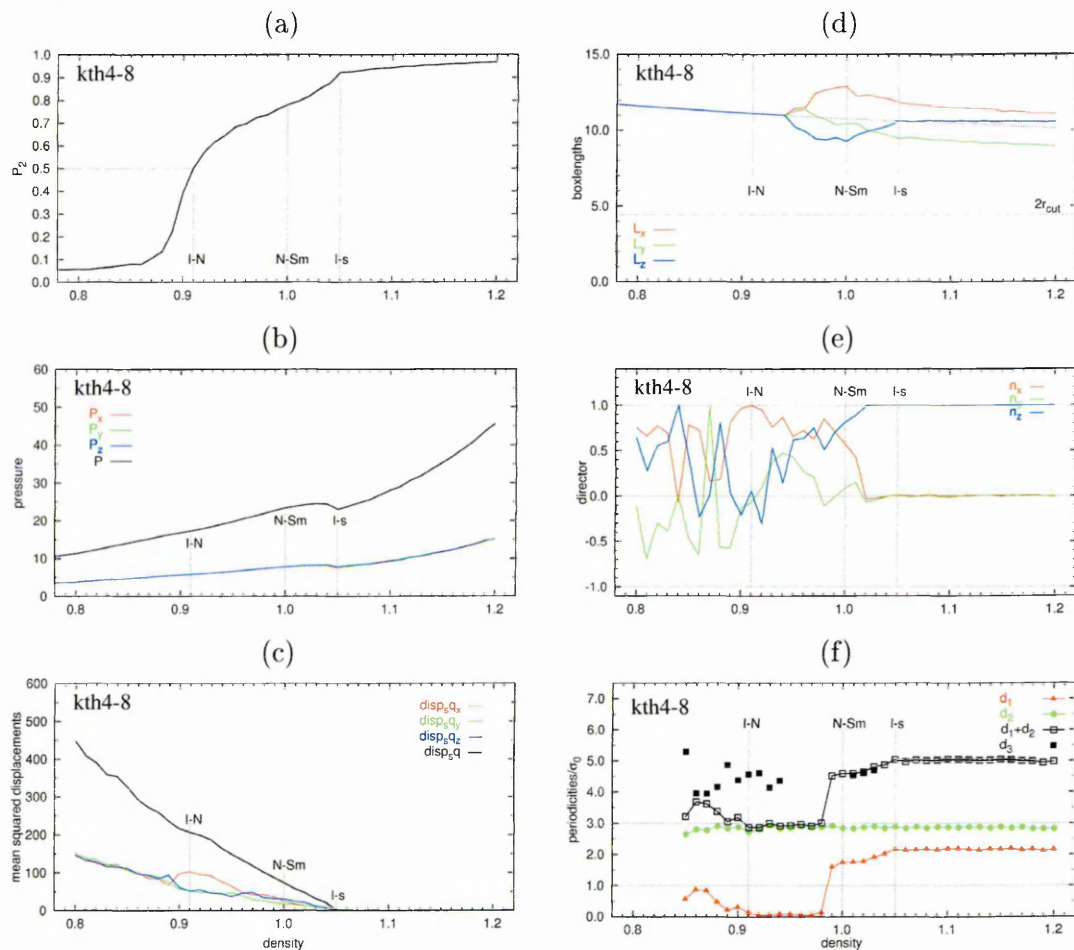
Fig. 6.12: The effect of particle shape on intra- and interlayer separations. The separations shown here are based on the positions of maxima in the g_1u profiles obtained from the $\rho = 1.10$ runs.



at the slightly lower density of 0.91, and then, at a density of around 1.00, starts to turn smectic, as indicated by the emergence of peaks in the g_1 profiles (not shown here). The onset of the smectic is also marked by a gradual decline in the gradient of the pressure profile (figure 6.13 (b)). The main difference between this smectic phase and its $k_\theta=2.2$ counterpart is that the former has a considerably larger intralayer separation and, hence, overall bilayer thickness. As illustrated

by figure 6.13 (f), d_1 for $k_\theta 4.8$ tends to a value of $\sim 2\sigma_w$ at high density compared to $\sim 1\sigma_w$ for $k_\theta 2.2$. This seems entirely reasonable since $k_\theta 4.8$ particles are only slightly tapered and so have less tendency to interdigitate. Figure 6.12 shows the periodicities, at $\rho = 1.10$, for all of the tapered particle systems up to $k_\theta 10.0$

Fig. 6.13: N1250 $\kappa 3$ $k_\theta 4.8$ compression data. The dashed vertical lines indicate the densities ascribed to the various transitions undergone by this system.

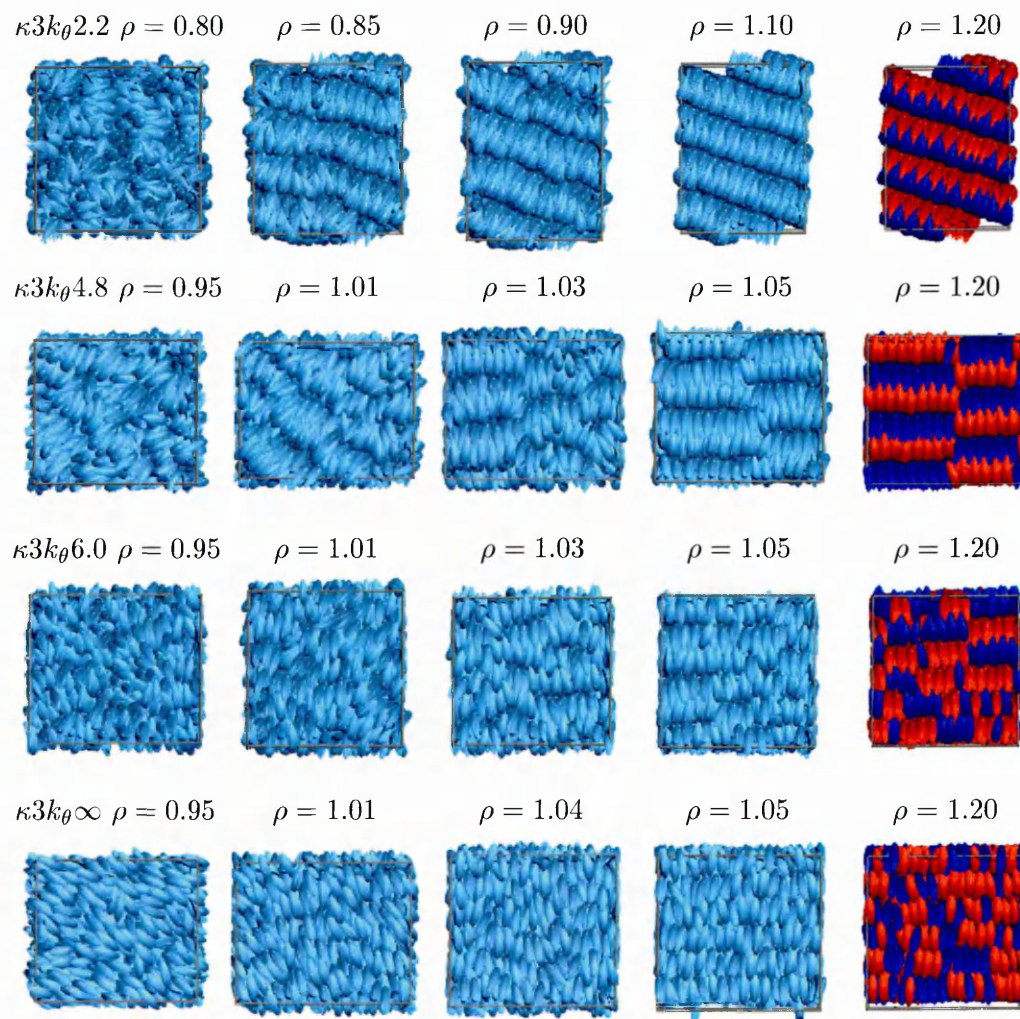


as determined from their g_{1u} profiles. From $k_\theta 2.0-4.5$, there is a gradual rise in the intralayer separation, however between $k_\theta 4.6$ and 4.8 a sizeable and abrupt increase in its value occurs. This marks the end of the CB region of the phase diagram, for with the marked increase in d_1 , the local structures that the particles adopt become more like monolayers which cannot exhibit the kinds of distortions (i.e. curvature) that bilayers do. As k_θ is further increased, there is a second phase of gradual increase in the intralayer separation. At the same time, the difference

between d_1 and d_2 diminishes and tends to zero in the limiting case of $k_\theta = \infty$. This defines particles that are uniaxially symmetric and, therefore, form a simple SmA phase with a repeat distance of approximately $2.62\sigma_w$, a little less than the nominal particle length.

A further trend related to increasing the particle symmetry is that the N-Sm transition is pushed to higher density until it virtually coincides with the liquid-solid transition. For $k_\theta \geq 4.8$, the freezing point occurs at around $\rho = 1.05$, as indicated

Fig. 6.14: N1250 $\kappa 3$ compression K3kth2-2 snapshots illustrating the transition into the smectic phase for a number of systems.

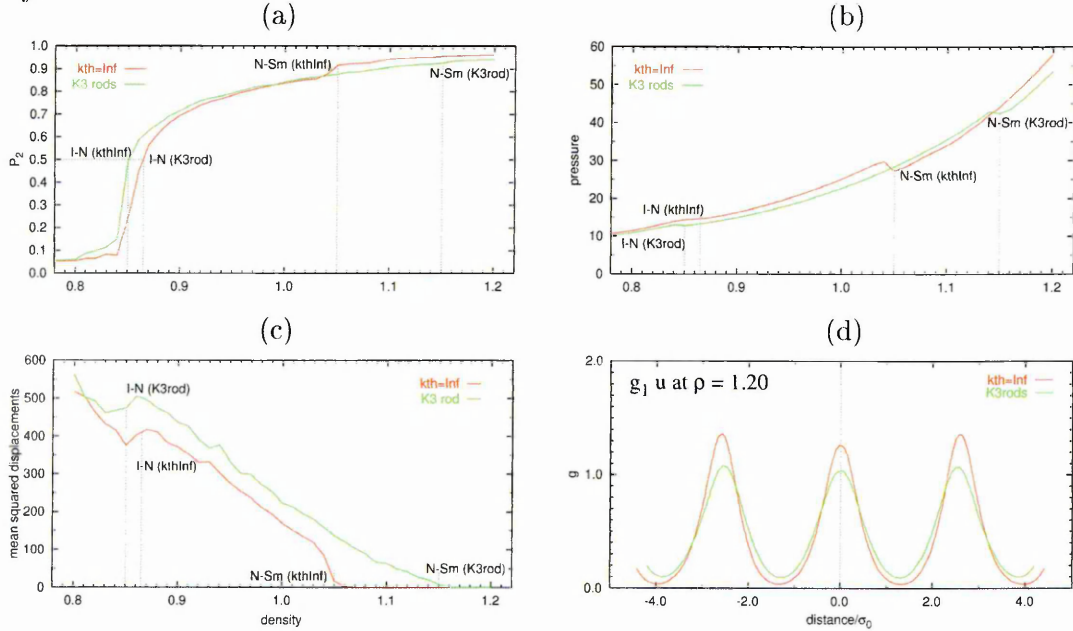


by a sharp discontinuity in the gradient of the P_2 curve and a downturn in the mean squared displacement as well as an inflection in the pressure. We also note, from the $\rho = 1.20$ images in figure 6.14, that, with increasing k_θ , polar correlations

within bilayers become reduced and eventually completely randomised.

To conclude our survey of the $\kappa 3$ phase space by compression, we briefly compare the results of the $k_{\theta}\infty$ simulation to those of a similar compression for $\kappa 3$ rods. Figures 6.15 (a-c) contrast the P_2 , pressure and overall mean squared dis-

Fig. 6.15: N1250 compression data, comparing $\kappa 3$ $k_{\theta}\infty$ and $\kappa 3$ rods. The dashed vertical lines indicate the densities ascribed to the various transitions undergone by these systems.

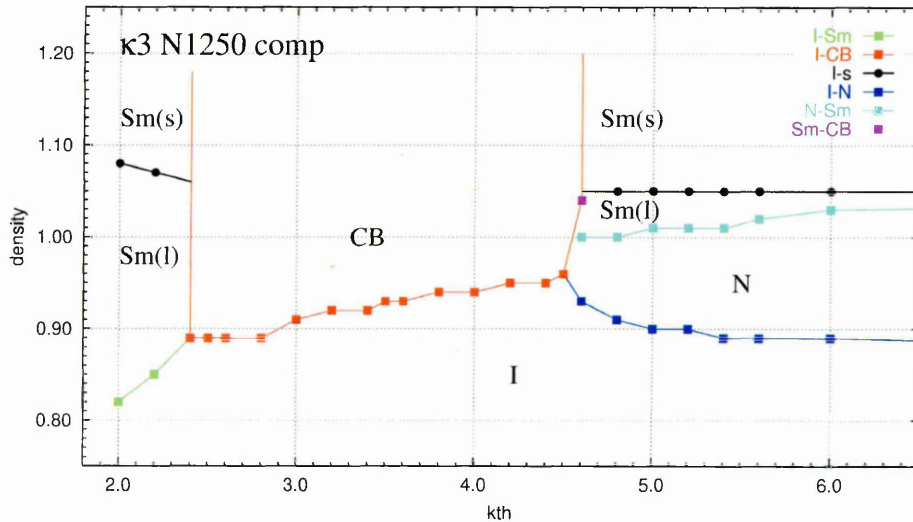


placements profiles. These show the I-N transitions to occur at similar densities, $\rho = 0.86$ and 0.85 for the $k_{\theta}\infty$ pears and $\kappa 3$ rods respectively. There is, however, a considerable difference at high density with the $k_{\theta}\infty$ system exhibiting a N-Sm transition at $\rho = 1.05$, whereas the rods go directly to the solid at $\rho = 1.15$. We attribute these differences to the somewhat lower volume of the latter type of particle, 1.57 as compared to 1.62 for the $k_{\theta}\infty$ pears. The difference in volume is also reflected in the lower pressure and higher mobility in the rod system. In addition the high density phase for the rods has a slightly smaller interlayer separation as illustrated by the $g_1 u$ profiles shown in figure 6.15 (d).

We now end this section by presenting, in figure 6.16, the phase diagram as constructed from the interpretation of the runtime data and distribution functions. The solid squares indicate the transition points that have been positively iden-

tified. Where appropriate, the lines representing the nominal phase boundaries have been extended so as to more clearly delineate the various phase regions. So, in summary, at low k_θ we observe a transition from the isotropic to the bilayer smectic phase which subsequently solidifies at higher density. In the central region we have a transition from the isotropic to a so-called curvy-bilayer phase which

Fig. 6.16: N1250 $\kappa 3$ compression phase diagram based on inspection of the changes in runtime observables and distribution functions as a function of density.



becomes glassy at high density. For $k_\theta \geq 4.8$, the system transforms first into a nematic and thence an interdigitated smectic phase which solidifies at approximately $\rho = 1.05$. With higher k_θ , whereby particles tend to the uniaxial ellipsoid shape, the N-Sm transition moves to higher density and ultimately coincides with the freezing point as $k_\theta \rightarrow \infty$.

6.3 Creation of artificial smectics

In order to test whether the curvy-bilayer phase encountered in the central portion of the phase diagram from compression was indeed a genuine phase, a second batch of simulations was set up with the purpose of approaching the CB region from the opposite direction, so to speak, by expanding high density smectic systems. Since the CB region effectively acts as a barrier to the self assembly of mid- k_θ smectics

via compression, it was necessary to generate ‘artificial’ smectic configurations to act as the starting points for these decompression sequences. To achieve this, a system of 1250 $\kappa 3k\theta 3.0$ particles was compressed to a density of 1.10 with an electric field, \mathbf{E} , applied in the positive z-direction during most of the compression to encourage the particles to align themselves along the z-axis. The coupling of the field to the particles was implemented by associating an induced axial dipole with each particle i :

$$\mathbf{p}_i = \alpha \mathbf{E}_{\parallel} = \alpha E (\hat{\mathbf{u}}_i \cdot \hat{\mathbf{z}}) \hat{\mathbf{u}}_i = \alpha E \cos(\theta) \hat{\mathbf{u}}_i \quad (6.1)$$

where \mathbf{E}_{\parallel} is the projection of the electric field onto particle $\hat{\mathbf{u}}_i$ and α is the polarisability of the particle, which we arbitrarily set at unity. In general, the energy associated with a dipole in an electric field is given by:

$$U_p = -(\mathbf{p} \cdot \mathbf{E}) \quad (6.2)$$

Substituting $\mathbf{p} = \mathbf{p}_i = \alpha E (\hat{\mathbf{u}}_i \cdot \hat{\mathbf{z}}) \hat{\mathbf{u}}_i$ and $\mathbf{E} = E \hat{\mathbf{z}}$ into equation 6.2 we obtain

$$U_p = -\alpha E (\hat{\mathbf{u}}_i \cdot \hat{\mathbf{z}}) \hat{\mathbf{u}}_i \cdot E \hat{\mathbf{z}} = -\alpha E^2 (\hat{\mathbf{u}}_i \cdot \hat{\mathbf{z}})^2 = -\alpha E^2 \cos^2(\theta) \quad (6.3)$$

In general a torque may be defined as the partial derivative of the potential energy with respect to a rotation θ about some arbitrary axis $\hat{\theta}$ thus

$$\tau = -\frac{\partial U}{\partial \theta} \hat{\theta} \quad (6.4)$$

Substituting U_p into equation (6.4) and choosing $(\hat{\mathbf{u}}_i \wedge \hat{\mathbf{z}})$ for the rotation axis gives us the torque exerted by the applied field on each particle:

$$\begin{aligned} \tau_i^{(E)} &= -\frac{\partial}{\partial \theta} \{-\alpha E^2 \cos^2(\theta)\} (\hat{\mathbf{u}}_i \wedge \hat{\mathbf{z}}) \\ &= \alpha E^2 \frac{\partial}{\partial \theta} \{\cos^2(\theta)\} (\hat{\mathbf{u}}_i \wedge \hat{\mathbf{z}}) \\ &= -2\alpha E^2 \sin(\theta) \cos(\theta) (\hat{\mathbf{u}}_i \wedge \hat{\mathbf{z}}) \end{aligned}$$

$$\begin{aligned}
&= -2p_i E \sin(\theta) (\hat{\mathbf{u}}_i \wedge \hat{\mathbf{z}}) \\
&= -2\mathbf{p}_i \wedge \mathbf{E} \\
&= -2\alpha E (\hat{\mathbf{u}}_i \cdot \hat{\mathbf{z}}) \hat{\mathbf{u}}_i \wedge E \hat{\mathbf{z}} \\
&= -2\alpha E^2 (\hat{\mathbf{u}}_i \cdot \hat{\mathbf{z}}) (\hat{\mathbf{u}}_i \wedge \hat{\mathbf{z}}) \\
\tau_i^{(E)} &= -2\alpha E^2 \hat{u}_z^{(i)} (\hat{u}_y^{(i)}, -\hat{u}_x^{(i)}, 0) \tag{6.5}
\end{aligned}$$

Through this term, which is simply added to the usual torque resulting from interparticle interactions, orientational order can be induced in the system. At a density of 0.80, at which the system would ordinarily be in the isotropic phase, the field was ramped up gradually from zero to $E = 2.0$ in increments of $\Delta E = 0.01$ at intervals of 1000 timesteps. Following this, the system was compressed using the scheme described previously. At the lower densities, the field promoted nematic ordering whilst at higher densities the expectation was that it would lead to the formation of a smectic phase. Anisotropic rescaling was therefore applied from $\rho = 0.90$ onwards, in anticipation of the need for changes in the aspect ratio of the simulation box to accommodate this phase. When the system had been compressed to a density of $\rho = 1.20$ the field was ramped down to zero. Then it was decompressed from $\rho = 1.20$ to 0.80 to compare the ordering within the system over that density range with the density range with the field-enhanced ordering. This sequence of runs is summarised in table 6.1.

Figure 6.17 shows the nematic order parameter and pressure data obtained during the three distinct simulation regimes, namely isotropic compression (black line), anisotropic compression with field applied (blue line) and anisotropic decompression (green line). When the field was first applied, at $\rho = 0.80$, the order parameter rose slightly from approximately 0.056 to 0.072. At the same time, the pressure increased from 11.35 to 12.22 as a result of the extra work done on the system by the electric field; the average potential energy per particle also rose from 0.981 to 1.053. Thereafter, there was a steady, almost linear, increase in P_2 over the density range $\rho = 0.80$ –0.93. This is reflected by the longitudinal distribution functions for the compression sequence, shown in the left panels of

figure 6.19, which indicate a smooth development of structural order. Another apparent result of applying the field was a rather sharp increase in the mean squared displacement, as shown in figure 6.18 (a). The fact that the x -, that this

Tab. 6.1: Summary of sequence of runs for compression/decompression of a system of 1250 $\kappa 3 k_{\theta} 3.0$ particles. The entire sequence is comprised of three simulation series:

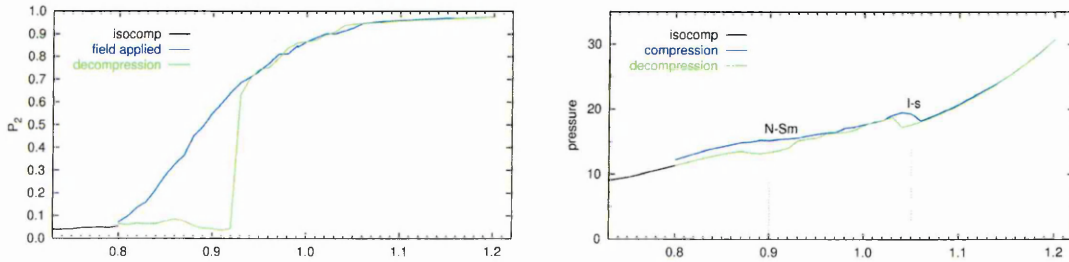
- (a) /Early_simulations/N1250_isocomps/2006-02-14_K3kth3-0_comp
- (b) /Early_simulations/N1250_anisocomps_E2-0/2006-03-01_K3kth3-0_anisocomp_E2-0
- (c) /K3BATCH_07/2006-04-14_K3kth3-0

ρ	treatment	ensemble	N_{step}
(a) 0.15-0.75	rapid isotropic compression	<i>NVT</i>	100k
(a) 0.75-0.80	isotropic compression	<i>NVT</i>	1000k
(b) 0.80	ramp up E-field	<i>NVT</i>	1000k
(b) 0.80-0.90	isotropic compression with field on	<i>NVT</i>	500k
(b) 0.90-1.00	anisotropic compression with field on	<i>NVT</i>	500k
(c) 1.00-1.10	anisotropic compression with field on	<i>NVT</i>	600k
(c) 1.10-1.20	anisotropic compression with field on	<i>NVT</i>	300k
(c) 1.20	ramp down E-field; anisorescaling on	<i>NVT</i>	1000k
(c) 1.20-0.80	anisotropic decompression	<i>NVT</i>	500k

increase of mobility owes more to the extra energy being put into the system, via the electric field, than it did to the increase in orientational order (as would be the case for a normal isotropic- nematic transition).

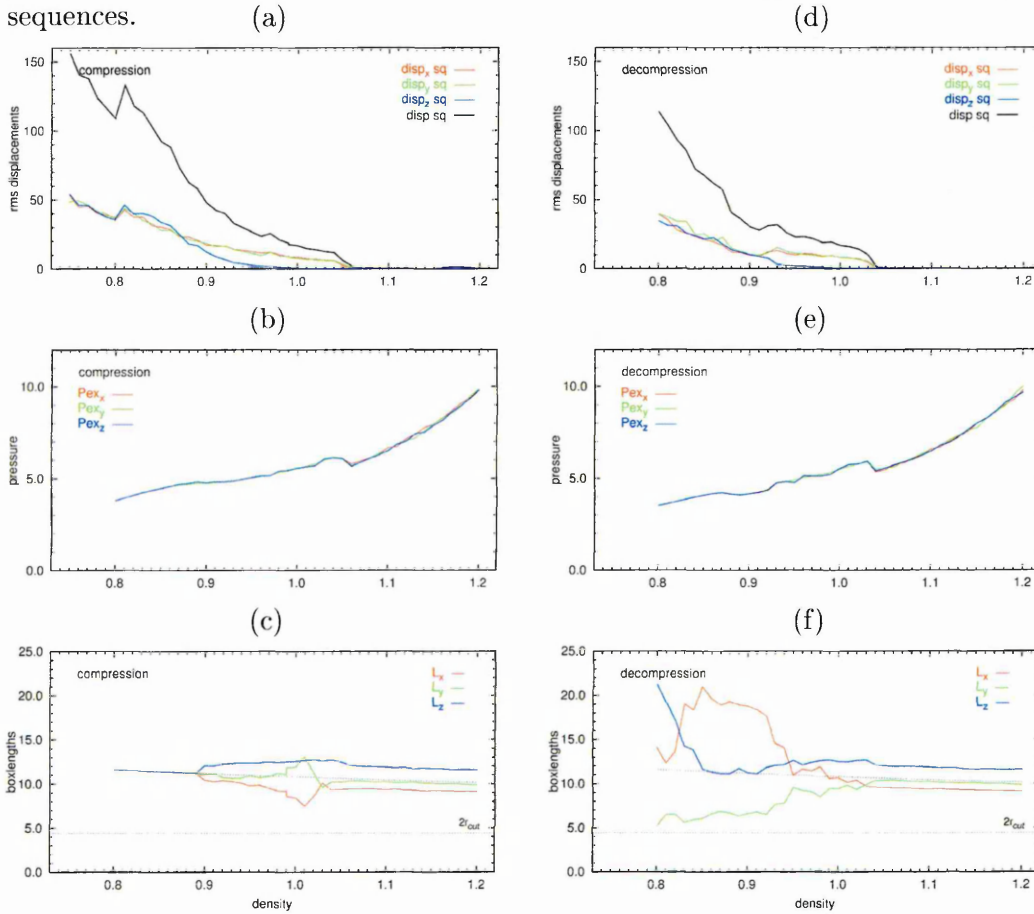
y - and z -components of the mean squared displacement remained essentially equal implies

Fig. 6.17: N1250 $\kappa 3 k_{\theta} 3.0$ system: Comparing order parameter and pressure profiles for the compression and decompression sequences.



At a density of around $\rho = 0.88$, the smectic phase began to emerge, as indicated by a gentle inflection in the pressure (figure 6.17 (b)). We also observe, at this point, the divergence of the mean squared displacement components, with diffusion in the x-y plane (parallel to the bilayers) clearly favoured over diffusion in the z-direction, a signature feature of the smectic phase. The transition is, of course,

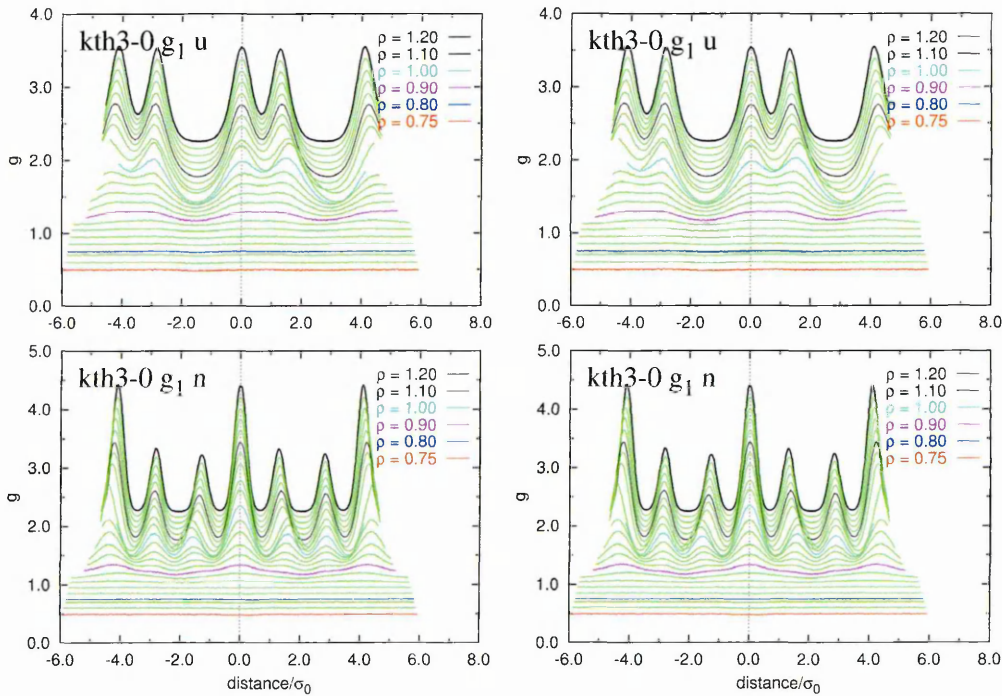
Fig. 6.18: N1250 $\kappa 3$ $k\theta 3.0$ system: Comparing mean squared displacements, excess pressure components and simulation boxlengths for the compression and decompression sequences.



also indicated by the appearance of regular peaks in g_1u and g_1n . Upon further compression, a liquid-solid transition occurred between $\rho = 1.04$ and 1.06 , as evidenced by a falling off of the mean squared displacement and a sharp inflection in the pressure. Throughout the compression, the excess pressure components (figure 6.18 (b)) remained essentially equal. The boxlengths (figure 6.18 (c)) also remained fairly stable, with L_z increasing steadily in the fluid smectic phase so as to accommodate four bilayers perpendicular to the z-direction.

Having obtained a stable, well-ordered smectic phase, at $\rho = 1.20$, via compression with an orienting field applied, the field was ramped down and the decompression commenced. From $\rho = 1.20 - 1.06$, the decompression data are virtually indistinguishable from the corresponding compression data. The first difference that we encounter between the two simulations is that the solid-liquid transition for the decompression occurred at a slightly lower density than it did for the compression,

Fig. 6.19: Comparing selected distribution functions for the N1250 $\kappa 3$ $k_{\theta} 3.0$ compression and decompression sequences.

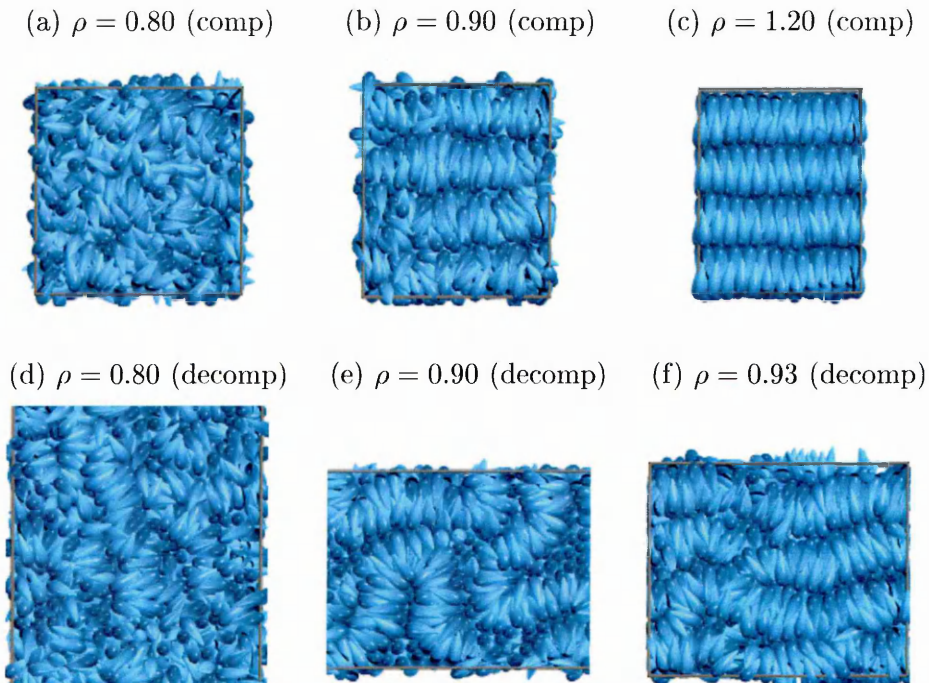


At $\rho = 1.04 - 1.03$ as opposed to 1.04-1.06, and it was more sharply defined. At $\rho = 0.93$ the smectic phase began to break down, as indicated by the collapse of P_2 and a slight pressure drop. There was also a reduction in the mean squared displacement, with mobility in the z-direction increasing whilst both the x and y mean squared displacements decreased until all three components converged. The boxlengths also began to diverge. Figure 6.20 (f) gives the impression that the demise of the smectic was initiated by fusion of adjacent bilayers. As the density was further decreased, the bilayers adopted curved conformations as shown in figure 6.20 (e), redolent of the CB phase encountered in the compression simulation,

ulations. These bilayers remained essentially intact until the density had fallen to around 0.89, at which point they begin to fragment thus marking the end of the CB phase and the return of the isotropic. This transition was also marked by an inflection in the pressure. We note that g_{1u} retains vestiges of the correlations associated with bilayer structure at $\rho = 0.80$ whereas the corresponding distribution obtained from the compression series was essentially flat at this point.

Rather than generate smectics for the other shape parameter values by carry-

Fig. 6.20: N1250 $\kappa 3$ $k_{\theta}3.0$ system: Snapshots looking down the y -axis. The upper snaps are taken from the compression phase during which an electric field was applied. The lower images are taken from the decompression phase.

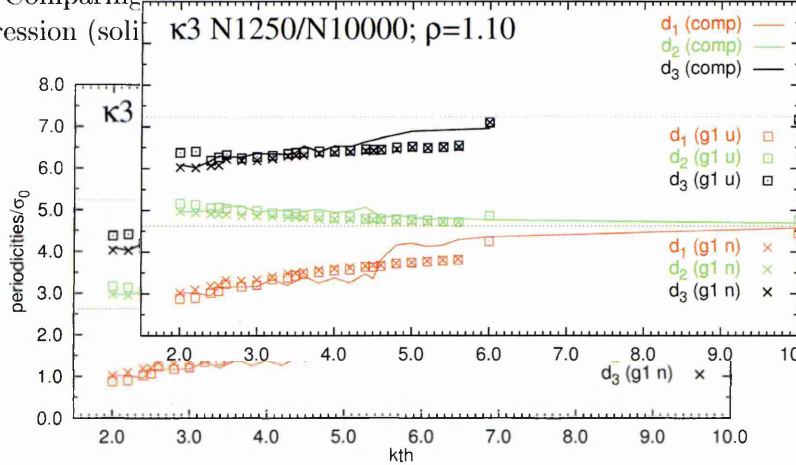


ing out compression sequences with a field applied for each system, a task which would occupy a large number of CPUs for many days, the required configurations were created simply by taking the $k_{\theta}3.0$ smectic at $\rho = 1.10$ as the starting configuration for a simulation of a $k_{\theta}2.8$ system at the same density. This approach proved viable because the difference in shape between $k_{\theta}3.0$ and $k_{\theta}2.8$ particles is very slight, such that a sudden switch in identity from the one to the other did not incur the creation of large overlaps or voids in the system. The $k_{\theta}2.8$ system

smectic thus created was then run for 10ksteps with anisotropic rescaling to allow the simulation box to adjust to the repeat distance associated with this shape of particle. A smectic for the next value of k_θ , namely 2.6, was then created by using the end configuration from the $k_\theta 2.8$ equilibration run as input to a similar equilibration run for a $k_\theta 2.6$ system. This process was repeated down to $k_\theta 2.0$. In a similar fashion the $k_\theta 3.0$ smectic was used as the seed for k_θ values higher than 3.0 to furnish a complete set of starting configurations as required for our survey of $\kappa 3$ pear phase behaviour via decompression.

Before moving on to the next section, it is interesting to look once again at the effect of particle shape upon the bilayer periodicities at $\rho = 1.10$. Figure 6.21 shows the d_1 , d_2 and d_3 obtained from distribution functions derived from smectics consisting of 10000 particles. These systems were obtained by taking eight replicas of each of the N1250 artificial smectics and joining them together, two

Fig. 6.21: Comparing interlayer separations at $\rho = 1.10$ for N1250 systems obtained from compression (solid symbols).



on each side, to form a larger simulation box with the same aspect ratio but having eight times the volume and, of course, eight times the number of particles. These configurations were then equilibrated over three 200kstep runs, the first was in NVT with rescaling applied throughout, the second in NVE with constant boxlengths, and the third another NVT run with rescaling. The configurations from the end of these three runs were subsequently used as the starting points for N10000 decompression sequences (not discussed at length here). The periodicities plotted in figure 6.21 are derived from configurations dumped over the course

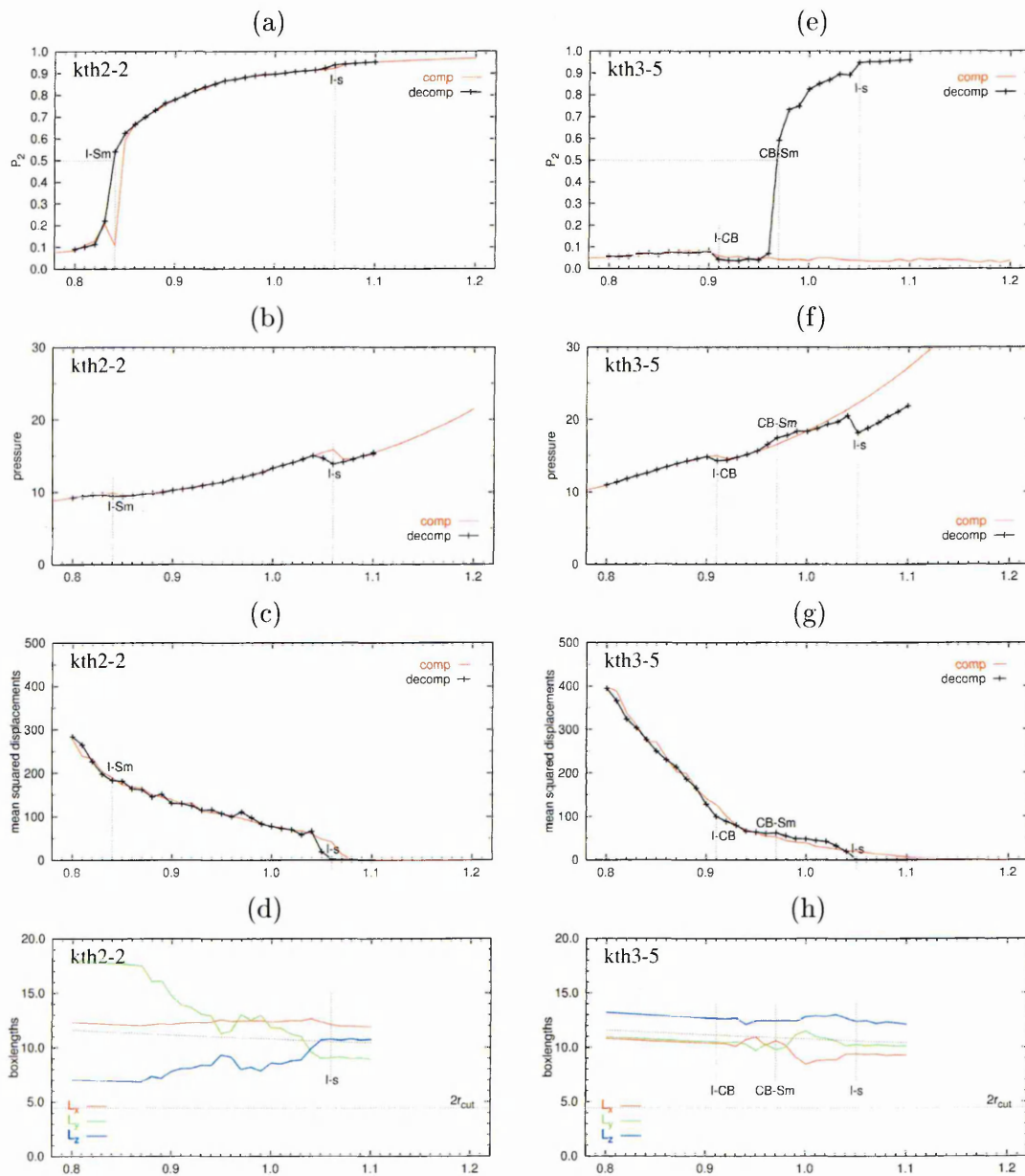
of the first production run of these decompressions. The data marked by boxes were computed from the g_1u whilst the crosses mark the data computed from g_1n . Also plotted, for comparison, are the periodicities that were shown earlier in figure 6.12, as determined from the g_1u originating from the N1250 compressions at $\rho = 1.10$. Broadly the data from the two different system sizes are in fairly good agreement except for the fact that the big step up in d_1 occurs between $k_\theta 4.6$ and 4.8 for N1250 whereas for N10000 it occurs somewhere between $k_\theta 5.6$ and 6.0. A possible explanation for this is that all of the N10000 systems were artificial smectics seeded from the field-induced $k_\theta 3.0$ smectic, which consisted of well interdigitated bilayers. It is therefore possible that the N10000 systems up to and including $k_\theta 5.6$ inherited and retained this structural characteristic. This is made more plausible by the fact that, at $\rho = 1.10$, all of the systems are solid and so perhaps less able to relax into their natural arrangements. To test this theory, one could try seeding artificial smectics from a high k_θ field-induced smectic system, say 6.0, and recomputing the periodicities. Nevertheless the qualitative similarity of the existing datasets shown in figure 6.21 strongly suggests that the shape-driven crossover from curvy-bilayer to nematic/smectic character in $\kappa 3$ systems, is abrupt and relates to a threshold in the degree of taper of the particles.

6.4 Phase diagram from decompressions

In terms of procedure, the decompressions, which were all started from $\rho = 1.10$, essentially amounted to a reversal of the compression sequences. All of the systems were initially held at $\rho = 1.10$ for 1000ksteps, then they were expanded via a sequence of 30 runs, in each of which the density was decreased by 0.01. As with the compressions, the change of density was applied gradually by small decreases of $\Delta\rho = 0.00001$ every 100 timesteps over the interval 100-200ksteps. All runs were of 1000kstep duration, with averages accumulated and configurations stored over the interval 100-200ksteps. Most of the simulations used, as their starting

configurations, the artificial smectics described in the previous section. However, a few, namely $k_{\theta}2.0, 2.2, 5.2, 5.4, 5.6$, were started from ‘natural’ smectics which formed during the compression sequences without the aid of an aligning field. The reason for this was to check if this choice would have any major effect on

Fig. 6.22: N1250 $\kappa 3$ $k_{\theta}2.2$ and $k_{\theta}3.5$ decompression data compared to corresponding compression data as well as boxlengths for the decompression series only.

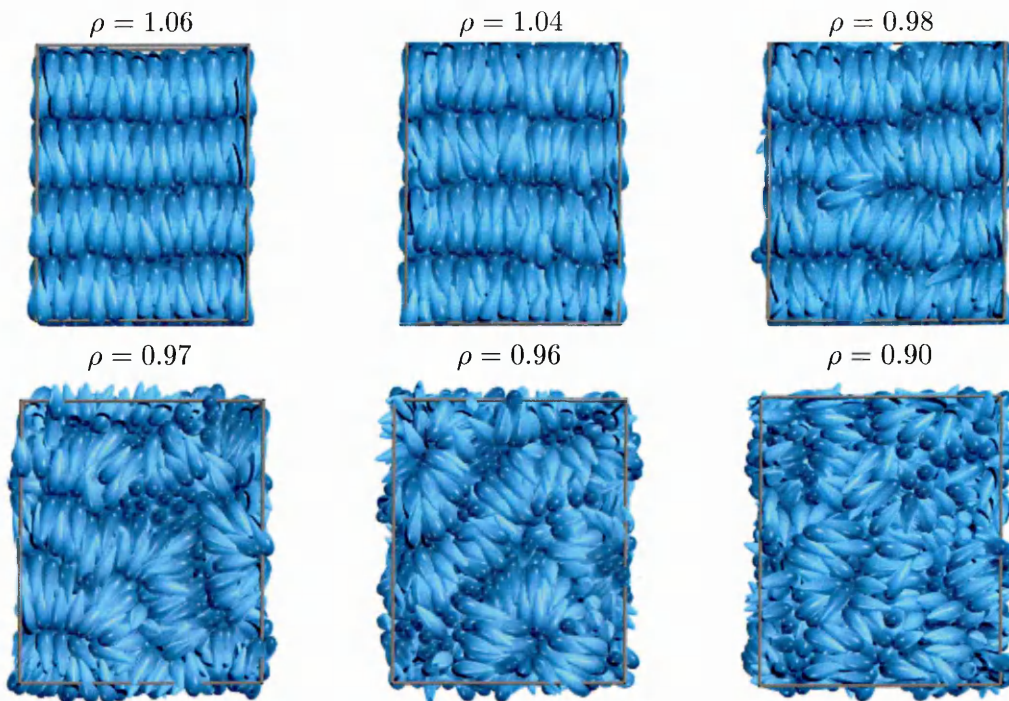


the subsequent behaviour of the systems during decompression. Plots (a) to (d) in figure 6.22 show key simulation data from the decompression of the $k_{\theta}2.2$ sys-

tem, the corresponding P_2 , pressure and diffusion profiles from the compression series are also included for comparison. A glance at these graphs tells us that the phase behaviour of this system on decompression closely resembles that which it exhibited on compression. The only differences are that the solid-liquid and smectic-isotropic transitions occur at slightly lower densities. The distribution functions from the decompression (not shown here) and compression also prove to match one another very well.

For systems $k_\theta 2.4-4.5$ encompassing the central region of the phase diagram, where the CB phase was previously encountered, we expect major differences between the decompression and compression data. These are illustrated for the $k_\theta 3.5$ system in plots (e) to (h) of figure 6.22. The system begins the decompression as a well-ordered artificial smectic with an intralayer separation of approximately $1.4\sigma_w$, as illustrated in figure 6.23. Note that the pressure (fig. 6.22(f)), for the

Fig. 6.23: Visualisations of the N1250 $\kappa 3k_\theta 3.5$ systems as it is decompressed. The melting point occurs at $\rho = 1.05$, the smectic to CB transition at $\rho = 0.97$ and the CB to isotropic transition at approximately $\rho = 0.91$.

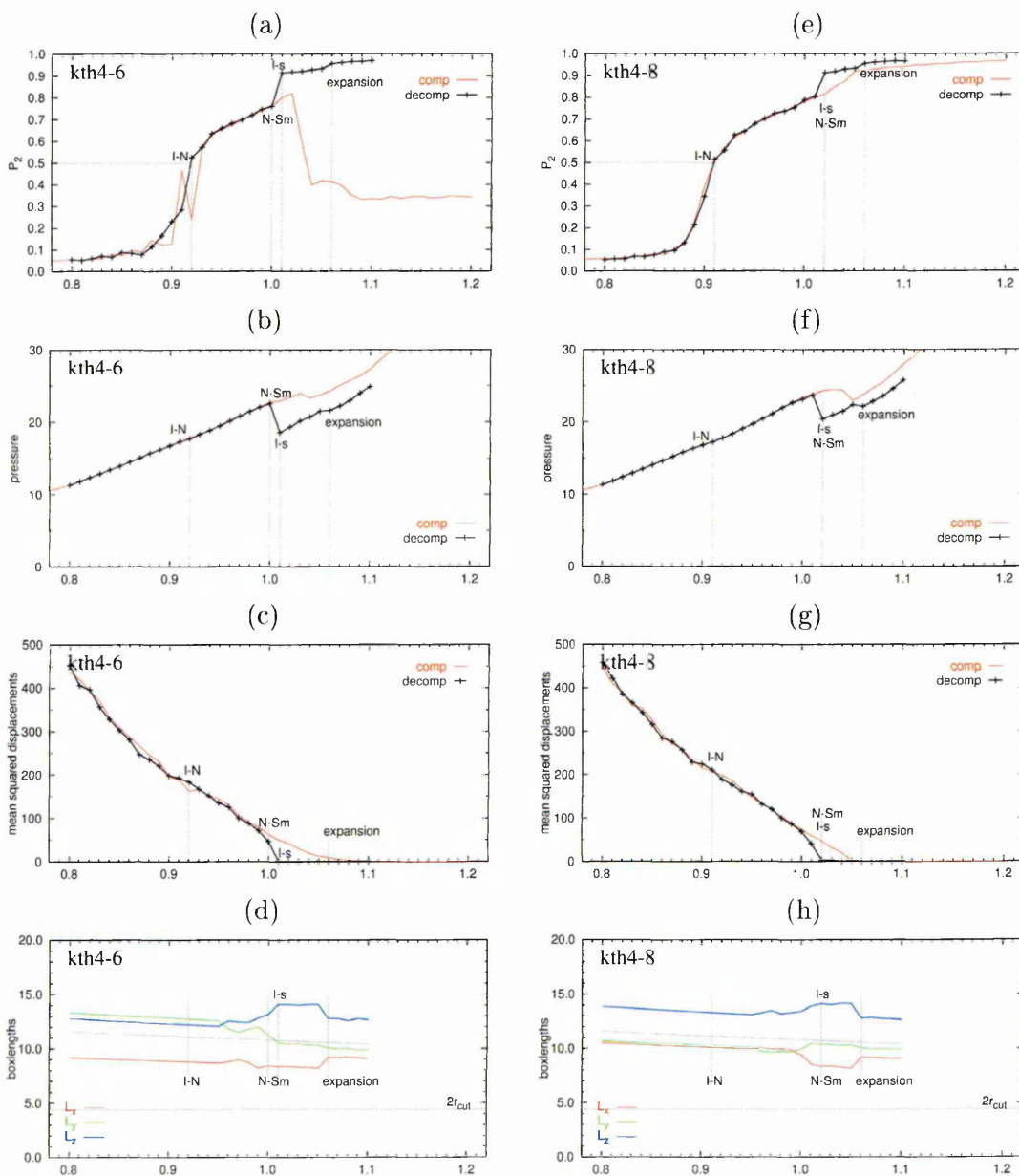


solid smectic phase is very much lower than it was in the compression simulation over the corresponding density range, in which the phase was curvy-bilayer. At a density of 1.05, the smectic melts, an event signified by a small but abrupt drop in P_2 and a rise in pressure, which brings it to a value only just below that measured in the CB phase at that density. With further lowering of the density, the bilayers become progressively more disordered, until, at a density of around 0.98, we observe a few particles that have escaped from their parent bilayer and lie horizontally between adjacent layers, as shown in the top right panel of figure 6.23. The bilayers also show undulations and what appear to be alternate regions of swelling and contraction. These changes would seem to prefigure the collapse of the smectic into the CB phase which occurs at a density of 0.97. This transitional stage is pictured in the bottom left panel of figure 6.23. This image suggests that the Sm-CB phase transformation is facilitated by some sort of fusion event, in which the second from top bilayer and the bottom bilayer link up through a perforation in the intervening bilayer. In terms of the simulation data, the transition is marked by a precipitous drop in the order parameter and a slight inflection in the pressure profile which brings it into coincidence with the corresponding compression profile. The CB phase itself starts to break up at a density of approximately 0.91 as indicated by yet another inflection in the pressure and a characteristic upturn in the rate of change of mean squared displacement. The CB-I transition occurs at a slightly lower density than the I-CB transition did in the compression.

Moving on to the $k_{\theta}4.6$ system, the data in figures 6.24 show that this system remains solid down to a density of 1.01, a considerably lower value than those found in any of the compressions sequences. Prior to the melting point, between $\rho = 1.05$ and 1.04, the boxlength L_z increases significantly which could only be due to a spontaneous expansion of the bilayers. Immediately thereafter, the aspect ratio of the simulation box remains essentially fixed until the melting point is reached. This suggests that the intralayer separation of the initial (artificial) smectic was not able to relax fully from the initial value inherited from the $\kappa 3k_{\theta}3.0$ seed to the

preferred value intrinsic to the $k_{\theta}4.6$ system. A similar expansion of the bilayers in the solid phase is also observed for systems $k_{\theta}4.2, 4.4, 4.5, 4.8$ and 5.0 but not for $k_{\theta}5.2, 5.4$ and 5.6 whose starting configurations were, significantly, smectics that

Fig. 6.24: N1250 $\kappa 3$ $k_{\theta}4.6$ and $k_{\theta}4.8$ decompression data compared to corresponding compression data as well as boxlengths for the decompression series only.



formed naturally during the compression sequences. Immediately following the solid-liquid transition, the $k_{\theta}4.6$ system undergoes a Sm-N transition as indicated by a sudden collapse of the regular peaks in the longitudinal distribution functions

(not shown) as well as by a drop in P_2 and the onset of drift and fluctuations in both the box lengths and director components. The nematic persists down to a density of 0.92, a similar value to that observed in the compression sequence.

The phase behaviour for $k_\theta \geq 4.8$ follows along similar lines to $k_\theta 4.6$ as illustrated by the data shown in figures 6.24(e)-(h). The solid-liquid transitions occur at lower densities than the liquid-solid transition on compression and coincide with the Sm-N transition. The subsequent N-I transitions for these systems occur at or near the densities that were observed for the compressions.

6.5 Summary and conclusions

Figure 6.26 presents the phase diagram from decompression alongside that obtained from compression. At the low k_θ end, both studies indicate an isotropic-Sm(l)-Sm(s) phase sequence. At the high k_θ end, on compression, the systems enter first a nematic phase and then a narrow liquid smectic region which disappears as k_θ tends to infinity, whereupon the N-Sm transition coincides with the liquid-solid phase boundary. Upon decompression from the solid smectic phase, the liquid-solid phase boundary is found to lie at lower density and there is no liquid smectic region. Rather the systems enter the nematic phase directly on melting. The lower boundaries of the nematic region, as mapped out by compression and decompression sequences, are in close agreement. Also these phase diagrams agree broadly with that obtained from the MC simulations (figure 6.1). The of the most important conclusions to be drawn from these studies is that the curvy-bilayer phase is observed both in compression and decompression, which strongly supports the view that this is a genuine phase and not a metastable state. Moving from left to right across the phase diagram, it would seem that the preference for smectic or CB structure at low to intermediate k_θ must be related in some way to the degree to which the particles interdigitate in, which in turn derives from their degree of taper. Certainly, at high k_θ , the particles are

only slightly tapered and so tend to behave more like uniaxial particles and thus favour the nematic phase. The observed step increase in the intralayer separation, as presented in figure 6.21, suggests that there may be a rather sharp threshold, in

Fig. 6.25: N1250 κ 3 compression phase diagram based on inspection of the changes in runtime observables and distribution functions as a function of density.

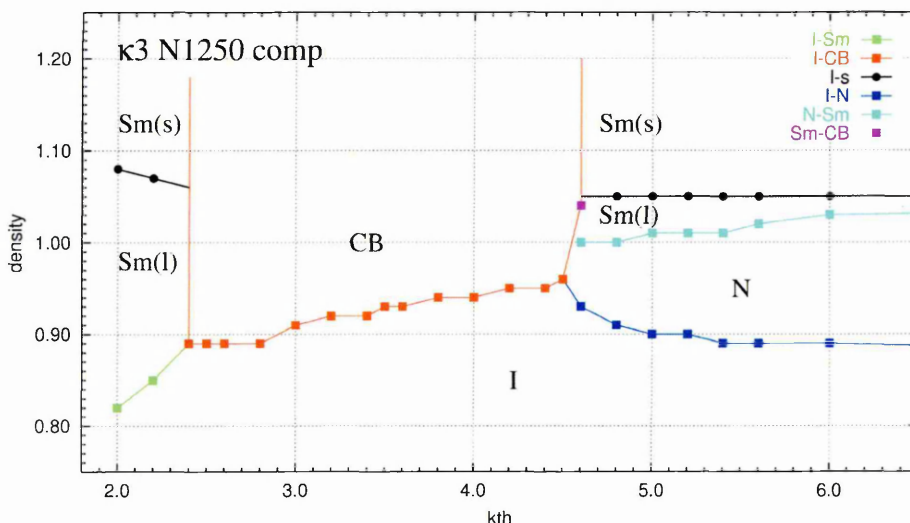
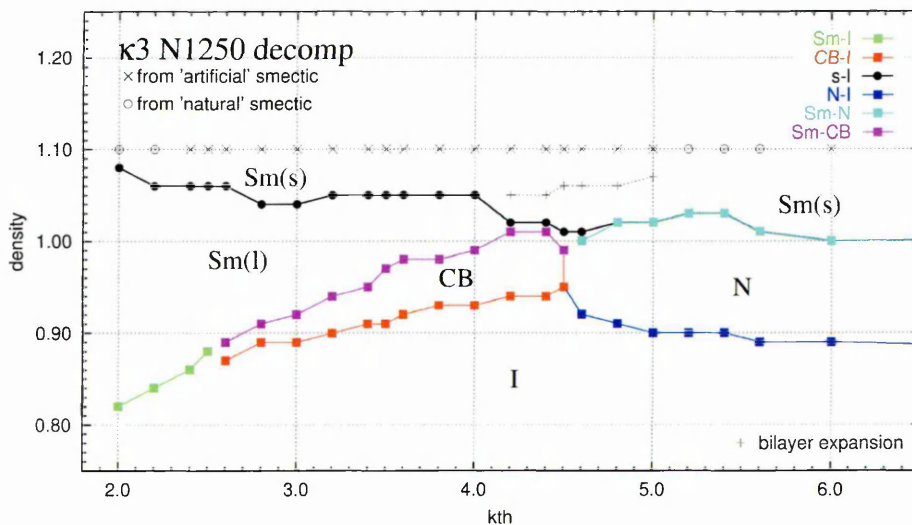


Fig. 6.26: N1250 κ 3 decompression phase diagram based on inspection of the changes in runtime observables and distribution functions as a function of density. The symbols along the horizontal $\rho = 1.10$ indicate the nature of the starting configuration for each system.



terms of shape, between the Sm/CB and nematic regimes. However, it is difficult to speculate on the factors which determine whether a bilayer-forming system will favour a planar or curved arrangement without a better understanding as to the precise nature of the CB phase. To try to improve our knowledge of this phase,

further simulations were carried out on larger CB-forming systems as reported in the next chapter.

It would also have been desirable to carry out a more detailed study of the phase behaviour in general. The following is a list of possible refinements and additions that could be made to the simulation and analysis procedures.

- Increase the system size to say 10000 to check whether this has any major effects on the phase behaviour. This would also provide better statistics in relation to the characterisation of structural details. The quality of the information provided by the distribution functions might also be improved by devising curve-fitting routines to facilitate more accurate and efficient determination of quantities such as the bilayer periodicities. Routine and reliable characterisation of bilayer periodicities as a function of density and k_0 value could turn out to be a crucial step in identifying the primary drivers of the observed phase transitions. This knowledge would be particularly valuable if it turned out that there was a relationship between say the intralayer separation and the mechanical properties of bilayers.
- Incorporation of runtime measurement of the components of the mean squared displacement parallel and perpendicular to the director. Besides providing better insight into the preferential mode of diffusion in the system, this would provide a more sensitive indicator of certain phase transitions, in particular the N-Sm transition.
- Introduce analysis procedures that better characterise the CB phase i.e. ones that take into consideration local curvature.
- Extend the analysis of particle dynamics to fully characterise the linear and rotational motion of the particles. This could provide a useful insight into the relative contributions of these modes to the entropy of system and, thus, provide pointers to the fundamental drivers of the observed phase transitions.

- Attempt to map out the phase boundaries more thoroughly, particularly for the regions $k_\theta 2.4 - 2.6$ and $k_\theta 4.4 - 4.8$. To establish the phase boundaries with greater precision would require simulations using a range of intermediate k_θ values, say 4.40 to 4.80 in increments of 0.02 (it might even be worth attempting to alter the k_θ value of a system whilst holding the density constant in order to map out small portions of the phase diagram horizontally. The application of more rigorous analysis techniques such as thermodynamic integration (see for example section 7.1 in [39]) would also be desirable in order to establish the equilibrium phase at a given state point with greater accuracy.
- Extend the study to systems of particles with different aspect ratios, e.g. $\kappa = 2.0, 4.0$ and 5.0 . This would effectively add an extra dimension to the phase space of tapered particles which might provide a useful alternative line of investigation in terms of understanding the fundamental drivers of the phase transitions.

CHAPTER 7

The gyroid phase

The investigation of the κ_3 phase diagram, described in the previous chapter, provided a fair characterisation of the isotropic, nematic and smectic phases formed by these particles. The structural nature of curvy-bilayer phase, however, remained unresolved. Some of the images of this phase were suggestive of long-ranged order on a scale comparable to the size of the N1250 simulation volume. For example the sinuous shapes traced out by the bilayers in figure 6.6 have the appearance of being tessellated. It was therefore natural to investigate the CB region further by carrying out simulations on a larger system size. The first section of this chapter discusses the first large system to be examined, which was the $\kappa_3 k_0$ 3.8. In the N1250 compression of this system, indications of periodic supramolecular organisation had emerged at high density. To obtain a larger version of this system, comprising 10000 particles, a configuration stored at a somewhat lower density was scaled up and run on in *NVE* for 10 million timesteps. Three-dimensional periodic order was indeed found to exist in this system. The structure was identified as the bicontinuous cubic phase $Ia\bar{3}d$, otherwise known as the gyroid (G). The second section of this chapter describes the results of a set of compressions of N10000 systems from the low density isotropic phase. Primarily these were designed to see if isotropic-gyroid (I-G) transitions would take place across the range

of particle shapes that had entered the CB phase in the course of the N1250 compressions, namely $k_{\theta}2.4-4.6$. Most of these systems did indeed form well-ordered gyroids. The phase seemed to assemble via the formation of small domains which subsequently grew and merged to form its distinctive interpenetrating double network structure. The third section reports the results of a set of decompressions of N10000 artificially created smectics aimed at capturing the transformation of these lamellar phases into the gyroid. The majority of the systems indeed underwent smectic-gyroid transitions. The transformation was found to be initiated by bilayer fusion events consisting essentially of the formation of ‘stalks’ between two bilayers which pass through pores in the intervening bilayer. The chapter concludes with a brief assessment of the wider relevance of simulations of the gyroid phase and an outline of further work that could be carried out to learn more about this fascinating structure.

7.1 Study of a scaled up CB system

That the CB phase might possess long-range order, was most forcibly suggested by the snapshot, shown in figure 7.1 (a), of a $\kappa3k_{\theta}3.8$ system that had undergone compression to a density of 1.10. The system appears to contain a diagonal row of circular features consisting of sections of bilayer looped back on themselves. One is tempted to interpret these arrangements as being the cross-sectional views through vesicle or tube like structures.

This system clearly merited further investigation. Therefore, it was decided to scale up the N1250 $\kappa3k_{\theta}3.8$ system to one consisting of 10000 particles simply by duplicating eight copies of a configuration from the former. However, the N1250 configuration actually chosen for duplication was taken from earlier on in the compression sequence at a density of 0.95. This system is shown in figure 7.1 (b). The reason for selecting the lower density configuration to generate the large system was that this less ordered system was judged fluid enough to eventually

Fig. 7.1: Snapshots of the N1250 $\kappa 3k_{\theta} 3.8$ system at (a) $\rho = 1.10$ and (b) $\rho = 0.95$. Panel (c) illustrates the N10000 obtained by duplicating eight times over the configuration shown in (b).

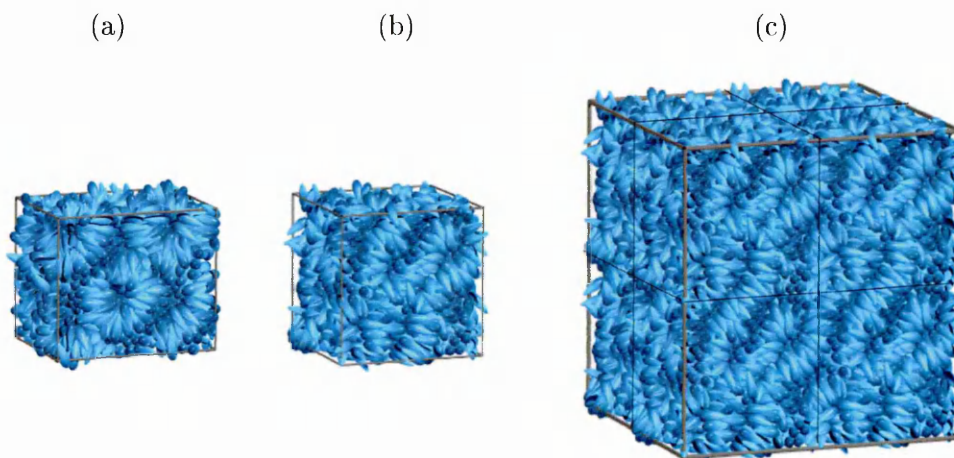
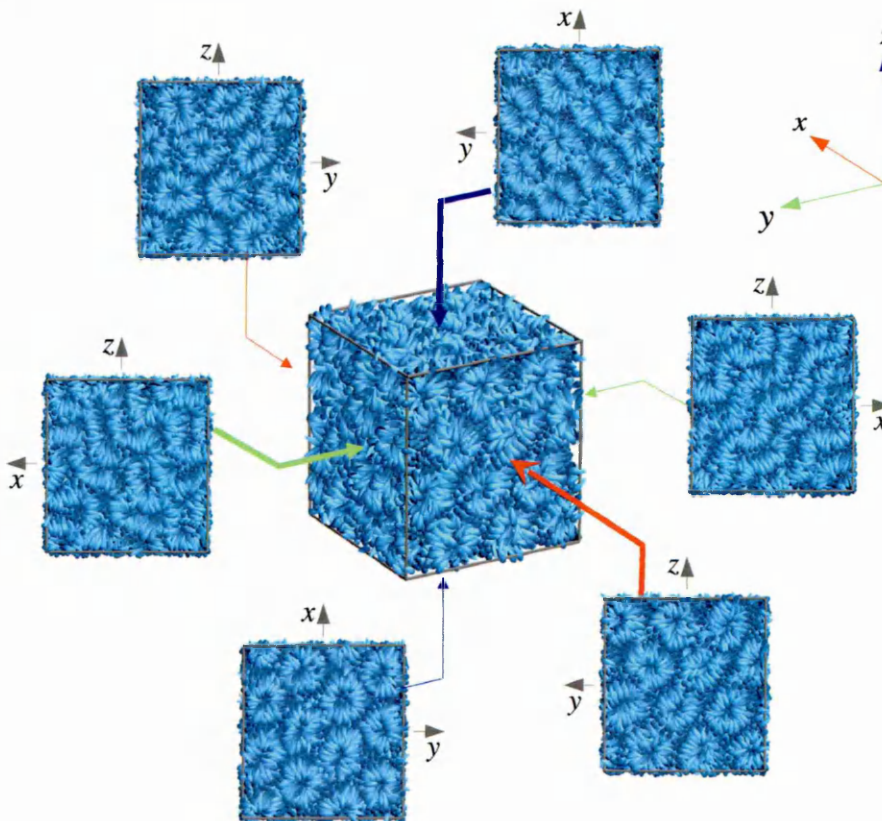


Fig. 7.2: Snapshots of the N10000 $\kappa 3k_{\theta} 3.8$ system at $\rho = 0.95$ after 1.5 million timesteps.



lose the periodicity inherited from the duplication of the smaller system. The intention here was to allow any structural periodicity intrinsic to the system to

emerge afresh in the larger simulation volume rather than replicate that which might have been inherited from the original boundary conditions.

The initial arrangement generated from the eight copies of the N1250 $\rho = 0.95$ configuration is shown in figure 7.1 (c). This system was simply run on in *NVE* at this density for 10 million timesteps. No rescaling of any kind was implemented during this first run. The progress of the simulation was frequently checked by inspection of the logged data as well as snapshots of the simulation box. For the first million or so timesteps of the $\rho = 0.95$ run, there were no significant changes. However, when a snapshot was made of the configuration at 1.5 million timesteps, the outward appearance of the system was noticeably altered as shown by figure 7.2, which includes head on views of each of the faces of the simulation box. The most striking aspect of this is the hexagonal distribution of circular features on the two opposite faces perpendicular to the x -direction. A similar pattern is seen on the faces perpendicular to the z -direction, although here the arrangement appears somewhat skewed. The remaining two faces, perpendicular to the y -direction, on the other hand, exhibit a staircase-like pattern of bilayers that zig-zag their way along face diagonals. Selected simulation data meanwhile indicate that the changes responsible for the emergence of this ordering occurred in the interval $\approx 1.2 - 1.4$ million timesteps. As figure 7.3 (a) shows, there is a drop in the excess pressure at this time. We note also that there is a suggestion of pressure anisotropy prior to the drop which appears to be redressed after it. Figures 7.3 (b) and (c) exhibit small but unmistakable increases in the average kinetic energy per particle coinciding with the pressure drop. However, the rate of increase of the mean squared displacement with time decreases slightly at around 1.5 million timesteps. This is perhaps due to the fact that, before the ordering transition occurred, particles were moving in concert to effect that transition and this would add to the apparent average mobility of the individual particles. Otherwise the mean squared diffusion is almost perfectly linear and its components isotropic.

Fig. 7.3: N10000 κ_3 $k_\theta 3.8$ runtime data logged from time zero to 2 million steps.

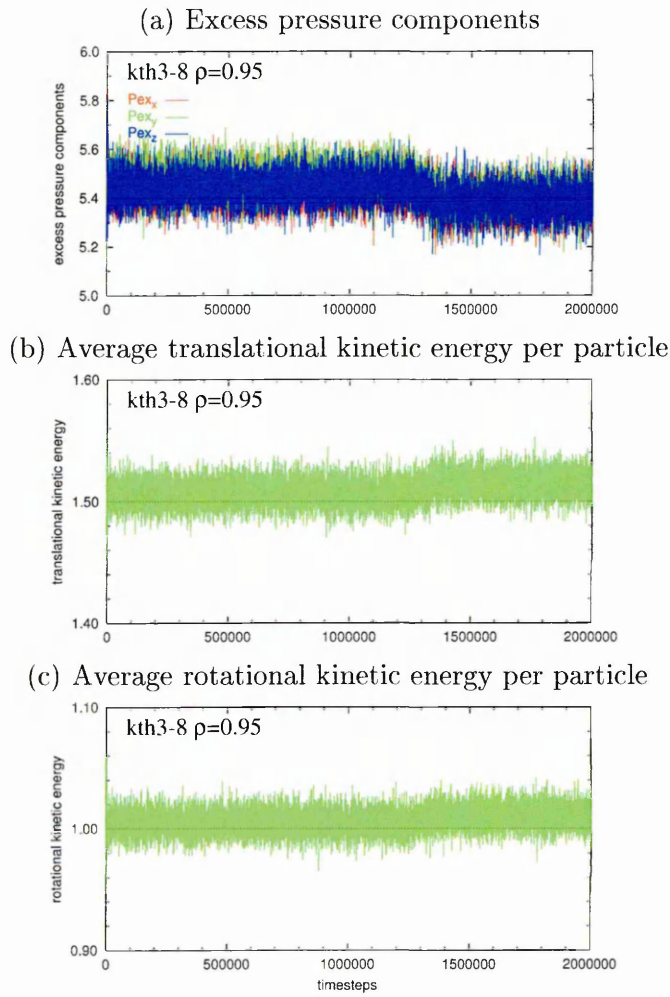
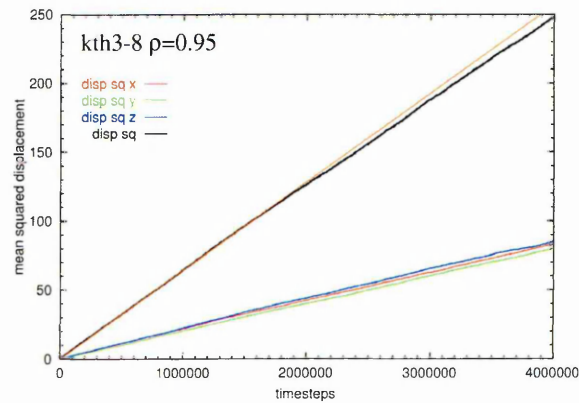


Fig. 7.4: N10000 κ_3 $k_\theta 3.8$ mean squared displacement as a function of time. The orange line is a guide to the eye for discerning the slight decrease in the gradient at 1.5 million steps or so.



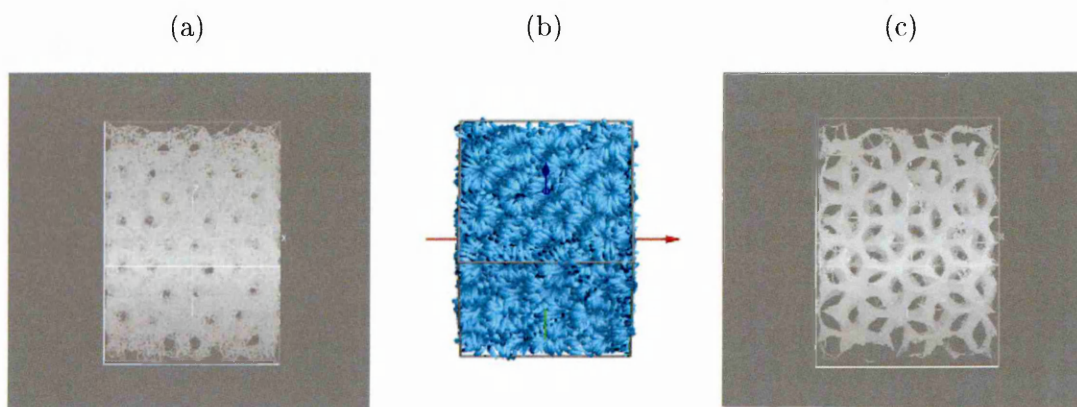
Returning now to the issue of visualising the phase, the programme used to generate snapshots of the simulation box was augmented so that arbitrary cross-sections and thin slices through the simulation volume could be viewed. These confirmed that the hexagonal ordering extended throughout the interior of the simulation volume. However this did not provide much insight into the overarching three-dimensional structure that underlies the superficial hexagonal and staircase patterns. In order to recognise what sort of phase we were dealing with, we needed to visualise the system in a more transparent mode, so to speak, to obtain a global view of it. Fortunately, a ready-made freeware application was available to provide this facility, namely ‘RasMol’¹, an application normally used for rendering ball and stick models of molecules. RasMol has a so-called wire frame mode, whereby lines are drawn between atoms that lie within a certain distance of each other. The utility of this approach, in the context of our system of 10000 particles, is that the wireframe construction is partially transparent, unlike the existing visualisations where solid figures represent the particles. Moreover, RasMol allows objects to be freely rotated, which provides further insight into their three-dimensional structure. Initially a wireframe image was constructed using simply the raw particle coordinates, as shown in figure 7.5 (a). The network is rather too dense to properly see through the system, however it is possible to discern that the surface formed by the locus of particle coordinates describes a network of some kind. From the angle shown, one can look down some of the channels of the network right through to the other side of the box. These channels coincide with the centres of the hexagonally arranged circular formations and with the interstices between them as seen in the full rendering of particles (figure 7.5 (b)). Now at these locations we find that the rounded ends of the particles (coloured dark) are very close to each other. This prompted the idea that if we were to subject the nominal coordinates of each individual particle to a translation along its orientation axis, i.e. towards the rounded end, then this might result in a more compact wireframe network which would afford a better view of its three-dimensional structure. The

¹RasMol Molecular Renderer, Roger Sayle, August 1995. (C) Roger Sayle 1992-1999; Version 2.7.1 June 1999; (C) Herbert J. Bernstein 1998-1999

translation chosen was -1.06 , or approximately $1.5 \sigma_w$ which is half the particle length, so the transformed coordinates approximately coincide with the rounded ends of the particles. The resulting wireframe image is shown in figure 7.5 (c).

By carefully inspecting this object whilst rotating it, it became apparent that the loci of translated coordinates, that is to say the positions of the rounded ends, formed two separate yet identical three- dimensional networks which interpene-

Fig. 7.5: Renderings of the N10000 $\kappa 3k\theta 3.8$ system at the end of a 10 million step *NVE* run at $\rho = 0.95$. (a) shows RasMol wireframe construction of raw particle coordinates, (b) the corresponding povray image and (c) wireframe image of coordinates whose positions have been translated a distance -1.06 along the orientation axis of each particle. All images are viewed from the same angle.

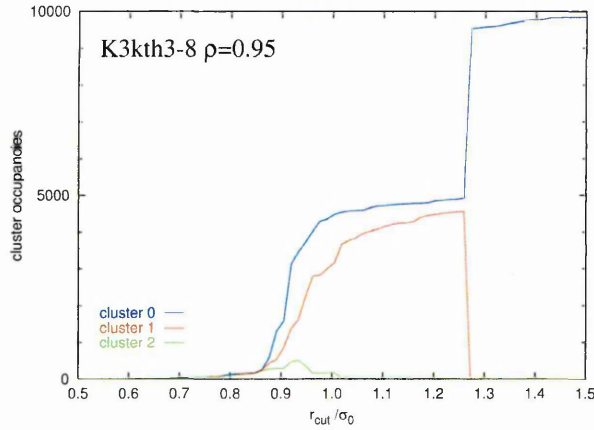


trated one another but never touched. In order to formally assign each of the translated particle coordinates to one or other of these networks, the former were subjected to a cluster analysis routine. In the cluster analysis algorithm used, a cluster is defined by the following statement: it is a set of particles, each member of which lies within a certain cutoff distance of at least one other member of the set. The hope was that, given a sensible choice of cutoff, the cluster analysis algorithm would pick out two large clusters corresponding to the two networks identified visually from the wireframe images.

As it turned out, the analysis easily picked out the networks as evidenced by the data presented in figure 7.6. This plot shows the numbers of particles (occupancies) belonging to the three largest clusters identified by the cluster analysis routine as a function of cutoff. For a broad range of r_{cut} , from approximately 1.0

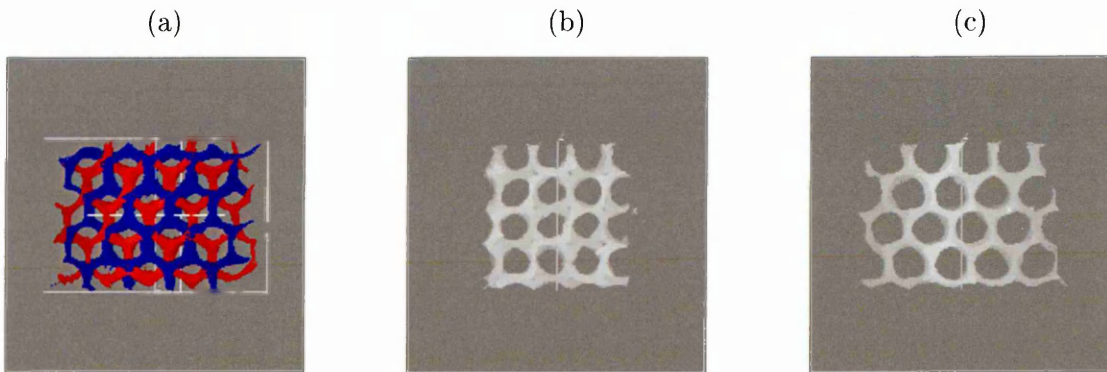
to $1.25 \sigma_w$, two large clusters containing at least 3000 particles (corresponding to the two networks) were identified. The next largest cluster contained at most only a few hundred particles. For this particular system, if the cutoff exceeded

Fig. 7.6: N10000 $\kappa_3 k_\theta 3.8$ the numbers of particles assigned to the three largest clusters identified by our cluster analysis algorithm as a function of cutoff distance.



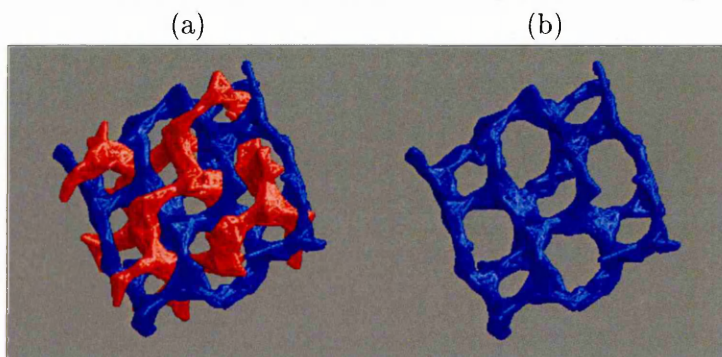
$\sim 1.25\sigma_w$, some particles became identified with both of these networks and the cluster identification algorithm failed to distinguish them. Figure 7.7 (a) shows a wireframe image of the two networks, coloured blue and red. Figures (b) and (c) show two images of one of these networks from slightly different viewpoints, clearly illustrating its two major symmetries.

Fig. 7.7: N10000 $\kappa_3 k_\theta 3.8$ system; end of 10 million step $\rho = 1.02$ run. Wireframe visualisations of the bicontinuous networks formed by the loci of the rounded ends of the particles. (a) shows the two separate but interpenetrating networks (b) and (c) show two views of a single network illustrating its four- and six-fold symmetries.



Closer inspection of a single network suggested that it consists of nodes, each having three branches which connect to other nodes (see figure 7.8). A rudimentary characterisation technique, with the working title of density analysis, was concocted with the aim of quantifying the positions and, hence, the connectivities of the nodes. This approach amounted to identifying the regions of network in which the highest densities of translated particle coordinates were to be found. In brief, this procedure involved the following steps. Firstly a number of saved configura-

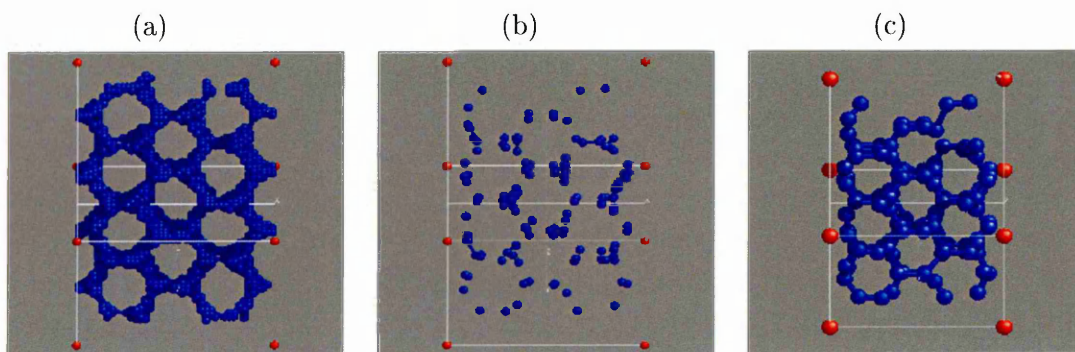
Fig. 7.8: Rasmol renderings of sections of the N10000 $\kappa 3k\theta 3.8$ system at the end of a 10 million step *NVE* run at $\rho = 0.95$. These images were made using the ‘stick’ display option to give a better impression of the networks in three-dimensions. (a) shows sections of both bicontinuous networks whilst (b) shows a single network only.



tions were subjected to cluster analysis to extract, from each, a set of coordinates for the larger of the two single networks. The configurations so analysed had been saved within a relatively short span of simulation time, namely 0-5000 timesteps at intervals of 100 steps. While the orientation and position of any given individual particle will tend to vary considerably over a sampling interval of this length, due to its finite mobility, the overall structure of the bicontinuous networks observed in this phase did not change significantly. Therefore the processing of such a set of configurations permits an averaging of the gross structural characteristics of the phase. The cubic simulation volume was then subdivided into a mesh of $42 \times 45 \times 42$ grid locations, this grid being chosen to correspond approximately to the proportions of the simulation box which had dimensions of $L_x = 20.910$, $L_y = 22.469$ and $L_z = 20.867$. The average number of particles within a certain radius, r_0 , of each mesh point was determined over the 51 saved configurations

and then normalised by dividing by $N_{config}(4/3)\pi r_0^3$. Next, all points having a particle density below a certain threshold were eliminated, the objective being to remove those not close to the nodes or their branches. As figure 7.9 (a) shows, this had the desired effect since all of the spheres shown in this image correspond to surviving meshpoints. A second elimination procedure was then implemented:

Fig. 7.9: N10000 $\kappa 3k_{\theta} 3.8$ system. Density analysis based on 51 single network configurations obtained by running on from the end of the 10 million step $\rho = 1.02$ run. Figure (a) shows all meshpoints which were surrounded by a local particle density exceeding a certain threshold. Figure (b) shows meshpoints which survived an elimination step designed to retain only the meshpoints associated with the nodes of the network. Figure (c) shows the meshpoints after their positions had been refined to bring them closer to the nominal centres of mass of the nodes.

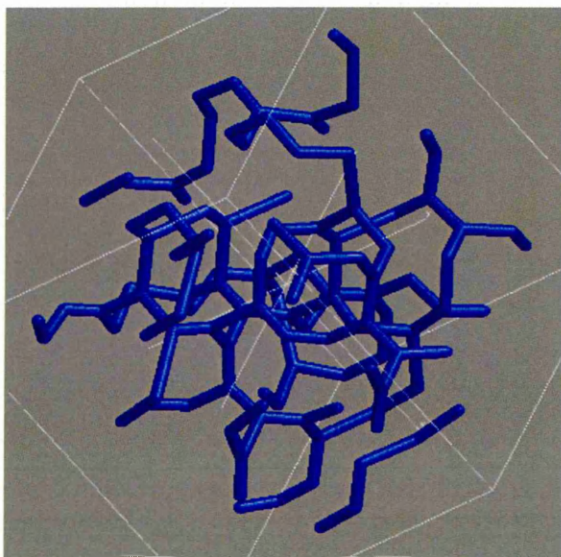


the density of each meshpoint, i , surviving the first round was compared to that of its neighbours, j , within a given radius r_1 . If the density of any neighbouring meshpoint was higher, then i was eliminated. This step was intended to single out the meshpoints lying closest to the node centres based on the hypothesis that these locations have greater densities of translated particle coordinates than the branches. Again, this filtering step appears to have succeeded, since the remaining meshpoints, shown in figure 7.9 (b), appear to be located close to node centres rather than the branches. Finally, the positions of the surviving meshpoints i were refined by determining the collective centre of mass of all meshpoints j within a given radius r_2 (including those that had been previously eliminated) and moving meshpoint i to this position. This algorithm was repeated several times so as to allow the surviving meshpoints to gravitate towards the geometric centres of the nodes.

The exercise described above involved quite a lot of trial and error in arriving at suitable values for the various parameters. In fact it has to be said that the procedure, as it stands, is something of a black art that demands a high level of manual input. In addition it proved effective only when a fine grid was used ($42 \times 45 \times 42 = 79380$ meshpoints) and a fairly large number of configurations were sampled (fifty here) with the result that each analysis took several minutes of CPU time. Development of the method into a more reliable and efficient characterisation tool would require considerable effort.

Nevertheless the process did provide important clarification as to the structure of the networks. Figure 7.10 shows a view of the surviving meshpoints or rather

Fig. 7.10: N10000 $\kappa 3k_{\theta}3.8$ system.

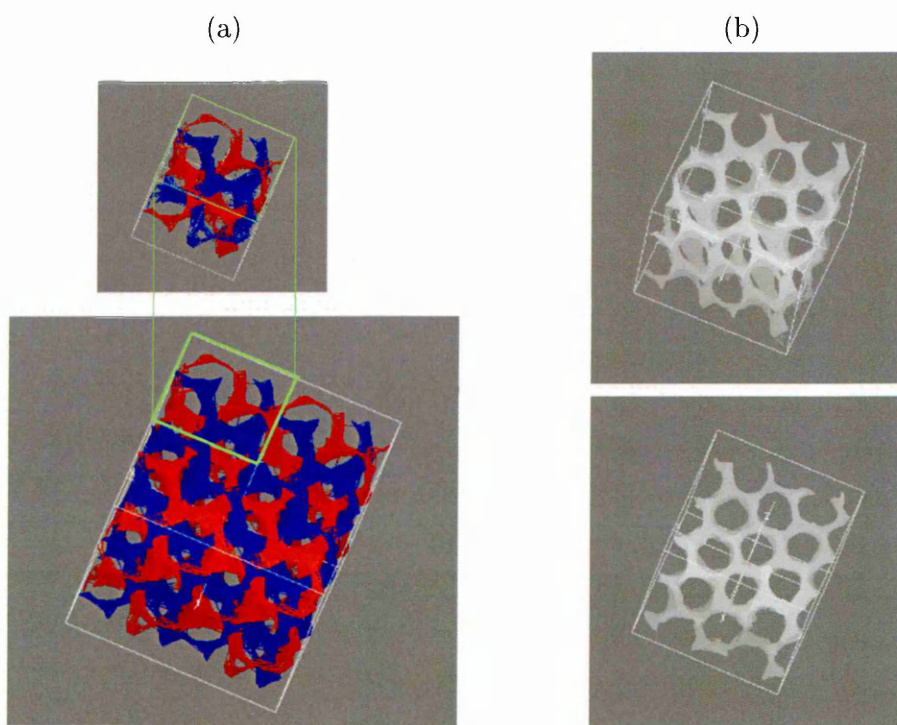


the branches joining them. It clearly demonstrates that the basic building blocks of the networks, the nodes, have three branches of approximately equal length. The structure overall is not perfectly symmetrical which is probably due to one or a combination of the following. Firstly, the simulation box may not have had dimensions that were perfectly commensurate with this phase and, therefore, may have introduced some degree of imperfection. Secondly, at a density of $\rho = 1.02$ the system was still fairly fluid, therefore one might not expect the phase to have perfect crystalline order. Thirdly, the cluster analysis procedure used to provide

the input for the density analysis was somewhat flawed in that it did not quite furnish complete networks – the trailing ends of clusters, at the boundaries of the simulation volume, tended to be somewhat straggly because the particles here were inherently more isolated (literally out on a limb) and, therefore, less likely to be picked up by the cluster analysis code.

So to summarise this section. We have found that the phase earlier christened the curvy-bilayer actually possesses well-defined three-dimensional positional order on a supramolecular lengthscale. This consists of two identical interpenetrating net-

Fig. 7.11: N10000 $\kappa 3k_{\theta}3.8$ system. Wireframe images of a single network at (a) the zeroth and (b) 10 millionth steps of the $\rho = 0.95$ run.



works defined by the loci of the rounded ends of the tapered $\kappa 3$ particles, the junctions of these networks all having three branches. This information strongly suggests that the phase is, in fact, the $Ia\bar{3}d$ or gyroid (G) cubic phase.

Before the results generated by the project were fully analysed, to prepare this thesis, it had been assumed that the gyroid phase was only able to form properly in a large simulation volume. But in fact analysis of the initial and final configu-

rations of the 10 million step run at $\rho = 0.95$ indicate that it was essentially intact before the system was scaled up. This is illustrated by figure 7.11 which shows the double network identified for the initial configuration of the scaled up system and also compares single networks identified for the system at the beginning and end of the $\rho = 0.95$ run. The latter show that although the initial system is a little distorted (no doubt due to the constraints of the original N1250 simulation box) it is nonetheless an essentially fully formed gyroid network. So what appears to have happened at around between ≈ 1.2 and 1.4 million timesteps, as marked by the drop in pressure over that interval (see figure 7.3), was simply a collective readjustment of the system resulting in a more symmetric network structure as exemplified by the single network identified from the end configuration.

7.2 The I-G transition

In an attempt to obtain gyroid phases across a range of k_θ values, compressions of a number of N10000 systems were performed. The system size was chosen in the belief that it would allow for the emergence of the fully-formed gyroid. Furthermore, the larger system volume would extend the distance range of the correlation functions, which might be expected to provide insight into the processes by which the phase assembles. On the other hand, this number of particles was not so large that it would necessitate excessively long simulations occupying a large fraction of the available computational resources. ²

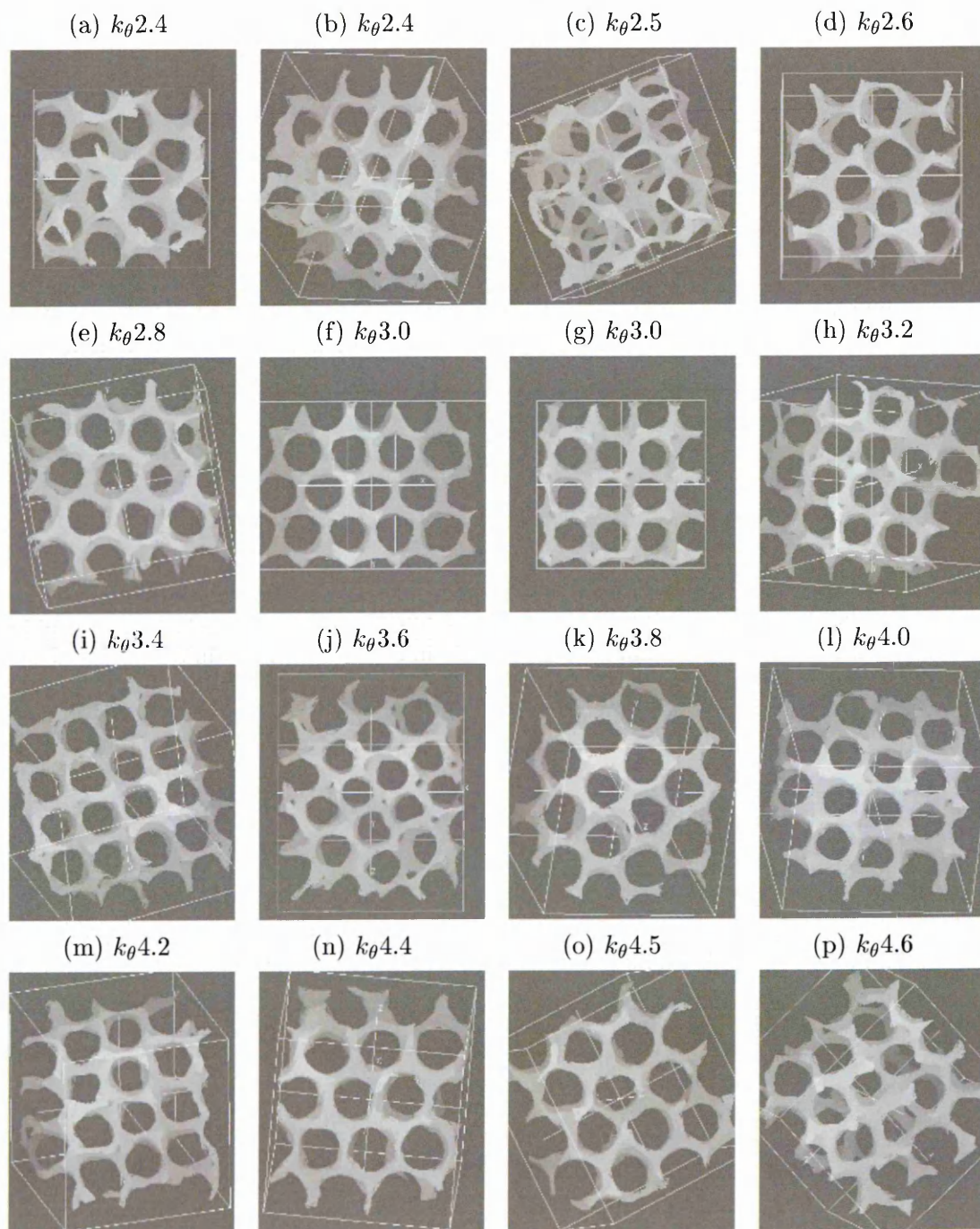
The initial configurations for these simulations consisted of 10000 particles arranged on an FCC lattice at a density of $\rho = 0.15$. These were rapidly compressed to $\rho = 0.85$ by increasing the density in increments of $\Delta\rho = 0.001$ every 100 timesteps. The systems were then compressed to $\rho = 1.02$ via a sequence of 1 million step runs in each of which the density was increased by 0.01. As with the N1250 compressions, this change of density was applied gradually by small

²Each compression series took approximately three weeks to run on two to four processors depending on the intrinsic speed of the processor type.

increases of $\Delta\rho = 0.00001$ every 100 timesteps over the interval 100-200ksteps. The systems were further compressed to $\rho = 1.10$ via a final run of 3 million steps duration in which the density was increased in increments of $\Delta\rho = 0.00001$ every 200 timesteps over the interval 100-1700ksteps. This was conceived as a means of capturing the liquid -solid transition in a more economical way (by looking for changes in the runtime data), rather than extending the series to higher densities by the more usual route of consecutive equilibration/production runs. Anisotropic rescaling was applied to all of the systems, with the density at which it was switched on chosen to approximately coincide with the onset of ordered phases. Compressions were carried out for the following set of shape parameter values: $k_\theta = 2.0, 2.2, 2.4, 2.5, 2.6, 2.8, 3.0, 3.2, 3.4, 3.6, 3.8, 4.0, 4.2, 4.4, 4.5, 4.6, 4.8, 5.0, 5.2, 5.4, 5.6, 6.0, 10.0, 50.0, \infty$.

All the systems from $k_\theta 2.4$ to 4.6 inclusive manifestly entered the gyroid phase, as evidenced by the wireframe images in figure 7.12 which show, for each system, one of the two bicontinuous networks. These were derived from cluster analysis of configurations stored at the ends of the $\rho = 1.02$ runs in the compressions. Nearly all of these systems clearly exhibit the distinctive square and hexagonal symmetries of the gyroid phase, although generally with some level of distortion. For example, the $k_\theta 2.4$ and 4.6 systems, at the edges of the gyroid region, appear to contain what might be described as stacking defects of the voids between networks when viewed from certain angles. Probably the most common form of distortion is shearing perpendicular to one or more of the directions along which the square symmetry is observed. It is present to some degree in systems $k_\theta 3.6$ through to 4.5. The $k_\theta 4.4$ and 4.5 systems suffer, in addition, from shear distortion of their hexagonal symmetry. The most poorly ordered of the systems is $k_\theta 2.5$ which contains multiple defects and disparity in the size and shape of the voids between the networks. Nevertheless the cluster analysis routine was still able to pick out two separate networks for this system without difficulty. The $k_\theta 3.0$ system on the other hand exhibits perfect symmetry. It is, perhaps, significant that the symmetry axes for this system lie in the planes defined by the Cartesian axes

Fig. 7.12: Wireframe images of gyroid phases formed during the compression of N10000 $\kappa 3$ systems with shape parameters in the range $k_\theta 2.4 - 4.6$. The density in all cases was $\rho = 1.02$ and the cluster analysis parameters $r_{cut} = 0.70$, u-shift = -1.06 .

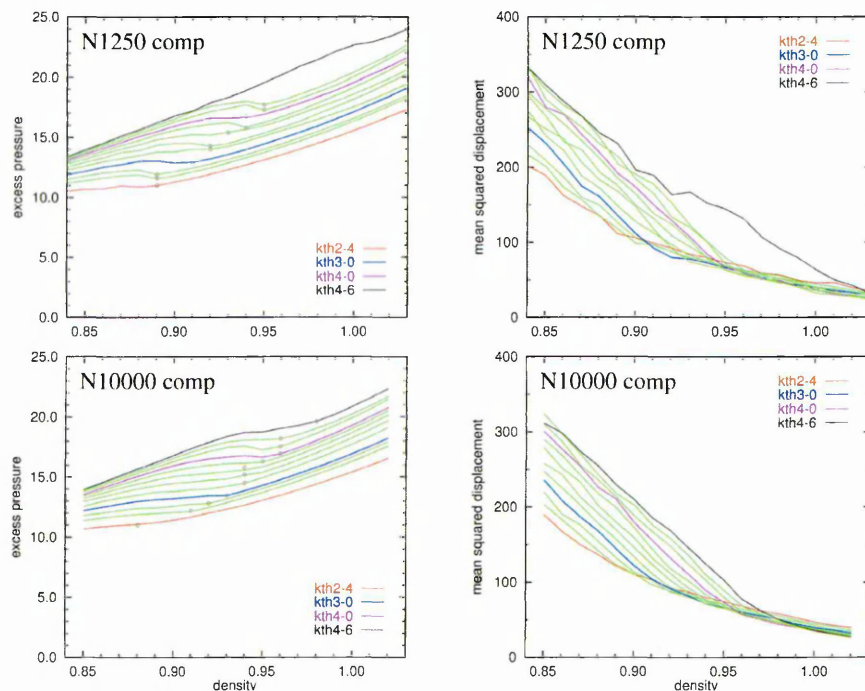


of the simulation box. This again suggests that the quality of the ordering in the gyroid phase depends strongly on the intrinsic commensurability of the simulation box and perhaps the orientation at which the phase happens to form within it.

It is possible that the formation of the gyroid phase could also be influenced by operational factors, principally the alteration of the simulation box aspect ratio as a result of anisotropic rescaling as well as insufficient run length at critical stages in the transition.

The time averaged observables, plotted as a function of density, closely resemble those calculated for the equivalent N1250 compressions, with the isotropic-gyroid transition marked by inflections in the pressure and mean squared displacement. Figure 7.13 presents these data for both system sizes. In both cases the general

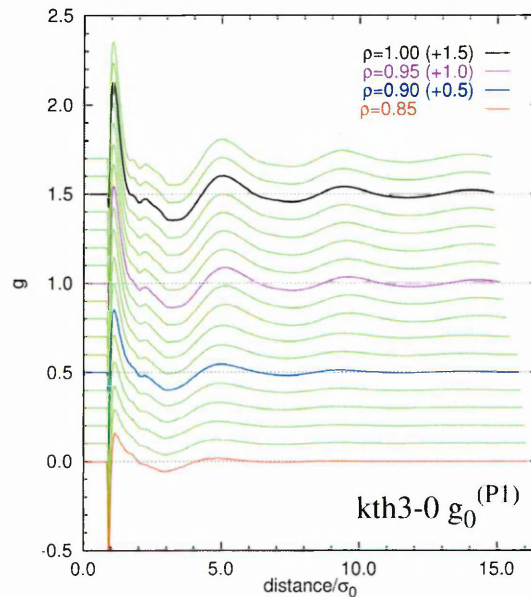
Fig. 7.13: Comparing families of excess pressure and mean squared displacement profiles obtained from the N1250 and N10000 compressions. The mean squared displacement values are those measured after 500 ksteps from the start of the run.



trend is for the isotropic-gyroid transition to move to higher density with increasing k_θ value. For most of the systems, the transition occurred at higher density (and therefore higher pressure) in the N10000 simulations than it did in the N1250 counterpart. Also in the N10000 compression, the $k_\theta 4.6$ system underwent a direct I-G transition whereas in the N1250 simulation the same system $k_\theta 4.6$ went through the sequence I-N-Sm-G albeit with a very narrow and possibly metastable smectic region.

The correlation functions for the $k_{\theta}3.0$ system were examined for features relating to the gyroid structure. This system was chosen because it appeared to be the one most free of defects or distortion. The polar radial distribution function, $g_0^{(P1)}$, as shown in figure 7.14, turned out to be the clearest indicator of gyroid order. At

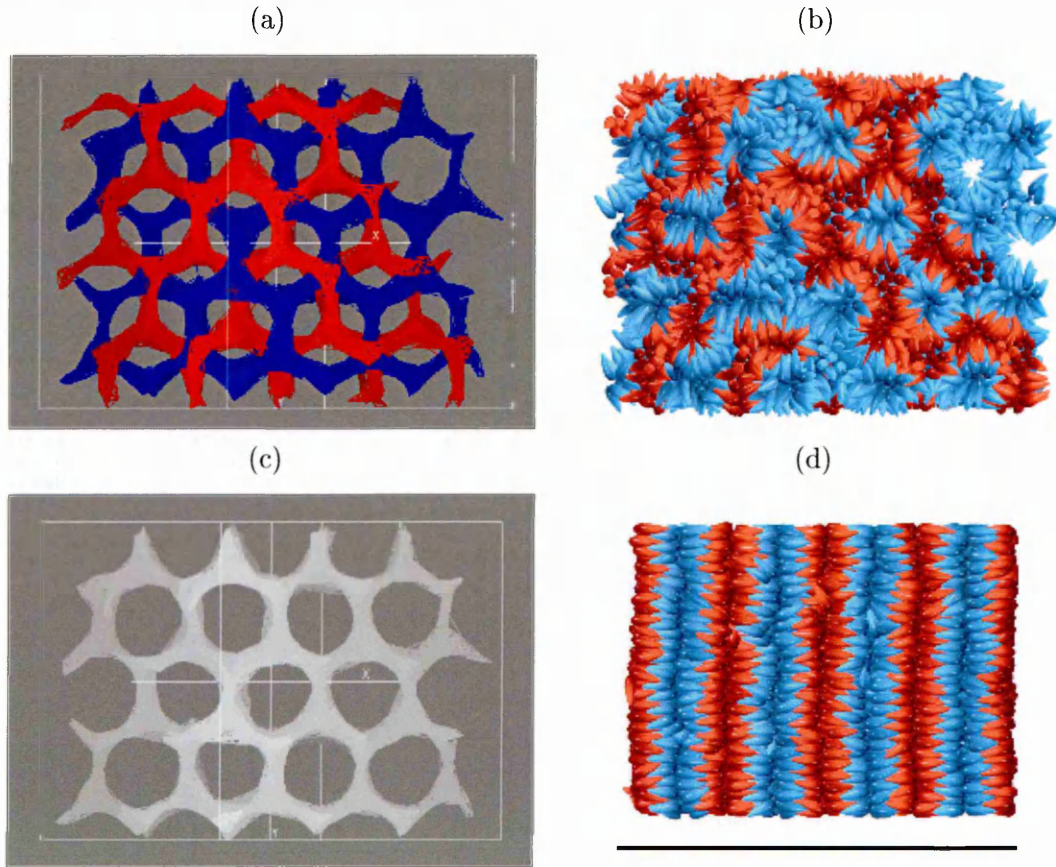
Fig. 7.14: N10000 $\kappa 3k_{\theta}3.0$ system. The evolution of the polar radial distribution function with increasing density. As usual, for the purposes of presentation, the profiles are displaced upwards in order of increasing density.



$\rho = 0.93$, the nominal density for the I-G transition in this system, three long-range peaks are clearly discernable at approximately 5.0, 9.7 and 14.3 σ_w . These can only be due to the correlations between corresponding, that is to say parallel, particles in neighbouring nodes of the networks. This much is confirmed by inspection of the full rendering of the networks, figure 7.15, which shows the true positions and orientations of the particles in both clusters. The first long-range peak is due to correlations between next-nearest nodes in *opposite* networks, the second between next nearest nodes in the *same* network and the third between second nearest neighbours in the opposite networks once more.

There are a number of similarities between the the distribution functions of the gyroid phase and those of the smectic. This is not so surprising given that both

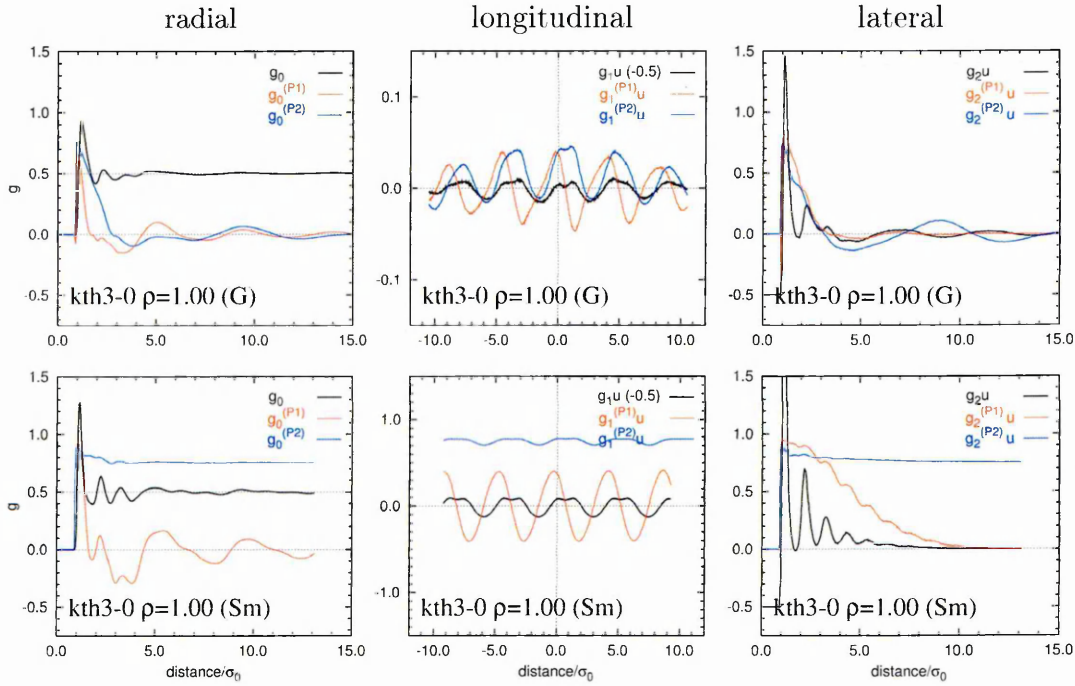
Fig. 7.15: Comparing the gyroid and smectic phases formed by a system of 10000 $\kappa 3k_{\theta}3.0$ particles. (a) Wireframe image showing the two interpenetrating networks of the gyroid phase. (b) An equivalent povray image of the two networks employing the same colour coding. (c) Wireframe image of a single network. (d) A povray image of the smectic system, here the colour coding is simply used to emphasise the similarities between the two systems in terms of the correlations between particles in alternate bilayers. The density of both phases is $\rho = 1.00$



phases consist of bilayers having similar intra- and interlayer distances, a fact emphasised by figure 7.15 (d). Figure 7.16 compares the distribution functions for the gyroid phase, as obtained by compression of the $\kappa 3k_{\theta}3.0$ system, with the smectic phase obtained from decompression of a field-induced artificial smectic also consisting of $\kappa 3k_{\theta}3.0$ particles. The radial distribution functions, g_0 , both show three prominent peaks at approximately 1.1, 2.2 and 3.3 σ_w , the first corresponds to a positive peak in $g_0^{(P1)}$, which indicates that the correlation is due to parallel nearest neighbours, i.e. particles lying side by side in the same leaflet of a bilayer.

The second peak in g_0 , for the smectic phase at least, coincides with a second positive peak in $g_0^{(P1)}$ which indicates that the correlation is due predominantly to next nearest neighbours in the same bilayer leaflet. The corresponding $g_0^{(P1)}$ value in the case of the gyroid system is however approximately zero, which probably stems from the fact that the bilayers that for this phase are curved rather than being flat. The third g_0 peak, at $\sim 3.3\sigma_w$, corresponds in both phases to a trough

Fig. 7.16: N10000 $\kappa 3k\theta 3.0$ system. Comparing key distribution functions at $\rho = 1.00$ for the gyroid phase (formed on compression) and the smectic phase (decompressed from a high density field induced smectic).



in $g_0^{(P1)}$ indicating that it relates principally to correlations between antiparallel leaflets of adjacent bilayers. The longer range peaks in g_0 , at approximately 5 and $9\sigma_w$, are weak for both the smectic and gyroid phases, however in both cases they are in phase with much more distinct peaks in $g_0^{(P1)}$. As mentioned earlier, this implies that these long-range features correspond to correlations between parallel particles in successive bilayers or network nodes.

The longitudinal distribution functions, $g_{1,u}$, exhibit double peaks with a periodicity of $\sim 4.4\sigma_w$. For each double peak of $g_{1,u}$, the maxima are in register with the positive peaks and negative troughs, respectively, of the $g_{1,u}^{(P1)}$ profile, thus

indicating that they correspond to correlations between parallel and antiparallel particles in successive bilayers.

As for the lateral distribution functions, the smectic phase exhibits four or five prominent short-range peaks at $1.1, 2.1, 3.2, 4.3,$ and $5.4\sigma_w$ corresponding to correlations between parallel particles in the same bilayer leaflet. These correlations diminish at long distances as a result of the tilting of particles with respect to the bilayer normal, as previously discussed in section 4.2. For the gyroid phase, the short-range correlations decay much more rapidly as a result of the curvature of the bilayers. However a long-range peak in $g_2^{(P1)}u$ is observed at $\sim 9.0\sigma_w$ which again is due to correlations between equivalent particles in next-nearest nodes in the same network.

The presence of a long range correlation in $g_0^{(P1)}$ (figure 7.14) at densities considerably lower than the I-G transition, which occurs at $\rho = 0.93$ for the $\kappa 3k_\theta$ system, suggests that the formation of the gyroid is gradual and that some sort of structural precursors are involved. This theory is supported by the wireframe images shown in figure 7.17, which feature the ten largest clusters identified at various points in the compression of the $\kappa 3k_\theta$ system. Figure 7.18 meanwhile charts the occupancies of these ten clusters as a function of density. At $\rho = 0.87$, well before the nominal I-G transition occurs, numerous clusters having occupancies of around one hundred are observed, many of which exhibit a three-branched structure. By $\rho = 0.89$, the size and morphology of the clusters would seem to indicate that they are the precursors to the gyroid networks which eventually formed. Subsequent images suggest that the gyroid forms by the growth and subsequent unification of individual branched nodes. At $\rho = 0.92$, two large clusters, containing around 3000 particles each, dominate the structure of the phase; they clearly form a pair of interpenetrating networks. The nominal I-G transition at $\rho = 0.93$ is marked by the appearance of the distinctive symmetry of the gyroid phase. As the system is compressed further, this structure becomes increasingly well defined, such that at a density of 1.02 nearly all the particles in the system are contained in the two networks comprising 4798 and 4465 members.

Fig. 7.17: Wireframe images of the ten largest clusters identified from the end configurations of selected runs during the compression of the N10000 $\kappa 3k_\theta$ system. In all cases the coordinate shift along the particle long axes was -1.06, the cutoff for the cluster analysis was 0.70 except for $\rho = 0.92$ where a slightly lower value of 0.695 was used in order to discriminate the emerging twin networks.

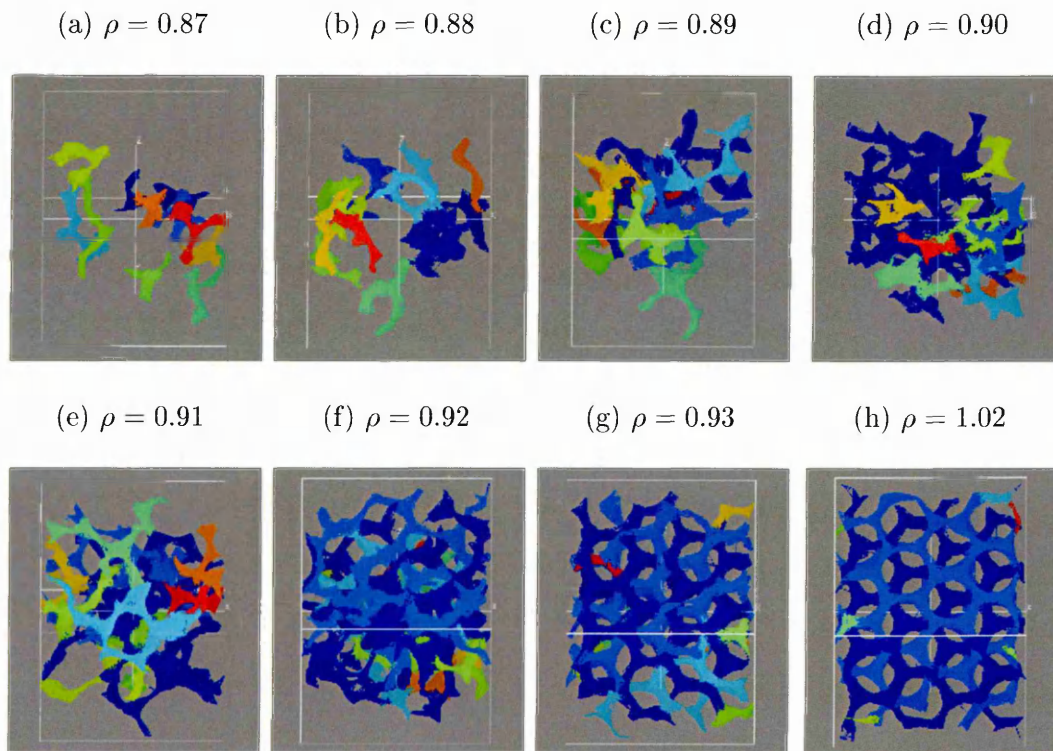
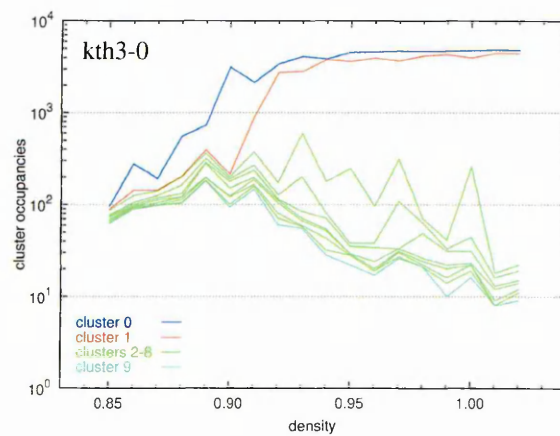


Fig. 7.18: The occupancies of the ten largest clusters identified during the compression of the N10000 $\kappa 3 k_\theta 3.0$ system. In all cases the cutoff used for the analysis was 0.70.



7.3 The Sm-G transition

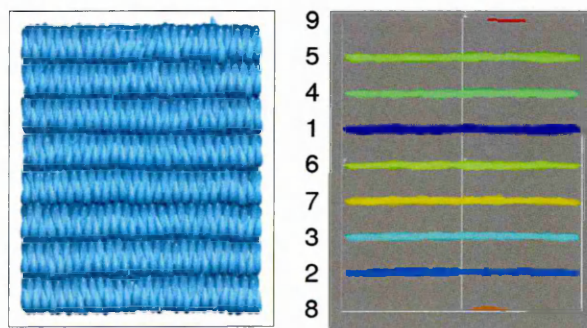
For all the decompressions of N10000 systems, the starting configurations were artificial smectics originating from the field induced N1250 $\kappa_3 k_\theta 3.0$ smectic. As a precaution these smectics were equilibrated, prior to starting the decompressions. In particular this was to check that the interlayer distances were stable. The equilibration sequence consisted of three 200 kstep runs at $\rho = 1.10$, the first and third were carried out in *NVT* with anisotropic rescaling moves attempted every 100 steps over the interval 1000-191000. The middle run was in *NVE* with the simulation box dimensions held constant.

The first stage of the decompression, from $\rho = 1.10 - 1.04$, was implemented via a sequence of 200kstep *NVT* runs with rescaling moves attempted every 100 steps over the interval 70000 to 120000. In each of these runs, the density was decreased in increments of $\Delta\rho = -0.00002$ every 100 timesteps over the interval 10000-60000. For the remainder of the decompression, from $\rho = 1.03 - 0.85$, the density was reduced by increments of $\Delta\rho = -0.00001$ every 100 timesteps over the interval 100000-200000. All of these runs were of 1 million steps duration except for $\rho = 1.00, 0.95, 0.90$ and 0.85 which were extended to 2 million steps. Rescaling moves were attempted every 100 steps over the interval 50000-250000. Rescaling was deactivated, in most cases, well in advance of the predicted break-up of the smectic. This early cessation of rescaling was intended to prevent extremes in the aspect ratios of the simulation box, particularly as these might prove detrimental to the formation of well-ordered gyroid phases. For $k_\theta 2.0 - 2.8$ inclusive, rescaling was applied down to a density of 0.95, for $k_\theta 3.0 - 3.8$ down to 0.98, for $k_\theta 4.0 - 4.8$ down to 1.01 and for $k_\theta 5.0 - \infty$ 1.07.

In what follows we shall show wireframe images of selected systems after the break-up of the smectic or, in some cases, just prior to it. It should be emphasised once again at this point that the cluster analysis procedure used to generate these images is based on particle coordinates that have been translated down the long axis of each so that they are situated at the particles' rounded ends. Therefore,

when a smectic phase is put through this analysis, the clusters identified are the loci of these points. Essentially, these are surfaces that demarcate the division between the structures that we conventionally label as bilayers, that is to say a pair of interdigitating leaflets of particles. This is illustrated by figure 7.19, which compares a wireframe image of the nine largest clusters of translated particle

Fig. 7.19: Povray and wireframe images of the same $\kappa 3k_{\theta}4.0$ system at a density of 1.10. The numbers on the left of the wireframe image indicate the order of cluster occupancy. The cluster containing the most particles is coloured deep blue and the one with the fewest red.

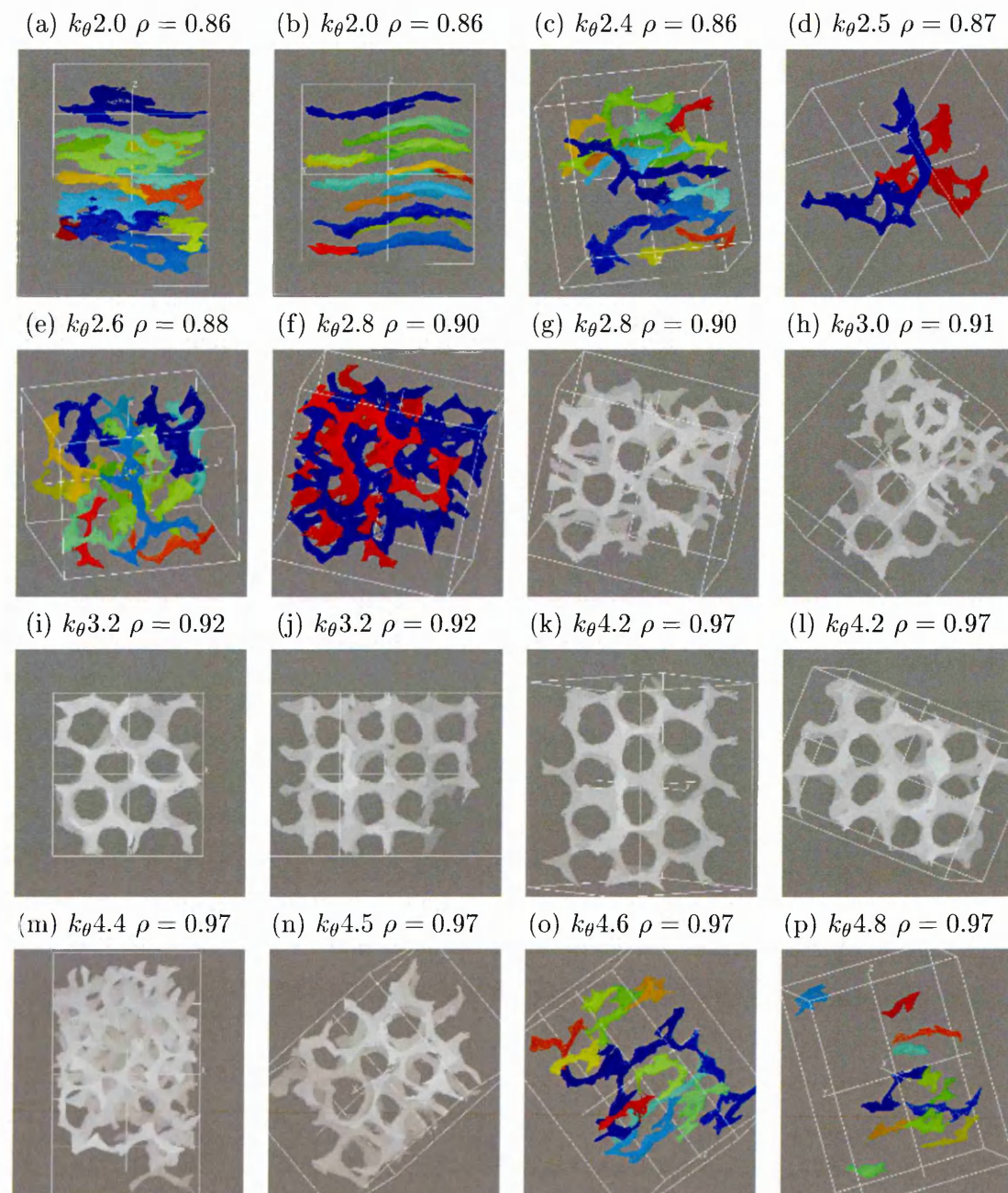


coordinates (right) with a full rendering of the structure (left). Note that the clusters are coloured from blue to red in descending order of their occupancies. Notice also that the analysis algorithm has identified only small regions of the top and bottom leaflets of the configuration as clusters. The reason for this is that these two leaflets, being on the edge of the configuration, have no abutting opposite leaflets and so, as far as the cluster identification scheme is concerned, lack the connectivity possessed by the pairs of adjacent leaflets in the interior of the configuration.

Turning now to figure 7.20, for the systems $k_{\theta}2.4$ to 2.6, we find that the lamellar phase disintegrates into a rather fragmented tracery of clusters. These do exhibit some of the characteristics of the gyroid phase in that many of the clusters have three branches and they intertwine like the bicontinuous network structure of the gyroid. However it was not possible to discriminate two large clusters for these systems and nor are the characteristic gyroid symmetries in evidence. Perhaps we should not be surprised that these systems failed to form orderly structures since the cubic region of the phase diagram from decompression has a narrow tail

at the low k_θ end (see figure 6.26). Also at 1 million steps, the run lengths at the assumed pivotal densities of $\rho = 0.86 - 0.88$ may simply not have been long enough to allow the cubic to form fully.

Fig. 7.20: Wireframe images of the phases formed during the decompression of N10000 $\kappa 3$ systems with shape parameters in the range $k_\theta 2.0 - 4.8$. In all cases the coordinate shift along the particle long axes was 1.06, the cutoff for the cluster analysis was 0.70 except for $k_\theta 2.8$ where it was 0.7250 and $k_\theta 3.0$ which used 0.7125.



In passing, it is interesting to observe the difference between the transition from the smectic to these quasi-cubic systems and the direct smectic-isotropic transition. Figures 7.20 (a) and (b) show two views of the latter – the $k_\theta 2.0$ in the process of disintegrating. This process seems to be preceded by large amplitude undulations of the bilayers which have a perforated appearance³. However, despite these considerable disturbances, the cluster images suggest that the bilayers manage to maintain an essentially sheet like topology right up to the point where they disintegrate completely. The bilayers of the $k_\theta 2.4$ system by contrast appear to break up via some sort of trans bilayer bridging mechanism, this will be investigated in more detail later in this section.

For the $k_\theta 2.8$ system, two distinct networks have been identified and for the $k_\theta 3.0$ system, additionally, the characteristic symmetry of the gyroid is beginning to emerge. Systems $k_\theta 3.2$ through to 4.2 all undergo transitions from the smectic to fairly well-defined gyroids. In general these are more distorted and have a somewhat more ragged appearance than the equivalent images of the gyroids obtained by compression, as shown in figure 7.12. However, it should be remembered that the latter were derived from configurations at a density of 1.02, whilst the former were taken at appreciably lower densities at which the systems would have been in a more fluid state.

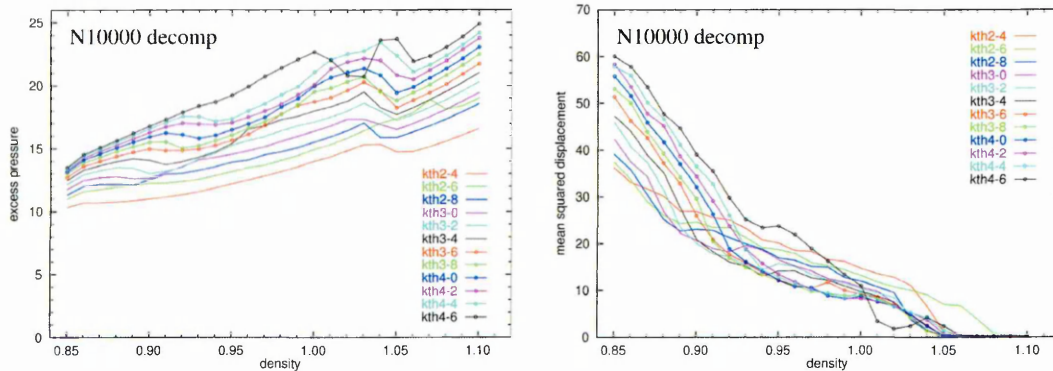
The $k_\theta 4.4$ system appears to be a failed gyroid phase – it consists of three-branched nodes but these could not be resolved into two separate networks. The $k_\theta 4.5$ could be resolved into two networks which have something of the gyroid symmetry about them but are otherwise badly distorted. The $k_\theta 4.6$ system, which on compression did form an orderly gyroid, does not appear to fall into the same phase on decompression. Although cluster analysis suggests that the smectic bilayers may have some tendency to break down into a network like structure, the runtime data shows that this system behaves more like a nematic – mobility is enhanced in the

³This is not due to actual voids in the bilayers, rather it is due to regions where there happen to be several particles with their orientations more or less parallel to the bilayers rather than perpendicular, as they are when the bilayers are well-ordered. Since the cluster analysis used here works on particle coordinates that have been translated towards the rounded ends of the particles, the clusters it identifies will appear depleted of coordinates where these regions exist

z-direction over the density range 0.99-0.94 besides which the order parameter, though in steep decline, remains appreciable over this range. Snapshots of the system at $\rho = 0.97$ also show the system to have all the appearance of a nematic, with weak and localised vestiges of smectic order.

The visual interrogation of the systems of tapered particles described above shows that, as well as self-assembling during the compression of isotropic fluids, gyroid phases also readily formed via the decompression of smectics and across a similar swathe of shape parameters. This is confirmed by the pressure and mean squared displacement profiles, shown in figure 7.21 which exhibit similar shapes to those of figure 7.13. It probably true to say that the decompression route is the more

Fig. 7.21: Families of excess pressure and mean squared displacement profiles obtained from the N10000 decompressions.

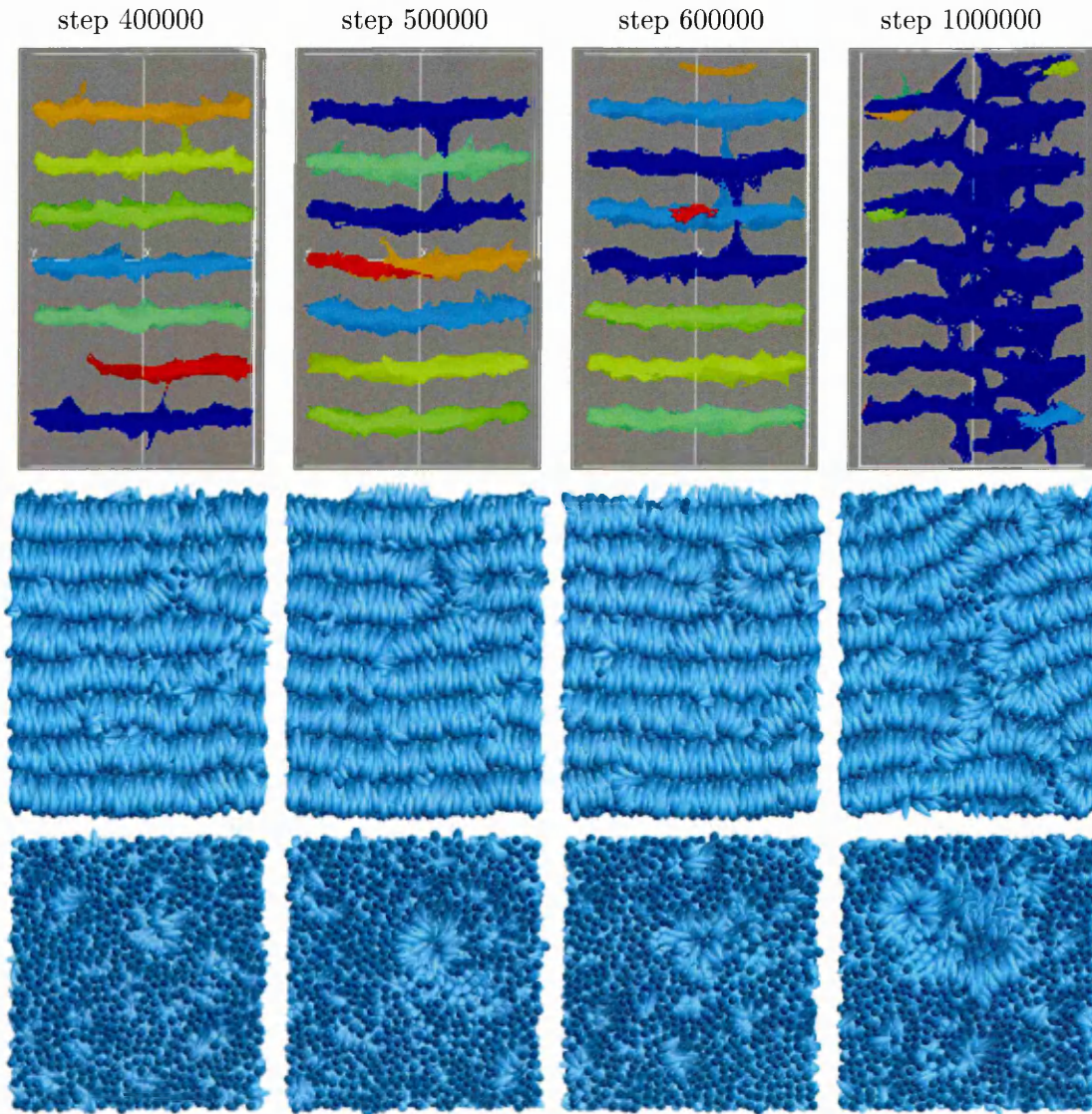


difficult of the two, given that it affords a narrower density range over which the gyroid can form before reaching the low-density isotropic region. This is reflected in the relatively untidy appearance of the pressure and displacement curves and also by the failure of systems with k_θ of 3.0 or less to form orderly bicontinuous networks.

Naturally, the next question to ask is: how does a system of flat bilayers with one-dimensional positional order transform into a highly curved double network of bilayers with three-dimensional positional order? To begin to answer this question we followed the break-up of the smectic bilayers using, once more, cluster analysis. The system chosen for study was $\kappa 3k_\theta 4.0$ since, out of all the systems, it

seemed to form the most orderly gyroid on decompression. Figure 7.22 illustrates the key stages which would appear to set in motion the transition from smectic to gyroid in that system. Following the gentle decompression of the system from

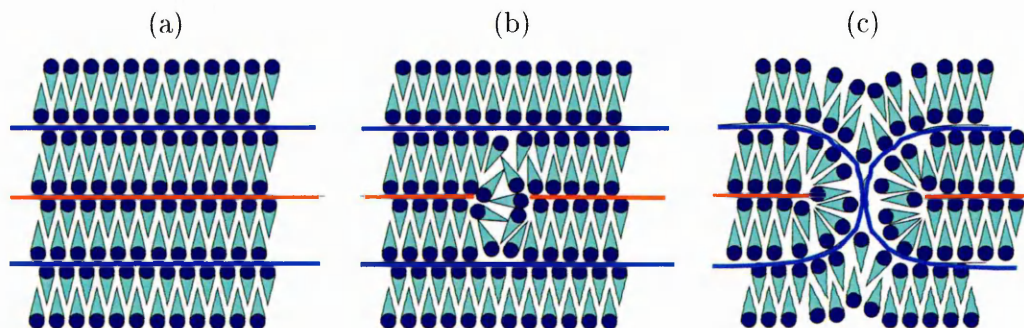
Fig. 7.22: Wireframe images (upper panels) and povray images (lower panels) illustrating the Sm-G transition in a system of 10000 $\kappa 3k_{\theta}4.0$ particles, which took place at a density of 1.00. The numbers above the figures refer to the number of timesteps elapsed in the run. The cluster analysis parameters used to produce the wireframe images were $r_{cut} = 0.70$, u-shift = -1.06 , in the images themselves the z-components of the coordinates have been scaled by a factor of 1.5.



$\rho = 1.01$ to 1.00 from 100-200ksteps, the bilayers, for a time, remain relatively stable. However they are somewhat distorted by undulations and the individual particles have a wide distribution of tilt angles with respect to the director. Also,

it is common to see individual particles that have been ejected from the structures we conventionally regard as bilayers and subsequently lie horizontally inbetween the lamellae. There are also occasions when a group of particles within a small region of a bilayer⁴ have toppled over and lie horizontally, an event possibly precipitated by some kind of undulation or stretching of the bilayer. Whatever the reason, when this does occur, particles from the bilayers above and below move into the space created. This is illustrated schematically in figure 7.23 (b) and can also be discerned in the circled regions of the step 400000 images in figure 7.22. If the disturbance is large enough, it would appear that particles from the bilayers above and below eventually interdigitate with those of the intervening bilayer as shown in 7.23 (c) and highlighted in the step 500000 images of 7.22. We can think

Fig. 7.23: Schematic illustrating the key stages in pore formation leading to the breakup of the smectic phase and the emergence of a bicontinuous gyroid phase. Panel (a) initial smectic bilayers, (b) a ‘stalk’ forms between the middle two bilayers, (c) a ‘pore’ bisecting the middle two bilayers and forming a bridge between the top and bottom bilayers.



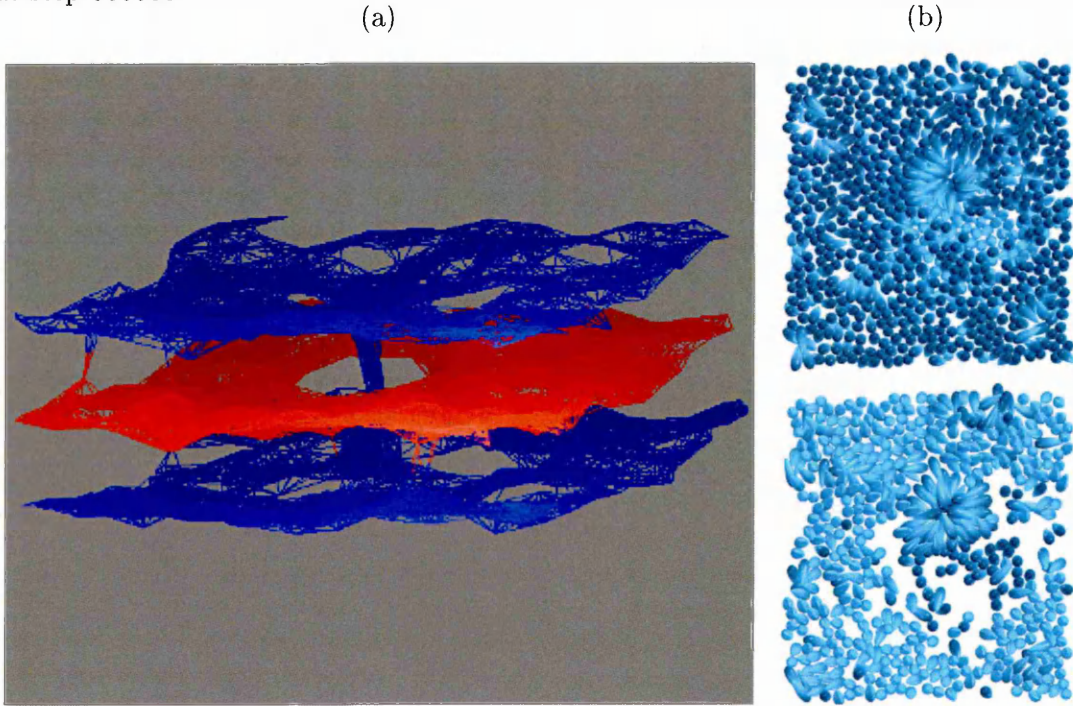
of this formation as a bridge which has grown between the first and third bilayers through a pore in the intervening second bilayer. Figure 7.24 shows a closer view of same along with two thin slices through the system which show separately the particles belonging to the lower and upper leaflets of the intervening bilayer and thus a cross-section of the bridge running through the pore. This is an event which marks the beginning of the end for the smectic phase, for a short time later, by step 600000, another bridge has formed between the second and fourth bilayers.

⁴Here, by bilayer, we mean the bilayers identified by the cluster analysis i.e. the abutting rounded ends of adjacent leaflets.

By the millionth step, stalk formation has spread throughout the entire right hand side of the system.

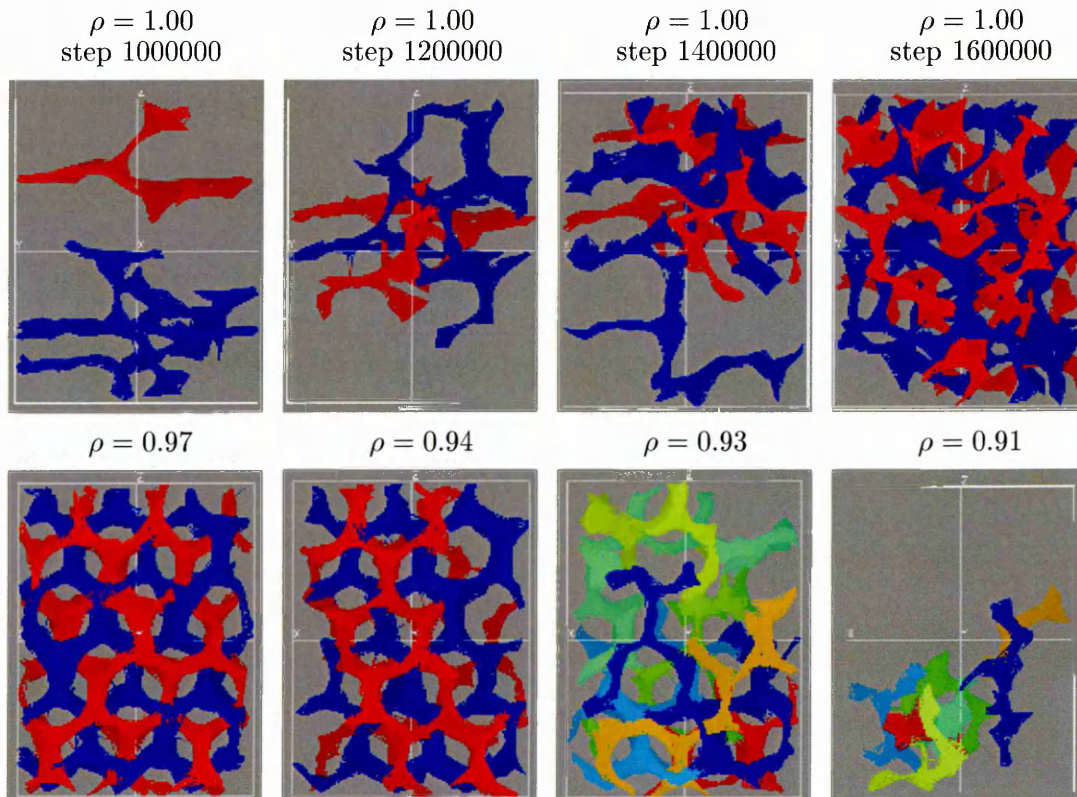
Subsequently the layered structure of the smectic phase begins to break down

Fig. 7.24: (a) Wireframe image illustrating the first ‘stalk’ structure to form in the N10000 $\kappa 3k_{\theta}4.0$ system. (b) Cross sections through the lower and upper leaflets of the bilayer through which the stalk passes. These images are based on configurations stored at step 500000.



and the characteristic double network of the gyroid emerges. This is illustrated in figure 7.25, the first six panels show the two largest clusters which, by step 1600000, extend throughout most of the simulation volume and are clearly interpenetrating. The structure is riddled with defects at this stage, and much making and breaking of bridge/pore pairs is required before, on decompression to $\rho = 0.93$, the networks attain the characteristic symmetry of the gyroid phase. This is maintained down to a density of approximately 0.93 at which point the twin networks start to disintegrate into the isotropic phase.

Fig. 7.25: Wireframe images illustrating the development of the bicontinuous network structure of the gyroid phase in a system of 10000 $\kappa 3k_{\rho} 4.0$ particles. The numbers above the figures refer to the number of timesteps elapsed in the run. The cutoff used to identify the clusters in the upper four images was $r_{cut} = 0.64$, this slightly lower value being necessary to discriminate the nascent twin networks. The cutoff used for the lower four images was the usual $r_{cut} = 0.70$.



7.4 Summary and conclusions

We have shown in this chapter that the curvy bilayer, or domain ordered phase as it was christened in Barmes work, is in fact the $Ia\bar{3}d$ gyroid cubic phase. This phase freely self-assembles from the isotropic fluid upon compression, to our knowledge this is the first time that such a phase transition has been observed in MD simulations. Furthermore it should be emphasised that it is particle shape alone that is responsible for this transition, a result that is without theoretical prediction. It is pertinent to note at this point that since our model is purely steric, i.e. no attractive interactions enter into it, its behaviour is not just relevant to

systems of molecules. It may in principle apply to any system of freely suspended bodies, in particular to colloidal solutions. The results of the simulations presented here therefore suggest that if the correct shape of colloidal particle could be synthesised then it might be possible to obtain, through self-assembly of such particles, three dimensional periodic structures across a range of length scales. If realised, such structures would present considerable scope for technological applications for example as photonic bandgap structures, high surface area frameworks for catalytic processes and scaffolds for tissue growth. We have also observed, in the decompression sequences, a transition from the smectic to the G phase. This transition appears to be mediated by the growth of stalks between two bilayers, subsequently leading to the opening up of pores which bisect the two bilayers and thus form a bridge between the bilayers immediately above and below. This sort of mechanism is thought to operate in systems of lipid bilayers and in particular may play an important role in the process of membrane fusion taking place at the cellular level in living organisms, see for example [40]. The detailed study of the stalk-pore formation dynamics in our model system may provide useful insights into this fundamental biological process.

Clearly then there is great incentive to intensify and extend these simulation studies of the gyroid phase in order to gain a better understanding of its properties and the processes that lead to its formation. The most pressing need is to develop the proper tools to characterise the overall structure of the gyroid phase. Initially this could be done by perfecting the density analysis routine described in section 7.1 in order to produce accurate maps of the network node locations. Batches of such maps could then be analysed using appropriate distribution functions to obtain the lengths of the branches between the nodes and their angles with respect to one another thus furnishing a precise quantitative description of the gyroids periodicities. Such knowledge might well lead to more effective simulation procedures in terms of assessing what size of simulation box is most commensurable to a particular phase. A more advanced level of structure characterisation would involve describing the surfaces formed by the loci of particle coordinates. The

loci of the points midway between the two interpenetrating networks is actually described by an infinite periodic minimal surface (IPMS) [41]. These are well-established mathematical structures and techniques exist to describe their global packing and curvature properties. This provides a part of a formal theoretical basis for understanding why it is that phases like the gyroid actually form in the first place. Some preliminary work has already been performed by Schröder-Turk in mapping particle coordinates from configuration files onto an IPMS [42].

Another important extension to the simulation studies of the gyroid phase would be to run polydisperse systems, i.e. systems with a distribution of particle shapes in terms of aspect ratio and/or degree of taper. Such polydispersity permits greater variation in the width of the ‘tunnels’ that run inbetween the periodic network and as a result different types of cubic network can form. Continuous transformations between the networks could be modelled by systematically varying particle shape distribution. It is known that there is polydispersity in the constituents of cell mebranes and that this is one of the factors that contributes to their functionality. Also synthetic colloidal dispersions exhibit varying degrees of polydispersity.

Finally, in relation to characterising the I-G and Sm-G phase transformations, it would be eminently possible to develop more sophisticated cluster analysis techniques which would allow one to track the evolution of individual clusters as the simulation progressed. Thus the changes in the morphology of aggregates of particles could be followed through the phase transitions thus providing greater insight into the transformation dynamics than isolated snapshots.

CHAPTER 8

Summary and Conclusions

Using the molecular dynamics technique, we have investigated the effect that polar shape anisotropy has upon the flexoelectric properties and phase behaviour of systems of soft repulsive particles.

In the studies of flexoelectricity, reported in chapter 5, we measured the splay and bend flexo coefficients, e_{11} and e_{33} , for four types of monodisperse nematic system each consisting of 10000 particles. The systems considered consisted of the tapered $\kappa 3k_{\theta} 5.0$, $\kappa 3k_{\theta} 7.0$ and $\kappa 5k_{\theta} 5.0$ particles as well as $\kappa 3k_{\theta} \infty$ particles, the latter being virtually equivalent to Gaussian ellipsoids. Each type of system was run for 10 million timesteps at various densities and, thus, different levels of prevailing nematic order. For the tapered systems, the e_{11} values, as measured in the director frame, were all positive and ranged from a minimum of +0.060 to a maximum value of +0.202, the e_{33} values on the other hand were all negative and ranged from -0.039 to -0.285. For the uniaxial particles the sign of e_{11} was not constant and the values varied between -0.011 to +0.022 whilst the e_{33} values were found to fall into a similar range of between -0.014 and +0.023. No clear trends in either coefficient were discerned for the tapered particles either as a function of particle shape or order parameter. The reasons for this were unclear but the

most likely cause would seem to be long-wavelength fluctuations in certain quantities from which the coefficients were derived. Extremely long simulation runs for the purposes of monitoring convergence (or lack thereof) for e_{11} , e_{33} and related quantities would be an obvious if rather crude way of testing this hypothesis.

Our study of the phase behaviour, upon compression, of tapered particles ranging from the highly tapered $k_\theta 2.0$ particles to Gaussian ellipsoids produced a phase diagram that was broadly in agreement with the one previously obtained by Monte Carlo simulations of hard particles [14, 43]. For $k_\theta \{2.0 - 2.2\}$ an I-Sm-Sm(solid) phase sequence was observed, for $k_\theta 4.8$ and upwards the sequence was I-N-Sm-Sm(solid). Particles with intermediate degrees of tapering, $k_\theta \{2.4 - 4.6\}$, entered, from the isotropic, a so called ‘curvy-bilayer’ (CB) phase, which persisted to high density but without undergoing a clear liquid-solid transition. High density smectic configurations were then generated for all shapes of particle from a ‘seed’ smectic configuration, this having been previously obtained by way of a compression run during which an orienting field was applied. Upon decompression, the $k_\theta \{2.0 - 2.5\}$ systems underwent a Sm(solid)-Sm-I phase sequence, $k_\theta \{2.6 - 4.5\}$ an Sm(solid)-Sm-CB-I sequence, whilst for k_θ values of 4.6 and above the progression was Sm(solid)-N-I.

The structure of the CB phase was studied more intensively and found to be the bicontinuous cubic phase $Ia\bar{3}d$ or gyroid (G) as it is also known. The I-G phase transition appeared to take place via the self-assembly of clusters with branches which, as the system was further compressed, joined up to form the phase’s distinctive double network. Most of the networks formed were highly orderly although some particularly those at the edges of the G phase region exhibited, shear distortions and in a few cases stacking defects. The Sm-G transition took place via a mechanism in which stalks formed between adjacent bilayers which were then subsequently bisected by pores which thus formed a bridge between the layers immediately above and below the two that were initially connected by the stalk. The free self-assembly, by either route, of the gyroid phase has never before been recognised in MD simulations.

In conclusion, the rich phase behaviour of $\kappa 3$ tapered particles is purely a function of shape. Because the particle interactions are purely steric, the behaviour observed in these studies may, in principle, be applicable to any collection of freely suspended bodies. Therefore, the mechanisms involved in the I-G transitions, observed in the simulations reported here, could equally apply to colloidal solutions. A route to the self-assembly of three dimensional periodic structures like the gyroid from colloidal solutions would be highly useful from a technological standpoint. Meanwhile the study of the Sm-G transition by way of stalk and pore formation could provide valuable insights into areas of biophysics such as cell membrane fusion, a process that is thought to take place by a similar mechanism. Here we have only investigated the effect of the degree of taper on gyroid phase formation. It would, however, be of considerable interest to achieve a more complete characterisation. as well as studying the effect of particle aspect ratio κ , for example¹, it would be fascinating to study mixture systems so as to learn whether other more complex mesophases can be accessed. The results presented in this thesis have shown that a relationship exists between particle shape polarity and mesophase structure – the outstanding future goal, therefore, is to determine what, fundamentally, drives this relationship and, thus, know how to exploit it.

¹In a one-off simulation, soon after our initial discovery of the G-phase in the $\kappa 3k_{\theta}3.8$ system, we did observe the same phase in a system of 16000 $\kappa 3k_{\theta}4.0$ particles, scaled up from a N2000 configuration generated by an isotropic compression sequence.

APPENDIX A

Reduced Units

Reduced quantities are expressed in terms of a fundamental set of basic units, typically a basic length unit, σ_0 (which we instead name σ_w to avoid confusion with the σ_0 that appears in the expression for the Gaussian overlap contact function and its variants), a basic energy unit ϵ_0 and a basic unit of mass m_0 . In general their values are chosen so as to be commensurate with the characteristic length, energy and mass scales of the system being simulated. So for example in a simulation of an atomic fluid, a suitable value for σ_0 would be the ionic radius of the atoms, ϵ_0 would be set at the value of potential minimum and m_0 would simply be set at the mass of each atom. Since the tapered particles in our simulations are essentially objects of a purely geometric nature, and not intended to represent any particular species of molecule, the numerical values we choose for our fundamental units are entirely arbitrary. Equally, the SI units in which these values are measured is immaterial. Therefore the basic units are defined simply as

$$\sigma_w = \sqrt{(0.5^2 + 0.5^2)} = 1/\sqrt{2} \approx 0.707 \quad (\text{A.1})$$

$$\epsilon_0 = 1 \quad (\text{A.2})$$

$$m_0 = 1 \quad (\text{A.3})$$

In this work we also find it convenient to arbitrarily define a reduced moment of inertia $I^* = 1$ and a reduced dipole moment $\mu^* = 1$ for our particles. The relationships between reduced quantities, x^* , and their equivalents, x , as expressed in SI units are obtained by dividing the SI quantity by the appropriate reduced unit, i.e. a unit expressed in terms of the fundamental basic units such as σ_w , ϵ_0 and m_0 .

$$\text{Potential } U^* = U\epsilon_0^{-1} \quad (\text{A.4})$$

$$\text{Time } t^* = t \left(\frac{\epsilon_0}{\sigma_w^2 m_0} \right)^{1/2} \quad (\text{A.5})$$

$$\text{Temperature } T^* = T (k_B \epsilon_0^{-1}) \quad (\text{A.6})$$

$$\text{Distance } r^* = r \sigma_w^{-1} \quad (\text{A.7})$$

$$\text{Linear velocity } v^* = v \left(\frac{m_0}{\epsilon_0} \right)^{1/2} \quad (\text{A.8})$$

$$\text{Linear acceleration } a^* = a \left(\frac{\sigma_w m_0}{\epsilon_0} \right) \quad (\text{A.9})$$

$$\text{Mass } m^* = m/m_0 \quad (\text{A.10})$$

$$\text{Linear momentum } p^* = p (m_0 \epsilon_0)^{-1/2} \quad (\text{A.11})$$

$$\text{Force } f^* = f \left(\frac{\sigma_w}{\epsilon_0} \right) \quad (\text{A.12})$$

$$\text{Angular velocity } \omega^* = \omega \left(\frac{m_0}{\sigma_w^2 \epsilon_0} \right)^{1/2} \quad (\text{A.13})$$

$$\text{Angular acceleration } \alpha^* = \alpha \left(\frac{\sigma_w^2 m_0}{\epsilon_0} \right) \quad (\text{A.14})$$

$$\text{Moment of inertia } I^* = I (m_0 \sigma_w^2)^{-1} \quad (\text{A.15})$$

$$\text{Angular momentum } L^* = L \left(\frac{\sigma_w^2}{m_0 \epsilon_0} \right)^{1/2} \quad (\text{A.16})$$

$$\text{Torque } \tau^* = \tau \epsilon_0^{-1} \quad (\text{A.17})$$

$$\text{Number Density } \rho^* = \rho \sigma_w^3 \quad (\text{A.18})$$

$$\text{Volume } V^* = V \sigma_w^{-3} \quad (\text{A.19})$$

$$\text{Pressure } P^* = P \frac{\sigma_w^3}{\epsilon_0} \quad (\text{A.20})$$

APPENDIX B

Potential, forces and torques

B.1 Summary of potential for tapered particles

The key ingredient in the potential for soft-repulsive tapered particles is the parameterised hard Gaussian overlap (PHGO) contact function

$$\sigma^{PHGO}(\hat{\mathbf{u}}_i, \hat{\mathbf{u}}_j, \hat{\mathbf{r}}_{ij}) = \sigma_0 \left[1 - \frac{\chi}{r_{ij}^2} \left\{ \frac{\alpha^2 a^2 + \alpha^{-2} b^2 - 2\chi abc}{1 - \chi^2 c^2} \right\} \right]^{-1/2} \quad (\text{B.1})$$

where

$$\sigma_0 = (d_i^2 + d_j^2)^{-1/2} \quad (\text{B.2})$$

$$\chi = \left[\frac{(l_i^2 - d_i^2)(l_j^2 - d_j^2)}{(l_j^2 + d_i^2)(l_i^2 + d_j^2)} \right]^{1/2} \quad (\text{B.3})$$

$$\alpha^2 = \left[\frac{(l_i^2 - d_i^2)(l_j^2 + d_i^2)}{(l_j^2 - d_j^2)(l_i^2 + d_j^2)} \right]^{1/2} . \quad (\text{B.4})$$

and

$$a = (\hat{\mathbf{u}}_i \cdot \mathbf{r}_{ij}) \quad b = (\hat{\mathbf{u}}_j \cdot \mathbf{r}_{ij}) \quad c = (\hat{\mathbf{u}}_i \cdot \hat{\mathbf{u}}_j) .$$

Equations B.1 – B.4 have exactly the same form as those used in the generalised contact function for uniaxially symmetric Gaussian overlap particles [22] however, crucially, the semiaxial lengths d_i , l_i , d_j , l_j contained within $\sigma^{PHGO}(\hat{\mathbf{u}}_i, \hat{\mathbf{u}}_j, \hat{\mathbf{r}}_{ij})$ are parameterised in order to model asymmetric uniaxial particles i.e. tapered particles. Specifically the semiaxial lengths for particle i and j are polynomials in (a/r_{ij}) and (b/r_{ij}) respectively

$$d_i(\hat{a}) = \sum_n^{N_d} k_d^{(n)} \hat{a}^n \quad l_i(\hat{a}) = \sum_n^{N_l} k_l^{(n)} \hat{a}^n \quad (\text{B.5})$$

$$d_j(\hat{b}) = \sum_n^{N_d} k_d^{(n)} \hat{b}^n \quad l_j(\hat{b}) = \sum_n^{N_l} k_l^{(n)} \hat{b}^n \quad (\text{B.6})$$

where

$$\hat{a} = (\hat{\mathbf{u}}_i \cdot \hat{\mathbf{r}}_{ij}) = a/r_{ij} \quad \hat{b} = (\hat{\mathbf{u}}_j \cdot \hat{\mathbf{r}}_{ij}) = b/r_{ij} .$$

In equations B.5 and B.6, N_d and N_l denote the numbers of terms in the polynomials for d and l respectively whilst the $k_d^{(n)}$ and $k_l^{(n)}$ are the polynomial coefficients. Note that the set of polynomial coefficients used to describe particle i may be the same as that used to describe particle j or two different sets may be used. To obtain a continuous soft-repulsive interparticle potential suitable for use in MD simulations, the PHGO contact function is incorporated into a shifted truncated form of the Lennard-Jones potential.

$$U_{ij}^{PHGO}(\hat{\mathbf{u}}_i, \hat{\mathbf{u}}_j, \mathbf{r}_{ij}) = \begin{cases} 4\epsilon_0 \{R^{12} - R^6\} + \epsilon_0 & r_{ij} < r_0 \\ 0 & r_{ij} \geq r_0 \end{cases} \quad (\text{B.7})$$

where

$$R = \left(\frac{\sigma_w}{r_{ij} - \sigma(\hat{\mathbf{u}}_i, \hat{\mathbf{u}}_j, \hat{\mathbf{r}}_{ij}) + \sigma_w} \right) \quad (\text{B.8})$$

and ϵ_0 is a constant. For all the simulations reported in this thesis, ϵ_0 was set at 1.0, whilst σ_w was set to a value appropriate for tapered particles having half-widths of 0.5 i.e.

$$\sigma_w = \sqrt{(0.5^2 + 0.5^2)} = \frac{1}{\sqrt{2}}. \quad (\text{B.9})$$

The cutoff distance, r_0 , at which the potential is truncated is defined as

$$r_0 = \sigma^{PHGO}(\hat{\mathbf{u}}_i, \hat{\mathbf{u}}_j, \hat{\mathbf{r}}_{ij}) + (2^{1/6} - 1)\sigma_w. \quad (\text{B.10})$$

B.2 Derivation of forces derivatives

In general, the force between two linear particles i and j interacting via a potential U_{ij} can be expressed as

$$\mathbf{f}_{ij} = -\nabla_{\mathbf{r}_{ij}} U_{ij}. \quad (\text{B.11})$$

U_{ij}^{PHGO} , equation B.7, contains three scalar products involving \mathbf{r}_{ij} , namely $a = (\hat{\mathbf{u}}_i \cdot \mathbf{r}_{ij})$, $b = (\hat{\mathbf{u}}_j \cdot \mathbf{r}_{ij})$ and $r = r_{ij} = (\hat{\mathbf{r}}_{ij} \cdot \mathbf{r}_{ij})$. Therefore equation B.11 may be written as

$$\mathbf{f}_{ij} = -\sum_{\mathbf{s}} \nabla_{\mathbf{r}_{ij}} U_{ij}(\mathbf{s} \cdot \mathbf{r}_{ij}) \quad (\text{B.12})$$

where

$$\mathbf{s} = \{\hat{\mathbf{u}}_i, \hat{\mathbf{u}}_j, \hat{\mathbf{r}}_{ij}\}$$

Expanding the gradient of the potential in equation B.12 yields

$$\nabla_{\mathbf{r}_{ij}} U_{ij}(\mathbf{s} \cdot \mathbf{r}_{ij}) = \hat{\mathbf{i}} \frac{\partial U_{ij}(\mathbf{s} \cdot \mathbf{r}_{ij})}{\partial r_{ij}^{(x)}} + \hat{\mathbf{j}} \frac{\partial U_{ij}(\mathbf{s} \cdot \mathbf{r}_{ij})}{\partial r_{ij}^{(y)}} + \hat{\mathbf{k}} \frac{\partial U_{ij}(\mathbf{s} \cdot \mathbf{r}_{ij})}{\partial r_{ij}^{(z)}} \quad (\text{B.13})$$

Then, by invoking the chain rule for each of the terms on the rhs of B.13, we obtain

$$\begin{aligned} & \nabla_{\mathbf{r}_{ij}} U_{ij}(\mathbf{s} \cdot \mathbf{r}_{ij}) \\ &= \hat{\mathbf{i}} \frac{\partial U_{ij}}{\partial(\mathbf{s} \cdot \mathbf{r}_{ij})} \frac{\partial(\mathbf{s} \cdot \mathbf{r}_{ij})}{\partial r_{ij}^{(x)}} + \hat{\mathbf{j}} \frac{\partial U_{ij}}{\partial(\mathbf{s} \cdot \mathbf{r}_{ij})} \frac{\partial(\mathbf{s} \cdot \mathbf{r}_{ij})}{\partial r_{ij}^{(y)}} + \hat{\mathbf{k}} \frac{\partial U_{ij}}{\partial(\mathbf{s} \cdot \mathbf{r}_{ij})} \frac{\partial(\mathbf{s} \cdot \mathbf{r}_{ij})}{\partial r_{ij}^{(z)}} \\ &= \frac{\partial U_{ij}}{\partial(\mathbf{s} \cdot \mathbf{r}_{ij})} \left\{ \hat{\mathbf{i}} \frac{\partial(\mathbf{s} \cdot \mathbf{r}_{ij})}{\partial r_{ij}^{(x)}} + \hat{\mathbf{j}} \frac{\partial(\mathbf{s} \cdot \mathbf{r}_{ij})}{\partial r_{ij}^{(y)}} + \hat{\mathbf{k}} \frac{\partial(\mathbf{s} \cdot \mathbf{r}_{ij})}{\partial r_{ij}^{(z)}} \right\} \end{aligned} \quad (\text{B.14})$$

The derivatives of the dot products $(\mathbf{s} \cdot \mathbf{r}_{ij})$ with respect to the components of r_{ij} simplify as follows

$$\frac{\partial(\mathbf{s} \cdot \mathbf{r}_{ij})}{\partial r_{ij}^{(x)}} = \frac{\partial}{\partial r_{ij}^{(x)}} \left(s^{(x)} r_{ij}^{(x)} + s^{(y)} r_{ij}^{(y)} + s^{(z)} r_{ij}^{(z)} \right) = s^{(x)}$$

and similarly

$$\frac{\partial(\mathbf{s} \cdot \mathbf{r}_{ij})}{\partial r_{ij}^{(y)}} = s^{(y)} \quad \frac{\partial(\mathbf{s} \cdot \mathbf{r}_{ij})}{\partial r_{ij}^{(z)}} = s^{(z)}$$

Substituting these results into B.13 leads to

$$\nabla_{\mathbf{r}_{ij}} U_{ij}(\mathbf{s} \cdot \mathbf{r}_{ij}) = \frac{\partial U_{ij}}{\partial(\mathbf{s} \cdot \mathbf{r}_{ij})} \left\{ \hat{\mathbf{i}} s^{(x)} + \hat{\mathbf{j}} s^{(y)} + \hat{\mathbf{k}} s^{(z)} \right\} = \frac{\partial U_{ij}}{\partial(\mathbf{s} \cdot \mathbf{r}_{ij})} \mathbf{s} \quad (\text{B.15})$$

Finally, substituting this into equation B.12 results in the following expression for the force

$$\begin{aligned} \mathbf{f}_{ij} &= - \sum_s \nabla_{\mathbf{r}_{ij}} U_{ij}(\mathbf{s} \cdot \mathbf{r}_{ij}) = - \sum_s \frac{\partial U_{ij}}{\partial(\mathbf{s} \cdot \mathbf{r}_{ij})} \mathbf{s} \\ &= - \frac{\partial U_{ij}}{\partial a} \hat{\mathbf{u}}_i - \frac{\partial U_{ij}}{\partial b} \hat{\mathbf{u}}_j - \frac{\partial U_{ij}}{\partial r} \hat{\mathbf{r}}_{ij} \end{aligned} \quad (\text{B.16})$$

$$\text{where } a = (\hat{\mathbf{u}}_i \cdot \mathbf{r}_{ij}) \quad b = (\hat{\mathbf{u}}_j \cdot \mathbf{r}_{ij}) \quad r = \hat{\mathbf{r}}_{ij} \cdot \mathbf{r}_{ij} .$$

The force on particle j due to i is equal and opposite to \mathbf{f}_{ij} , i.e. $\mathbf{f}_{ji} = -\mathbf{f}_{ij}$

B.3 Derivation of torque derivatives

In general, the torque exerted on a linear particle i by a second similar particle j is given by

$$\boldsymbol{\tau}_{ij} = - [\hat{\mathbf{u}}_i \wedge \nabla_{\hat{\mathbf{u}}_i} U_{ij}(\hat{\mathbf{u}}_i, \hat{\mathbf{u}}_j, \mathbf{r}_{ij})] = [\hat{\mathbf{u}}_i \wedge \mathbf{g}_{ij}] \quad (\text{B.17})$$

where \mathbf{g}_{ij} is termed the ‘gorque’. We note that U_{ij}^{PHGO} contains two scalar products involving $\hat{\mathbf{u}}_i$, namely $\hat{a} = a/r_{ij} = (\hat{\mathbf{u}}_i \cdot \hat{\mathbf{r}}_{ij})$ and $c = (\hat{\mathbf{u}}_i \cdot \hat{\mathbf{u}}_j)$. The gorgue may therefore be written as

$$\mathbf{g}_{ij} = -\nabla_{\hat{\mathbf{u}}_i} U_{ij}(\hat{\mathbf{u}}_i, \hat{\mathbf{u}}_j, \mathbf{r}_{ij}) = -\sum_s \nabla_{\hat{\mathbf{u}}_i} U_{ij}(\mathbf{s} \cdot \hat{\mathbf{u}}_i) \quad (\text{B.18})$$

where

$$\mathbf{s} = \{\hat{\mathbf{u}}_j, \hat{\mathbf{r}}_{ij}\}$$

By analogy to equation B.15 we may write

$$\nabla_{\hat{\mathbf{u}}_i} U_{ij}(\mathbf{s} \cdot \hat{\mathbf{u}}_i) = \frac{\partial U_{ij}}{\partial (\mathbf{s} \cdot \hat{\mathbf{u}}_i)} \mathbf{s} \quad (\text{B.19})$$

substituting this into B.18 results in

$$\begin{aligned} \mathbf{g}_{ij} &= -\sum_s \frac{\partial U_{ij}}{\partial (\mathbf{s} \cdot \hat{\mathbf{u}}_i)} \mathbf{s} \\ &= -\frac{\partial U_{ij}}{\partial \hat{a}} \hat{\mathbf{r}}_{ij} - \frac{\partial U_{ij}}{\partial c} \hat{\mathbf{u}}_j \\ &= -\frac{\partial U_{ij}}{\partial a} \mathbf{r}_{ij} - \frac{\partial U_{ij}}{\partial c} \hat{\mathbf{u}}_j \end{aligned} \quad (\text{B.20})$$

The gorque on particle j due to i is derived in a similar fashion, simply by interchanging $\hat{\mathbf{u}}_i$ and $\hat{\mathbf{u}}_j$, hence

$$\begin{aligned} \mathbf{g}_{ji} &= -\sum_s \frac{\partial U_{ij}}{\partial (\mathbf{s} \cdot \hat{\mathbf{u}}_i)} \mathbf{s} \\ &= -\frac{\partial U_{ij}}{\partial \hat{b}} \hat{\mathbf{r}}_{ij} - \frac{\partial U_{ij}}{\partial c} \hat{\mathbf{u}}_i \\ &= -\frac{\partial U_{ij}}{\partial b} \mathbf{r}_{ij} - \frac{\partial U_{ij}}{\partial c} \hat{\mathbf{u}}_i \end{aligned} \quad (\text{B.21})$$

APPENDIX C

Equations of motion

C.1 The Velocity-Verlet integration algorithm

Given the positions, linear velocities and forces on the particles at time step s , the following four steps are applied to obtain $\mathbf{r}_i^{(s+1)}$, $\mathbf{v}_i^{(s+1)}$ and $\mathbf{f}_i^{(s+1)}$

$$\mathbf{v}_i^{(s+1/2)} = \mathbf{v}_i^{(s)} + \frac{\Delta t}{2m_i} \mathbf{f}_i^{(s)} \quad (\text{C.1})$$

$$\mathbf{r}_i^{(s+1)} = \mathbf{r}_i^{(s)} + \Delta t \mathbf{v}_i^{(s+1/2)} \quad (\text{C.2})$$

$$\text{Calculate } \mathbf{f}_i^{(s+1)} \quad (\text{C.3})$$

$$\mathbf{v}_i^{(s+1)} = \mathbf{v}_i^{(s+1/2)} + \frac{\Delta t}{2m_i} \mathbf{f}_i^{(s+1)} \quad (\text{C.4})$$

An analogous set of steps are used to advance the orientations, angular velocities and torques

$$\dot{\mathbf{u}}_i^{(s+1/2)} = \dot{\mathbf{u}}_i^{(s)} + \frac{\Delta t}{2I_i} \mathbf{g}_{\perp i}^{(s)} + \lambda'' \mathbf{u}_i^{(s)} \quad (\text{C.5})$$

$$\mathbf{u}_i^{(s+1)} = \mathbf{u}_i^{(s)} + \Delta t \dot{\mathbf{u}}_i^{(s+1/2)} \quad (\text{C.6})$$

$$\text{Calculate } \mathbf{g}_i^{(s+1)} \quad (\text{C.7})$$

$$\dot{\mathbf{u}}_i^{(s+1)} = \dot{\mathbf{u}}_i^{(s+1/2)} + \frac{\Delta t}{2I_i} \mathbf{g}_{\perp i}^{(s+1)} + \left(\dot{\mathbf{u}}_i^{(s+1/2)} \cdot \mathbf{u}_i^{(s+1)} \right) \mathbf{u}_i^{(s+1)} \quad (\text{C.8})$$

The factor λ'' in C.6 is a Lagrangian correction factor whose initial value is obtained from equation C.9 and then refined by two identical iterative steps C.10 and C.11.

$$\lambda_0 = -\frac{\Delta t}{2} \left\{ \dot{\mathbf{u}}_i^{(s)} \cdot \dot{\mathbf{u}}_i^{(s)} + \frac{\Delta t}{2I_i} \mathbf{g}_{\perp i}^{(s)} \cdot \left(2\dot{\mathbf{u}}_i^{(s)} + \frac{\Delta t}{2I_i} \mathbf{g}_{\perp i}^{(s)} \right) \right\} \quad (\text{C.9})$$

$$\lambda' = \lambda_0 - \frac{(1 + \lambda_0 \Delta t)^2 (\mathbf{u}_i^{(s)} \cdot \mathbf{u}_i^{(s)}) - 1 - \lambda_0 \Delta t}{2\Delta t(1 + \lambda_0 \Delta t)} \quad (\text{C.10})$$

$$\lambda'' = \lambda' - \frac{(1 + \lambda' \Delta t)^2 (\mathbf{u}_i^{(s)} \cdot \mathbf{u}_i^{(s)}) - 1 - \lambda_0 \Delta t}{2\Delta t(1 + \lambda' \Delta t)} \quad (\text{C.11})$$

If transcribing these equations into computer code, note well that the λ that appears in the final term of the numerator in C.11 retains the original value λ_0 as given by C.9, whilst the λ that appear elsewhere in C.11 have the value λ' obtained from the preceding iteration, C.10.

APPENDIX D

Mathematics

The Levi-Civita tensor, $\epsilon_{\alpha\beta\gamma}$ is defined by.

$$\epsilon_{\alpha\beta\gamma} = \begin{cases} +1 & \text{even permutations of } \alpha, \beta, \gamma \text{ i.e. } \{1, 2, 3\}, \{3, 1, 2\}, \{2, 3, 1\}, \\ -1 & \text{odd permutations of } \alpha, \beta, \gamma \text{ i.e. } \{3, 2, 1\}, \{1, 3, 2\}, \{2, 1, 3\}, \\ 0 & \text{all other permutations.} \end{cases}$$

and the Kronecker delta $\delta_{\alpha\beta}$ by

$$\delta_{\alpha\beta} = \begin{cases} 1 & \alpha = \beta, \\ 0 & \alpha \neq \beta. \end{cases}$$

A number of useful identities exist which derive from the relationship between ϵ and $\delta_{\alpha\beta}$ (see for example [44] for a their derivation).

$$\epsilon_{\alpha\beta\gamma}\epsilon_{\gamma\mu\nu} = \delta_{\alpha\mu}\delta_{\beta\nu} - \delta_{\alpha\nu}\delta_{\beta\mu}$$

$$\epsilon_{\alpha\beta\gamma}\epsilon_{\alpha\mu\nu} = \delta_{\beta\mu}\delta_{\gamma\nu} - \delta_{\beta\nu}\delta_{\gamma\mu}$$

$$\epsilon_{\alpha\beta\gamma}\epsilon_{\beta\mu\nu} = \delta_{\gamma\mu}\delta_{\alpha\nu} - \delta_{\gamma\nu}\delta_{\alpha\mu}$$

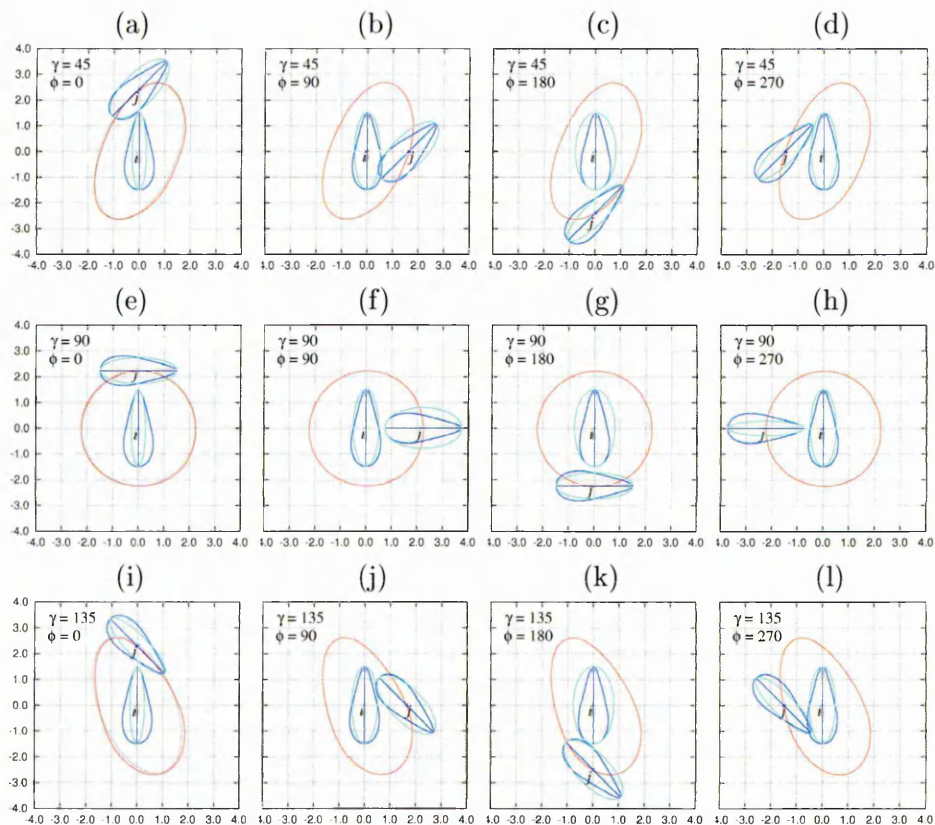
$$\epsilon_{\alpha\beta\gamma}\epsilon_{\alpha\beta\nu} = \delta_{\beta\beta}\delta_{\gamma\nu} - \delta_{\beta\nu}\delta_{\gamma\beta} = 3\delta_{\beta\nu} - \delta_{\beta\nu} = 2\delta_{\beta\nu}$$

$$\epsilon_{\alpha\beta\gamma}\epsilon_{\alpha\beta\gamma} = 6$$

APPENDIX E

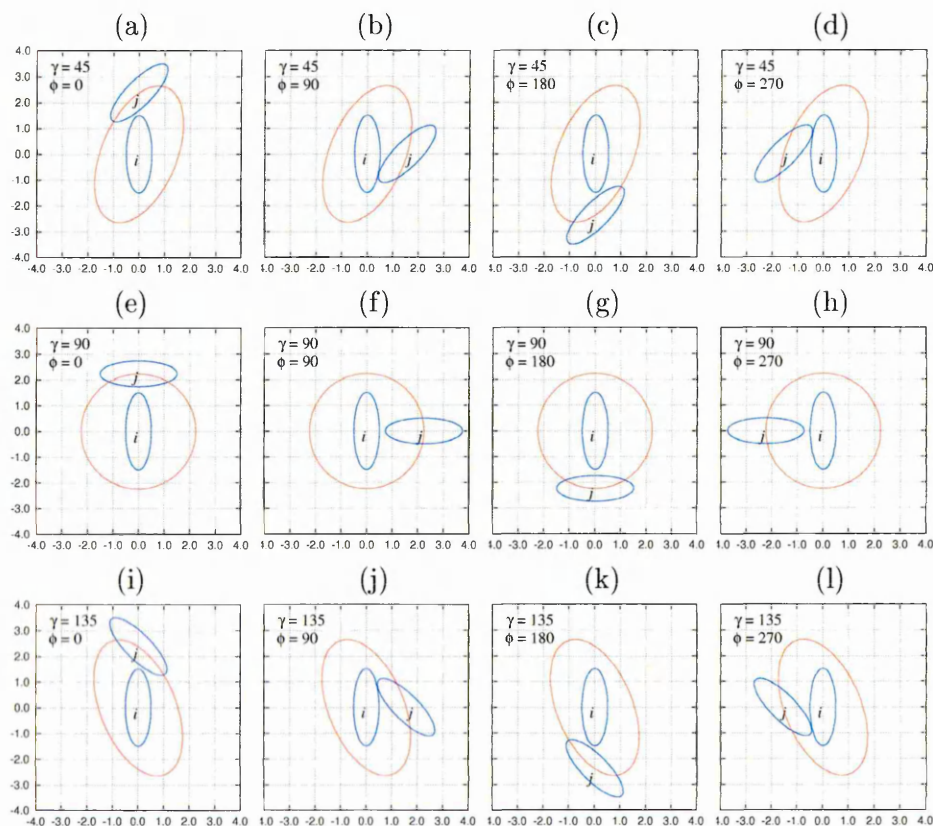
Contact profiles

Fig. E.1: Further $\kappa 3k\theta 3.0$ contact profiles for a variety of mutual orientations. The dashed profiles appearing in (a) (e) and (i) are the equivalent contact profiles for $\kappa 3$ Gaussian ellipsoids.



Equivalent Gaussian ellipsoid contact profiles

Fig. E.2: κ_3 Gaussian ellipsoid contact profiles for mutual orientations equivalent to those of the $\kappa_3 k_{\theta} 3.0$ pears featured in figure E.1.



APPENDIX F

Flexo data

Tab. F.1: Flexoelectric coefficients (quoted to 3 decimal places) for rodlike particles as calculated from 0.5 Mstep runs

κ	k_θ	ρ	\bar{P}_2	e_{11} (lab-frame)	e_{11} (\hat{n} -frame)	e_{11} (covariant)
3	∞	0.877	0.568	0.832	0.401	0.251
"	"	0.894	0.660	-0.216	0.659	0.019
"	"	0.911	0.706	-1.993	-1.689	-0.276
"	"	0.929	0.743	0.247	1.454	-0.244
"	"	0.945	0.767	-21.769	-19.125	-0.509
κ	k_θ	ρ	\bar{P}_2	e_{33} (lab-frame)	e_{33} (\hat{n} -frame)	e_{33} (covariant)
3	∞	0.877	0.568	-0.011	0.007	0.161
"	"	0.894	0.660	-0.446	0.162	0.315
"	"	0.911	0.706	-0.267	0.034	0.307
"	"	0.929	0.743	0.132	0.444	-0.031
"	"	0.945	0.767	0.109	0.893	0.252

Tab. F.2: Flexoelectric coefficients (quoted to 3 decimal places) for tapered particles as calculated from 0.5 Mstep runs

κ	k_θ	ρ	\overline{P}_2	e_{11} (lab-frame)	e_{11} (\hat{n} -frame)	e_{11} (covariant)
3	5	0.92	0.568	0.192	0.215	0.153
"	"	0.94	0.659	0.252	0.151	0.117
"	"	0.96	0.703	0.126	0.138	0.135
"	"	0.98	0.743	0.111	0.090	0.079
"	"	1.00	0.777	0.350	0.153	0.152
3	7	0.90	0.614	0.007	0.085	0.111
"	"	0.92	0.682	0.295	0.271	0.070
"	"	0.94	0.725	-0.007	0.114	0.078
"	"	0.96	0.756	-0.015	-0.004	0.014
"	"	0.98	0.782	0.012	-0.133	0.068
5	5	0.38	0.616	0.100	0.037	0.029
"	"	0.40	0.703	0.434	0.347	0.118
"	"	0.42	0.753	0.623	0.549	0.053
"	"	0.44	0.792	4.147	0.057	0.024
"	"	0.47	0.834	1.959	0.089	0.089
"	"	0.50	0.879	0.038	0.103	0.100
κ	k_θ	ρ	\overline{P}_2	e_{33} (lab-frame)	e_{33} (\hat{n} -frame)	e_{33} (covariant)
3	5	0.92	0.568	-0.259	-0.123	-0.123
"	"	0.94	0.659	-0.228	-0.192	-0.100
"	"	0.96	0.704	-0.232	-0.103	-0.096
"	"	0.98	0.743	-0.198	-0.116	-0.100
"	"	1.00	0.777	-0.238	-0.222	-0.019
3	7	0.90	0.614	-0.142	-0.115	-0.045
"	"	0.92	0.682	-0.140	-0.075	-0.072
"	"	0.94	0.725	-0.165	-0.060	-0.048
"	"	0.96	0.756	-0.130	-0.115	-0.117
"	"	0.98	0.782	-0.124	-0.259	-0.110
5	5	0.38	0.616	-0.083	-0.113	-0.076
"	"	0.40	0.703	-0.123	-0.135	-0.083
"	"	0.42	0.753	-0.132	-0.104	-0.086
"	"	0.44	0.792	-0.096	-2.083	-0.021
"	"	0.47	0.834	-0.147	-0.934	-0.012
"	"	0.50	0.879	-0.171	-0.014	0.003

Tab. F.3: Flexoelectric coefficients (quoted to 3 decimal places) for tapered particles as calculated from 10 Mstep runs.

κ	k_θ	ρ	\bar{P}_2	e_{11} (lab-frame)	e_{11} (\hat{n} -frame)	e_{11} (covariant)
3	5	0.92	0.580	0.188	0.160	0.160
"	"	0.94	0.659	0.165	0.139	0.139
"	"	0.96	0.702	0.090	0.132	0.132
"	"	0.98	0.740	0.250	0.148	0.137
"	"	1.00	0.775	0.161	0.141	0.148
3	7	0.90	0.608	0.173	0.114	0.114
"	"	0.92	0.678	0.156	0.148	0.147
"	"	0.94	0.723	0.256	0.202	0.199
"	"	0.96	0.757	0.152	0.156	0.155
"	"	0.98	0.785	0.060	0.103	0.091
5	5	0.38	0.611	0.081	0.081	0.082
"	"	0.40	0.700	0.068	0.060	0.060
"	"	0.42	0.753	0.080	0.074	0.072
"	"	0.44	0.791	0.529	0.099	0.083
"	"	0.47	0.834	0.315	0.083	0.067
"	"	0.50	0.882	0.070	0.087	0.085
κ	k_θ	ρ	\bar{P}_2	e_{33} (lab-frame)	e_{33} (\hat{n} -frame)	e_{33} (covariant)
3	5	0.92	0.580	-0.229	-0.156	-0.156
"	"	0.94	0.659	-0.229	-0.135	-0.135
"	"	0.96	0.702	-0.220	-0.075	-0.066
"	"	0.98	0.740	-0.253	-0.185	-0.164
"	"	1.00	0.775	-0.257	-0.117	-0.049
3	7	0.90	0.608	-0.178	-0.130	-0.130
"	"	0.92	0.678	-0.177	-0.136	-0.135
"	"	0.94	0.723	-0.169	-0.150	-0.151
"	"	0.96	0.757	-0.165	-0.119	-0.119
"	"	0.98	0.785	-0.169	-0.074	-0.074
5	5	0.38	0.611	-0.102	-0.087	-0.087
"	"	0.40	0.700	-0.114	-0.082	-0.083
"	"	0.42	0.753	-0.112	-0.058	-0.046
"	"	0.44	0.791	-0.135	-0.285	-0.221
"	"	0.47	0.834	-0.158	-0.211	-0.111
"	"	0.50	0.882	-0.165	-0.039	-0.021

Tab. F.4: Flexoelectric coefficients (quoted to 3 decimal places) for rodlike particles as calculated from 10 Mstep runs

κ	k_θ	ρ	\bar{P}_2	e_{11} (lab-frame)	e_{11} (\hat{n} -frame)	e_{11} (covariant)
3	∞	0.877	0.573	0.010	0.015	0.015
"	"	0.894	0.659	0.002	0.022	0.024
"	"	0.911	0.707	0.019	-0.005	-0.002
"	"	0.929	0.741	0.011	-0.006	-0.003
"	"	0.945	0.769	-0.040	-0.011	-0.001
κ	k_θ	ρ	\bar{P}_2	e_{33} (lab-frame)	e_{33} (\hat{n} -frame)	e_{33} (covariant)
3	∞	0.877	0.573	-0.014	0.000	0.001
"	"	0.894	0.659	-0.003	0.023	0.022
"	"	0.911	0.707	0.006	-0.014	-0.012
"	"	0.929	0.741	-0.001	-0.014	-0.012
"	"	0.945	0.769	-0.004	0.010	0.012

Bibliography

- [1] P. J. Collings and M. Hird. *Introduction to Liquid Crystals: Chemistry and Physics*. Taylor & Francis, London, 1997.
- [2] S. Chandrasekhar. *Liquid Crystals*. Cambridge University Press, 2nd edition, 1992.
- [3] P. G. deGennes. *The Physics of Liquid Crystals*. Oxford University Press, 1974.
- [4] L. Onsager. The effects of shape on the interaction of colloidal particles. *Annals of the New York Academy of Sciences*, 51:627–659, 1949.
- [5] B. J. Alder, T. E. Wainwright, and B. M. Mulder. Phase transition for a hard sphere system. *Journal of Chemical Physics*, 27:1208–09, 1957.
- [6] F. C. Bawden, N. W. Pirie, J. D. Bernal, and I. Fankuchen. Liquid crystalline substances from virus-infected plants. *Nature*, 138(5):1051–52, 1936.
- [7] M. P. Allen. Simulations using hard particles. *Phil. Trans. R. Soc. London. A*, 344:323–327, 1993.
- [8] D. J. Cleaver and C. M. Care. Computer simulation of liquid crystals. *Reports on Progress in Physics*, 68(11):2665–2700, 2005.
- [9] J. Vieillard-Baron. The equation of state of a system of hard spherocylinders. *Molecular Physics*, 28(3):6809–818, 1974.
- [10] P. Bolhuis and D. Frenkel. Tracing the phase boundaries of hard spherocylinders. *Journal of Chemical Physics*, 106(2):666–687, 1997.

- [11] J. Vieillard-Baron. Phase transitions of the classical hard-ellipse system. *Journal of Chemical Physics*, 56(10):4729–44, 1972.
- [12] D. Frenkel and B. M. Mulder. The hard ellipsoid of revolution fluid I. Monte Carlo simulations. *Journal of Chemical Physics*, 55(5):1171–92, 1985.
- [13] R. Eppenga and D. Frenkel. Monte Carlo study of the isotropic and nematic phases of infinitely thin hard platelets. *Molecular Physics*, 52(6):1303–34, 1984.
- [14] F. Barmes, M. Ricci, C. Zannoni, and D. J. Cleaver. Computer simulations of pear-shaped particles. *Physical Review E*, 68: art no. 021708, 2003.
- [15] L. J. Ellison, D. J. Michel, F. Barmes, and D. J. Cleaver. Entropy-driven formation of the gyroid cubic phase. *Physical Review Letters*, 97(23): art no.237801, 2006.
- [16] D. Marsh. *Applied geometry for computer graphics and CAD 2nd ed.* Springer, London, 2005.
- [17] R. Berardi, M. Ricci, and C. Zannoni. Ferroelectric nematic and smectic liquid crystals from tapered molecules. *Chem Phys Chem*, 2(7):443–447, 2001.
- [18] J. Vieillard-Baron. Distance of closest approach of two arbitrary hard ellipses in two dimensions. *Physical Review E*, 75(6): art no.061709, 2007.
- [19] J. W. Perram and M. S. Wertheim. Statistical mechanics of hard ellipsoids: I. Overlap algorithm and the contact function. *Journal of Computational Physics*, 58(3):409–416, 1985.
- [20] B. J. Berne and P. Pechukas. Gaussian model potentials for molecular interactions. *Journal of Chemical Physics*, 56(8):4213–16, 1972.
- [21] J. G. Gay and B. J. Berne. Modification of the overlap potential to mimic a linear site-site potential. *Journal of Chemical Physics*, 74(6):3316–19, 1981.

- [22] D. J. Cleaver, C. M. Care, M. P. Allen, and M. P. Neal. Extension and generalisation of the Gay-Berne potential. *Phys. Rev. E*, 54(1):559–67, 1996.
- [23] M. P. Allen and D. J. Tildesley. *Computer Simulation of Liquids*. Oxford University Press, 1987.
- [24] W.C. Swope, H.C. Andersen, P.H. Berens, and K.R. Wilson. A computer simulation method for the calculation of equilibrium constants for the formation of physical clusters of molecules: Application to small water clusters. *Journal of Chemical Physics*, 76(1):637–49, 1982.
- [25] K. Singer, A. Taylor, and J. V. L. Singer. Thermodynamic and structural-properties of liquids modelled by 2-Lennard-Jones centers pair potentials. *Molecular Physics*, 33(5):1757–95, 1977.
- [26] M. P. Allen. Diffusion coefficient increases with density in hard ellipsoid liquid crystals. *Physical Review Letters*, 65(23):2881–84, 1990.
- [27] K. M. Aoki and F. Yonezawa. Constant-pressure molecular-dynamics simulations of the crystal-smectic transition in systems of soft parallel spherocylinders. *Physical Review A*, 46(10):6541–49, 1992.
- [28] H. Dominguez, E. Velasco, and J. Alejandre. Stress anisotropy in liquid crystalline phases. *Molecular Physics*, 100(16):2739–44, 2002.
- [29] J. Prost and J. P. Marcerou. Microscopic interpretation of flexo-electricity. *Journal de Physique*, 38(3):315–24, 1977.
- [30] R. B. Meyer. Piezoelectric effects in liquid crystals. *Physical Review Letters*, 22(18):918–21, 1969.
- [31] M. P. Allen and A. J. Masters. Molecular simulation and theory of liquid crystals: Chiral parameters, flexoelectric coefficients, and elastic constants. *Journal of Materials Chemistry*, 11(11):2678–89, 2001.
- [32] R. Kubo. *Thermodynamics of Irreversible Processes*. IL, Moscow, 1962.

- [33] V. B. Nemtsov and M. A. Osipov. Statistical theory of the flexoelectric effect in liquid crystals. *Kristallografiya*, 31(2):213–218, 1986.
- [34] J. L. Billeter and R. A. Pelcovits. Molecular shape and flexoelectricity. *Liquid Crystals*, 27(9):1151–60, 2000.
- [35] D. L. Cheung, S. J. Clark, and M. R. Wilson. Calculation of flexoelectric coefficients for a nematic liquid crystal by atomistic simulation. *Journal of Chemical Physics*, 121(18):9131–39, 2004.
- [36] A. Dewar. *Computer simulations of liquid crystals*. Phd. thesis, University of Edinburgh, 2005.
- [37] A. Dewar and P. J. Camp. Dipolar interactions, molecular flexibility and flexoelectricity in bent-core liquid crystals. *Journal of Chemical Physics*, 123(17): art no.174907, 2005.
- [38] S. M. Morris, M. J. Clarke, A. E. Blatch, and H. J. Coles. Structure-flexoelastic properties of bimesogenic liquid crystals. *Physical Review E*, 75(4 Pt.1):041701, 2007.
- [39] D. Frenkel and B. Smit. *Understanding Molecular Simulation*. Academic Press, London, 1996.
- [40] D. P. Siegel. The modified stalk mechanism of lamellar/inverted phase transitions and its implications for membrane fusion. *Biophysical Journal*, 76(1):291–313, 1999.
- [41] G. E. Schröder-Turk, A. Fogden, and S. T. Hyde. Bicontinuous geometries and molecular self-assembly: Comparison of local curvature and global packing variations in genus-three cubic, tetragonal and rhombohedral surfaces. *European Physics Journal*, 54(4):509–24, 2006.
- [42] G. E. Schröder-Turk, D. J. Cleaver, and L. J. Ellison. Work in progress. 2007.
- [43] F. Barmes. Unpublished simulation studies. 2003.

[44] K. F. Riley, M. P. Hobson, and S. J. Bence. *Mathematical Methods for Physics and Engineering*. Cambridge University Press, 1997.